EPFL

# Multimodal transcriptomic atlases of mouse spinal cord injury

École
polytechnique
fédérale
de Lausanne

2024

*Tout ce qui est impossible reste à accomplir*

— Jules Verne

# Acknowledgments

Reflecting on the past five years spent at the G-Lab and .NeuroRestore, I'm amazed by how much happened. In 2018, when I joined the lab, the notion of neuroprosthetics for spinal cord-injured patients still seemed like science fiction. However, my perspective shifted after attending my first "G-Lab party" where I had the privilege of witnessing a patient, once confined to a wheelchair, rise and offer a toast.

Later that same year, the lab achieved a groundbreaking milestone by publishing the first study demonstrating the recovery of walking in patients with complete paralysis through spatiotemporal stimulation. Since then, .NeuroRestore has continued to unveil remarkable studies almost every year, reaching a pinnacle with the development of the first-ever digital bridge connecting the brain and spinal cord, and the development of the first-ever regenerative strategy to repair a complete spinal cord injury.

I can't emphasize enough how grateful and proud I am to have had the opportunity to witness and contribute to such numerous breakthroughs, alongside so many incredible scientists.

I would like to express my deepest gratitude to Grégoire and Jocelyne for creating such an outstanding work environment.

I especially want to thanks Grégoire, my thesis director, for offering me the opportunity to work on such remarkable projects. His scientific guidance and infinite patience (especially during my struggles with administrative catastrophes) pushed me into being a better researcher. His unwavering commitment and visionary outlook have inspired me, and I am genuinely convinced that his groundbreaking work will allow patients all over the world to walk out of the hospital on their own two legs after spinal cord injuries.

I also want to thank Jocelyne, as the co-director of .Neurorestore, her input has been critical to guide the clinical relevance of the projects contained within this thesis. She provided constant guidance throughout my thesis to ensure the questions we asked, as well as the results that we presented, could help the clinical spinal cord injury field move forward.

I extend my thanks to my thesis jury—Prof. Fides Zenk, Prof. Brian Kwon, Prof. Binhai Zheng, and Prof. Carl Petersen—for their time, expertise, and constructive feedback.

A heartfelt acknowledgment goes to Jordan, my mentor and friend, whose exceptional guidance and support have been instrumental in shaping my academic and personal growth. I am deeply impressed by your academic career and consider it a privilege to have worked alongside you on all these exciting projects. Your constant availability, willingness to celebrate, genuine enthusiasm for

research, and seemingly endless energy are a source of inspiration to me.

I want to thank my dear friend Mark, whose unwavering support convinced me to embark on this Ph.D. journey and who continued to encourage me through moments of doubt, be it scientific, sentimental or simply one more repetition of burpees.

A special thanks to Loïs, the best office mate/well being officer/general practitioner, for constantly uplifting the mood, coping with my disastrous desktop and taking care of my good health.

To Mike, whose impressive intellect and support have been a cornerstone of my early academic career.

I also want to thank everyone that made the lab such an amazing environment to work in: The OG autonomic team, Remi and Elaine; Mark's angels, Alex, Suje and Viviana; Marco, Nico, Inssia, Victor, Alan, Achilleas and Vi Anh. Tom and Claudia, Nick, Steven, Antoine, Andrea, Leonie and Ed. Arnaud, Katia. The design dream team, Jimmy and Fred. With a special thanks to the .NeuroRestore crew that had to deal with my administrative challenges at one point or the other, Q, Christelle, Laeti, Dylan, Suzanne, thanks for the amazing support.

Last but not least I want to thank my family and friends for their unwavering support. To my wife, who provided me something I never knew I missed, a home to return to. To my good friends Julien and Aurelien for the much needed breathers. To my parents, for consistently trusting in me, even during times when I doubted myself. To my aunt for her genuine curiosity. To my grandparents who ignited my initial scientific curiosity.

*Genève, January 29, 2024*                                                                 Matthieu Gautier

# Abstract

A spinal cord injury (SCI) triggers a cascade of molecular and cellular responses involving inflammatory cell infiltration and cytokine release, apoptosis, demyelination, excitotoxicity, ischemia, and the formation of a fibrotic scar surrounded by an astrocyte border. Altering the course of this cascade to improve neurological outcome is a major challenge in the medical management of SCI, and will require a complete understanding of how neural and non-neural cells coordinate the response to the injury over time and across distinct lesion compartments. Previous attempts to delineate the molecular logic governing this response initially turned to bulk transcriptomics and proteomics of the entire lesion. However, these attempts were technically limited in their ability to resolve cell-type-specific molecular programs triggered by injury, or else focused on isolated aspects of the injury response.

In the work presented in this thesis, I introduce the roadmap toward the establishment of the tabulae paralytica, four molecular and cellular atlases of spinal cord injury (SCI), comprising a single-nucleus transcriptome atlas of half a million cells, a multi-omic atlas pairing transcriptomic and epigenomic measurements within the same nuclei, and two spatial transcriptomic atlases of the injured spinal cord spanning four spatiotemporal dimensions. We faced two main challenges in the establishment of single cell sequencing as a routine tool for the interrogation of spinal circuitry within our group.

First, classical approach to compare cell states across two or more experimental conditions did not allow for the accurate identification of specific cell populations undergoing subtle yet profound transcriptional change. We formulated a fundamentally new perspective on how to identify the specific cell types responding to a perturbation, a statistical measure that leverages a machine-learning algorithm to quantify the relative difficulty of separating cells of each type between experimental conditions.

On the other hand, deciphering the cellular responses to perturbation primarily rely on differential expression (DE) analysis. The central role of DE in the comparative analysis of scRNA-seq data has made it the focus of several recent benchmarks, however these studies have all come to the unsatisfying conclusion that different methods perform best depending on the circumstances. In an attempt to select a robust methodology, we established the first compendium of single-cell datasets in which the experimental ground truth was known, uncovering the principle that dictates the biological accuracy of DE methods.

We built on the expertise acquired in the field of single cell transcriptomic, and established

the *Tabulae Paralytica*, a foundational resource that allowed us to understand the biology of SCI at unprecedented resolution. We uncovered conserved and divergent neuronal responses to the injury, specific neuronal subpopulation primed to become circuit reorganizing neurons and the necessity to reestablish a tripartite neuroprotective barrier between immune-privileged tissues and the lesion compartments. These discoveries allowed us to develop a rejuvenative gene therapy that restored walking after paralysis in old mice. We believe this work represents a biological, technical, and therapeutic landmark in the fields of SCI and genomics.

# Résumé

Les lésions de la moelle épinière déclenchent une cascade de réponses moléculaires et cellulaires impliquant une infiltration de cellules inflammatoires et la libération de cytokines, l'apoptose, la démyélinisation, l'excitotoxicité, l'ischémie et la formation d'une cicatrice fibrotique entourée d'une bordure d'astrocytes. Modifier le cours de cette cascade pour améliorer la récupération neurologique est un défi majeur dans la gestion médicale des lésions médullaires, et nécessitera une compréhension complète de la façon dont les cellules neurales et non neurales coordonnent la réponse à la lésion dans le temps et à travers des compartiments lésionnels distincts. Les tentatives précédentes de délimiter la logique moléculaire régissant cette réponse se sont d'abord tournées vers la transcriptomique et la protéomique de l'ensemble de la lésion. Cependant, ces tentatives étaient techniquement limitées dans leur capacité à résoudre les programmes moléculaires spécifiques à un type de cellule déclenchés par la lésion, ou se concentrent sur des aspects isolés de la réponse à la lésion.

Dans le travail présenté dans cette thèse, je présente la feuille de route pour l'établissement des tabulae paralytica, quatre atlas moléculaires et cellulaires des lésions de la moelle épinière, comprenant un atlas transcriptomique d'un seul noyau d'un demi-million de cellules, un atlas multi-omique associant des mesures transcriptomiques et épigénomiques dans les mêmes noyaux, et deux atlas transcriptomiques spatiaux de la moelle épinière lésée couvrant quatre dimensions spatiotemporelles. Nous avons été confrontés à deux défis principaux dans l'établissement du séquençage de cellules uniques en tant qu'outil de routine pour l'interrogation des circuits de la moelle épinière au sein de notre groupe.

Tout d'abord, l'approche classique consistant à comparer les états cellulaires entre deux ou plusieurs conditions expérimentales ne permettait pas d'identifier avec précision les populations cellulaires spécifiques subissant des changements transcriptionnels subtils mais profonds. Nous avons formulé une perspective fondamentalement nouvelle sur la manière d'identifier les types de cellules spécifiques répondant à une perturbation, une mesure statistique qui s'appuie sur un algorithme d'apprentissage automatique pour quantifier la difficulté relative de séparer les cellules de chaque type entre les conditions expérimentales.

D'autre part, le décryptage des réponses cellulaires aux perturbations repose principalement sur l'analyse de l'expression différentielle (DE). Le rôle central de l'expression différentielle dans l'analyse comparative des données scRNA-seq a fait l'objet de plusieurs études comparatives récentes, mais ces études sont toutes arrivées à la conclusion insatisfaisante que différentes méthodes sont

plus performantes selon les circonstances. Dans le but de sélectionner une méthodologie robuste, nous avons établi le premier recueil d'ensembles de données de scRNA-seq dans lesquels la "ground truth" expérimentale était connue, découvrant ainsi le principe qui dicte la précision biologique des méthodes d'analyse génétique.

Nous nous sommes appuyés sur l'expertise acquise dans le domaine de la transcriptomique sur cellule unique et avons créé les *Tabulae Paralytica*, une ressource fondamentale qui nous a permis de comprendre la biologie des lésions médullaires avec une résolution sans précédent. Nous avons découvert des réponses neuronales conservées et divergentes à la lésion, une sous-population neuronale spécifique prête à devenir des neurones réorganisateurs de circuits et la nécessité de rétablir une barrière neuroprotectrice tripartite entre les tissus immunisés et les compartiments de la lésion. Ces découvertes nous ont permis de mettre au point une thérapie génique qui a rétabli la marche après une paralysie chez de vieilles souris. Nous pensons que ce travail représente un jalon biologique, technique et thérapeutique dans les domaines des neurosciences et de la génomique.

# Contents

# Chapter 1

# Introduction

## 1.1  General introduction

Each year, approximately 800,000 patients around the world suffer an acute spinal cord injury (SCI) (Alizadeh et al., 2019), leaving them to endure one of the most physically and psychologically devastating injuries known to humankind. Traumatic SCI is predominant in males, and the age of incidence peaks in young adults (< 30 years old), with a secondary peak in individuals over 60 years old (Alizadeh et al., 2019; Ahuja et al., 2017; Dobkin et al., 2007). This devastating condition causes a vast range of physiological impairments, such as complete or incomplete paralysis, bladder and bowel dysregulation, sexual, and cardiovascular dysfunctions (Ahuja et al., 2017). This profound dysregulation of almost every bodily function results in a severe reduction in quality and quantity of life, and is also extremely costly to society, with direct lifetime costs of millions of Swiss francs per patient (Krueger et al., 2013).

## 1.2  Clinical approach

For many years, SCI was considered an irreversible condition; recent advances in clinical management have brought about significant improvements in the lives of individuals affected by SCI. One crucial aspect of this progress lies in recognizing the importance of the acute phase in clinical management, where swift intervention can make a substantial difference in patient outcomes.

SCI can be broadly classified as incomplete or complete. Following incomplete SCI, the axons of neurons above the injury leave residual projections below and are responsible for improved recovery of neurological functions. At present, the only effective strategy to augment this recovery is epidural electrical stimulation combined with rehabilitation. Our research group has pioneered the use of

EES to augment the recovery of walking (Lorach et al., 2023; van den Brand et al., 2012; Wagner et al., 2018), as well as hemostatic management of blood pressure (Squair et al., 2021).

However, the effectiveness of this intervention is dependent on the amount of spared tissue and becomes less effective with increasing injury severity. Indeed, following anatomically complete SCI, in which few to no axons remain below the injury, this intervention is ineffective in augmenting recovery of function. In such cases, the only way to augment the recovery of function is to biologically repair the spinal cord. However, every single clinical trial aimed at repairing the injured spinal cord has failed, and there are currently no available treatments. We reason that a better fundamental understanding of the biology of SCI is required in order to develop effective therapeutics. Our lab has recently developed an active interest in understanding lesion site biology and in leveraging this information to develop targeted repair strategies for SCI.

## 1.3   Primary and secondary injury

In SCI, the initial traumatic insult is rarely itself the primary determinant of neurological outcome, but instead initiates a complex and progressive cascade of biochemical processes, collectively termed the 'secondary injury'. This cascade is initially triggered by ischemia, often caused by trauma to the spinal column resulting in disruption to the blood-brain barrier, vasospasm, and intraparenchymal hemorrhage (Amar & Levy, 1999). Ischemia subsequently triggers a series of inflammatory processes, including infiltration of macrophages, neutrophils, microglia, and release of proinflammatory cytokines and matrix metalloproteinases (Bartholdi & Schwab, 1997; Dusart & Schwab, 1994; Kerr & Patterson, 2004; Popovich et al., 1997). This influx, as well as the subsequent degradation of neuronal tissue, propagate the secondary damage and lead to free radical generation as well as lipid peroxidation, ultimately destroying cellular membranes and thereby propagating excitotoxicity (Cuzzocrea et al., 2001; Hall & Braughler, 1993). These processes in turn lead to destruction of neural and glial cells through necrosis and signaled apoptosis, which then drives the development of a functional astrocytic scar. Once this process has taken place, the spinal cord shows very little capacity for repair.

The scientific development of novel therapies to increase sparing at the lesion itself depends upon a detailed, mechanistic understanding of how neural and non-neural cells coordinate the response to SCI over time and across distinct lesion compartments. Previous attempts to delineate the molecular logic governing this response initially turned to bulk transcriptomics (Delahaye-Duriez et al., 2016; Parikshak et al., 2013; Voineagu et al., 2011; Zhang et al., 2013) and proteomics of the entire lesion. While this work demonstrated that systems biology approaches can be productively applied in the setting of neurotrauma, conventional 'bulk' RNA sequencing profiles millions of cells at once, and therefore aggregates highly heterogeneous responses across many different cells within a complex tissue with distinct and reorganizing compartments. This aggregation masks changes in gene expression directed to specific types of cells, such as identifying whether specific neuronal

subpopulations are undergoing apoptosis or contributing to recovery. Moreover, the dramatic shifts in cell type proportions caused by immune infiltration, apoptosis and gliogenesis makes SCI particularly susceptible to the many biases of bulk transcriptomics. These limitations have impeded our understanding of the molecular responses to SCI within individual subpopulations of cells, but such an understanding is essential to successfully alter the course of the secondary injury cascade.

## 1.4    Single cell transcriptomic

A technological revolution in RNA-sequencing technology has made it possible to profile the entire transcriptome of individual cells on a massive scale—a technique known as single-cell RNA-sequencing or scRNA-seq (Svensson et al., 2018). Advances in microfluidic instrumentation (Shalek et al., 2014; Treutlein et al., 2014) and droplet-based methods (Klein et al., 2015; Macosko et al., 2015) now permit sequencing thousands of cells in a single experiment. The rapid pace of methodological and computational progress in single-cell biology has fostered initiatives to profile the transcriptome of cells across the entire nervous system (Zeisel et al., 2018; La Manno et al., 2021), including the spinal cord (La Manno et al., 2021; Delile et al., 2019; Häring et al., 2018; Osseward et al., 2021; Rosenberg et al., 2018; Russ et al., 2021; Sathyamurthy et al., 2018; Skinnider et al., 2021).

These technologies encouraged new terminologies to catalog the cellular diversity in the spinal cord (Zeisel et al., 2018; Häring et al., 2018; Rosenberg et al., 2018). Subsequent work integrated the subpopulations identified in single-cell data with the known lineages of the spinal cord in both the developing (Delile et al., 2019) and post-natal spinal cords (Osseward et al., 2021; Rosenberg et al., 2018; Sathyamurthy et al., 2018). These efforts provide a starting point to interrogate the function of every cell type in the spinal cord.

Single-cell transcriptomics offers an opportunity to elucidate how individual types of cells coordinate their activity to drive pathophysiological processes, and how cell type-specific responses might be targeted to treat disease. Such comparative single-cell experiments, which span multiple experimental conditions, can identify the function of all the cell types in a given tissue, within a single experiment (Sathyamurthy et al., 2018; Arneson et al., 2018; Avey et al., 2018; Bhattacherjee et al., 2019; Davie et al., 2018; Grubman et al., 2019; Hrvatin et al., 2018; Hu et al., 2017; Kim et al., 2019; Mathys et al., 2019; Ximerakis et al., 2019). For example, scRNA-seq or snRNA-seq has implicated the function of key cell types in Alzheimer's disease (Grubman et al., 2019; Mathys et al., 2019), traumatic brain injury (Arneson et al., 2018), recovery of walking after SCI (Skinnider et al., 2021; Kathe et al., 2022), and torpor (Hrvatin et al., 2020). In the field of regeneration, scRNA-seq identified adult progenitor cells recruited after an injury to generate new tissue (Ayyaz et al., 2019), and provided new insights into the molecular mechanisms of regeneration in model organisms (Aztekin et al., 2019; Fincher et al., 2018; Plass et al., 2018; Siebert et al., 2019). These high-throughput experiments are becoming increasingly useful as a complement to hypothesis-driven transcription factors or viral-driven isolation of neuronal subpopulations as for understanding forelimb movements (Esposito

et al., 2014; Ruder et al., 2021), walking (Asboth et al., 2018; Capelli et al., 2017), pain (Choi et al., 2020), itch (Gatto et al., 2021), sleep (Leung et al., 2019), and thirst (Betley et al., 2015).

## 1.5 Multiomic

More recent efforts have further expanded the repertoire of molecular features that can be measured with single cell resolution, including high-order chromatin organization (Nagano et al., 2013), chromatin accessibility via assay for transposase-accessible chromatin assays (snATAC-seq) (Buenrostro et al., 2015; Cusanovich et al., 2015), histone modifications and transcription factor (TF) binding (Carter et al., 2019; Harada et al., 2019; Kaya-Okur et al., 2019; Hainer et al., 2019; Rotem et al., 2015), DNA base modifications (Guo et al., 2013; Mooijman et al., 2016; Wu et al., 2017; Zhu et al., 2017), or mitochondrial DNA (Lareau et al., 2021). Multi-omics methods now also enable combining molecular profiling repertoires within the same cells (Lareau et al., 2021; Cao et al., 2018; S. Chen et al., 2019; Fiskin et al., 2022; Luo et al., 2022; Ma et al., 2020; Mimitou et al., 2021; Zhu et al., 2019, 2020, 2021). Measuring transcriptomic readouts in tandem with regulatory elements enables the identification of cell types that align with existing snRNA-seq atlases of cell types across the nervous system prior to any downstream analysis of the paired modality. This feature makes multi-omic approaches such as combined snRNA-seq and snATAC-seq powerful to incorporate epigenomic data into our understanding of the single-cell biology of SCI.

## 1.6 Spatial transcriptomic

Whereas single-cell transcriptomics and multi-omics have catalyzed a paradigm shift in the study of human disease, a fundamental limitation of these methods is that the requirement for tissue dissociation entails a loss of information about the spatial context of each cell. To overcome this limitation, methods for profiling the entire transcriptome with spatial resolution have recently emerged. These methods attach a short barcode to each mRNA that reflects its position in a two-dimensional tissue (Maynard et al., 2021; Rao et al., 2021). Studies have demonstrated how spatial transcriptome profiling can provide spatial context to single-cell atlases (Asp et al., 2019; (BICCN), 2021; Lake et al., 2023; Maniatis et al., 2019), mapping cell types identified by scRNA-seq to their positions in a complex tissue (Baccin et al., 2020; H. Chen et al., 2021; Foster et al., 2021; Srivatsan et al., 2021). Recent studies have demonstrated how spatial transcriptomics can resolve the spatial distribution of changes in transcription in disease, such as heart disease and amyotrophic lateral sclerosis (Maniatis et al., 2019; Kuppe et al., 2022).

## 1.7 Outline of the thesis

Following the rapid increases in scale and accessibility of single cell technologies, our group began several lines of work involving transcriptomic and epigenomic in the context of SCI. In an effort to optimize and further improve our therapies, we identified a specific neuron subpopulation that makes rehabilitation possible (Kathe et al., 2022) and delineated how natural and spontaneous recovery occurs following a severe but incomplete type of SCI, leading to a targeted and cell type specific repair strategy restoring walking following anatomically complete SCI (Squair et al., 2023).

In this thesis I will present the roadmap toward establishing four multimodal atlases of the spinal cord response to injury, along with two methodological advances to the field of bioinformatic that made it possible.

Computational tools used so far to interpret the results of single cell sequencing relied on the identification of individual genes, proteins, or chromatin regions undergoing significant changes between conditions. This approach does not allow the accurate identification of specific cell populations undergoing the most profound transcriptional change in response to experimental conditions, indeed subtle but meaningful changes in small populations are being overshadowed by broader changes in overrepresented cell types.

The work presented in the second chapter of this thesis introduces a new analytical paradigm we refer to as cell type prioritization, implemented as a freely available, ultra-fast method that we name Augur. The development of Augur was motivated by our effort to identify neural circuits involved in the recovery of walking after paralysis in response to neurostimulation therapies (Kathe et al., 2022). Due to the subtle biological effect size of the rehabilitation paradigm, we initially failed to pinpoint the specific neuron subtypes involved in recovery. Our response to this challenge was to formulate a fundamentally new perspective on how to identify the specific cell types responding to a perturbation. Since this question relies on the highly multivariate data captured by genome-scale technologies, we reasoned that aggregating many independent univariate comparisons is a misguided approach to prioritize these cell types. Instead, we developed a statistical measure that leverages a machine-learning algorithm to quantify the relative difficulty of separating cells of each type between experimental conditions.

Differential expression (DE) methods have been the focus of several recent benchmarks, and hold a central role in the comparative analysis of scRNA-seq data. However these benchmarks reached little consensus on the optimal statistical approach for single cell DE and instead concluded that different methods performed best in different scenarios. This observation compelled us to perform our own comparison, which relied on simulations and a compendium of single cell datasets in which the experimental ground truth was known.

The third chapter of this thesis introduces the establishment of the first compendium of "ground-truth" single cell dataset. This compendium allowed us to benchmark DE methods, highlighting a

striking superiority of so-called "pseudo-bulk" methods compared to default analysis. In addition we devised a progression of experiments to clarify the requirements for valid DE analysis. We show that the performance of statistical methods in single-cell data is contingent on their ability to account for the intrinsic variability of biological replicates. This principle dictates the biological accuracy of DE methods.

In the last chapter of this thesis, I'll introduce the *Tabulae paralytica*, a compendium of four molecular and cellular atlases of SCI, comprising a single-nucleus transcriptome atlas of half a million cells, a multi-omic atlas pairing transcriptomic and epigenomic within the same nuclei, and two spatial transcriptomics atlases of the injured spinal cord spanning the spatiotemporal evolution of the lesion core. These atlases allowed us to understand the biology of SCI at unprecedented resolution; to uncover new principles governing the responses to SCI; and to leverage these discoveries to propose a rejuvenative gene therapy that restored walking after paralysis in old mice.

# Chapter 2

# Cell type prioritization in single-cell data

In this chapter we formulate a fundamentally new perspective on how to identify the specific cell types responding to a perturbation. When we first tried to harness scRNAseq data to identify neurons implicated in recovery of walking, we encountered two main challenges. The existing methods to prioritize cell types responsive to a perturbation were relying on the abundance genes identified as differentially expressed, which strongly correlate with the number cells available, introducing a bias toward larger populations. In addition, complex experimental designs can introduce subtle but meaningful changes in lowly expressed genes that typically would not be detected as differentially expressed. To overcome these limitations we developed a statistical measure that leverages a machine-learning algorithm to quantify the relative difficulty of separating cells of each type between experimental conditions. This algorithm, Augur, enabled the discovery of the spinal circuits restoring walking in response to neurostimulation therapies.

My contribution as a co-second author : I participated in the collection, reprocessing and reanalysis of the compendium of 29 papers used to validate our method. I analyzed the experimental validation data. I participated in the edition and preparation of the manuscript.

# Cell type prioritization in single-cell data

Michael A. Skinnider [1,2,9 ✉], Jordan W. Squair [1,3,4,9 ✉], Claudia Kathe [1,3], Mark A. Anderson[1,3], Matthieu Gautier [1,3], Kaya J. E. Matson[5], Marco Milano [1,3], Thomas H. Hutson [1,3], Quentin Barraud[1,3], Aaron A. Phillips[6], Leonard J. Foster[2,7], Gioele La Manno[1], Ariel J. Levine[5] and Grégoire Courtine [1,3,8 ✉]

**We present Augur, a method to prioritize the cell types most responsive to biological perturbations in single-cell data. Augur employs a machine-learning framework to quantify the separability of perturbed and unperturbed cells within a high-dimensional space. We validate our method on single-cell RNA sequencing, chromatin accessibility and imaging transcriptomics datasets, and show that Augur outperforms existing methods based on differential gene expression. Augur identified the neural circuits restoring locomotion in mice following spinal cord neurostimulation.**

Within a decade, single-cell technologies have scaled from individual cells to entire organisms[1,2]. Investigators are now able to quantify RNA and protein expression, resolve their spatial organization in complex tissues and dissect their regulation in hundreds of thousands of cells. This exponential increase in scale is enabling a transition from atlasing of healthy tissues to delineating the cell-type-specific responses to disease and experimental perturbation[3,4]. This shift requires a parallel analytical transition, from cataloguing the marked molecular differences between cell types to resolving more subtle phenotypic alterations within cell types. Existing tools focus on identifying individual genes or proteins with statistically significant differences between conditions[5]. However, inferences at the level of individual analytes are ill-suited to address the broader question of which cell types are most responsive to a perturbation in the multidimensional space of single-cell data. Such prioritizations could clarify the contribution of each cell type to organismal phenotypes such as disease state, or identify cellular subpopulations that mediate the response to external stimuli such as drug treatment. Cell type prioritization could also guide downstream investigation, including the selection of experimental systems such as Cre lines or fluorescence-activated cell sorting (FACS) gates to support causal experiments. However, investigators currently lack bespoke tools to identify cell types affected by perturbation.

Here, we introduce Augur, a versatile method to prioritize cell types on the basis of their molecular response to a biological perturbation (Fig. 1a). We reasoned that cell types most responsive to a perturbation should be more separable, within the multidimensional space of single-cell measurements, than less affected ones, and that the relative difficulty of this separation would provide a quantitative basis for cell type prioritization. We formalized this difficulty as a classification task, asking how accurately disease or perturbation state could be predicted from highly multidimensional single-cell measurements. For each cell type, Augur withholds a proportion of sample labels, and trains a classifier on the labeled subset. The classifier predictions are compared with the experimental labels, and cell types are prioritized on the basis of the area under the receiver operating characteristic curve (AUC) of these predictions in cross-validation.

As the amount of available training data typically has a strong effect on classifier performance, we anticipated that the uneven relative abundances of cell types in single-cell datasets could confound cell type prioritization. In both simulated data and a compendium of 22 published single-cell RNA sequencing (scRNA-seq) datasets, we found that the AUC scaled with the number of cells, as opposed to the perturbation intensity (Extended Data Figs. 1a,b and 2a,b). To overcome this confounding factor, Augur repeatedly draws small samples from the dataset, and reports the mean AUC across samples. We found that this procedure abolished the dependence on the total number of cells (Fig. 1b,c and Extended Data Figs. 1c,d and 2b). Moreover, we established that Augur correctly prioritized cell types subjected to simulated perturbations of known intensities, finding the AUC increased monotonically with both the amount and magnitude of simulated differential expression (DE; Fig. 1d and Extended Data Fig. 1e,f).

We compared Augur to previously described approaches that have attempted to prioritize cell types on the basis of the relative number of genes passing a statistical threshold for DE[3,6-9]. In both simulated and experimental datasets, we found that the number of DE genes was strongly correlated with the number of cells per type (Extended Data Figs. 1g–i and 2c), causing abundant cell types with modest transcriptional perturbations to be prioritized over rare but more strongly perturbed cell types (Fig. 1e and Extended Data Fig. 1j). Consequently, we found that in simulated datasets with increasingly uneven cell type proportions, the performance of DE methods declined rapidly (Fig. 1f,g and Extended Data Fig. 3a,b). Importantly, this decline occurred even for cell type distributions that were substantially less uneven than those observed in real scRNA-seq data (Extended Data Fig. 3c). In contrast, Augur prioritized cell types with high accuracy regardless of cell type distributions ($r \geq 0.95$; Fig. 1f). In published datasets, we confirmed that this bias led DE methods to prioritize highly abundant cell

types, even when such prioritizations were biologically unlikely (Extended Data Fig. 2d–f). For instance, DE methods identified oligodendrocytes as most strongly perturbed in Alzheimer's disease[10], likely due to their relative abundance in the brain (Extended Data Fig. 2g–j).

We next applied Augur to published scRNA-seq datasets with a quantitative measure of ground truth to evaluate its ability to prioritize cell types exposed to stimuli of known intensity. In homogeneous cell populations, Augur detected the expected dose–response relationships in mononuclear phagocytes from 4 species stimulated with lipopolysaccharide (LPS) ranging from 2 to 6 h[11], whereas DE methods yielded biologically incongruent results (Fig. 1h,i and Supplementary Fig. 1a). To evaluate the performance of Augur in a complex tissue, we analyzed an scRNA-seq dataset of peripheral blood mononuclear cells stimulated with interferon[4], comparing cell type prioritizations to an independent microarray experiment on FACS-purified cells[12]. We observed an almost perfect correspondence between Augur and the number of DE genes in this FACS gold standard, whereas single-cell DE methods were uncorrelated with the gold standard (Fig. 1j,k and Supplementary Fig. 1b).

To evaluate the reproducibility of cell type prioritization, we applied Augur to two independent scRNA-seq studies comparing individuals with Alzheimer's disease and healthy controls[3,10]. Augur produced nearly identical prioritizations, identifying the most profound transcriptional perturbations in neurons and endothelial cells (Fig. 1l). Similarly, we investigated whether Augur could prioritize cell types from identical experimental perturbations, but obtained with orthogonal single-cell technologies. We applied Augur to scRNA-seq[7] and single-cell imaging transcriptomics (STARmap)[13] datasets from the visual cortex after exposure to light. Despite technical differences between the datasets, Augur consistently prioritized excitatory neurons, and even ranked subpopulations of excitatory neurons from specific cortical layers in identical order (Extended Data Fig. 3d). Finally, we applied Augur to single-cell assay for transposase-accessible chromatin sequencing (scATAC-seq) data from bone-marrow-derived cells stimulated with LPS[14], and found that Augur cell type prioritizations mirrored a gold standard from bulk RNA-seq of FACS-sorted cells (Fig. 1m)[15].

Augur can flexibly incorporate continuous or multiclass sample labels in addition to conventional treatment versus control designs. We applied Augur to prioritize cell types of the prefrontal cortex on the basis of quantitative measures of amyloid burden, neuritic plaques and neurofibrillary tangles in individuals with Alzheimer's disease[3]. Cell type prioritizations were strongly correlated to those based on clinical diagnosis, reflecting the pathogenesis of the disease (Supplementary Fig. 2). Likewise, Augur can readily be applied to prioritize cell types in datasets with more than two perturbations (Supplementary Fig. 3).

To apply Augur to single-cell datasets with more complex experimental designs, we devised a test for differential cell type prioritization (Extended Data Fig. 4a). Applying differential prioritization to a single-cell imaging transcriptomics (MERFISH) dataset[16], Augur identified multiple neuron subtypes preferentially activated during parenting in either male or female mice (Extended Data Fig. 4b,c). Similarly, in an scRNA-seq dataset[17], Augur prioritized several neuron subtypes with differential responses to whisker lesioning in $Cx3cr1^{+/-}$ and $Cx3cr1^{-/-}$ mice (Extended Data Fig. 4d).

We also considered whether Augur could be applied directly to single-cell measures of transcriptome dynamics, such as the RNA velocity[18], to specifically prioritize cell types undergoing an acute response to a perturbation on the timescale of transcription. We found that both experimental measurements[19] and computational inference[18] of transcriptional activity consistently captured more information than total RNA abundance in perturbations ranging from 45 min to 4 h in duration (Extended Data Fig. 5a–g). Conversely, we confirmed that transcriptome dynamics did not confer an appreciable information gain to cell type prioritization when the perturbation is chronic (Extended Data Fig. 5h,i).

We finally aimed to demonstrate the relevance of Augur to discover new biological mechanisms. We recently showed that targeted epidural spinal stimulation (TESS) of lumbar segments, augmented by monoaminergic stimulation[20], restores walking after spinal cord injury in individuals with paralysis[21]. However, the neural circuits engaged by this treatment remain enigmatic. We devised an experiment to expose the neuron subtypes recruited by TESS using single-cell transcriptomics (Fig. 2a). Mice received a severe

**Fig. 1 | Augur correctly prioritizes cell types in synthetic and experimental single-cell datasets. a**, A schematic overview of Augur. WT, wild type. KO, knockout. **b**, AUCs of Augur and a naive random forest classifier without subsampling in simulated scRNA-seq datasets containing increasing numbers of cells. Cell type prioritizations are confounded by training dataset size for the naive classifier, but Augur abolishes this confounding factor. The mean and standard deviation of $n=10$ independent simulations are shown. The dotted lines show linear regression; the shaded areas show 95% confidence intervals. **c**, Pearson correlations between the AUC of each cell type and the number of cells of that type sequenced, across a compendium of 22 scRNA-seq datasets, for Augur and a naive random forest classifier without subsampling. Box plot shows the median (horizontal line), interquartile range (hinges) and smallest and largest values no more than 1.5 times the interquartile range (whiskers). **d**, Augur AUCs scale monotonically with both the proportion of DE genes and the magnitude of DE in simulated cell populations of $n=200$ cells. **e**, The relationship between the number of DE genes detected by a representative test for single-cell differential gene expression (Wilcoxon rank-sum test) and the proportion of DE genes simulated between the two populations, for simulated populations of between $n=100$ and $n=1,000$ cells. **f**, Cell type prioritization in simulated scRNA-seq data from a tissue with 5,000 cells, 8 cell types and increasingly unequal numbers of cells per type, as quantified by the Gini coefficient. The Pearson correlation to the simulation ground truth (proportion of DE genes) is shown for Augur and a representative test for single-cell DE (Wilcoxon rank-sum test). The mean and standard deviation of $n=10$ independent simulations are shown. The dotted line shows the mean cell type Gini coefficient across $n=22$ published scRNA-seq datasets (0.52). **$P < 0.01$; ***$P < 0.001$, two-sided paired $t$-test. **g**, Pearson correlation between cell type prioritizations (AUC/number of DE genes) and simulation ground truth for Augur and six tests for single-cell DE in simulated tissues containing 8 cell types ($n=5,000$ cells) with a cell type Gini coefficient of 0.50, approximately equal to the mean of 0.52 in 22 published scRNA-seq datasets. **h**, Cell type prioritizations of bone-marrow-derived mononuclear phagocytes from four species stimulated with LPS for between 2 and 6 h for Augur and a representative test for single-cell DE (Wilcoxon rank-sum test). **i**, Pearson correlation between cell type prioritizations and the duration of LPS exposure for Augur and six tests for single-cell DE (in the same order as in **g**). Pearson correlations with a two-sided $P < 0.05$ are shown in orange. NS, not significant. **j**, Left, Augur cell type prioritizations mirror the number of DE genes in a microarray dataset of FACS-purified cells (two-sided Pearson correlation, $n=6$ cell types matching between bulk and single-cell datasets). Right, the number of DE genes detected in the scRNA-seq dataset by a Wilcoxon rank-sum test is uncorrelated with the FACS gold standard. **k**, Pearson correlation between cell type prioritizations and the FACS gold standard for Augur and 6 tests for single-cell DE ($n=6$ cell types matching between bulk and single-cell datasets). Pearson correlations with a two-sided $P < 0.05$ are shown in orange. **l**, Reproducibility of cell type prioritization in two independent studies of Alzheimer's disease ($n=6$ cell types matching between single-cell datasets, two-sided Pearson correlation). **m**, Augur cell type prioritizations in a scATAC-seq dataset track with the number of DE genes in an RNA-seq dataset of FACS-purified cells ($n=3$ cell types matching between bulk and single-cell data).

contusion of the thoracic spinal cord that led to permanent paralysis of both legs. In the presence of serotonergic and D1 agonists, TESS immediately enabled walking in paralyzed mice (Fig. 2b,c). We performed single-nucleus RNA-seq of 18,514 nuclei from mice walking for 30 min with TESS and control mice, identifying all of the major cell types of the lumbar spinal cord (Fig. 2d and Supplementary Fig. 4). We then subjected the 6,035 identified neurons to an additional round of clustering. This analysis identified 38 neuron subtypes expressing classical marker genes that were detected across experimental conditions (Fig. 2e and Extended Data Fig. 6).

We reasoned that applying Augur directly to the RNA velocity of these neurons could prioritize subtypes that are immediately engaged

by the therapy. Previous studies suggested that TESS generates an electrical field that depolarizes proprioceptive afferent fibers[22]. Consistent with this prediction, Augur robustly prioritized interneurons with the molecular profiles of V2a and V1/V2b neurons, which are known to receive synapses from proprioceptive afferents (Fig. 2f and Extended Data Fig. 7). V2a interneurons have been implicated in left–right alternation[23], whereas V2b interneurons are critical for flexor–extensor alternation[24]. Augur also prioritized *Spp1*-positive neurons, typically associated with motor neurons (Fig. 2f). Virus-mediated anatomical tracing in transgenic mice revealed dense synaptic projections from the prioritized interneurons onto motor neurons (Fig. 2g). The induction of immediate early genes in V2a and V1/V2b interneurons
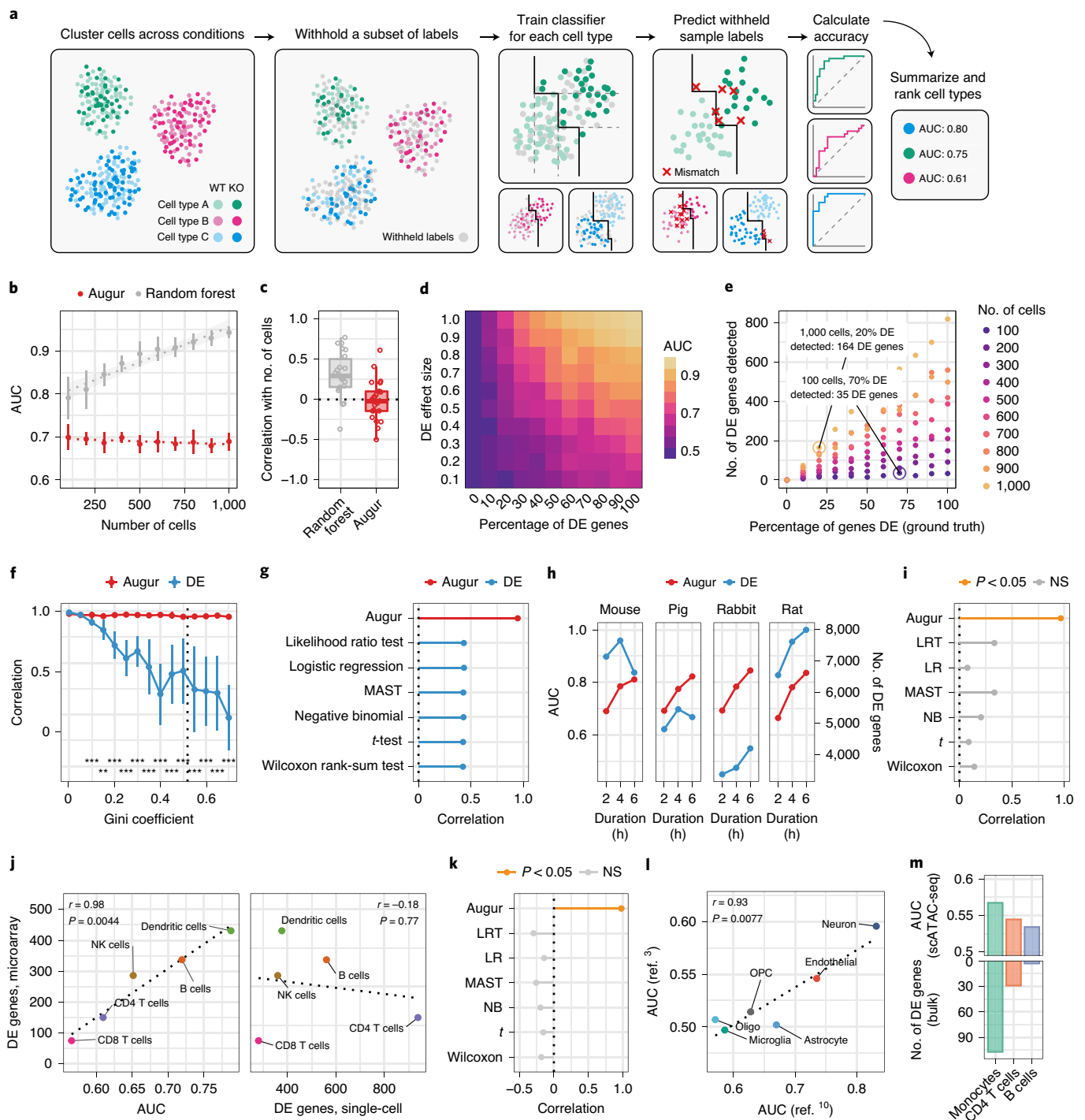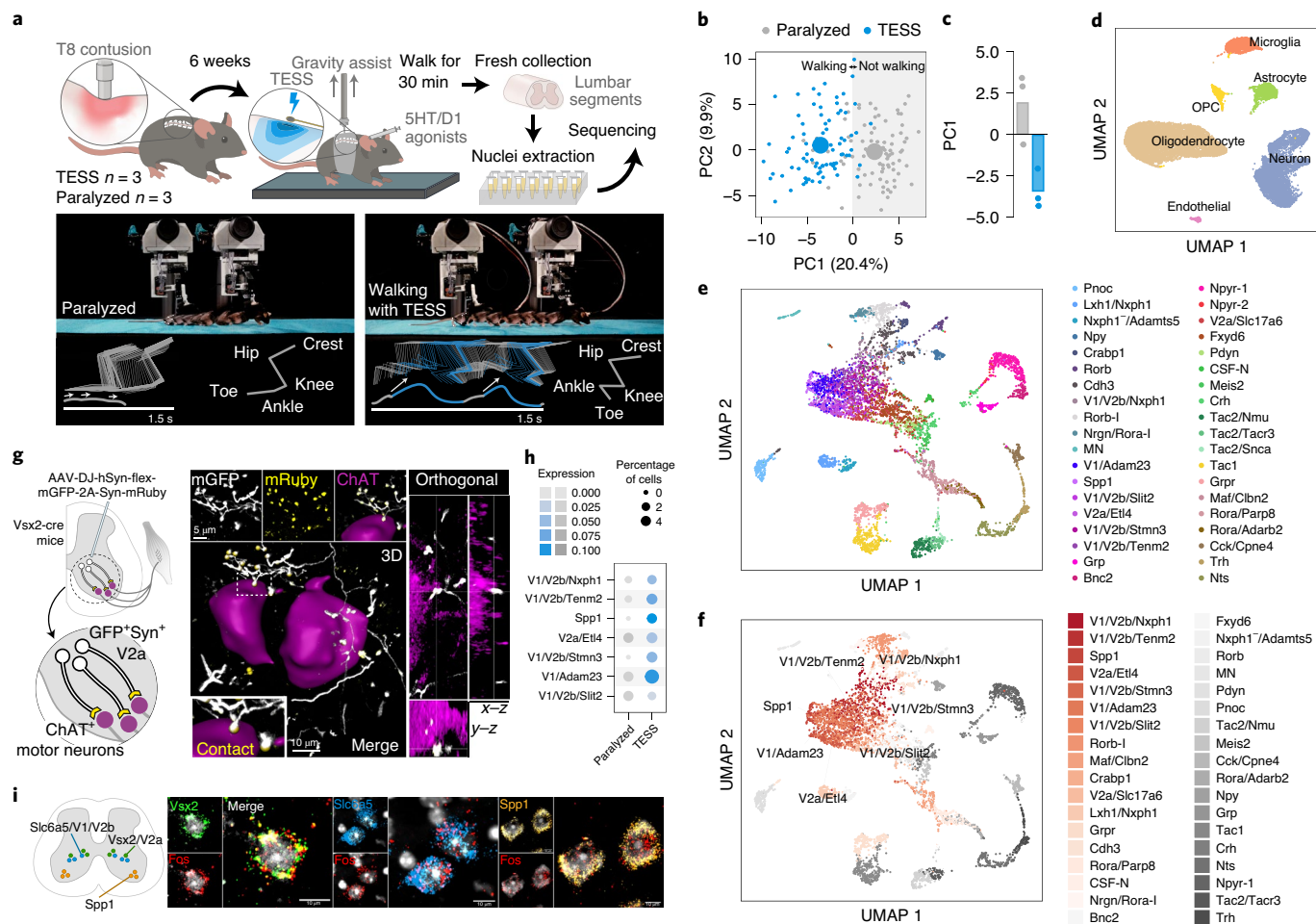
**Fig. 2 | Augur identifies neuron subtypes that enable walking after paralysis. a**, Top, the single-nucleus RNA-seq experimental design to prioritize neuron subtypes recruited by TESS. Middle, chronophotography of mice in the presence or absence of TESS and monoaminergic agonists. Bottom, stick diagram decompositions of right leg movements; leg endpoint trajectory with acceleration at toe-off. **b**, Principal component analysis (*n* = 3 mice) of gait parameters for each condition (small circles). The large circles show the average per group. **c**, Bar plot showing the average scores on principal component 1 (PC1), which quantify the locomotor performance of paralyzed mice (*n* = 3) and mice walking with TESS (*n* = 3). **d**, Uniform manifold approximation and projection (UMAP) visualization of 18,514 nuclei, revealing the 6 major cell types of the mouse lumbar spinal cord. **e**, UMAP visualization of 6,035 neurons subjected to an additional round of subclustering and the 38 identified neuron subtypes. **f**, UMAP visualization of 6,035 neurons, colored by Augur cell type prioritization (AUC). The seven prioritized neuron subtypes with the highest AUCs are highlighted. **g**, Monosynaptically restricted anterograde tracing in Vsx2-Cre mice reveals V2a interneurons densely innervating motor neurons (anti-choline acetyltransferase (ChAT)). Similar results were obtained from three independent experiments. **h**, A dot plot showing the expression of the immediate early gene *Fos* in neuron subtypes prioritized by Augur. **i**, Confirmation of colocalization of V2a, V1/V2b and Spp1 marker genes (Vsx2, Slc6a5 and Spp1, respectively) and Fos by RNAscope in situ hybridization. The schematic indicates the location of imaging for each marker within the spinal cord to aid specificity. Similar results were obtained from two independent experiments.

(Fig. 2h) confirmed their activation in response to TESS-enabled walking, a finding we verified by in situ hybridization (Fig. 2i and Extended Data Fig. 8). In contrast, interneurons not prioritized by Augur showed minimal amounts of *Fos* mRNA (Extended Data Fig. 8). These results illustrate the value of Augur to expose neural circuits underlying complex behaviors.

Augur is computationally efficient, requiring a median of 49.7 min and 2.3 GB of RAM to analyze our compendium of 22 scRNA-seq datasets (Supplementary Fig. 5a,b). Inherent to the design of Augur is the ability to scale to datasets containing hundreds of thousands or even millions of cells on a laptop (Supplementary Fig. 5c,d). Moreover, Augur is robust to sequencing depth and classifier hyperparameters (Supplementary Figs. 6 and 7), and is compatible with both 3' and full-length sequencing protocols (Supplementary Fig. 8). In contrast to single-cell DE methods, Augur incorporates information from both highly and lowly expressed genes (Extended

Data Fig. 9). Augur is robust to several forms of batch effect, and computational batch correction can rescue accurate cell type prioritization under highly confounded experimental designs (Extended Data Fig. 10). Conversely, a limitation of Augur is that inferences at the level of cell types aggregate continuous underlying gradients of response intensity within cell populations, to achieve accurate cell type prioritization. As an efficient and principled method for cell type prioritization, we envision that Augur will facilitate the interpretation of a growing resource of single-cell data spanning multiple experimental conditions, and help single-cell technologies realize their potential to pinpoint cell types underlying organism-level phenotypes.

**Online content**

Any methods, additional references, Nature Research reporting summaries, source data, extended data, supplementary

## References

1. Tang, F. et al. mRNA-Seq whole-transcriptome analysis of a single cell. *Nat. Methods* **6**, 377–382 (2009).
2. Cao, J. et al. Comprehensive single-cell transcriptional profiling of a multicellular organism. *Science* **357**, 661–667 (2017).
3. Mathys, H. et al. Single-cell transcriptomic analysis of Alzheimer's disease. *Nature* **570**, 332–337 (2019).
4. Kang, H. M. et al. Multiplexed droplet single-cell RNA-sequencing using natural genetic variation. *Nat. Biotechnol.* **36**, 89–94 (2018).
5. Soneson, C. & Robinson, M. D. Bias, robustness and scalability in single-cell differential expression analysis. *Nat. Methods* **15**, 255–261 (2018).
6. Rossi, M. A. et al. Obesity remodels activity and transcriptional state of a lateral hypothalamic brake on feeding. *Science* **364**, 1271–1274 (2019).
7. Hrvatin, S. et al. Single-cell analysis of experience-dependent transcriptomic states in the mouse visual cortex. *Nat. Neurosci.* **21**, 120–129 (2018).
8. Avey, D. et al. Single-cell RNA-Seq uncovers a robust transcriptional response to morphine by glia. *Cell Rep.* **24**, 3619–3629 (2018).
9. Chen, R., Wu, X., Jiang, L. & Zhang, Y. Single-cell RNA-Seq reveals hypothalamic cell diversity. *Cell Rep.* **18**, 3227–3241 (2017).
10. Grubman, A. et al. A single-cell atlas of entorhinal cortex from individuals with Alzheimer's disease reveals cell-type-specific gene expression regulation. *Nat. Neurosci.* **22**, 2087–2097 (2019).
11. Hagai, T. et al. Gene expression variability across cells and species shapes innate immunity. *Nature* **563**, 197–202 (2018).
12. Mostafavi, S. et al. Parsing the interferon transcriptional network and its disease associations. *Cell* **164**, 564–578 (2016).
13. Wang, X. et al. Three-dimensional intact-tissue sequencing of single-cell transcriptional states. *Science* **361**, 6400 (2018).
14. Lareau, C. A. et al. Droplet-based combinatorial indexing for massive-scale single-cell chromatin accessibility. *Nat. Biotechnol.* **37**, 916–924 (2019).
15. Reyes, M. et al. Multiplexed enrichment and genomic profiling of peripheral blood cells reveal subset-specific immune signatures. *Sci. Adv.* **5**, eaau9223 (2019).
16. Moffitt, J. R. et al. Molecular, spatial, and functional single-cell profiling of the hypothalamic preoptic region. *Science* **362**, 6416 (2018).
17. Gunner, G. et al. Sensory lesioning induces microglial synapse elimination via ADAM10 and fractalkine signaling. *Nat. Neurosci.* **22**, 1075–1088 (2019).
18. La Manno, G. et al. RNA velocity of single cells. *Nature* **560**, 494–498 (2018).
19. Erhard, F. et al. scSLAM-seq reveals core features of transcription dynamics in single cells. *Nature* **571**, 419–423 (2019).
20. Courtine, G. et al. Transformation of nonfunctional spinal circuits into functional states after the loss of brain input. *Nat. Neurosci.* **12**, 1333–1342 (2009).
21. Wagner, F. B. et al. Targeted neurotechnology restores walking in humans with spinal cord injury. *Nature* **563**, 65–71 (2018).
22. Formento, E. et al. Electrical spinal cord stimulation must preserve proprioception to enable locomotion in humans with spinal cord injury. *Nat. Neurosci.* **21**, 1728–1741 (2018).
23. Crone, S. A. et al. Genetic ablation of V2a ipsilateral interneurons disrupts left–right locomotor coordination in mammalian spinal cord. *Neuron* **60**, 70–83 (2008).
24. Zhang, J. et al. V1 and v2b interneurons secure the alternating flexor–extensor motor activity mice require for limbed locomotion. *Neuron* **82**, 138–150 (2014).

## Methods

**Design and implementation of Augur.** Single-cell technologies increasingly allow investigators to collect datasets that span multiple experimental conditions: for instance, patients with a particular disease compared to healthy controls, animals exposed to a specific behavioral stimulus compared to unstimulated animals, or organisms subject to a particular genetic manipulation and wild-type controls. A number of tools have been developed to identify individual analytes (for instance, genes, proteins or accessible chromatin regions) that exhibit statistically significant differences between experimental conditions[5,25]. However, for many biological questions, the analytical level of interest is not individual differentially abundant features, but rather the specific cell types that are most strongly affected by a stimulus. For instance, investigators may design a single-cell transcriptomics experiment to identify particular cell types in a complex tissue that undergo the most marked transcriptional changes in response to treatment with a drug, to clarify its mechanism of action. We refer to the process of ranking cell types on the basis of their molecular response to a biological perturbation as cell type prioritization.

We designed Augur as a method to prioritize cell types on the basis of their molecular response to a perturbation in highly multidimensional single-cell data. We reasoned that cells undergoing a profound response to a given experimental stimulus should become more separable, in the space of molecular measurements, than cells that remain unaffected by the stimulus. We sought to design a quantitative metric of this separability that would be robust to heteroscedasticity between cell types, and account for the specific biological and technical variability within each cellular subpopulation. Accordingly, Augur quantifies this separability by asking how readily the experimental sample labels associated with each cell (for example, treatment versus control) can be predicted from molecular measurements alone. In practice, this is achieved by training a machine-learning model specific to each cell type, to predict the experimental condition from which each individual cell originated. The accuracy of each cell-type-specific classifier is evaluated in cross-validation, providing a quantitative basis for cell type prioritization.

We reasoned that an ideal method for cell type prioritization would make no assumptions about the distributions of features provided as input, and more broadly, would be agnostic to the particular molecular features provided as input: that is, it would readily incorporate scRNA-seq, proteomics, epigenomics and imaging transcriptomics datasets, among other modalities. Accordingly, Augur uses a random forest classifier to predict sample labels for each cell type. Random forests have the advantage that they do not make any parametric assumptions about the distribution of the input features, and consequently are robust to both the nature of the molecular measurements themselves, and to the specific pre-processing and normalization steps applied to obtain the input features-by-cells matrix.

When training machine-learning models, model performance generally improves as the size of the training dataset increases. We anticipated that this well-known phenomenon could present a critical confounding factor to cell type prioritization, because cell types are unevenly represented in most single-cell datasets for both biological and technical reasons. To account for this confounding factor, Augur repeatedly draws small samples of fixed size from each cell-type-specific gene expression matrix, and performs cross-validation on these subsampled matrices (by default, 50 subsamples of 20 cells per condition are drawn). Augur then reports the mean cross-validation AUC across many small subsamples. We confirmed that this procedure abolishes the relationship between the number of cells of a particular type and the cross-validation AUC, in both real and simulated datasets (Fig. 1b,c and Extended Data Figs. 1 and 2).

To further improve computational efficiency, Augur incorporates two feature selection steps to minimize the number of analytes provided to the classifier as input. First, for each cell type in turn, Augur removes features with little cell-to-cell variation within that cell type. This procedure, commonly referred to as highly variable gene identification in the context of scRNA-seq[26], also has the effect of removing noise. To flexibly account for the mean–variance relationship without making assumptions about the form of this relationship, Augur fits a local polynomial regression between the mean and the coefficient of variation[27,28] using the 'loess' function, and ranks features on the basis of their residuals in this model. A fixed quantile of the most highly variable features are retained for each cell type (specified using the 'var_quantile' parameter, which defaults to 50% to remove only features that show less-than-expected variation based on their mean abundance). Second, for each iteration, a random proportion of features are randomly removed to improve speed and memory usage (specified using the 'feature_perc' parameter, which also defaults to 50%). In combination, these steps substantially reduce the size of the matrix that must be taken out of a sparse representation for input to the classifier, from ~20,000 genes to ~5,000 genes in a typical scRNA-seq dataset. To avoid discarding information in datasets where fewer analytes are measured, feature selection is performed only for datasets exceeding a certain minimum number of features (with this cutoff set, by default, to 1,000).

*Implementation.* Augur is implemented as an R package, available from https://github.com/neurorestore/Augur (Supplementary Fig. 9). Augur takes as input a features-by-cells (for example, genes-by-cells for scRNA-seq) matrix, and a data frame containing metadata associated with each cell, minimally including the cell type annotations and sample labels to be predicted. Alternatively, a Seurat[29], monocle3[30] or SingleCellExperiment[31] object can be provided as input. To optimize both speed and memory usage, all computations are implemented for sparse matrices, up to the classification procedure itself. As the feature selection, classification and cross-validation procedures are independent for each cell type, Augur can readily be parallelized over the cell types in the input dataset, using the 'mclapply' package for parallelization, and runs on four cores by default.

*Multiclass classification and regression.* Augur quantifies the accuracy by which cell type labels can be predicted from molecular measurements using the AUC, or the macro-averaged AUC in the case of multiclass classification. For experiments in which the perturbation can be interpreted as a continuous or ordinal variable, the classification objective is replaced with a regression task, and the accuracy of the corresponding random forest regression models is quantified using the concordance correlation coefficient[32], a measure of both the precision and accuracy of the relationship between predicted and experimental sample labels. By default, Augur returns the mean AUC (or concordance correlation coefficient) for each cell type as a summary of cell type classification, but also calculates a larger suite of metrics for each fold of each subsampling iteration, including accuracy, precision, recall, sensitivity, specificity, negative predictive value and positive predictive value, for users interested in investigating predictions in more detail. Augur also returns the feature importance associated with each input gene (Supplementary Fig. 11).

*Differential prioritization.* To compare cell type prioritizations between related conditions, we devised a permutation-based test for differential prioritization. To obtain a null distribution of AUCs for each cell type that reflected variability associated with the number of cells sequenced, read depth and other technical factors, we permuted sample labels within each cell type, and ran Augur on the permuted dataset. We repeated this permutation procedure 1,000 times. We then compared the observed difference between condition-specific AUCs, $\Delta AUC_{obs}$, for each cell type to the difference under permuted sample labels, $\Delta AUC_{rnd}$, and calculated permutation $P$ values[33].

**Simulations.** We initially tested Augur on simulated scRNA-seq data, using the 'Splatter' R package[34]. Initial simulation parameters were estimated from the Kang et al. dataset[4] using the 'splatEstimate' function, and populations of 100–1,000 cells from two experimental conditions were generated, in increments of 100. We then simulated DE in varying proportions of genes (using the 'de.prob' parameter), and with varying magnitudes (using the 'de.facLoc' parameter). To specifically evaluate the ability of Augur to abolish the relationship between the number of cells in a particular population and the AUC of sample label classification, we compared Augur to cell type prioritization using an identical feature selection and classification procedure, but without drawing small subsamples from the dataset, by setting the 'n_subsamples' argument to 0. We additionally implemented a cell type prioritization scheme based on the number of DE genes between conditions, as previously described[3,6]. Cell types were ranked on the basis of the number of DE genes using six different tests for DE in single-cell transcriptomics datasets (*t*-test, Wilcoxon rank-sum test, likelihood ratio test[35], logistic regression[36], MAST[37] and a negative binomial generalized linear model), implemented through the Seurat 'FindMarkers' function.

To evaluate the impact of different scRNA-seq protocols on cell type prioritization, we repeated these simulations with parameters estimated from libraries prepared by Ziegenhain et al.[38], using six prominent scRNA-seq methods (CEL-seq2, Drop-seq, MARS-seq, SCRB-seq, Smart-seq and Smart-seq2; Supplementary Fig. 8).

To evaluate the impact of mean expression levels on cell type prioritization, we binned genes on the basis of their mean expression into quintiles, and then repeated these simulation experiments with either Augur or a representative single-cell test for DE, the Wilcoxon rank-sum test, run separately on genes from each quintile (Extended Data Fig. 9). To ensure that these two methods were provided with the same genes as input, filtering of lowly variable genes was performed for the entire gene expression matrix, and then Augur was subsequently run with no additional feature selection. We additionally confirmed that these trends were not an artifact of our simulated datasets by performing an identical DE analysis in the Kang et al. dataset[4], again finding that the vast majority of DE genes were detected within the top 20% of the most highly expressed genes.

To evaluate the impact of the distribution of cell type proportions on cell type prioritization in complex tissues, we simulated scRNA-seq experiments with eight cell types. These simulated cell types displayed a graded response to perturbation, having between 10% and 80% of their genes differentially expressed in response to the stimulus in 10% increments. The unevenness of the distribution of cell type frequencies, as quantified by the Gini coefficient, was systematically varied. A total of 5,000 cells were simulated, with the number of cells of each type drawn randomly from a gamma distribution such that the distribution of cell type frequencies achieved a prespecified Gini coefficient in the range from 0 to 0.7, in increments of 0.05. The accuracy of cell type prioritization was quantified as the correlation between the AUC, for Augur, or the number of DE genes, for the six single-cell tests for DE described above, and the proportion of DE genes under the simulation ground truth. To compare these simulations to real scRNA-seq datasets,

we calculated the Gini coefficient of cell type frequencies using the 'reldist' R package across 22 published studies, as described below, obtaining a mean Gini coefficient of 0.52.

Finally, because separability within cell types can arise not only from the cell-intrinsic response to perturbation but also from a number of technical factors, we evaluated the impact of batch effects on cell type prioritization (Extended Data Fig. 10). In simulated populations of 200 cells from 2 experimental conditions, sequenced in 2 batches, we simultaneously varied both the proportion of DE genes and the location parameter for the batch effect factor log-normal distribution ('batch.facLoc'), fixing the location parameter of the DE factor log-normal distribution ('de.facLoc') at 0.5, as above. Under the default model in Splatter, technical batch effects are orthogonal to both the magnitude of perturbation-dependent DE, and the likelihood that a given cell is observed in either the stimulated or unstimulated condition. As the separability between conditions is effectively unchanged in this scenario ('scenario 1'), we extended the Splatter package to incorporate confounding between batch and DE ('scenario 2'), and between batch and experimental condition ('scenarios 3–5'). Confounding between batch and DE is achieved by adjusting the order of operations in Splatter such that DE is simulated before the application of a batch effect, with the result that the batch effect amplifies the perturbation in one of the two batches. Confounding between batch and condition is achieved by adjusting the proportion of cells from each experimental condition within each batch, such that one batch is more likely to contain cells from the stimulated population. The fork of the Splatter repository implementing confounded batch effects is available from https://github.com/jordansquair/splatter_batch. Last, we investigated whether computational methods for batch effect correction could restore the expected gradient of perturbation response in confounded datasets. Using an exemplary approach, the mutual-nearest-neighbors method[39] as implemented in the 'batchelor' R package, we found that computational correction of batch effects restored accurate cell type prioritization. We suggest exploration and, if necessary, computational correction of any batch effects before cell type prioritization with Augur.

**RNA velocity analysis.** To generate intronic and exonic read count matrices for each dataset, data were downloaded from the SRA and converted to FASTQ format using the SRA toolkit. In the case of inDrops data, annotated BAM files were obtained using dropTag[40] with flags -s -S -c. Reads were then aligned to the latest Ensembl release (GRCm38.93), using STAR (v.2.5.3a)[41]. For Drop-seq data, files were first converted from FASTQ to BAM format using the Picard function 'FastqtoSam'. Reads were then aligned to the latest Ensembl release using the Drop-seq toolkit (https://github.com/broadinstitute/Drop-seq). Next, count matrices of exonic and intronic reads were obtained using dropEst with flags -m -V -L eEBA -F. Barcodes were filtered to match those present in the processed datasets uploaded to the Gene Expression Omnibus for each dataset. RNA velocity was subsequently calculated using the 'velocyto' R package[18]. Features were first chosen by filtering for genes with a minimum expression value per cell type using the function 'filter.genes.by.cluster.expression', with filters adjusted on the basis of the read count distributions for each dataset (GSE102827: exon filter, 0.5, intron filter, 0.1; GSE130597: exon filter, 0.03, intron filter, 0.02; GSE103976, exon filter, 0.05, intron filter, 0.03). We then calculated gene-relative velocity using $k$-nearest-neighbor pooling with $k = 10$ (default) and fit.quantile $= 0.01$. By default, the function 'gene.relative.velocity.estimates' in velocyto.R returns a matrix containing only those features for which accurate estimates of $\gamma$ and velocity could be obtained. Consequently, we ran Augur without either variable gene or random gene filters, as feature selection had already been performed during the creation of the RNA velocity matrix used as input. To compare AUCs for cell type prioritization on matrices of exonic or total counts, we retained only those genes for which velocity estimates could be calculated, and likewise disabled the variable gene and random gene filters. All other parameters were left as default.

**Computational benchmarking.** To quantify the computational resources required for cell type prioritization (Supplementary Fig. 5), we ran Augur with default settings on our compendium of 22 scRNA-seq datasets. The R package 'peakRAM' was used to monitor peak memory usage, and the base R function 'system.time' was used to monitor wall time.

**Hyperparameter analysis.** To characterize the robustness of Augur prioritizations to hyperparameters associated with its subsampling or feature selection procedures, the random forest classifier and the choice of classifier itself, we evaluated the impact of systematically varying each of these parameters (Supplementary Fig. 6). We first investigated the impact of the number and size of subsamples from each cell-type-specific gene expression matrix on cell type prioritization, finding that the ranks of each cell type stabilized around 50 subsamples. While larger subsample sizes generally yielded more robust ranks, these thresholds also precluded analysis of several cell types represented by fewer cells in existing datasets, and consequently we opted for an inclusive subsample size of 20 cells per experimental condition. Similarly, we ran Augur on gene expression matrices consisting of the top 10–100% of highly variable genes, followed by selection of a random subset of 10–100% of these, but found that Augur was generally robust to the features provided as input. (We used the default thresholds of 50% on the variable gene

and random selection filters throughout, unless otherwise specified.) To assess the robustness of Augur prioritizations to random forest hyperparameters, we varied the number of trees in the forest between 10 and 1,000, the minimum number of cells required to split an internal node between 2 and 10 and the number of features sampled per split between 2 and 500. Finally, to assess the impact of the classifier itself, we implemented L1-penalized logistic regression in Augur using the R package 'glmnet', with the optimal value of the regularization parameter $\lambda$ determined for each iteration using the function 'cv.glmnet'.

The AUC of cell type prioritization ranges from 0 to 1, where an AUC of 0.5 corresponds to the accuracy of a random classifier, and an AUC of 1 represents perfect classification. Cell type prioritization is most effective when the distribution of AUCs spans a wide range, distinguishing cell types that are unaffected by the perturbation from those that are profoundly affected. However, in situations where all cell types are undergoing a profound perturbation response, or when datasets are sequenced very deeply (and thus more information is available to the classifier), many cell types may have an AUC of 1, representing perfect separability. In this case, Augur hyperparameters may be modified to purposefully degrade the performance of the classifier, and thereby achieve a broader range in the distribution of AUCs across cell types. Conceptually, this can be thought of as effectively the opposite of the hyperparameter tuning step that would typically be performed during the optimization of a machine-learning classifier. Importantly, this intervention is feasible because Augur hyperparameters have remarkably little effect on the rank of different cell types: that is, the cell type prioritizations as such (Supplementary Fig. 6 and Extended Data Fig. 7d). However, although the cell type prioritizations remain consistent, a subset of parameters have a marked effect on the magnitude of the AUCs (Supplementary Fig. 10). Empirically, we suggest decreasing the number of trees in the random forest classifier in scenarios where perfect classification can be achieved for many cell types (Supplementary Fig. 10g). Alternatively, the number of trees may be increased in scenarios where all AUCs are close to 0.5 (for instance, cells undergoing an exceptionally subtle perturbation, or very sparsely sequenced datasets).

**Downsampling analysis.** Motivated by the observation that only a fraction of reads at conventional depths are required to detect transcriptional programs and assign cell types[42], we also evaluated the impact of sequencing depth on Augur cell type prioritizations by downsampling published scRNA-seq datasets to between 5% and 95% of their original depths (Supplementary Fig. 7). Reads were downsampled from the processed count matrices using the 'downsampleMatrix' function from the 'DropletUtils' package[43], with the argument 'bycol = FALSE' to sample without replacement from all reads in the entire dataset rather than from each cell individually.

**Preprocessing and analysis of published single-cell datasets.** Data from a total of 28 published single-cell studies were processed and analyzed with Augur as described in detail in Supplementary Note 1. Unless otherwise noted, expression matrices and metadata were stored as Seurat objects, and genes detected in fewer than three cells were removed.

**Application of Augur to TESS.** To experimentally validate the ability of Augur to uncover new biological mechanisms and identify neuron subtypes involved in complex behaviors, we applied Augur to investigate the neural circuits underlying the functional response to TESS following a field-standard contusion spinal cord injury[44,45] using single-nucleus transcriptomics. Details on the animal model, surgical procedures, post-surgical care, electrochemical stimulation and kinematic analysis are provided in Supplementary Note 2.

*Single-nucleus RNA-seq.* Single-nucleus dissociation was completed with a modified protocol based on our previous work[46]. Briefly, animals were euthanized by isoflurane inhalation and cervical dislocation. The thoracic spinal cord injury site was rapidly dissected and frozen on dry ice. Spinal cords were dounced in 500 μl of sucrose buffer (0.32 M sucrose, 10 mM HEPES (pH 8.0), 5 mM CaCl$_2$, 3 mM Mg acetate, 0.1 mM EDTA, 1 mM DTT) and 0.1% Triton X-100 with the Kontes Dounce Tissue Grinder. A 2 ml volume of sucrose buffer was added and filtered through a 40-μm cell strainer. The lysate was subsequently centrifuged at 3,200$g$ for 10 min at 4 °C. The supernatant was decanted, and 3 ml of sucrose buffer was added to the pellet and incubated for 1 min. The pellet was homogenized using an Ultra-Turrax and 12.5 ml of density buffer (1 M sucrose, 10 mM HEPES (pH 8.0), 3 mM Mg acetate, 1 mM DTT) was added below the nuclei layer. The tube was centrifuged at 3,200$g$ at 4 °C and the supernatant was immediately poured off. The nuclei on the bottom half of the tube wall were collected with 100 μl of PBS with 0.04% BSA and 0.2 U μl$^{-1}$ RNase inhibitor. Resuspended nuclei were filtered through a 30-μm strainer. The nuclei suspension was finally adjusted to 1,000 nuclei per microliter.

*Library preparation.* Library preparation was carried out with 10x Genomics Chromium Single Cell Kit Version 2. The nuclei suspension was added to the Chromium RT mix to achieve loading numbers of 5,000. For downstream cDNA synthesis (13 PCR cycles), library preparation and sequencing, the manufacturer's instructions were followed.

*Read alignment.* Reads were aligned to the latest Ensembl release (GRCm38.93), and a matrix of unique molecular identifier counts was obtained using CellRanger count. Velocyto[18] was subsequently used to obtain count matrices of exonic and intronic reads. Seurat[29] was used to calculate quality control metrics, including the number of genes detected, the number of unique molecular identifiers per cell and the percentage of mitochondrial genes, to filter low-quality cells appropriately (cells with the number of genes expressed <200; cells with the percentage of mitochondrial reads >5%; genes expressed in <3 cells). The matrix used for downstream analysis consisted of 19,954 genes and 18,514 cells.

*Clustering and integration.* To integrate datasets across different experimental conditions, we took advantage of recently developed bioinformatic tools that align datasets from multiple conditions into a unified space[29]. Gene expression data were first normalized using regularized negative binomial models[47], and then integrated across batches using Seurat[29]. Batch effects were regressed out using the 'latent. vars' argument. Normalized and integrated gene expression matrices were clustered using Seurat[29] to identify cell types in the integrated dataset using a standard workflow, including highly variable gene identification, principal component analysis, nearest-neighbor graph construction and graph-based community detection. Following the identification of coarse-grained cell types (for example, 'neuron'), we identified fine-grained neuron subtypes by subclustering major cell types. We used clustering trees[48] to guide the decision of the optimal resolution (Extended Data Fig. 7a). Cell types were manually annotated by using DE analysis to identify marker genes[5,29]. Putative cell types were assigned on the basis of marker gene expression, guided by previous work[46,49–51].

*RNA velocity.* RNA velocity was calculated using the 'velocyto' R package[18]. Velocyto estimates cell velocities from their spliced and unspliced mRNA content. We generated the annotated spliced and unspliced reads using the 'run10x' function of the Velocyto command line tool, as described above. We then calculated gene-relative velocity using $k$-nearest-neighbor pooling with $k = 10$ (default).

*Viral tract tracing.* All surgeries on mice were performed at EPFL under general anesthesia with isoflurane in oxygen-enriched air using an operating microscope, and rodent stereotaxic apparatus (David Kopf). To trace the efferent connections of Vsx2 (V2a) neurons, AAV-DJ-hSyn-flex-mGFP-2A-Syn-mRuby (Stanford Vector Core Facility, reference AAV DJ GVVC-AAV-100, titer $1.15 \times 10^{12}$ genome copies per milliliter[52]) was injected on each side of the cord of Vsx2-Cre mice at the L2 spinal level, 0.25 μl 0.6 mm below the surface at 0.1 μl per minute using glass micropipettes (ground to 50 to 100 μm tips) connected via high-pressure tubing (Kopf) to 10-μl syringes under the control of microinfusion pumps.

*Immunohistochemistry.* After terminal anesthesia by barbiturate overdose, mice were perfused transcardially with 4% paraformaldehyde and spinal cords were processed for immunofluorescence as previously described[53,54]. Primary antibodies were: goat anti-choline acetyltransferase (1:50, Millipore, AB144P). Secondary antibodies were: Alexa Fluor 647 donkey anti goat (1:200; Life Technologies, AB32849). Immunofluorescence was imaged digitally using a slide scanner (Olympus VS-120 Slide scanner) or confocal microscope (Zeiss LSM880 + Airy fast module with ZEN 2 Black software (Zeiss)). Images were digitally processed using ImageJ (NIH) or Imaris (Bitplane, v.9.0.0).

*RNAscope.* We confirmed the in situ localization of cell type markers and the expression of the immediate early gene *Fos* using RNAscope. Briefly, 16-μm cryosections were obtained from fixed frozen spinal cords of animals undergoing identical experimental procedures. We used these sections to confirm the localization of *Spp1* (catalog no. 435191), *Slc6a5* (catalog no. 409741-C3) and *Vsx2* (catalog no. 438341). We additionally included an analysis of negative controls that were not prioritized by Augur including *Cck* (catalog no. 402271-C3), *Npy* (catalog no. 313321), *Rorb* (catalog no. 444271-C3), *Pnoc* (catalog no. 437881), *Gal* (catalog no. 400961-C3) and *Trh* (catalog no. 436811 neurons). All of these cell types have also been validated elsewhere[46,50,51]. We combined gene markers with *Fos* (catalog no. 316921-C2) to confirm the presence of immediate early gene activation in these cell types[46]. To detect the transcripts, we used the RNAscope assay for fixed frozen tissue (Advanced Cell Diagnostics)[55]. Probes were designed and provided by Advanced Cell Diagnostics, Inc. Staining was performed according to standard procedures, using the RNAscope Fluorescent Multiplex Reagent Kit (catalog no. 323133).

**Visualization.** Throughout the manuscript, the box plots show the median (horizontal line), interquartile range (hinges) and smallest and largest values no more than 1.5 times the interquartile range (whiskers), and the error bars show the standard deviation.

**Reporting Summary.** Further information on research design is available in the Nature Research Reporting Summary linked to this article.

## Data availability
Raw sequencing data and count matrices have been deposited to the Gene Expression Omnibus (GSE142245).

## Code availability
Augur is available from GitHub (https://github.com/neurorestore/Augur) and as Supplementary Software 1.

## References
25. Crowell, H. L. et al. On the discovery of population-specific state transitions from multi-sample multi-condition single-cell RNA sequencing data. Preprint at *bioRxiv* https://doi.org/10.1101/713412 (2019).
26. Yip, S. H., Sham, P. C. & Wang, J. Evaluation of tools for highly variable gene discovery from single-cell RNA-seq data. *Brief. Bioinform.* **20**, 1583–1589 (2019).
27. Brennecke, P. et al. Accounting for technical noise in single-cell RNA-seq experiments. *Nat. Methods* **10**, 1093–1095 (2013).
28. Grün, D., Kester, L. & van Oudenaarden, A. Validation of noise models for single-cell transcriptomics. *Nat. Methods* **11**, 637–640 (2014).
29. Stuart, T. et al. Comprehensive integration of single-cell data. *Cell* **177**, 1888–1902 (2019).
30. Cao, J. et al. The single-cell transcriptional landscape of mammalian organogenesis. *Nature* **566**, 496–502 (2019).
31. Amezquita, R. A. et al. Orchestrating single-cell analysis with Bioconductor. *Nat. Methods* **17**, 137–145 (2020).
32. Lin, L. I. A concordance correlation coefficient to evaluate reproducibility. *Biometrics* **45**, 255–268 (1989).
33. Phipson, B. & Smyth, G. K. Permutation P-values should never be zero: calculating exact P-values when permutations are randomly drawn. *Stat. Appl. Genet. Mol. Biol.* **9**, https://doi.org/10.2202/1544-6115.1585 (2010).
34. Zappia, L., Phipson, B. & Oshlack, A. Splatter: simulation of single-cell RNA sequencing data. *Genome Biol.* **18**, 174 (2017).
35. McDavid, A. et al. Data exploration, quality control and testing in single-cell qPCR-based gene expression experiments. *Bioinformatics* **29**, 461–467 (2013).
36. Ntranos, V., Yi, L., Melsted, P. & Pachter, L. A discriminative learning approach to differential expression analysis for single-cell RNA-seq. *Nat. Methods* **16**, 163–166 (2019).
37. Finak, G. et al. MAST: a flexible statistical framework for assessing transcriptional changes and characterizing heterogeneity in single-cell RNA sequencing data. *Genome Biol.* **16**, 278 (2015).
38. Ziegenhain, C. et al. Comparative analysis of single-cell RNA sequencing methods. *Mol. Cell* **65**, 631–643 (2017).
39. Haghverdi, L., Lun, A. T. L., Morgan, M. D. & Marioni, J. C. Batch effects in single-cell RNA-sequencing data are corrected by matching mutual nearest neighbors. *Nat. Biotechnol.* **36**, 421–427 (2018).
40. Petukhov, V. et al. dropEst: pipeline for accurate estimation of molecular counts in droplet-based single-cell RNA-seq experiments. *Genome Biol.* **19**, 78 (2018).
41. Dobin, A. et al. STAR: ultrafast universal RNA-seq aligner. *Bioinformatics* **29**, 15–21 (2013).
42. Heimberg, G., Bhatnagar, R., El-Samad, H. & Thomson, M. Low dimensionality in gene expression data enables the accurate extraction of transcriptional programs from shallow sequencing. *Cell Syst.* **2**, 239–250 (2016).
43. Griffiths, J. A., Richard, A. C., Bach, K., Lun, A. T. L. & Marioni, J. C. Detection and removal of barcode swapping in single-cell RNA-seq data. *Nat. Commun.* **9**, 2667 (2018).
44. Scheff, S. W., Rabchevsky, A. G., Fugaccia, I., Main, J. A. & Lumpp, J. E. Experimental modeling of spinal cord injury: characterization of a force-defined injury device. *J. Neurotrauma* **20**, 179–193 (2003).
45. Squair, J. W. et al. Integrated systems analysis reveals conserved gene networks underlying response to spinal cord injury. *Elife* **7**, e39188 (2018).
46. Sathyamurthy, A. et al. Massively parallel single nucleus transcriptional profiling defines spinal cord neurons and their activity during behavior. *Cell Rep.* **22**, 2216–2225 (2018).
47. Hafemeister, C. & Satija, R. Normalization and variance stabilization of single-cell RNA-seq data using regularized negative binomial regression. *Genome Biol.* https://doi.org/10.1186/s13059-019-1874-1 (2019).
48. Zappia, L. & Oshlack, A. Clustering trees: a visualization for evaluating clusterings at multiple resolutions. *Gigascience* **7**, giy083 (2018).
49. Rosenberg, A. B. et al. Single-cell profiling of the developing mouse brain and spinal cord with split-pool barcoding. *Science* **360**, 176–182 (2018).
50. Häring, M. et al. Neuronal atlas of the dorsal horn defines its architecture and links sensory input to transcriptional cell types. *Nat. Neurosci.* **21**, 869–880 (2018).
51. Zeisel, A. et al. Molecular architecture of the mouse nervous system. *Cell* **174**, 999–1014 (2018).
52. Grimm, D. et al. In vitro and in vivo gene therapy vector evolution via multispecies interbreeding and retargeting of adeno-associated viruses. *J. Virol.* **82**, 5887–5911 (2008).
53. Anderson, M. A. et al. Astrocyte scar formation aids central nervous system axon regeneration. *Nature* **532**, 195–200 (2016).

54. Asboth, L. et al. Cortico-reticulo-spinal circuit reorganization enables functional recovery after severe spinal cord contusion. *Nat. Neurosci.* **21**, 576–588 (2018).

55. Wang, F. et al. RNAscope: a novel in situ RNA analysis platform for formalin-fixed, paraffin-embedded tissues. *J. Mol. Diagn.* **14**, 22–29 (2012).

## Author contributions

M.A.S. and J.W.S. contributed equally to this work. C.K., M.A.A. and M.G. contributed equally to this work and are co-second authors. M.A.S. and J.W.S. designed and implemented Augur, and performed all computational analyses. M.A.S., J.W.S. and M.G. processed published datasets. J.W.S., C.K., M.A.A., T.H.H. and M.M. performed experimental validation work, including viral tract tracing and RNAscope. C.K., K.J.E.M. and A.J.L. performed nucleus extraction and single-nucleus RNA-seq. M.G. and Q.B. analyzed experimental validation data. A.A.P., L.J.F., G.L.M. and G.C. supervised the work. M.A.S., J.W.S. and G.C. wrote the manuscript; all authors contributed to its editing.

## Competing interests

G.C. is a founder and shareholder of GTXmedical, a company with no direct relationships with the present work. M.A.S., J.W.S. and G.C. are named as co-inventors on a patent application related to this work.

## Additional information

**Extended data** is available for this paper at https://doi.org/10.1038/s41587-020-0605-1.

**Supplementary information** is available for this paper at https://doi.org/10.1038/s41587-020-0605-1.

**Correspondence and requests for materials** should be addressed to M.A.S., J.W.S. or G.C.

**Reprints and permissions information** is available at www.nature.com/reprints.
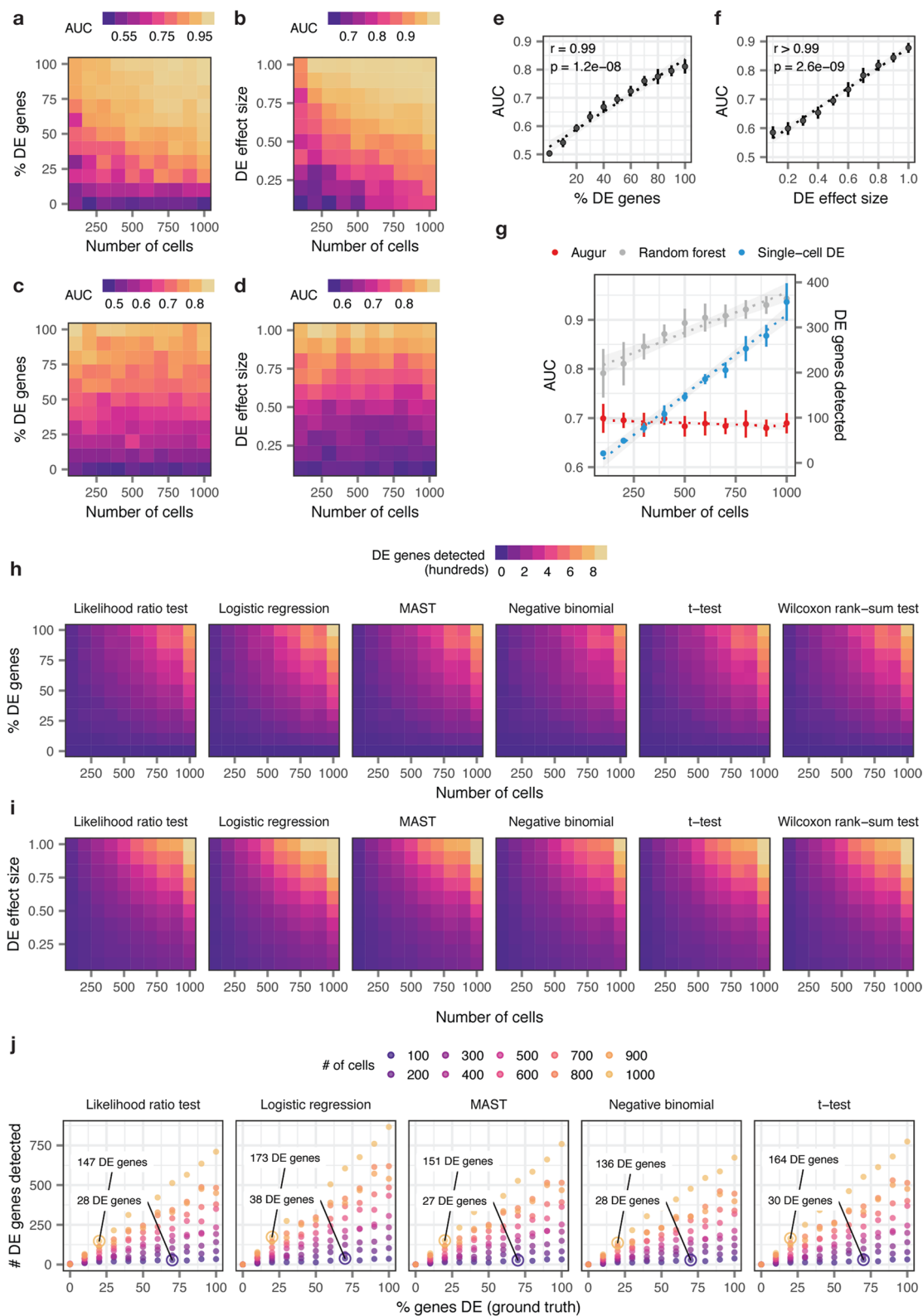
**Extended Data Fig. 1 | See next page for caption.**

**Extended Data Fig. 1 | Augur overcomes confounding factors to cell type prioritization in simulated cell populations. a-b**, Area under the receiver operating characteristic curve (AUC) of a random forest classifier trained in three-fold cross-validation to distinguish two simulated populations of cells[56], with the total number of cells increasing from $n = 100$ to $n = 1,000$ and the proportion of differentially expressed genes between the two populations varying from 0% to 100%, **a**, or the location parameter of the differential expression factor log-normal distribution varying from 0.1 to 1.0, **b**. **c-d**, As in **a-b**, but with the naive random forest classifier replaced with the subsampling procedure employed by Augur. **e-f**, Relationship between Augur AUC and the proportion of differentially expressed genes, **e**, or the location parameter of the differential expression factor log-normal distribution, **f**, in distinguishing two simulated populations ($n = 200$ cells total). The mean and standard deviation of $n = 10$ independent simulations are shown. Inset, two-sided Pearson correlation. **g**, Cell type prioritizations (AUC or number of differentially expressed genes) for a naive random forest classifier, Augur, and an exemplary single-cell differential expression test[5], the Wilcoxon rank-sum test, for two simulated populations of cells with 50% of genes differentially expressed and a log-normal location parameter of 0.5, with the total number of cells increasing from $n = 100$ to $n = 1,000$ cells. Like a naive random forest strategy, the number of differentially expressed genes detected by the Wilcoxon rank-sum test scales linearly with the number of cells. The mean and standard deviation of $n = 10$ independent simulations are shown. Dotted lines show linear regression; shaded areas show 95% confidence intervals. **h-i**, Number of differentially expressed genes detected by six tests for single-cell differential gene expression between two simulated populations of cells, with the total number of cells increasing from 100 to 1,000 and the proportion of differentially expressed genes between the two populations varying from 0% to 100%, **h**, or the location parameter of the differential expression factor log-normal distribution varying from 0.1 to 1.0, **i. j**, Relationship between number of differentially expressed genes detected by five tests for single-cell differential gene expression and the proportion of differentially expressed genes simulated between the two populations, for simulated populations of between 100 and 1,000 cells (see also Fig. 1e). All single-cell differential expression tests detect a larger number of differentially expressed genes in a large population of cells with modest transcriptional perturbation (20% of genes differentially expressed) than in a smaller population of cells with more profound perturbation (70% of genes differentially expressed).

56. Zappia, L., Phipson, B. & Oshlack, A. Splatter: simulation of single-cell RNA sequencing data. *Genome Biol.* **18**, 174 (2017).
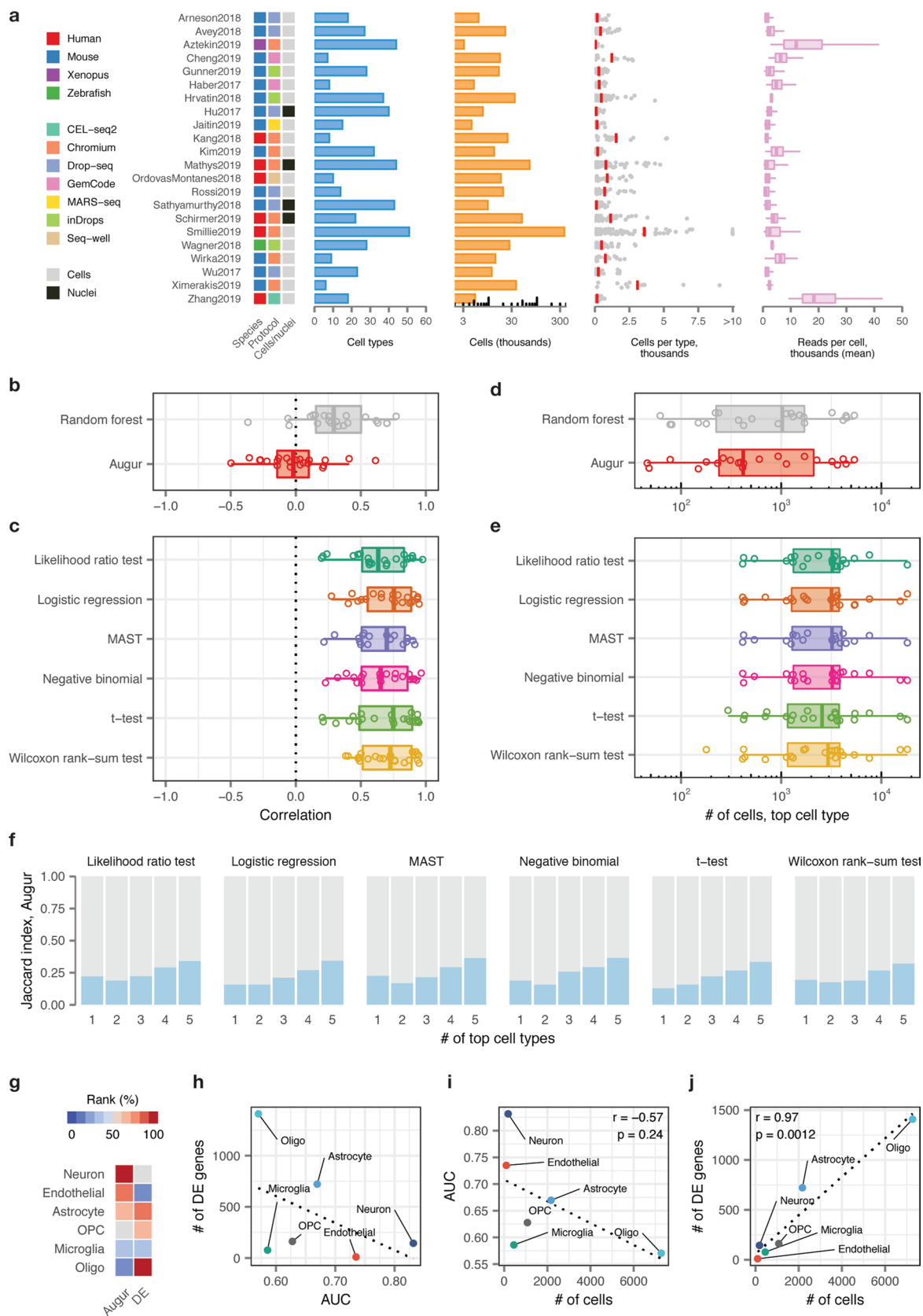
**Extended Data Fig. 2 | See next page for caption.**

**Extended Data Fig. 2 | Augur overcomes confounding factors to cell type prioritization in a compendium of published single-cell RNA-seq datasets.**
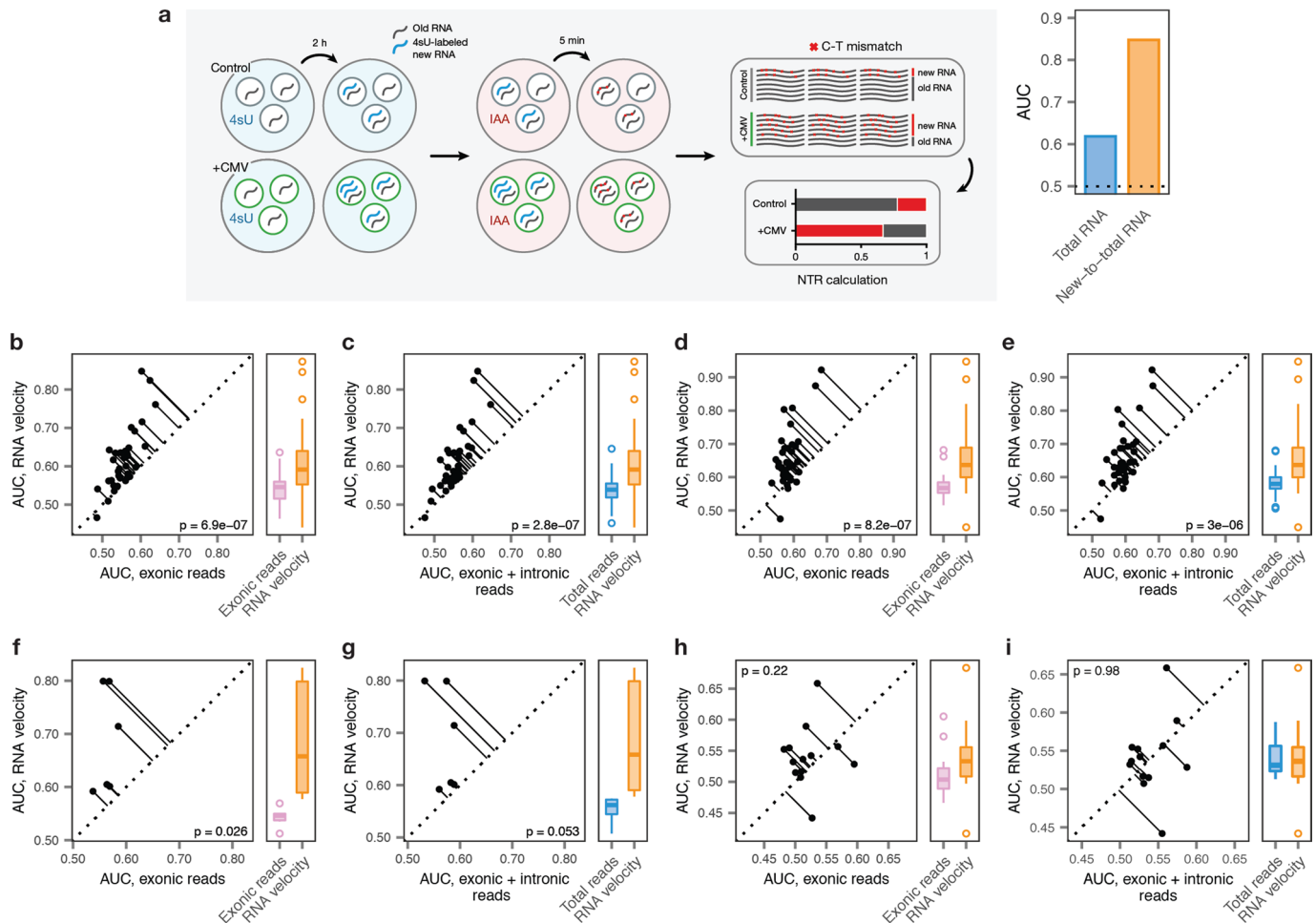**a**, Overview of $n$ = 22 published scRNA-seq datasets comparing two or more experimental conditions, used to verify the relationship between cell type prioritizations from a random forest classifier, Augur, or single-cell differential expression tests. Left, heatmap indicating the species of origin, the sequencing protocol, and whether cells or nuclei were sequenced. Right, properties of each dataset, including the total number of cell types identified in the original studies; the total number of cells sequenced; the number of cells per type (red bars indicate mean); and the mean number of reads for cells of each type. **b**, Pearson correlations between the AUC of each cell type, and the number of cells of that type sequenced, across 22 datasets for Augur, bottom, and a naive random forest classifier without subsampling, top, as shown in Fig. 2c. **c**, Pearson correlations between the number of differentially expressed genes per cell type, at 5% FDR, and the number of cells of that type sequenced, across 22 datasets for six statistical tests for single-cell differential expression. **d**, Number of cells in the top-ranked cell type across 22 datasets for Augur, bottom, and a naive random forest classifier without subsampling, top. **e**, Number of cells in the top-ranked cell type across 22 datasets for six statistical tests for single-cell differential expression. **f**, Jaccard index between the top-ranked 1 to 5 cell types across 22 datasets, comparing Augur and six statistical tests for single-cell differential expression. **g**, Cell type prioritizations in the Grubman et al.[10] dataset by Augur and a representative test for single-cell differential expression, the Wilcoxon rank-sum test ("DE"). **h**, Relationship between AUC and number of differentially expressed genes per cell type, at 5% FDR, in the Grubman et al.[10] dataset. Dotted line shows linear regression. **i**, Relationship between AUC and number of cells sequenced in the Grubman et al.[10] dataset. Augur cell type prioritizations are uncorrelated with the number of cells per type. Dotted line shows linear regression; inset shows two-sided Pearson correlation. **j**, Relationship between number of differentially expressed genes and number of cells sequenced in the Grubman et al.[10] dataset. Cell type prioritizations based on the number of differentially expressed genes are strongly correlated with the number of cells per type. Dotted line shows linear regression; inset shows two-sided Pearson correlation.
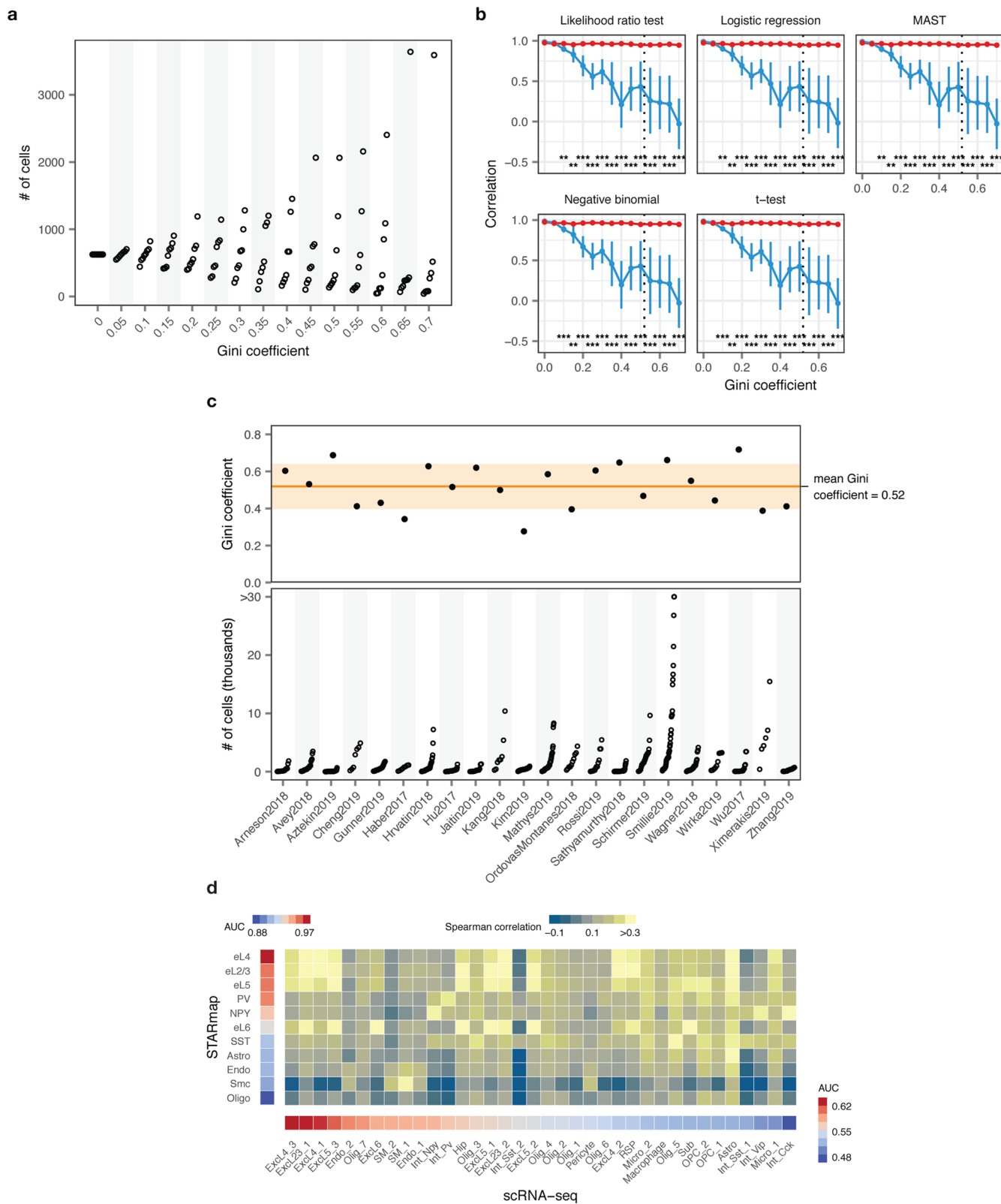
**Extended Data Fig. 3 | See next page for caption.**

**Extended Data Fig. 3 | Augur overcomes confounding factors to cell type prioritization in simulated tissues and across single-cell modalities.**
**a**, Number of cells within each of eight cell types in a simulated tissue with increasingly unequal cell type proportions, as quantified by the Gini coefficient.
**b**, Cell type prioritization in simulated scRNA-seq data from a tissue with 5,000 cells distributed in eight cell types, with 10-80% of genes DE in response to perturbation, and increasingly unequal numbers of cells per type (as quantified by the Gini coefficient). The correlation to simulation ground truth (proportion of DE genes) is shown for five tests for single-cell differential gene expression. The mean and standard deviation of $n = 10$ independent simulations are shown. Dashed line shows mean Gini coefficient of cell type frequencies across 22 published scRNA-seq datasets. **, $p < 0.01$; ***, $p < 0.001$, two-sided paired t-test. **c**, Inequality of cell type proportions in published scRNA-seq data. Top, Gini coefficient of cell type proportions across 22 published scRNA-seq datasets. Horizontal line and shaded area show the mean and standard deviation of the Gini coefficient across all datasets. Bottom, number of cells of each type across 22 published scRNA-seq datasets. **d**, Comparison of cell type prioritization in independent scRNA-seq and single cell imaging transcriptomics (STARmap) studies of the mouse visual cortex after light exposure. Left, Augur cell type prioritization in the STARmap dataset[13]. Bottom, Augur cell type prioritization in the scRNA-seq dataset[7]. Center, correspondence between cell types defined in the scRNA-seq and STARmap datasets, quantified as the Spearman correlation coefficient between average profiles for each cell type across 139 genes present in both datasets.

**Extended Data Fig. 4 | Differential cell type prioritization in single-cell RNA-seq data. a**, Schematic overview of the permutation-based test for differential prioritization with Augur. First, cell type prioritization is performed within each of two conditions separately, yielding condition-specific AUCs for each cell type. Next, sample labels are randomly permuted within each cell type, and cell type prioritization is performed on shuffled data, yielding a null distribution of AUCs for each cell type and condition. AUCs for matching cell types are compared across conditions to calculate a 'ΔAUC score' for each cell type, and a null distribution of ΔAUC scores is calculated using the permuted data. Permutation p-values can then be calculated for each cell type, enabling the identification of statistically significant differences in cell type prioritization between conditions, as well as the condition in which the cell type is more transcriptionally separable. **b**, Neuron subtypes with statistically significant differences in AUC between female and male mice during parenting, in a single-cell imaging transcriptomics experiment employing multiplexed error robust fluorescence in situ hybridization (MERFISH)[6] ($n = 79$ subtypes). Eleven subtypes have significantly higher AUCs in female parents, whereas two have significantly higher AUCs in male parents.
**c**, Relationship between differential prioritization ΔAUC for parenting between male and female mice, and AUC for sex in naive mice. Several neuronal subtypes preferentially activated during parenting in female mice are also transcriptionally distinct in naive mice, such as the I-32 cluster, which is enriched for aromatase expression, and expresses multiple sex steroid hormone receptors[16]. **d**, Neuron subtypes with statistically significant differences in AUC in response to whisker lesioning in *Cx3cr1*^{+/−} as compared to *Cx3cr1*^{−/−} mice, in a single-cell RNA-seq experiment[17] ($n = 28$ subtypes). Four subtypes are have significantly higher AUCs in homozygous mice, whereas one subtype has a significantly higher AUC in heterozygous mice.

**Extended Data Fig. 5 | Cell type prioritization from transcriptional dynamics in acute experimental perturbations. a**, Left, schematic overview of the scSLAM-seq[19] workflow. Cells are exposed to the nucleoside analogue 4-thiouridine (4sU), which is incorporated during transcription and converted to a cytosine analogue by iodoacetamide prior to RNA sequencing. This labeling permits *in silico* deconvolution of RNA molecules transcribed before and after 4sU exposure ('old' and 'new', respectively), and calculation of the ratio of new to total RNA (NTR), an experimental analogue to the computationally determined 'RNA velocity'[18,19]. Right, AUCs for mouse fibroblasts exposed to lytic mouse cytomegalovirus (CMV) at 2 h post-infection, calculated by applying Augur to either total RNA or the NTR. The greater separability for the NTR reflects additional information specifically captured by the temporal dynamics of RNA expression in the context of this acute perturbation[19]. **b-e**, Cell type prioritization based on exonic reads, total RNA, or RNA velocity for cells of the mouse visual cortex after exposure to light for 1 h, **b-c**, or 4 h, **d-e**, in the Hrvatin et al.[7] dataset. The AUC is significantly higher for RNA velocity than for either exonic reads (1 h, *n* = 34 cell types, 4 h, *n* = 35 cell types; two-sided paired t-tests: **b**, 1 h, p = 6.9 × 10^{-7}; **d**, 4 h, p = 8.2 × 10^{-7}) or total RNA (**c**, 1 h, p = 2.8 × 10^{-7}; **e**, 4 h, p = 3.0 × 10^{-6}), reflecting additional information specifically captured by acute transcriptional dynamics. **f-g**, Cell type prioritization based on exonic reads, total RNA, or RNA velocity in an Act-seq[57] dataset, which minimizes transcriptional changes induced by single-cell dissociation. Cell types of the medial amygdala in mice subjected to 45 min of immobilization stress and control mice were profiled by Drop-seq[58] after treatment with the transcription inhibitor actinomycin D. The AUC is higher for RNA velocity than for either exonic reads (**f**, p = 0.026, *n* = 6 cell types) or total RNA (**g**, p = 0.053), reflecting the additional information specifically captured by acute transcriptional dynamics, and indicating this is not an artefact related to the transcriptional perturbations known to be induced by conventional dissociation procedures[59]. **h-i**, Cell type prioritization based on exonic reads, total RNA, or RNA velocity in a chronic perturbation. Cell types of the lateral hypothalamic area were profiled by Drop-seq[58] in mice after 9-16 weeks of maintenance on either high-fat diet or control diet[6]. No significant difference in AUCs was observed for RNA velocity compared to either exonic reads (**h**, p = 0.22, *n* = 13 cell types) or total RNA (**i**, p = 0.98), consistent with the time scale of the experimental perturbation.

57. Wu, Y. E., Pan, L., Zuo, Y., Li, X. & Hong, W. Detecting activated cell populations using single-cell RNA-seq. *Neuron* **96**, 313–329.e6 (2017).
58. Macosko, E. Z. et al. Highly parallel genome-wide expression profiling of individual cells using nanoliter droplets. *Cell* **161**, 1202–1214 (2015).
59. van den Brink, S. C. et al. Single-cell sequencing reveals dissociation-induced gene expression in tissue subpopulations. *Nat. Methods* **14**, 935–936 (2017).
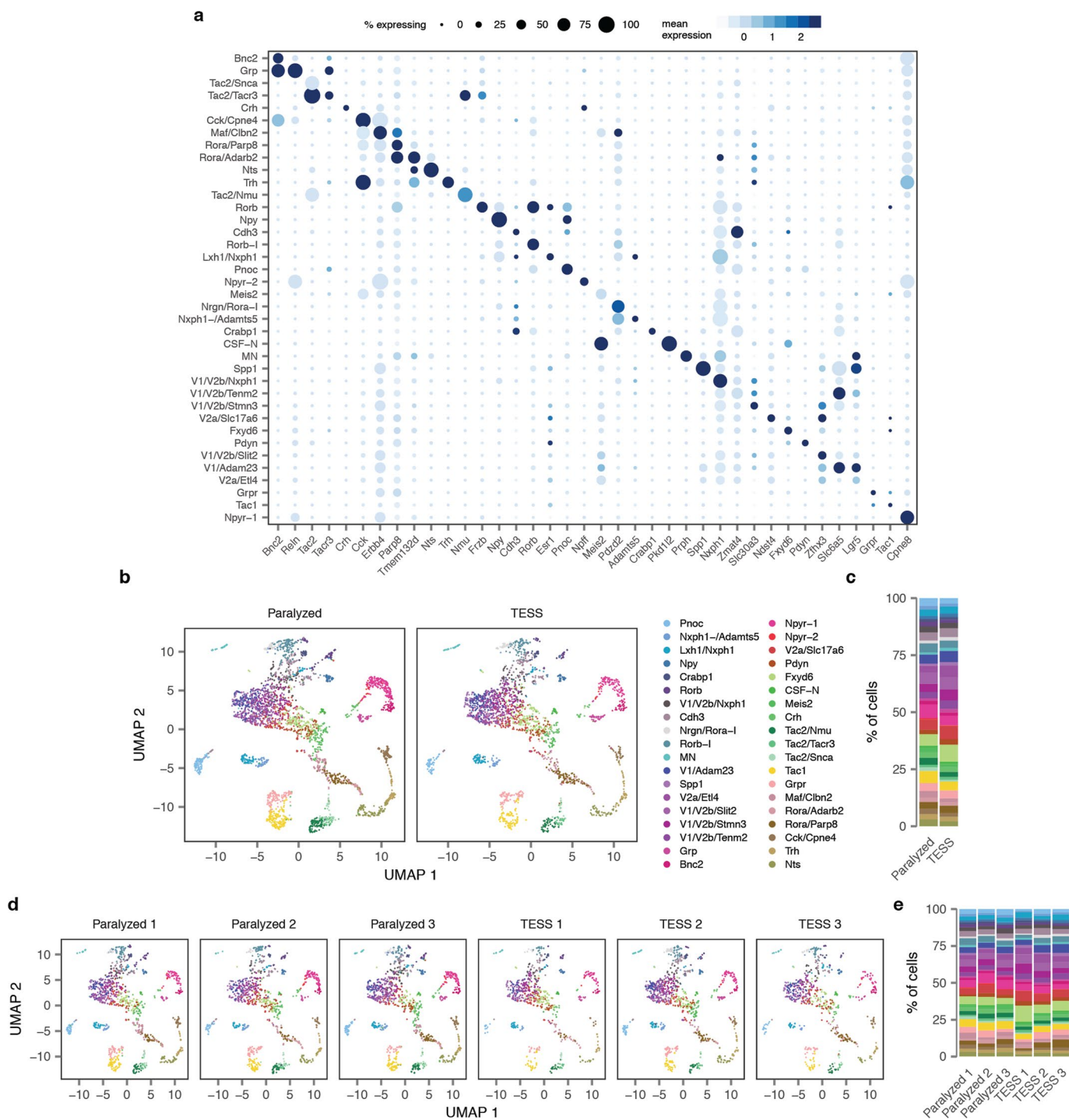
**Extended Data Fig. 6 | Subclustering of single-neuron transcriptomes identifies 38 neuron subtypes in the mouse lumbar spinal cord.** See also Extended Data Fig. 7a. **a**, Dot plot showing expression of one marker gene per cell type for the 38 neuron subtypes of the mouse lumbar spinal cord. **b**, Neuron subtype detection across experimental conditions (*n* = 6,035 neurons). TESS, targeted electrical epidural stimulation of the lumbar spinal cord. **c**, Proportion of neurons of each subtype detected in each experimental condition. **d**, Neuron subtype detection across experimental replicates (n = 3 mice per condition). **e**, Proportion of neurons of each subtype detected in each experimental replicate.
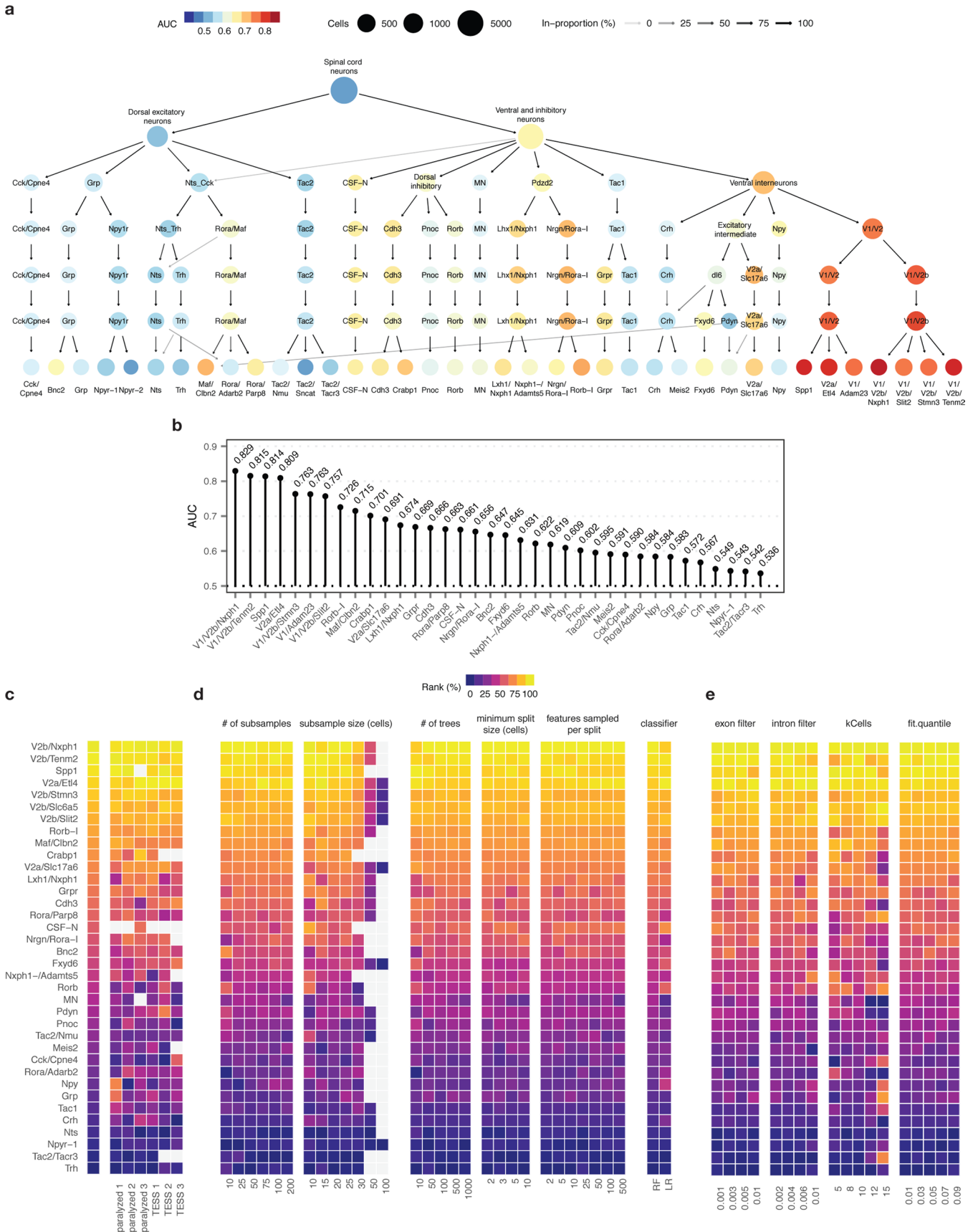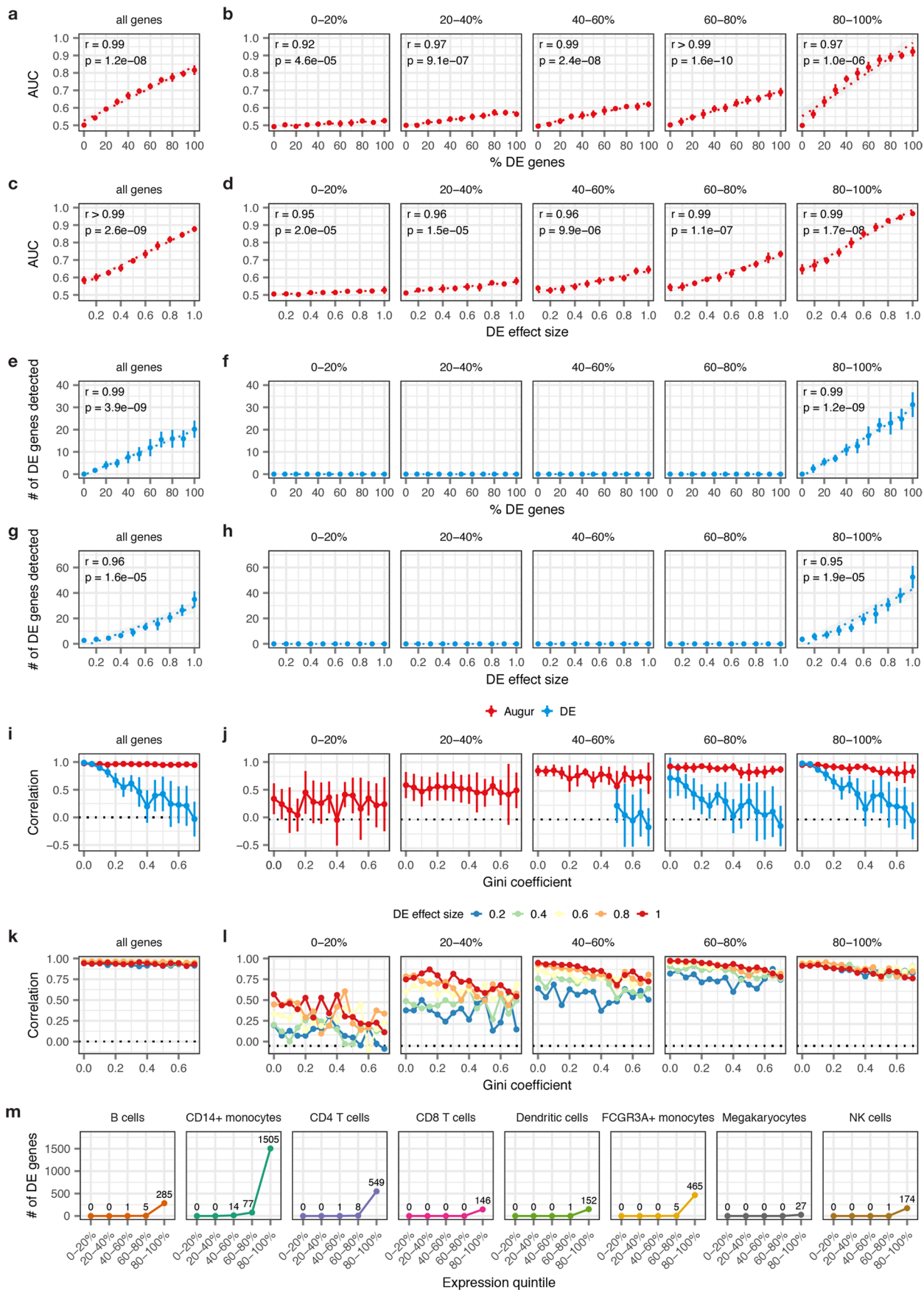
**Extended Data Fig. 7 | See next page for caption.**

**Extended Data Fig. 7 | Robustness of Augur cell type prioritizations for mouse lumbar spinal cord neurons. a**, Clustering tree[48] of mouse spinal cord neurons over seven clustering resolutions, revealing the hierarchical relationships between spinal cord neuron subtypes. Node color reflects AUCs for cell type prioritization in targeted electrical epidural stimulation. **b**, AUCs for each of 36 neuron subtypes represented by at least 20 cells in both control and TESS-treated mice. **c-e**, Robustness of cell type prioritization for neuron subtypes of the mouse lumbar spinal cord. **c**, Impact of systematically withholding cells from each of six replicates ($n = 3$ per group) on cell type prioritization. Left, cell type prioritization with all six replicates, as in Fig. 2f. Grey tiles indicate neuron subtypes that were not represented by at least 20 cells in each condition after removal of cells from an experimental replicate. **d**, Impact of varying Augur parameters, including the number of subsamples and the size of each subsample; random forest-specific hyperparameters (number of trees, minimum split size, number of features sampled per split); and the choice of classifier (random forest, RF; L1-penalized logistic regression, LR) on cell type prioritization. Grey tiles indicate sample sizes larger than the number of cells of that type in the dataset. **e**, Impact of varying RNA velocity parameters, including exonic and intronic expression filters, the number of cells in the k-nearest neighbors pooling, and the extreme quantiles used to fit γ coefficients, on cell type prioritization.
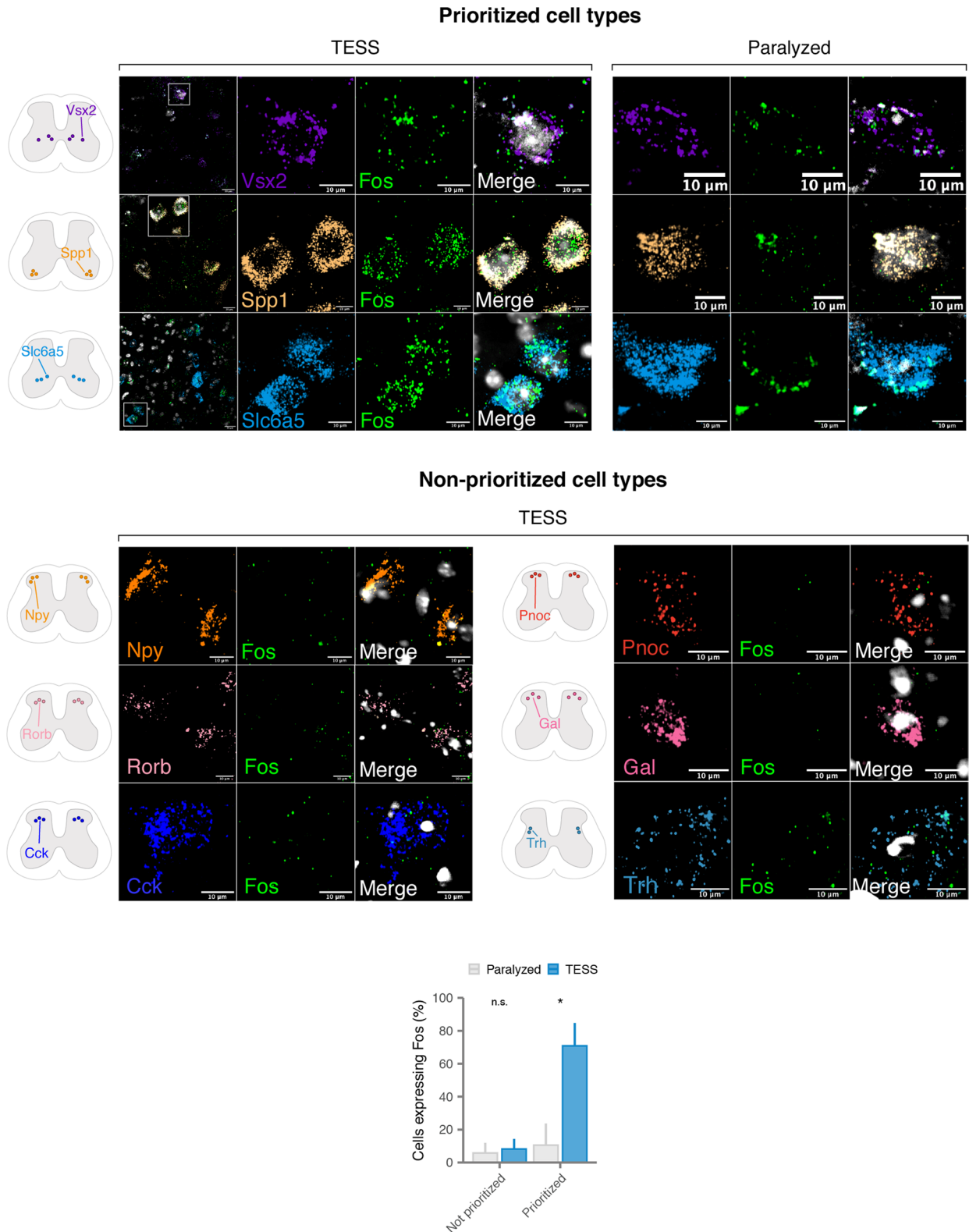
**Extended Data Fig. 8 | Absence of colocalization of canonical marker genes for cell types not prioritized by Augur and Fos by RNAscope *in situ* hybridization.** Schematic indicates imaging location for each marker within the spinal cord. Bottom, proportion of cells expressing Fos from cell types prioritized by Augur ($n = 3$ cell types) or not prioritized by Augur ($n = 6$ cell types). Cell types prioritized by Augur are significantly more likely to express Fos after walking with TESS, compared to controls ($p = 0.01$, two-sided Fisher's exact test), whereas cell types not prioritized by Augur do not display a statistically significant difference ($p = 0.74$). Error bars show standard deviation of the sample proportion.

**Extended Data Fig. 9 | See next page for caption.**

**Extended Data Fig. 9 | Impact of mean gene expression level on cell type prioritization.** Cell type prioritizations were performed using both Augur and a representative single-cell differential expression method, the Wilcoxon rank-sum test, using the entire transcriptome (left column) or genes divided into five quintiles based on mean expression (right columns). Insets show two-sided Pearson correlations throughout. **a**, Relationship between Augur cell type prioritizations (AUC) and the proportion of differentially expressed genes between two simulated populations of cells ($n = 200$ cells total), as shown in Extended Data Fig. 1e. The mean and standard deviation of $n = 10$ independent simulations are shown. **b**, As in **a**, but with Augur applied to each quintile of gene expression separately. The AUC remains strongly correlated with the ground-truth perturbation intensity, regardless of mean expression levels ($r \geq$ 0.92). **c**, Relationship between Augur cell type prioritizations (AUC) and the location parameter of the differential expression factor log-normal distribution between two simulated populations of cells ($n = 200$ cells total), as shown in Supplementary Fig. 1f. The mean and standard deviation of $n = 10$ independent simulations are shown. **d**, As in **c**, but with Augur applied to each quintile of gene expression separately. The AUC remains strongly correlated with the ground-truth perturbation intensity, regardless of mean expression levels ($r \geq 0.95$). **e-f**, As in **a-b**, but showing the number of differentially expressed genes detected by a Wilcoxon rank-sum test at 5% FDR, either across the entire transcriptome, **e**, or within each expression quintile, **f**. No differentially expressed genes are detected at 5% FDR outside of the top expression quintile. **g-h**, As in **c-d**, but showing the number of differentially expressed genes detected by a Wilcoxon rank-sum test at 5% FDR, either across the entire transcriptome, **g**, or within each expression quintile, **h**. No differentially expressed genes are detected at 5% FDR outside of the top expression quintile. **i**, Cell type prioritization in simulated scRNA-seq data from a tissue with 5,000 cells, distributed in eight cell types, with increasingly unequal numbers of cells per type, as quantified by the Gini coefficient and shown in Fig. 1f. The correlation to simulation ground truth (proportion of DE genes) is shown for Augur and a representative test for single-cell DE (Wilcoxon rank-sum test). The mean and standard deviation of $n = 10$ independent simulations are shown. **j**, As in **i**, but with both Augur and the Wilcoxon rank-sum test applied to each quintile of gene expression separately. **k**, Pearson correlation between Augur cell type prioritizations (AUC) and simulation ground truth (proportion of DE genes) in simulated scRNA-seq data from tissue with eight cell types, subjected to perturbations of varying intensity, as quantified by the the location parameter of the differential expression factor log-normal distribution. The mean of $n = 10$ independent simulations is shown for each perturbation intensity.. **l**, As in **k**, but with Augur applied to each quintile of gene expression separately. Augur incorporates information from lowly expressed genes even in subtle perturbations. **m**, Number of differentially expressed genes detected by a Wilcoxon rank-sum test at 5% FDR for each cell type in the Kang et al. dataset[4], within each expression quintile, confirming the simulations in **a-l** reflect trends in real data.
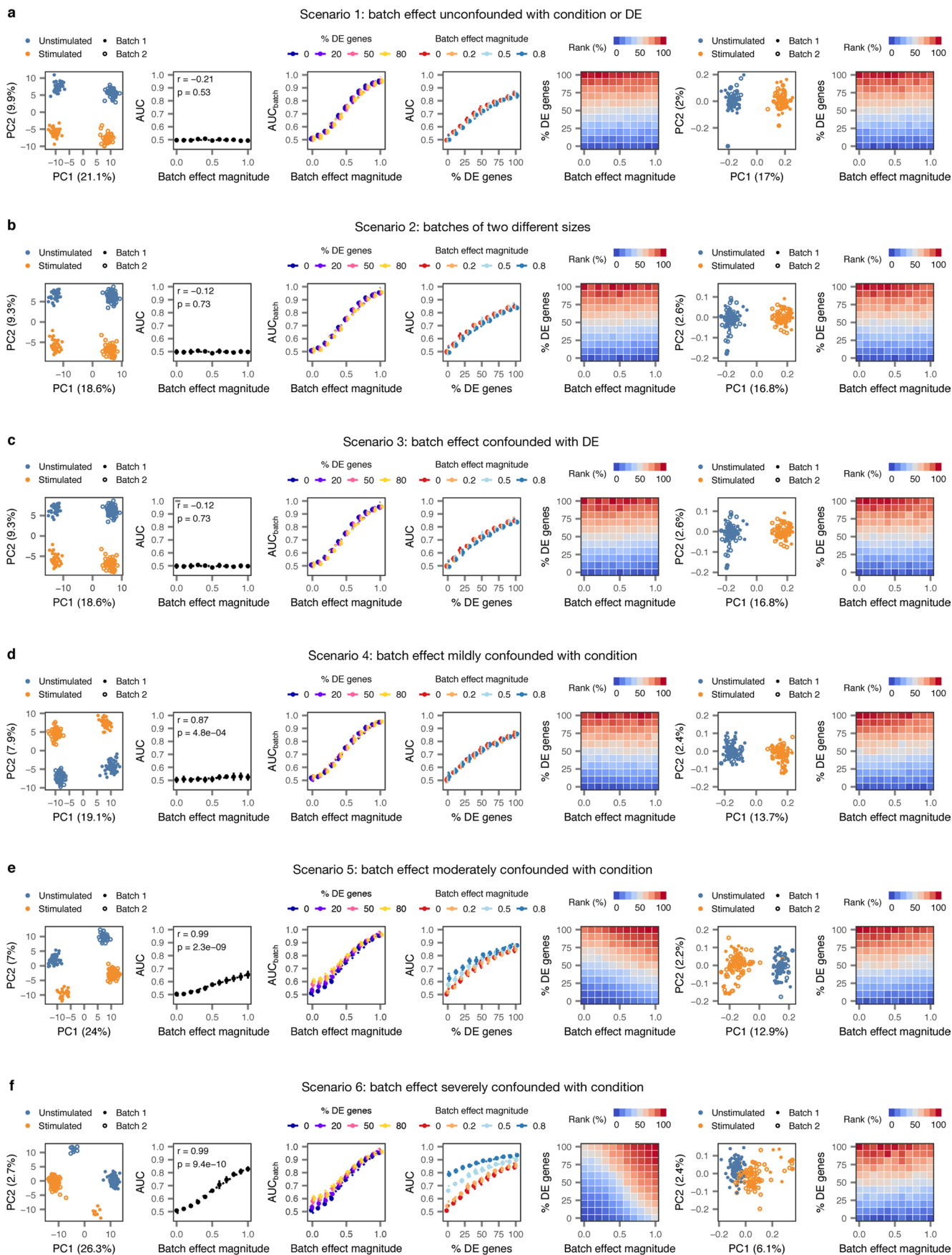
**Extended Data Fig. 10 | See next page for caption.**

**Extended Data Fig. 10 | Impact of batch effects on cell type prioritization.** Two populations of cells ($n = 200$ cells total) were simulated, with each condition sequenced in two batches, and varying degrees of perturbation-dependent differential expression and/or technical batch effects were introduced according to five different batch effect scenarios. For each of the five scenarios, the following panels are shown from left to right: *i*, Principal component analysis (PCA) of a representative simulation. *ii*, Correlation between AUC and magnitude of simulated batch effect with 0% of genes differentially expressed in response to perturbation, reflecting the introduction of a spurious difference between conditions where none exists (inset, two-sided Pearson correlation). *iii*, Correlation between AUC and magnitude of simulated batch effect when the random forest classifier is tasked with predicting batch rather than condition (AUC$_{batch}$), confirming the batch effect introduces the expected separability. *iv*, Correlation between proportion of genes differentially expressed in response to perturbation and AUC for simulated populations of cells with no batch effect, and batch effects of three different magnitudes. *v*, Cell type prioritizations in simulated populations of cells with varying perturbation intensity (% DE genes) and batch effect magnitudes. *vi*, As in *i*, but after computational batch effect correction by alignment of mutual nearest neighbors[39]. *vii*, As in *v*, but after computational batch effect correction by alignment of mutual nearest neighbors. **a**, Impact of batch effects on cell type prioritization when technical batch is unconfounded with either condition or differential expression. **b**, Impact of batch effects on cell type prioritization when batch #1 is twice as large as batch #2. **c**, Impact of batch effects on cell type prioritization when perturbation-dependent differential expression is stronger in one of the two batches. **d**, Impact of batch effects on cell type prioritization when technical batch is mildly confounded with condition (simulated cells are overrepresented in batch 1 by a factor of 20%). **e**, Impact of batch effects on cell type prioritization when technical batch is moderately confounded with condition (simulated cells are overrepresented in batch 1 by a factor of 50%). **f**, Impact of batch effects on cell type prioritization when technical batch is severely confounded with condition (simulated cells are overrepresented in batch 1 by a factor of 80%).

# Chapter 3

# Confronting false discoveries in single-cell differential expression

In this chapter we aimed to ensure the robustness of the differential genes expression (DE) methods classically used by the field. We established a compendium of datasets from studies performing matched bulk and scRNA-seq on purified cell populations, exposed to the same perturbation. We then systematically compared the most widely used packages for single cell DE analysis on their ability to generate concordant results with the bulk DE. We exposed that most of these default methods produce hundreds of false discoveries in the absence of any biological differences and clarified the requirements for valid DE analysis. These findings were validated by a systematic in vivo screen of gene expression in the injured spinal cord, which confirmed a proliferation of false positives.

My contribution as a second author : I participated in the collection, reprocessing and reanalysis of the compendium of 18 papers used to benchmark DE methods. I analyzed the experimental validation data. I participated in the edition and preparation of the manuscript.

# Confronting false discoveries in single-cell differential expression

Jordan W. Squair [1,2,3], Matthieu Gautier [1,2], Claudia Kathe [1,2], Mark A. Anderson[1,2], Nicholas D. James[1,2], Thomas H. Hutson [1,2], Rémi Hudelle[1,2], Taha Qaiser [3], Kaya J. E. Matson[4], Quentin Barraud [1,2], Ariel J. Levine [4], Gioele La Manno[1], Michael A. Skinnider [1,2,5,6 ✉] & Grégoire Courtine [1,2,6 ✉]

Differential expression analysis in single-cell transcriptomics enables the dissection of cell-type-specific responses to perturbations such as disease, trauma, or experimental manipulations. While many statistical methods are available to identify differentially expressed genes, the principles that distinguish these methods and their performance remain unclear. Here, we show that the relative performance of these methods is contingent on their ability to account for variation between biological replicates. Methods that ignore this inevitable variation are biased and prone to false discoveries. Indeed, the most widely used methods can discover hundreds of differentially expressed genes in the absence of biological differences. To exemplify these principles, we exposed true and false discoveries of differentially expressed genes in the injured mouse spinal cord.

[1] Center for Neuroprosthetics and Brain Mind Institute, Faculty of Life Sciences, École Polytechnique Fédérale de Lausanne (EPFL), Lausanne, Switzerland. [2] NeuroRestore, Department of Clinical Neuroscience, Lausanne University Hospital (CHUV) and University of Lausanne (UNIL), Lausanne, Switzerland. [3] International Collaboration on Repair Discoveries (ICORD), University of British Columbia, Vancouver, BC, Canada. [4] Spinal Circuits and Plasticity Unit, National Institute of Neurological Disorders and Stroke, Bethesda, MD, USA. [5] Michael Smith Laboratories, University of British Columbia, Vancouver, BC, Canada. [6] These authors contributed equally: Michael A. Skinnider, Grégoire Courtine. ✉email: michaelskinnider@gmail.com; gregoire.courtine@epfl.ch

The abundance of RNA species informs on the past, present and future state of cells and tissues. By enabling the complete quantification of mRNA populations, RNA sequencing (RNA-seq) has provided unprecedented access to the molecular processes active in a biological sample[1]. Diseases, traumas, and experimental manipulations perturb these processes, which leads to changes in the expression of specific mRNAs. Historically, these altered mRNAs were identified using bulk RNA-seq in non-perturbed versus perturbed tissues[2]. However, biological tissues are composed of multiple cell types, whose responses to a perturbation can differ dramatically. Changes in mRNA abundance within multicellular tissues are confounded by different responses across cell types and changes in the relative abundance of these cell types[3]. Consequently, the resolution of bulk RNA-seq is insufficient to characterize the multifaceted responses to biological perturbations.

Single-cell RNA-seq (scRNA-seq) enables the quantification of RNA abundance at the resolution of individual cells[4]. The maturation of single-cell technologies now enables large-scale comparisons of cell states within complex tissues, thus providing the appropriate resolution to dissect cell-type-specific responses to perturbation[5,6]. The sparsity and heterogeneity of single-cell data initially encouraged the development of specialized statistical methods to identify differentially expressed mRNAs[7,8]. The proliferation of statistical methods for differential expression analysis prompted investigators to ask which methods produced the most biologically accurate results. To answer this question, investigators turned to simulations in an attempt to create a ground truth against which the various methods could be benchmarked. However, simulations require specifying a model from which synthetic patterns of differential expression are generated. Differences in the specification of this model have led investigators to contrasting conclusions[9,10].

These divergences emphasize the importance of developing a sound epistemological foundation for differential expression in single-cell data[11]. In this work, we reasoned that developing such a foundation would require quantifying the performance of the available methods across multiple datasets in which an experimental ground truth is known, and defining the principles that are responsible for differences in performance. We therefore first established a methodological framework that enabled us to curate a resource of ground-truth datasets. Using this resource, we conduct a definitive comparison of the various available methods for differential expression analysis. We find that differences in the performance of these methods reflect the failure of certain methods to account for intrinsic variation between biological replicates. Our understanding of this principle led us to discover that the most frequently used methods can identify differentially expressed genes even in the absence of biological differences. These false discoveries are poised to mislead investigators. However, we show that false discoveries can be avoided using statistical methodologies that account for between-replicate variation. In summary, we expose the principles that underlie valid differential expression analysis in single-cell data, and provide a toolbox to implement relevant statistical methods for single-cell users.

## Results

### A ground-truth resource to benchmark single-cell differential expression

We aimed to compare available statistical methods for differential expression (DE) analysis based on their ability to generate biologically accurate results. We reasoned that performing this comparison in real datasets where the experimental ground truth is known would faithfully reflect differences in the performance of these methods, while avoiding the shortcomings of simulated data. We posited that the closest possible approximation to this ground truth could be obtained from matched bulk and scRNA-seq performed on the same population of purified cells, exposed to the same perturbations, and sequenced in the same laboratories. An extensive survey of the literature identified a total of eighteen 'gold standard' datasets that met these criteria (Fig. 1a)[12–15]. This compendium allowed us to carry out a large-scale comparison of DE methods in experimental settings where the ground truth is known.

### Pseudobulk methods outperform generic and specialized single-cell DE methods

We selected a total of fourteen DE methods, representing the most widely used statistical approaches for single-cell transcriptomics, to compare (Methods, "Differential expression analysis methods"). Together, these methods have been used by almost 90% of recent studies (Fig. 1b). We evaluated the relative performance of each method based on the concordance between DE results in bulk versus scRNA-seq datasets. To quantify this concordance, we calculated the area under the concordance curve (AUCC) between the results of bulk versus scRNA-seq datasets[16,17].

We compared the performance of the fourteen methods across the entire compendium of the eighteen gold standard datasets. This analysis immediately revealed that all six of the top-performing methods shared a common analytical property. These methods aggregated cells within a biological replicate, to form so-called 'pseudobulks', before applying a statistical test (Fig. 1c)[18]. In comparison, methods that compared individual cells performed poorly. The differences between pseudobulk and single-cell methods were highly significant (Fig. 1d), and robust to the methodology used to quantify concordance (Supplementary Fig. 1a-d). Moreover, comparisons to matching proteomics data[13] revealed that pseudobulk methods also more accurately predicted changes in protein abundance (Supplementary Fig. 1e-f).

We asked whether the differences between DE methods could also impact the functional interpretation of transcriptomic experiments. For this purpose, we compared Gene Ontology (GO) term enrichment analyses in bulk versus scRNA-seq DE. We found that pseudobulk methods again more faithfully reflected the ground truth, as captured in the bulk RNA-seq (Fig. 1e and Supplementary Fig. 1g). For example, single-cell methods failed to identify the relevant GO term when comparing mouse phagocytes stimulated with poly(I:C)[12], a synthetic double-stranded RNA (Fig. 1f).

### Single-cell DE methods are biased towards highly expressed genes

The unexpected superiority of pseudobulk methods compelled us to study the mechanisms that are responsible for their ability to recapitulate biological ground truth. To investigate these mechanisms, we formulated and tested several hypotheses that could potentially explain these differences in performance.

Previous studies demonstrated that inferences about DE are generally more accurate for highly expressed genes[19,20]. Measurements of gene expression in single cells are inherently sparse. By aggregating cells within each replicate, pseudobulk methods dramatically reduce the number of zeros in the data, especially for lowly expressed genes (Fig. 2a). Consequently, we initially hypothesized that the difference in accuracy between pseudobulk and single-cell methods could be explained by superior performance of pseudobulk methods among lowly expressed genes.

To test this hypothesis, we allocated genes into three equally sized bins, comprising lowly, moderately, and highly expressed genes. We then re-calculated the concordance between bulk and scRNA-seq DE within each bin. Contrary to our prediction, we
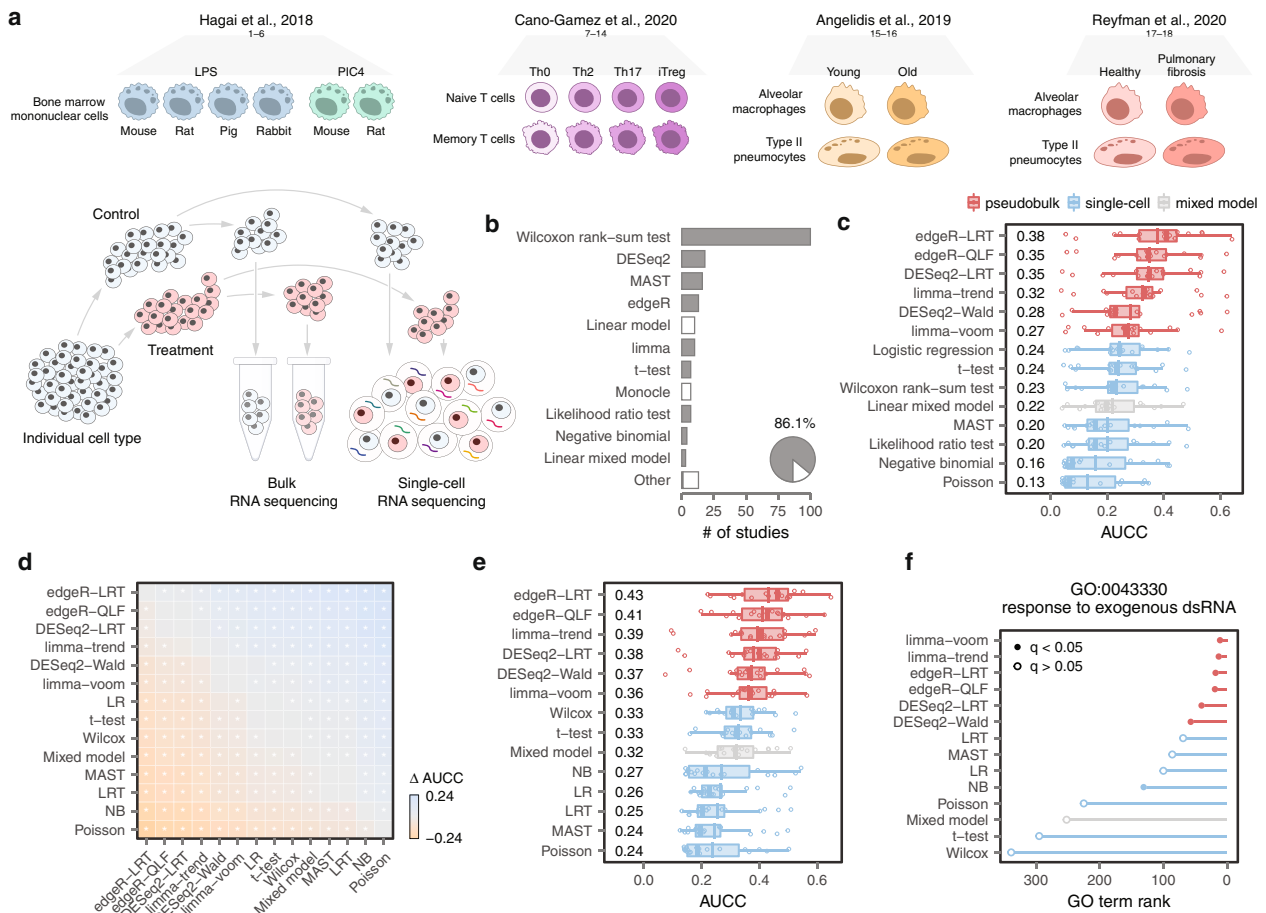
**Fig. 1 A systematic benchmark of differential expression in single-cell transcriptomics. a** Schematic overview of the eighteen ground-truth datasets analyzed in this study. **b** Statistical methods for DE analysis employed in 500 recent scRNA-seq papers. Grey bars represent DE analysis methods included in this study. "Other" includes methods used in two or fewer studies. Inset pie chart shows the total proportion of recent scRNA-seq papers that employed DE analysis methods included in this study. Source data are provided as a Source Data file. **c** Area under the concordance curve (AUCC) for fourteen DE methods in the eighteen ground-truth datasets shown in **a**. **d** Mean difference in the AUCC (Δ AUCC) between the fourteen DE methods shown in **c**. Asterisks indicate comparisons with a two-tailed t-test p-value less than 0.05. **e** AUCC of GO term enrichment, as evaluated using gene set enrichment analysis[46], in the eighteen ground-truth datasets shown in **a**. **f** Rank and statistical significance of the GO term GO:0043330 ("response to exogenous dsRNA") in GSEA analyses of mouse bone marrow mononuclear cells stimulated with poly-I:C, a type of synthetic dsRNA, for four h, using the output of fourteen DE methods. Source data are provided as a Source Data file.

observed minimal differences between pseudobulk and single-cell methods for lowly expressed genes (Fig. 2b and Supplementary Fig. 2a). Instead, the most pronounced differences between pseudobulk and single-cell methods emerged among highly expressed genes.

This unexpected result led us to ask whether single-cell DE methods produce systematic errors for highly expressed genes. To explore this possibility, we scrutinized the bulk datasets to identify genes falsely called as DE by each method within scRNA-seq data. We found that false positives identified by single-cell DE methods were more highly expressed than those identified by pseudobulk methods (Fig. 2c and Supplementary Fig. 2b). Conversely, false-negatives overlooked by single-cell DE methods tended to be lowly expressed (Supplementary Fig. 2c-d). Together, these findings implied a systematic tendency for single-cell methods to identify highly expressed genes as DE, even when their expression remained unchanged.

To validate this conclusion experimentally, we analyzed a dataset in which a population of synthetic mRNAs were spiked into each well containing a single cell[12,21]. Each of these single-cell libraries therefore contained equal concentrations of each synthetic mRNA. We found that single-cell methods incorrectly

identified many abundant spike-ins as DE (Fig. 2d-e and Supplementary Fig. 2e-f). In contrast, pseudobulk methods avoided this bias.

We then asked whether this bias was universal in single-cell transcriptomics. We assembled a compendium of 46 scRNA-seq datasets that encompassed disparate species, cell types, technologies, and biological perturbations (Supplementary Fig. 3). We found that single-cell DE methods displayed a systematic preference for highly expressed genes across the entire compendium (Fig. 2f).

Together, these experiments suggest that the inferior performance of single-cell methods can be attributed to their bias towards highly expressed genes.

**DE analysis of single-cell data must account for biological replicates**. These findings implied that pseudobulk methods possess a common analytical property that allows them to avoid this bias. We conducted a series of experiments to identify this mechanism.

The statistical tools applied to identify DE genes in pseudobulk data (i.e., edgeR, DESeq2, and limma) have been refined over
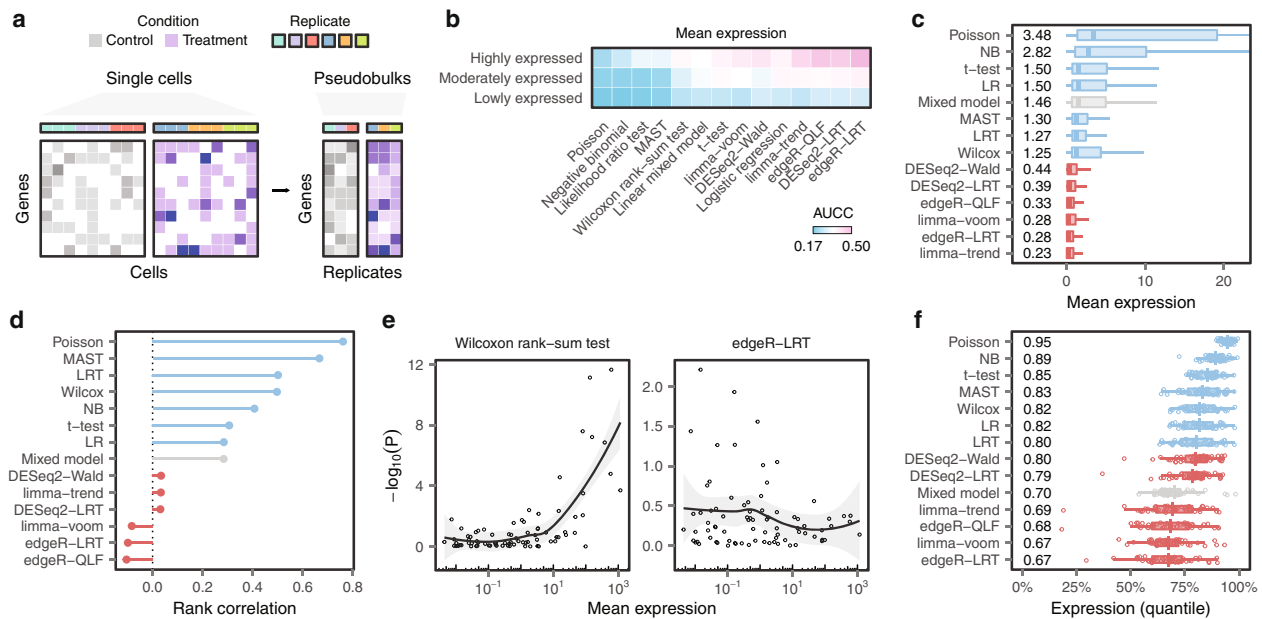
**Fig. 2 Single-cell DE methods are biased towards highly expressed genes. a** Schematic illustration of the creation of 'pseudobulks' from single-cell data. Top, biological replicate from which each cell was obtained. Bottom, simulated gene expression matrix. Read counts for each gene are aggregated across cells of a given type within each biological replicate. **b** Mean AUCCs across eighteen ground-truth datasets after dividing the transcriptome into terciles of lowly, moderately, or highly expressed genes. **c** Mean expression levels of the 100 top-ranked false-positive genes from each DE method. **d** Spearman correlation between the mean expression of 80 ERCC spike-ins expressed in at least three cells and the $-\log_{10}$ $p$-value of differential expression assigned by each DE method. **e** Scatterplots of mean ERCC expression vs. $-\log_{10}$ $p$-value for exemplary single-cell and pseudobulk DE methods. Trend lines and shaded areas show local polynomial regression and the 95% confidence interval, respectively. **f** Mean expression levels of the 200 top-ranked genes from each DE method in a collection of 46 scRNA-seq datasets.

many years of development. We therefore asked whether these methods incorporate inherent advantages that are independent from the procedure of aggregating gene expression across cells. To test this possibility, we disabled the aggregation procedure and applied the pseudobulk methods to individual cells (Fig. 3a). Strikingly, this procedure abolished the superiority of the pseudobulk methods (Fig. 3b and Supplementary Fig. 4a). The emergence of a bias towards highly expressed genes paralleled this decrease in performance (Fig. 3b and Supplementary Fig. 4b-c).

This result raised the possibility that the aggregation procedure itself was directly responsible for the superiority of pseudobulk methods. To evaluate this notion, we applied the aggregation procedure to random groups of cells, which produced a pseudobulk matrix composed of 'pseudo-replicates' (Fig. 3c). This experiment induced a similar decrease in the performance of pseudobulk methods, combined with the re-emergence of a bias towards highly expressed genes (Fig. 3d and Supplementary Fig. 4d–f).

We sought to understand the common factors that could explain the decreased performance of pseudobulk methods in these two experiments. We recognized that both experiments entailed a loss of information about biological replicates. Aggregating random groups of cells to form pseudo-replicates, or ignoring replicates altogether in comparisons of single cells, both introduced a bias towards highly expressed genes and a corresponding loss of performance.

Within the same experimental condition, replicates exhibit inherent differences in gene expression, which reflect both biological and technical factors[22]. We reasoned that failing to account for these differences could lead methods to misattribute the inherent variability between replicates to the effect of the perturbation. To study this potential mechanism, we compared the variance in the expression of each gene in pseudobulks and pseudo-replicates. Initially, we performed this comparison in a

dataset of bone marrow mononuclear cells stimulated with poly-I:C[12]. We found that shuffling the replicates produced a systematic decrease in the variance of gene expression, affecting 98.2% of genes (Fig. 3e). We next tested whether this decrease in variance occurred systematically across our compendium of 46 datasets. Every comparison displayed the same decrease in the variance of gene expression (Fig. 3f).

The decrease in the variance of gene expression led statistical tests to attribute small changes in gene expression to the effect of the perturbation. For instance, in the poly-I:C dataset, failing to account for the variable expression of *Txnrd3* across replicates led to the spurious identification of this gene as differentially expressed (Fig. 3g). Moreover, we found that highly expressed genes exhibited the largest decrease in variance in pseudo-replicates, thus explaining the bias of single-cell methods towards highly expressed genes (Supplementary Fig. 4g-k).

Together, this series of experiments exposed the principle underlying the unexpected superiority of pseudobulk methods. Statistical methods for differential expression must account for the intrinsic variability of biological replicates to generate biologically accurate results in single-cell data. Accounting for this variability allows pseudobulk methods to correctly identify changes in gene expression caused by a biological perturbation. In contrast, failing to account for biological replicates causes single-cell methods to systematically underestimate the variance of gene expression. This underestimation of the variance biases single-cell methods towards highly expressed genes, compromising their ability to generate biologically accurate results.

**False discoveries in single-cell DE**. We realized that if failing to account for the variation between biological replicates could produce false discoveries in the presence of a real biological perturbation, then false discoveries might also arise in the absence
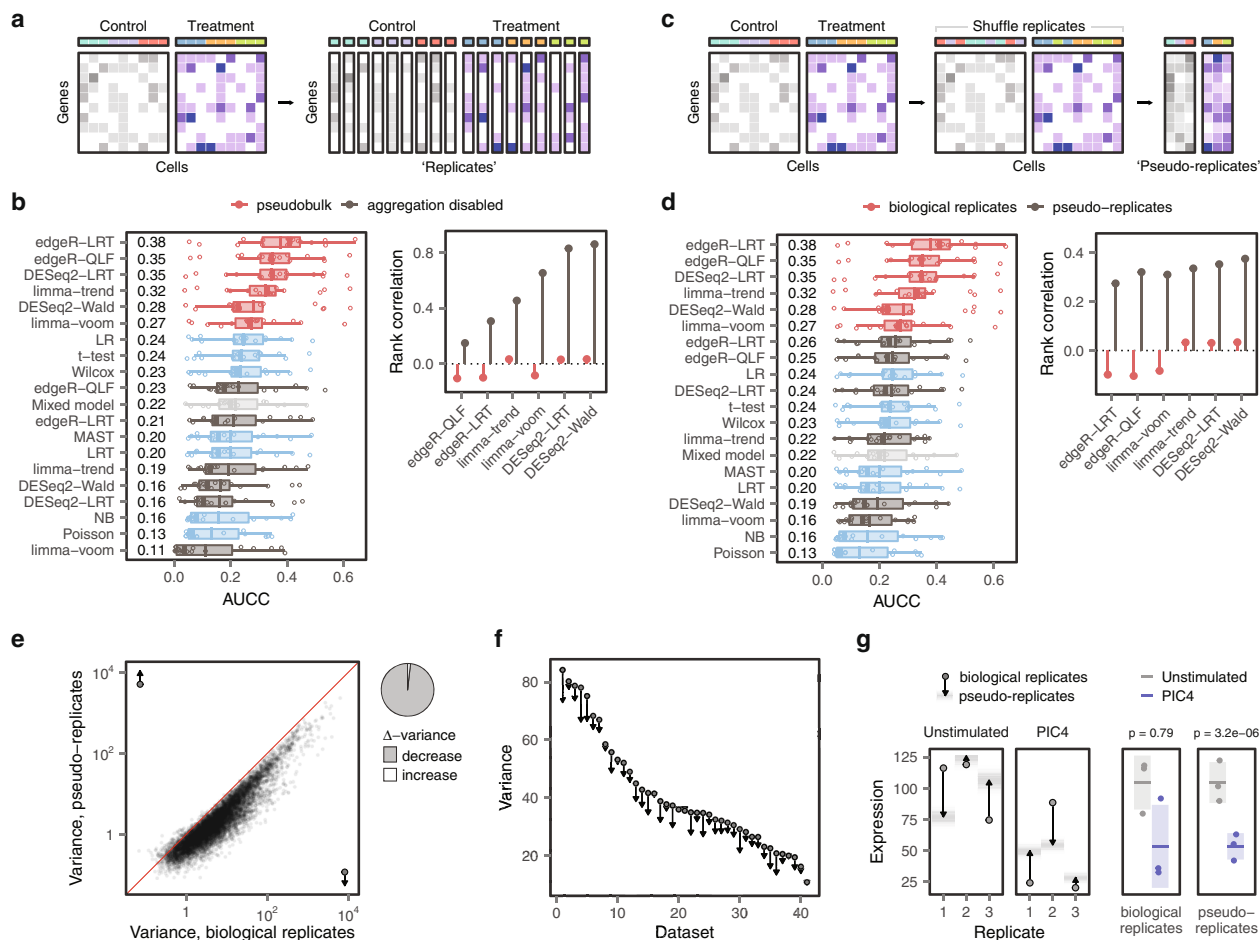
**Fig. 3 DE analysis of single-cell data must account for biological replicates. a** Schematic illustration of the experiment shown in **b**, in which the aggregation procedure was disabled and pseudobulk DE methods were applied to individual cells. **b** Left, AUCC of the original fourteen DE methods, plus six pseudobulk methods applied to individual cells, in the eighteen ground-truth datasets. Right, Spearman correlation between ERCC mean expression and −log$_{10}$ p-value assigned by six pseudobulk DE methods, before and after disabling the aggregation procedure. **c** Schematic illustration of the experiment shown in **d**, in which the replicate associated with each cell was shuffled to produce 'pseudo-replicates.' **d** Left, AUCC of the original fourteen DE methods, plus six pseudobulk methods applied to pseudo-replicates, in the eighteen ground-truth datasets. Right, Spearman correlation between ERCC mean expression and −log$_{10}$ p-value assigned by six pseudobulk DE methods, before and after shuffling replicates to produce pseudo-replicates. **e** Variance of gene expression in pseudobulks formed from biological replicates and pseudo-replicates in mouse bone marrow mononuclear cells stimulated with poly-I:C. Shuffling the replicate associated with each cell produced a systematic decrease in the variance of gene expression. Right, pie chart shows the proportion of genes with increased or decreased variance in pseudo-replicates, as compared to biological replicates. **f** Decreases in the variance of gene expression in pseudo-replicates as compared to biological replicates across 46 scRNA-seq datasets. Points show the mean variance in biological replicates; arrowheads show the mean variance in pseudo-replicates. **g** Left, expression of the gene c in biological replicates (points) and pseudo-replicates (arrowheads) from unstimulated cells and cells stimulated with poly-I:C, with the range of possible pseudo-replicate expression values shown as a density. Right, mean (horizontal line) and variance (shaded area) of Txnrd3 expression in biological replicates (left) and pseudo-replicates (right). P-values were calculated by edgeR-LRT.

of any biological difference. To test this possibility, we simulated single-cell data with different degrees of heterogeneity between replicates in the absence of any difference between groups (Fig. 4a). We randomly assigned each replicate to an artificial 'control' or 'treatment' group, and tested for DE between the two conditions. Strikingly, single-cell methods identified hundreds of DE genes in the absence of any perturbation (Fig. 4b and Supplementary Fig. 4a). Moreover, in line with our understanding of the mechanisms underlying the failure of single-cell DE methods, the genes that were falsely called as DE were those whose expression was most variable between replicates (Fig. 4c and Supplementary Fig. 4b). Pseudobulk methods abolished the false detection of DE genes. However, creating pseudo-replicates led to the reappearance of spurious DE genes (Fig. 4b-c and Supplementary Fig. 4a-b), further corroborating the requirements for

accurate DE analyses. The number of false discoveries was reduced when additional replicates were introduced to the dataset (Supplementary Fig. 4c). In contrast, introducing additional cells to the simulated data only exacerbated the underlying problem (Supplementary Fig. 4d).

These findings compelled us to investigate whether similar false discoveries could arise in real single-cell data. To explore this possibility, we initially analyzed a dataset of human peripheral blood mononuclear cells (PBMCs) exposed to interferon[5]. We extracted the control samples that had not been exposed to interferon, and split them randomly into two groups. We then performed DE analysis. Failing to account for the intrinsic variability of biological replicates produced hundreds of DE genes between randomly assigned replicates (Fig. 4d and Supplementary Fig. 6a, b).
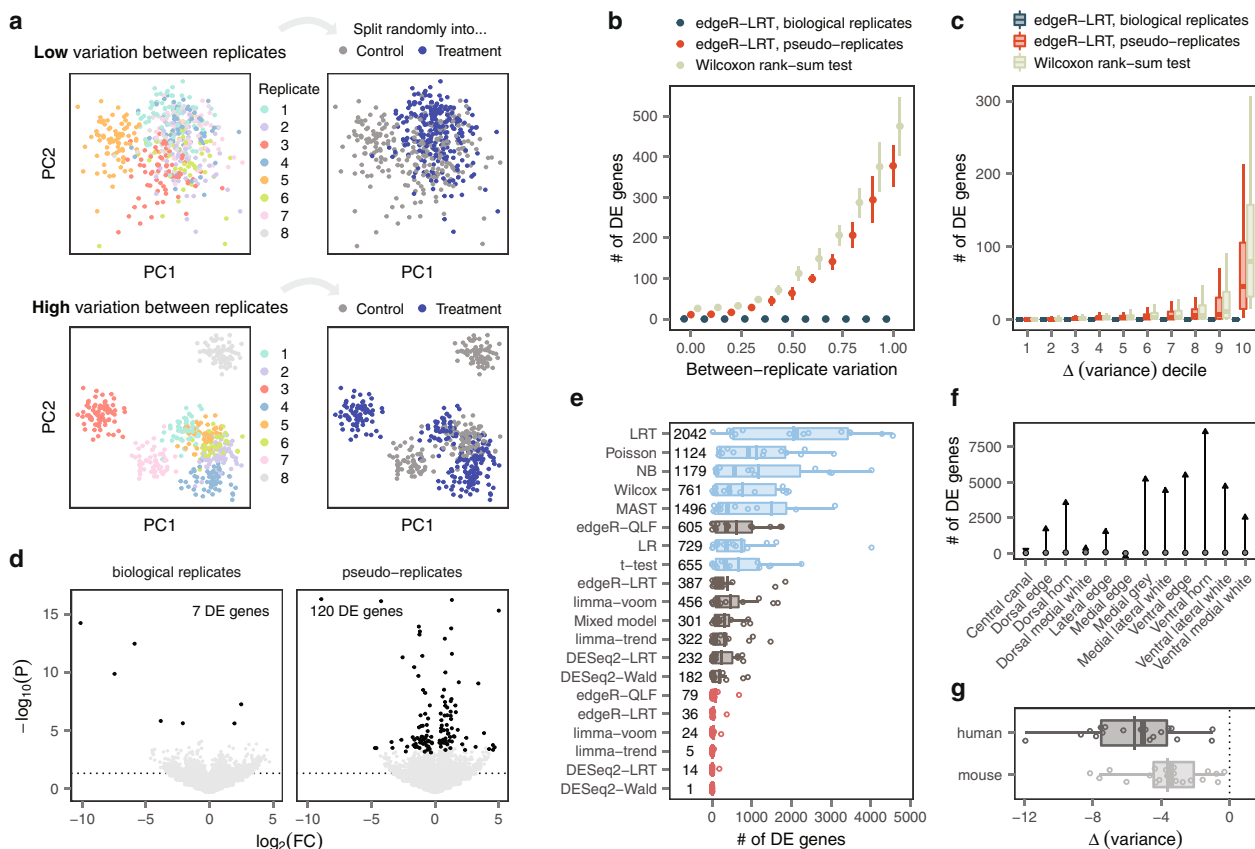
**Fig. 4 False discoveries in single-cell DE. a** Schematic illustration of simulation experiments. Single-cell RNA-seq datasets were simulated with varying degrees of heterogeneity between replicates. Replicates were then randomly assigned to either a 'treatment' or 'control' group, and DE analysis was performed between groups. **b** Number of DE genes detected in stimulation experiments with varying degrees of heterogeneity between replicates by a representative single-cell DE method, a representative pseudobulk method, and the same pseudobulk method applied to pseudo-replicates. Points and error bars show the mean and standard deviation across ten independent simulations. **c** Number of DE genes detected by the tests shown in **b** for genes divided into deciles by the magnitude of the change in variance between biological replicates and pseudo-replicates (Δ-variance). **d** Volcano plots showing DE between T cells from random groups of unstimulated controls drawn from Kang et al.[5] using a representative pseudobulk method, edgeR-LRT, applied to biological replicates or pseudo-replicates. Discarding information about biological replicates leads to the appearance of false discoveries. **e** Number of DE genes detected in comparisons of random groups of unstimulated controls from 14 scRNA-seq studies with at least six control samples. **f** Number of DE genes detected within spinal cord regions from control mice profiled by spatial transcriptomics[24] using a representative pseudobulk method, edgeR-LRT (points), or a representative single-cell method, the Wilcoxon rank-sum test (arrowheads). **g** Mean change in variance between biological replicates and pseudo-replicates for 18 human and 20 mouse scRNA-seq datasets.

Unsettled by this appearance of false discoveries, we asked whether this observation reflected a universal pitfall. To address this concern comprehensively, we identified a total of fourteen datasets that included at least six replicates in the control condition. As in the previous experiment, we split these unperturbed samples randomly into synthetic control and treatment groups, before conducting DE analyses between these two groups. This systematic analysis confirmed that single-cell methods produced a systematic excess of false positives compared to pseudobulk methods (Fig. 4e). The resulting DE genes were enriched for hundreds of Gene Ontology (GO) terms, despite a complete absence of biological perturbation (Supplementary Fig. 6c). Moreover, we again confirmed that the genes falsely identified as DE corresponded to those with the highest variability between replicates (Supplementary Fig. 6d).

Together, these experiments exposed a fundamental pitfall for DE analysis in single-cell transcriptomics. We intuited, however, that this pitfall could afflict any technology in which many observations are obtained from each biological replicate. For example, we anticipated that false discoveries would also emerge in spatial transcriptomics data[23]. To test this prediction, we

analyzed a spatial transcriptomics dataset that profiled spinal cords from a model of amyotrophic lateral sclerosis (ALS)[24]. We randomly partitioned data from control mice into two groups, and performed DE within each region of the spinal cord. Statistical methods that failed to account for variability between biological replicates identified thousands of DE genes within each region (Fig. 4f and Supplementary Fig. 6e). In contrast, pseudobulk methods abolished these false discoveries.

These experiments demonstrated that the variability between biological replicates can confound the identification of genes affected by a biological perturbation. Many of the factors that produce this variability between replicates can be minimized in animal models, including the genetic background, environment, intensity and timing of the biological perturbation, and sample processing. In contrast, these sources of variation are inherently more difficult to control in experiments involving human subjects. This distinction raised the possibility that single-cell studies of human tissue would exhibit greater variability between biological replicates, and consequently, would be more vulnerable to false discoveries. To evaluate this possibility systematically, we calculated the variability between replicates within 41 human and
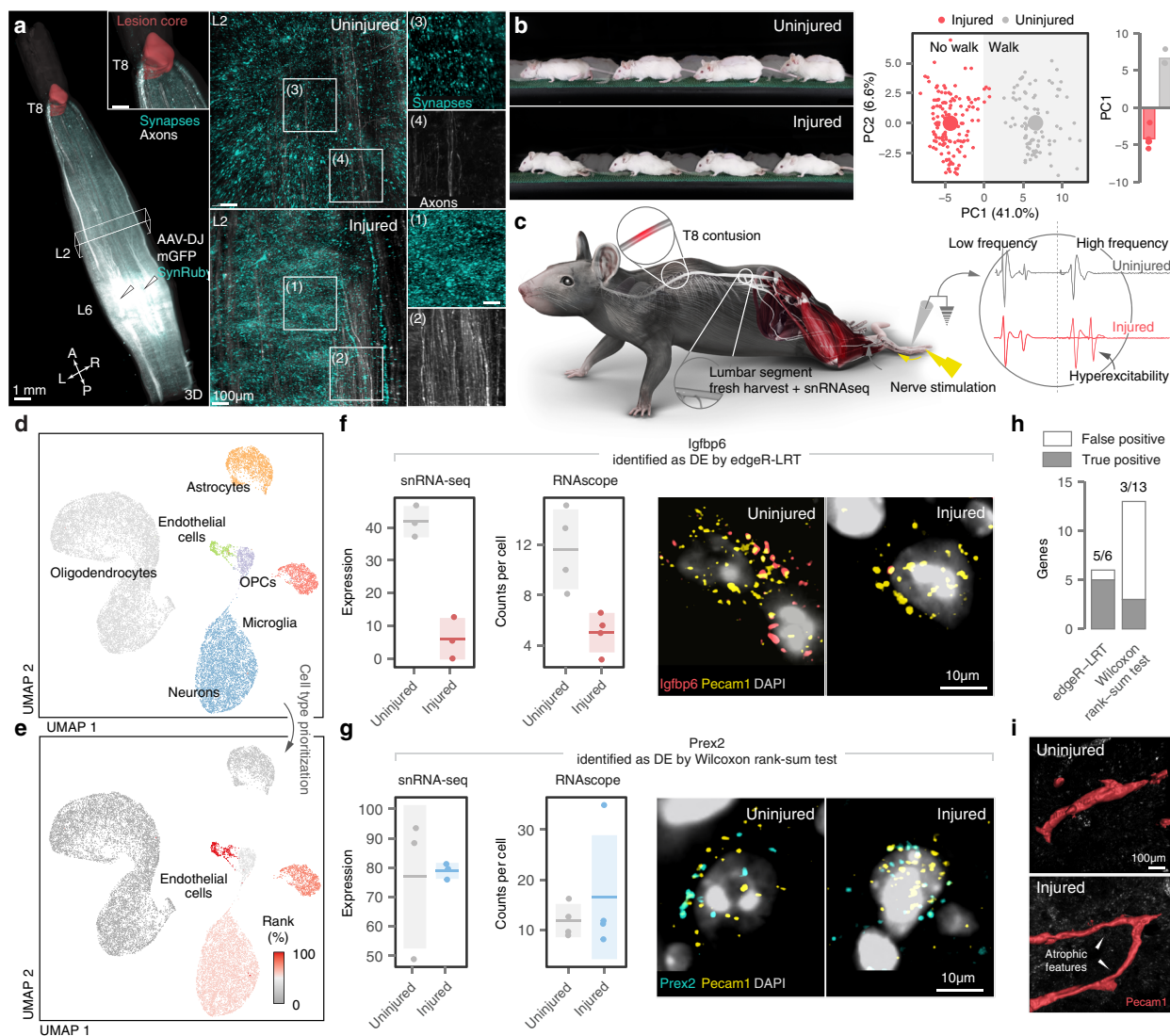
**Fig. 5 True and false discoveries in the injured mouse spinal cord. a** Synapses and projections of $Vglut2^{ON}$ neurons in the mouse lumbar spinal cord before and after SCI. Experiments were repeated in $n = 3$ mice. **b** Top, chronophotography of mice before and after SCI. Bottom left, principal component analysis of gait parameters for each condition (small circles). Large circles show the average per group. Bottom right, bar plot showing the average scores on principal component 1 (PC1), which quantify the locomotor performance of injured and uninjured mice. **c** snRNA-seq experimental design. Inset demonstrates persistent amplitude at increasing frequency of the H-reflex in response to plantar stimulation, reflecting hyperexcitability. **d** Uniform manifold approximation and projection (UMAP) visualization of 19,237 nuclei, revealing the major cell types of the mouse lumbar spinal cord. **e** UMAP visualization colored by the AUC of cell type prioritizations, as calculated by Augur[27]. Endothelial cells are highlighted as the cell type with the highest AUC. **f** Pseudobulk expression levels in lumbar spinal cord endothelial cells by snRNA-seq (in counts per 10,000), left, and mean counts per $Pecam1^{ON}$ cell by RNA-scope, center, for *Igfbp6*, a gene identified as DE only by edgeR-LRT. Horizontal line and shaded area show the mean and standard deviation, respectively. Right, colocalization of *Igfbp6* with the endothelial marker gene *Pecam1* in RNAscope in situ hybridizations from injured and uninjured mouse spinal cords. **g** As in **f**, but for *Prex2*, a gene identified as DE only by the Wilcoxon rank-sum test. **h** Summary of in vivo screen results. Filled bars represent genes validated by RNAscope. **i**, Immunohistochemistry reveals $Pecam1^{ON}$ cells with atrophic features after SCI. Experiments were repeated in $n = 3$ mice. Source data are provided as a Source Data file.

mouse scRNA-seq datasets. In agreement with our hypothesis, we detected significantly more variability between replicates in the human datasets (Fig. 4g). While we show that accounting for biological replicates is critical for any DE analysis, this result stresses the paramount importance of addressing this issue in single-cell studies of human tissue.

**True and false discoveries in the injured mouse spinal cord**. We finally sought to demonstrate the extent to which DE analyses can produce true and false discoveries in previously unexplored biological tissues. For this purpose, we characterized the impact of a spinal cord injury (SCI) on gene expression in cells located below

the injury. We specifically focused on the lumbar spinal cord, since this region undergoes multifaceted changes that lead to the irreversible degradation of neuronal function[25,26].

We performed experiments in mice that received a severe contusion of the mid-thoracic spinal cord (Fig. 5a-c). Multifactorial quantification of whole-body kinematics revealed profound impairments in the ability of the mice to produce locomotion (Fig. 5b and Supplementary Fig. 8a). We found that the injury triggered the aberrant growth of new synapses throughout lumbar segments, combined with the emergence of abnormal segmental reflexes (Fig. 5a and Supplementary Fig. 8a). This chaotic reorganization of circuits below the SCI has been

linked to spasticity and neuronal dysfunction (Fig. 5b and Supplementary Fig. 8b-c)[25,26].

We then harvested the lumbar spinal cords of mice with chronic SCI and uninjured controls, and performed single-nucleus RNA-seq (snRNA-seq) of these tissues[27]. We sequenced a total of 19,237 cells that encompassed all the major cell types of the lumbar spinal cord (Fig. 5d).

We initially aimed to identify the cell types in which transcription was most perturbed by the injury. To answer this question, we performed cell type prioritization using Augur[27,28]. This unbiased analysis indicated that endothelial cells underwent the most profound transcriptional changes in the spinal cord below the injury (Fig. 5e).

This unexpected finding spurred us to investigate the specific transcriptional changes underlying this prioritization, and the capacity of different statistical methods to reveal these changes. For this purpose, we performed DE analyses between injured and uninjured endothelial cells using representative single-cell and pseudobulk methods. We selected the Wilcoxon rank-sum test as a single-cell method, since this test has been the most widely used approach in the field of single-cell transcriptomics (Fig. 1b), and edgeR-LRT[29] as a pseudobulk method due to its high level of performance (Fig. 1c). These methods identified largely distinct sets of DE genes, with only four genes overlapping between the two methods. Conversely, the Wilcoxon rank-sum test and edgeR-LRT each nominated an additional 44 and 12 genes as DE, respectively (Supplementary Fig. 9a).

Our results thus far have demonstrated that failing to account for variation between replicates can lead single-cell DE methods to produce false discoveries. We therefore suspected that some of the additional genes identified by the Wilcoxon rank-sum test in this dataset could represent false positives. To clarify the ground truth expression of these genes in the injured spinal cord, we carried out a systematic in vivo screen. We obtained RNAscope probes for nineteen putatively DE genes identified by only one of the two methods, and quantified the expression of these genes in endothelial cells from injured and uninjured mice[30] (Supplementary Fig. 9b). RNAscope validated five of the six genes called as DE by edgeR-LRT. In marked contrast, only three of thirteen genes called as DE by the Wilcoxon rank-sum test could be corroborated ($p < 0.05$, $\chi^2$ test; Fig. 5f-h). Several of the validated edgeR-LRT genes, including *Slc7a11* and *Igfbp6*, are involved in the response to hypoxia within endothelial cells, supporting the establishment of a chronically hypoxic state in the lumbar spinal cord[31–33]. In line with the expected consequences of chronic hypoxia, we detected the presence of numerous atrophic blood vessels below the level of injury (Fig. 5i).

Together, these observations illustrate the potential for single-cell DE methods to produce false discoveries. Conversely, valid single-cell DE analysis that accounted for variation between biological replicates yielded reproducible conclusions that could be validated in vivo.

**DE analysis with mixed models**. Our experiments established that accounting for variation between biological replicates dictated the performance of single-cell DE methods. We were therefore puzzled by the unsatisfying performance of a linear mixed model. By explicitly modeling variation both within and between biological replicates, mixed models should benefit from increased statistical power compared to pseudobulk methods[9]. To clarify this discrepancy, we evaluated eight additional Poisson or negative binomial generalized linear mixed models (GLMMs; Supplementary Fig. 10a-b). In datasets of 25-50 cells, GLMMs could produce accurate results under very specific parameter combinations. However, in datasets comprising 500 or more cells, their performance converged to that of pseudobulk DE methods.

Moreover, the computational resources required to fit the best-performing GLMMs were enormous. Even in downsampled datasets, DE analysis of a single cell type took an average of 13.5 h (Supplementary Fig. 10c-d). In contrast, pseudobulk methods required only minutes per cell type in our compendium of 46 datasets (Supplementary Fig. 10e-f). These observations suggest that, in practice, pseudobulk approaches provide an excellent trade-off between speed and accuracy for single-cell DE analysis.

## Discussion

Accurate DE analysis in single-cell transcriptomics is required to dissect the transcriptional programs underlying the multifaceted responses to disease, trauma, and experimental manipulations. Despite the importance of statistical methods for DE analyses, the principles that determine their performance have remained elusive. Here, we demonstrate that the central principle underlying valid DE analysis is the ability of statistical methods to account for the intrinsic variability of biological replicates. Accounting for this variability dictates the biological accuracy of statistical methods. Conversely, methods that fail to account for the variability of biological replicates can produce hundreds of false discoveries in the absence of any biological difference.

Investigators study single cells to understand more general principles underlying the response to a biological perturbation. Clarifying these principles requires statistical inferences that generalize beyond the individual cells that constitute any particular dataset. Our results demonstrate that by performing a statistical inference at the level of individual cells, single-cell DE methods conflate variability between biological replicates with the effect of a biological perturbation. The presence of variability between replicates is unavoidable, and can be attributed to both technical factors and intrinsic biological differences[22]. The possibility that conflating variability between replicates with the biological effect of interest can lead to spurious findings has previously been recognized[18,34]. However, these studies relied almost entirely on synthetic data, supplemented by a few illustrative case studies. Consequently, the pervasiveness of false discoveries in published analyses of single-cell data and the propensity for these false discoveries to affect the biological conclusions of a study have remained unclear.

Here, we show that the appearance of false discoveries is a universal phenomenon. Leveraging a collection of 18 single-cell datasets with an experimental ground truth, we demonstrate that the use of inappropriate statistical methodology can produce false discoveries that compromise the biological interpretation of a single-cell experiment. These false discoveries have the potential to squander time, effort, and financial resources in pursuit of misleading hypotheses. For example, we show through a systematic in vivo screen of the injured mouse spinal cord that most DE genes identified by the most commonly used statistical method are false discoveries. Moreover, we elucidate the progression of mechanisms by which failing to account for biological and technical variability makes certain genes disproportionately likely to be spuriously identified as DE. We demonstrate the universality of these mechanisms in multifaceted datasets from an additional 46 single-cell RNA-seq studies. Understanding these mechanisms led us to discover that the same fundamental issues affect other high-dimensional assays, including spatial transcriptomics, and are most likely to manifest in studies of human tissue, suggesting that inference at the level of biological replicates is critical to understand the cellular and molecular basis for human disease.

Our results demonstrate that single-cell DE methods are poised to produce false discoveries. This understanding uncovers an enormous risk for the field. Our findings suggest that many

published findings may be false. Moreover, if left unresolved, substantial research funding may be allocated to follow up on these false discoveries, to the detriment of science. However, this concerning possibility is straightforward to correct with the use of DE methods that account for variability between replicates. Among these, we found that pseudobulk methods achieve the highest fidelity to the experimental ground truth at the levels of the transcriptome, proteome, and functional interpretation. Consequently, we contend that there is an urgent need for a paradigm shift in the statistical methods that are used for DE analysis of single-cell data. The need for such a shift is underscored by our observation that most studies published in the past two years have used inappropriate statistical methods for DE analysis. Moreover, the most widely used analysis packages in the field currently employ DE methods prone to false discoveries by default[35,36]. The increasing prevalence of multi-condition datasets stresses the importance of employing appropriate statistical methodologies to prevent a proliferation of false discoveries. To catalyze this transition, we implement all of the methods tested here in an R package (Supplementary Software 1).

## Methods

**Literature review.** To identify which statistical methods for DE analysis have been most commonly used within the field, we conducted an extensive literature review. We annotated the statistical method used to perform DE analysis across experimental conditions within cell types for each publication included in a large, curated database of scRNA-seq studies[37]. The database was accessed on November 4, 2020. Because the single-cell studies catalogued in this database span a long period of time, and we aimed to establish which methods for DE analysis are currently in wide use, we limited our analysis to the 500 most recently published studies. Accordingly, the inclusion criteria for our review were (i) studies present in the curated database as of November 4, 2020, and (i) studies within the 500 most recent entries in this database at the time it was accessed. Each of these 500 studies were then manually reviewed to determine the statistical methodology used to compare cells of the same type between experimental conditions. We did not annotate methods used to identify genes differentially expressed between cell types (i.e., marker gene identification), as this problem presents a distinct set of statistical challenges[10,38]. In total, 205 of the 500 studies conducted DE analysis between biological conditions. The complete list of all 500 studies is provided as Source Data.

**Ground-truth datasets.** Previous benchmarks of DE analysis methods for single-cell transcriptomics have relied heavily on simulated data, or else have compared the results of different methods in scenarios where no ground truth was available[10,17]. We reasoned that the best possible approximation to the biological ground truth in a scRNA-seq experiment would consist of a matched bulk RNA-seq dataset in the same purified cell type, exposed to the same perturbation under identical experimental conditions, and sequenced in the same laboratory. We surveyed the literature to identify such matching single-cell and bulk RNA-seq datasets, which led us to compile a resource of eighteen ground truth datasets from four publications[12–15]. Datasets of mouse, rat, pig, and rabbit bone marrow-derived mononuclear phagocytes stimulated with either lipopolysaccharide or poly-I:C for 4 h were obtained from Hagai et al.[12] Datasets of naive or memory T cells stimulated for 5 d with anti-CD3/anti-CD28 coated beads in the presence or absence of various combinations of cytokines (Th0: anti-CD3/anti-CD28 alone; Th2: IL-4, anti-IFNγ; Th17: TGFβ, IL6, IL23, IL1β, anti-IFNγ, anti-IL4; iTreg: TGFβ, IL2) were obtained from Cano-Gamez et al.[13] We additionally obtained label-free quantitative proteomics data for the same comparisons from this study. Datasets of alveolar macrophages and type II pneumocytes from young (3 m) and old (24 m) mice were obtained from Angelidis et al.[14] Datasets of alveolar macrophages and type II pneumocytes from patients with pulmonary fibrosis and control individuals were obtained from Reyfman et al.[15]

**Differential expression analysis methods.** We compared fourteen statistical methods for DE analysis of single-cell transcriptomics data on their ability to recover ground-truth patterns of DE, as established through bulk RNA-seq analysis of matching cell populations. These fourteen methods comprised seven statistical tests that compared gene expression in individual cells ("single-cell methods"); six tests that aggregated cells within a biological replicate to form pseudobulks before performing statistical analysis ("pseudobulk methods"); and a linear mixed model. The seven single-cell methods analyzed here included a t-test, a Wilcoxon rank-sum test, logistic regression[39], negative binomial and Poisson generalized linear models, a likelihood ratio test[40], and the two-part hurdle model implemented by MAST[7]. The implementation provided in the Seurat function 'FindMarkers' was used for all seven tests, with all filters ('min.pct', 'min.cells.feature', and

'logfc.threshold') disabled. In addition, we implemented a linear mixed model within Seurat, using the 'lmerTest' R package to optimize the restricted maximum likelihood and obtain p-values from the Satterthwaite approximation for degrees of freedom. We observed that some statistical tests returned a large number of p-values below the double precision limit in R (approximately $2 \times 10^{-308}$), potentially confounding the calculation of the concordance metrics described below. To avoid this pitfall, we modified the Seurat implementation to also return the value of the test statistic from which the p-value was derived. The modified version of Seurat 3.1.5 used to perform all single-cell DE analyses reported in this study is available from http://github.com/jordansquair/Seurat.

The pseudobulk methods employed the DESeq2[41], edgeR[29], and limma[42] packages for analysis of aggregated read counts. Briefly, for cells of a given type, we first aggregated reads across biological replicates, transforming a genes-by-cells matrix to a genes-by-replicates matrix using matrix multiplication. For DESeq2, we used both a Wald test of the negative binomial model coefficients (DESeq2-Wald) as well as a likelihood ratio test compared to a reduced model (DESeq2-LRT) to compute the statistical significance. For edgeR, we used both the likelihood ratio test (edgeR-LRT)[43] as well as the quasi-likelihood F-test approach (edgeR-QLF)[44]. For limma, we compared two modes: limma-trend, which incorporates the mean-variance trend into the empirical Bayes procedure at the gene level, and voom (limma-voom), which incorporates the mean-variance trend by assigning a weight to each individual observation[45]. Log-transformed counts per million values computed by edgeR were provided as input to limma-trend.

DE analysis of bulk RNA-seq datasets was performed with six methods (DESeq2-LRT, DESeq2-Wald, edgeR-LRT, edgeR-QLF, limma-trend, and limma-voom), except for the two pulmonary fibrosis datasets[15]; for these datasets, the raw bulk RNA-seq data from sorted cells could not be obtained, so only the results of the bulk DE analysis performed by the authors of the original publication were used. The AUCC and rank correlation were calculated for each bulk DE analysis method separately, and subsequently averaged over all six methods. DE analysis of normalized bulk proteomics data was performed using the moderated t-test implemented within limma, as in the original publication.

**Measuring concordance between single-cell and bulk RNA-seq.** To evaluate the concordance between DE analyses of matched single-cell and bulk RNA-seq data, we computed two metrics, designed to evaluate the concordance between only the most highly ranked subset of DE genes and across the entire transcriptome, respectively. To calculate the first of these metrics, the area under the concordance curve (AUCC)[16,17], we ranked genes in both the single-cell and bulk datasets in descending order by the statistical significance of their differential expression. Then, we created lists of the top-ranked genes in each dataset of matching size, up to some maximum size $k$. For each of these lists (that is, for the top-1 genes, top-2 genes, top-3 genes, and so on), we computed the size of the intersection between the single-cell and bulk DE genes. This procedure yielded a curve relating the number of shared genes between datasets to the number of top-ranked genes considered. The area under this curve was computed by summing the size of all intersections, and normalized to the range [0, 1] by dividing it by its maximum possible value, $k \times (k + 1) / 2$. To evaluate the concordance of DE analysis, we used $k = 500$ except where otherwise noted, but found our results were insensitive to the precise value of $k$. To compute the second metric, the transcriptome-wide rank correlation, we multiplied the absolute value of the test statistic for each gene by the sign of its log-fold change between conditions, and then computed the Spearman correlation over genes between the single-cell and bulk datasets.

In addition to evaluating the consistency of DE analyses at the gene level, we also asked whether each DE method yielded broader patterns of functional enrichment that were similar between the single-cell and bulk datasets, allowing for some divergence in the rankings of individual genes. To address this question, we performed gene set enrichment analysis[46] using the 'fgsea' R package[47]. GO term annotations for human and mouse (2019-12-09 release) were obtained from the Gene Ontology Consortium website. GO terms annotated to less than 10 genes or more than 1,000 genes within each dataset were excluded in order to mitigate the influence of very specific or very broad terms. Genes were ranked in descending order by the absolute value of the test statistic, and $10^6$ permutations were performed. To evaluate the concordance of GO term enrichment, we used $k = 100$, on the basis that fewer top-ranked GO terms are generally of interest than are top-ranked genes.

**Impact of mean expression.** We initially hypothesized that differences between single-cell DE analysis methods could be attributed to their differing sensitivities towards lowly expressed genes. To explore this hypothesis, we performed the following analyses. First, we divided genes from the eighteen gold standard datasets into three equally sized bins on the basis of their mean expression, then recalculated the AUCC as described above within each bin separately. Second, we inspected the properties of genes falsely called as DE in the single-cell data (false positives) or incorrectly inferred to be unchanging in the single-cell data (false negatives). To identify false positive genes, we used the bulk DE analysis to exclude genes called as DE at a false discovery rate of 10% from the matched single-cell results, then retained the 100 top-ranked remaining genes in the single-cell data. To identify false negative genes, we used the bulk DE analysis to identify genes called as DE at a false discovery rate of 10%, but with a false discovery rate exceeding 10%

in the matched single-cell results, again retaining the 100 top-ranked such genes. For each of these genes, we computed both the mean expression level and the proportion of zero gene expression measurements. Third, we analyzed a Smart-seq2 dataset of human dermal fibroblasts stimulated with interferon-β, in which a mixture of synthetic RNAs was spiked into each individual cell[12]. We performed DE analysis on the synthetic spike-ins, then calculated the Spearman correlation between the mean expression level of each spike-in and the statistical significance of differential expression, as assigned by each single-cell DE method. Fourth, we assembled a compendium of 46 published scRNA-seq datasets, and asked whether the genes called as DE by each method tended to be more or less highly expressed across the entire compendium. Complete details on the preprocessing of these 46 datasets are provided below. Because each of these datasets were sequenced to different depths, and captured different total numbers of genes (depending on both the sequencing depth and the biological system under study), mean expression values were not directly comparable across datasets. To enable such a comparison, we first calculated the mean expression for each gene, then converted this value into the quantile of mean expression using the empirical cumulative distribution function. We then calculated the mean expression quantile of the 200 top-ranked genes from each method in each of the 46 datasets.

**Dissecting pseudobulk DE methods**. To understand the principles underlying the improved performance of the six pseudobulk DE methods, we performed the following analyses. First, we disabled the aggregation procedure that led to the creation of pseudobulks (that is, we treated each individual cell as its own replicate), then performed an identical DE analysis of individual cells. For each DE method, we then re-calculated both the AUCC and the bias towards highly expressed genes, as quantified by (i) the rank correlation to mean-spike in expression, and (ii) the expression quantile across 46 scRNA-seq datasets. Second, we aggregated random groups of cells into 'pseudo-replicates' by randomizing the replicate associated with each cell. We then again re-calculated both the AUCC and the bias towards highly expressed genes.

These experiments led us to suspect that discarding information about the inherent variability of biological replicates caused both the bias towards highly expressed genes and the attendant decrease in performance. To test this hypothesis, we compared the variance of gene expression in pseudobulks and pseudo-replicates. For each gene, we calculated the difference in variance (Δ-variance) between pseudobulks and pseudo-replicates. We initially visualized the Δ-variance in an exemplary dataset, consisting of mouse bone marrow mononuclear cells stimulated with poly-I:C12. Subsequently, we calculated the mean Δ-variance across all genes in each of the 46 datasets in our scRNA-seq compendium, observing a decrease in the variance in all 46 cases. To clarify the relationship between the Δ-variance and mean gene expression, we computed the correlation between Δ-variance and mean expression, first in the poly-I:C dataset and then across all 46 datasets in the compendium. We observed a significant negative correlation, confirming that the variance of highly expressed genes is disproportionately underestimated when discarding information about biological replicates. We performed a similar analysis correlating the original variance of gene expression to the Δ-variance, demonstrating that the variance of the most variable genes is disproportionately underestimated when discarding information about biological replicates. However, in partial correlation analyses, only gene expression variance remained correlated with Δ-variance, implying that failing to account for biological replicates induces a bias towards highly expressed genes because these genes are also more variably expressed. Supplementary Fig. 4h-i employ the signed pseudo-logarithm transformation from the 'ggallin' R package to visualize the Δ-variance.

**Simulation studies**. Our understanding of the importance of accounting for variability between biological replicates led us to ask whether failing to account for biological replication could lead to the appearance of false discoveries in the absence of a perturbation. To test this hypothesis, we simulated scRNA-seq data with no biological effect, in which we systematically varied the degree of heterogeneity between replicates. Simulations were performed using the 'Splatter' R package[48], with simulation parameters estimated from the Kang et al. dataset[5] using the 'splatEstimate' function. Populations of between 100 and 2,000 cells were simulated, with between 3 and 20 replicates per condition. DE of varying magnitudes was simulated between replicates by varying the location parameter of the DE factor log-normal distribution ('de.facLoc') between 0 and 1, treating each replicate as its own group, and the total proportion of DE genes ('de.prob') set to 0.5. Then, half of the replicates were randomly assigned to an artificial 'treatment' condition and the remaining half to a 'control' condition, and DE analysis was performed between the treatment and control groups. Except where otherwise noted, plots show results from a simulated population of 500 cells, with three replicates per condition.

**Analysis of published scRNA-seq control groups**. To confirm that the trends observed in simulation studies were reflective of experimental datasets, we performed a similar analysis using published scRNA-seq data. Within our compendium, we identified a total of fourteen studies with control groups that included six or more samples[5,6,15,49–59]. Details on the preprocessing of each of these datasets

are provided below. For each of these studies, we split the control group randomly into artificial 'control' and 'treatment' groups, and performed DE analysis. In addition to computing the total number of DE genes, we identified GO terms enriched among DE genes using a hypergeometric test. We also performed a similar analysis for one spatial transcriptomics dataset24, identifying DE genes between random groups of control mice with barcodes grouped by spinal cord region rather than cell type. Spatial transcriptomics data was downloaded from the supporting website at https://als-st.nygenome.org. Only data from wild-type mice was retained for the analysis. Last, we hypothesized that scRNA-seq studies of human tissues would display more heterogeneity between replicates than studies of animal models, where factors such as genotype, environment, and perturbation can be precisely controlled. To test this hypothesis, we computed the mean Δ-variance across all genes in the 38 human or mouse scRNA-seq datasets in our compendium (n = 18 human datasets and 20 mouse datasets).

**Application to spinal cord injury**. To demonstrate the relevance of our findings to the discovery of new biological mechanisms, we collected scRNA-seq data of the mouse lumbar spinal cord after SCI, and performed DE analysis.

*Animal model*. Experiments were conducted on adult male or female C57BL/6 mice (15-35 g body weight, 12-30 weeks of age). Vglut2:Cre (Jackson Laboratory 016963) transgenic mice were used and maintained on a mixed genetic background (129/C57BL/6). Housing, surgery, behavioral experiments and euthanasia were performed in compliance with the Swiss Veterinary Law guidelines. Animal care, including manual bladder voiding, was performed twice daily for the first 3 weeks after injury and once daily for the remaining post-injury period. All procedures and surgeries were approved by the Veterinary Office of the Canton of Geneva (Switzerland; GE/57/20 A).

*Surgical procedures and post-surgical care*. Surgical procedures were performed as previously described[25,60–62]. Briefly, a laminectomy was made at the mid-thoracic level (T9 vertebra). We performed a contusion injury using a force-controlled spinal cord impactor (IH-0400 Impactor, Precision Systems and Instrumentation LLC, USA[63]), as previously described[60,64]. The applied force was set to 90 kdyn. Analgesia (buprenorphine, Essex Chemie AG, Switzerland, 0.01–0.05 mg per kg, s.c.) was provided for three days after surgery.

*Kinematic recordings*. Kinematic recordings were performed as previously described[25,60,61,65–67]. Bilateral leg kinematics were captured using a 12-camera infrared (200 Hz) Vicon high-speed motion capture system (Vicon Motion Systems, UK). We attached reflective markers bilaterally at the iliac crest, the greater trochanter (hip joint), the lateral condyle (knee joint), the lateral malleolus (ankle), and the distal end of the fifth metatarsophalangeal joint.

*Kinematic analysis*. For each leg, 15 step cycles were extracted for each mouse. A total of 75 parameters quantifying kinematic and kinetic features were computed for each gait cycle accordingly. To evaluate differences between conditions we implemented a multistep statistical procedure based on principal component analysis, as previously described[25,60,61,65–67].

*Electrophysiology*. Mice were anaesthetised using a ketamine/xylazine anesthesia mixture. Stainless steel needle electrodes (30 G) were inserted through the posterior surface of the ankle for nerve stimulation and into the lateral, plantar surface of the foot for digital electromyographic recordings. Responses were recorded at a stimulation intensity of 2 x threshold for evoking an H-wave. Signals were amplified and filtered (1000x and 300 Hz–5 kHz, AM Systems differential amplifier) then digitised (PowerLab, AD instruments) for acquisition. Twenty recordings were made at each of 5 different stimulation frequencies (0.1, 0.5, 1, 2, and 5 Hz) with a one minute break between each frequency setting. Peak to peak amplitudes for at least three responses were measured for both M and H waves at each frequency, for each animal. Response amplitudes were first normalized to the amplitude of the M wave at each frequency, and then normalized to the H/M ratio at 0.1 Hz for comparisons across animals.

*Single-nucleus RNA sequencing*. Single-nucleus dissociation of the mouse spinal cord was performed as previously described[27,51]. Animals were first euthanized by isoflurane inhalation and cervical dislocation. The lumbar spinal cord site was rapidly dissected and frozen on dry ice. Spinal cords were dounced in 500 μl sucrose buffer (0.32 M sucrose, 10 mM HEPES [pH 8.0], 5 mM CaCl₂, 3 mM Mg acetate, 0.1 mM EDTA, 1 mM DTT) and 0.1% Triton X-100 with the Kontes Dounce Tissue Grinder. 2 mL of sucrose buffer was added and filtered through a μm cell strainer. The lysate was centrifuged at 3200 g for 10 min at 4 °C. The supernatant was decanted, and 3 mL of sucrose buffer added to the pellet and incubated for 1 min. The pellet was homogenized using an Ultra-Turrax and 12.5 mL of density buffer (1 M sucrose, 10 mM HEPES [pH 8.0], 3 mM Mg acetate, 1 mM DTT) was added below the nuclei layer. The tube was centrifuged at 3200 g at 4 °C and supernatant poured off. Nuclei on the bottom half of the tube wall were collected with 100 μl PBS with 0.04% BSA and 0.2 U/μl RNase inhibitor.

Resuspended nuclei were filtered through a 30 μm strainer, and adjusted to 1000 nuclei/μl.

*Library preparation.* Library preparation was carried out using the 10x Genomics Chromium Single Cell Kit Version 2. The nuclei suspension was added to the Chromium RT mix to achieve loading numbers of 5,000. For downstream cDNA synthesis (13 PCR cycles), library preparation and sequencing, the manufacturer's instructions were followed.

*Read alignment.* Reads were aligned to the most recent Ensembl release (GRCm38.93) using Cell Ranger, and a matrix of unique molecular identifier (UMI) counts, including both intronic and exonic reads, was obtained using velocyto[68]. Seurat[35] was then used to calculate quality control metrics for each cell barcode, including the number of genes detected, number of UMIs, and proportion of reads aligned to mitochondrial genes. Low-quality cells were filtered by removing cells expressing less than 200 genes or with more than 5% mitochondrial reads. Genes expressed in less than 3 cells were likewise removed, yielding a count matrix consisting of 22,806 genes and 19,237 cells.

*Clustering and integration.* Prior to clustering analysis, we first performed batch effect correction and data integration across the two different experimental conditions as previously described[27]. Gene expression data were normalized using regularized negative binomial models[69], then integrated across batches using the data integration workflow within Seurat. The normalized and integrated gene expression matrices were then subjected to clustering to identify cell types in the integrated dataset, again using the default Seurat workflow. Cell types were manually annotated on the basis of marker gene expression, guided by previous studies of the mouse spinal cord[27,51,70].

*Viral tract tracing.* All surgeries on mice were performed at EPFL under general anaesthesia with isoflurane in oxygen-enriched air using an operating microscope, and rodent stereotaxic apparatus (David Kopf). We identified plasticity of excitatory neurons in the lumbar spinal cord after SCI using AAV-DJ-hSyn Flex mGFP 2 A synaptophysin mRuby (Stanford Vector Core Facility, reference AAV DJ GVVC-AAV-100, titer 1.15E12 genome copies per ml[71]) injections on each side of the cord of Vglut2:Cre mice at the L6 spinal level, 0.25 μl 0.6 mm below the surface at 0.1 μl per minute using glass micropipettes (ground to 50 to 100 μm tips) connected via high-pressure tubing (Kopf) to 10-μl syringes under the control of microinfusion pumps.

*Immunohistochemistry.* After terminal anaesthesia by barbiturate overdose, mice were perfused transcardially with 4% paraformaldehyde and spinal cords processed for immunofluorescence as previously described[60,72]. Primary antibodies were: rat anti-Pecam1 (BD Biosciences 550274, 1:200). Secondary antibodies were: Alexa Fluor 555 Goat Anti Rat (1:200, Life Technologies, A21434). Immunofluorescence was imaged digitally on a slide scanner [Olympus VS-120 Slide scanner] or confocal microscope [Zeiss LSM880 + Airy fast module with ZEN 2 Black software (Zeiss, Oberkochen, Germany)]. Images were processed using ImageJ (NIH) or Imaris (Bitplane, version 9.0.0).

*Tissue clearing.* Mouse spinal cords were cleared using CLARITY[73] four weeks after injection of AAV-DJ-hSyn-flex-mGFP-2A-Synaptophysin-mRuby[71]. Mice were perfused transcardially first with 0.1 M PBS followed by 4% PFA (in 0.1 M PBS, pH 7.4) at 4 °C. The spinal cords were dissected and post-fixed in 4% PFA (in 0.1 M PBS) for 24 h at 4 °C. The dura was removed from the samples prior to clearing. Samples were incubated in A4P0 hydrogel solution (4% acrylamide in 0.001 M PBS with 0.25% of the photoinitiator 2,2′-azobis[2-(2-imidazolin-2-yl)propane] dihydrochloride (Wako Pure Chemical, Osaka, Japan)) for 24 h at 4 °C with gentle nutation. Samples were degassed by bubbling nitrogen gas through the tube for 3 m. Hydrogel polymerization was initiated by incubating the sample in a 37 °C water bath for 2 h. Tissue was washed in 0.001 M PBS for 5 m at room temperature. Samples were then placed in the X-CLARITY Tissue Clearing System I (Logos Biosystems Inc., South Korea) set to 1.2 A, 100 RPM, 37 °C. Clearing solution was made in-house from 40 g of sodium dodecyl sulfate (SDS), 200 mM boric acid, and filled to a total volume of 1 L with dH2O (pH adjusted to 8.5). Samples cleared after ~10–15 h. The sample was then washed for at least 24 h at room temperature with shaking in 1x PBS and 0.1% Triton-X (with 0.02% sodium azide) to remove excess SDS. The sample was then incubated in RIMS (40 g of Histodenz dissolved in 30 mL of 0.02 M PB, pH 7.5, 0.01% sodium azide, refractive index 1.465) for at least 24 h at room temperature with gentle shaking prior to imaging. Imaging was performed using a custom-built MesoSPIM[74] and CLARITY-optimized light-sheet microscope (COLM) as described[73]. A customized sample holder was used to secure the spinal cords in a chamber filled with RIMS. Samples were imaged using a 2.5× objective at the MesoSPIM and a 4x objective at the COLM with two lightsheets illuminating the sample from the left and the right sides. The pixel resolution was 2.6 μm × 2.6 μm × 3 μm for the 2,5x acquisition; and 1.4 μm by 1.4 μm by 5 μm for the 4x acquisition in the x-, y-, and z-directions. Images were acquired as 16-bit TIFF files. 3D reconstructions of the raw images were produced using Arivis (v3.4) and Imaris softwares (Bitplane, v.9.0.0).

*RNAscope.* To corroborate the results suggested by DE analysis of scRNA-seq data, we analyzed the in situ co-localization of putatively DE genes and cell type marker genes using RNAscope (Advanced Cell Diagnostics)[30]. Lists of putatively DE genes were obtained for representative single-cell and pseudobulk DE methods (the Wilcoxon rank-sum test and edgeR-LRT, respectively), and cross-referenced against a list of validated probes designed and provided by Advanced Cell Diagnostics, Inc. In total, probes were obtained for 13 genes identified as DE by the Wilcoxon rank-sum test (Sgms1, catalog no. 538561; Pcdh9, catalog no. 524921; Epas1, catalog no. 314371; Tcaf1, catalog no. 466921; Gspt1, catalog no. 530471; Prex2, catalog no. 432481; Sema7a, catalog no. 437261; Zfp366, catalog no. 443301; Cpe, catalog no. 454091; Afap1l2, catalog no. 556251; Nedd4l, catalog no. 491981; Adipor2, catalog no. 452861; Ptpn14, catalog no. 493181) and 7 genes identified by edgeR-LRT (Slc7a11, catalog no. 422511; Gjb2, catalog no. 518881; Pi16, catalog no. 451311; Rbp4, catalog no. 508501; Col1a1, catalog no. 319371; Igfbp6, catalog no. 425721). In addition, we obtained probes for Pecam1 (catalog no. 316721), a classic endothelial cell marker gene. We then obtained 16 μm cryosections from fixed-frozen spinal cords as previously described[27] and performed staining for each probe according to the manufacturer's instructions, using the RNAscope Fluorescent Multiplex Reagent Kit (cat. no. 323133). For each biological replicate (n = 4 per condition for both injured and uninjured mice), we analyzed ten cells positive for *Pecam1* and tallied the number of speckles for each gene of interest. The mean expression of each gene was then calculated for each biological replicate, and a one-tailed t-test was conducted based on the directional change in the snRNA-seq data.

**Mixed models.** Having established that the performance of DE methods is contingent on their ability to account for biological replicates, we asked why mixed models failed to match the performance of pseudobulk methods. In addition to the linear mixed model described above, we implemented generalized linear mixed models (GLMMs) based on the negative binomial or Poisson distributions, adapting implementations provided in the 'muscat' R package[10]. For each of these models, we evaluated the impact of incorporating the library size factors as an offset term, and compared the Wald test of model coefficients to a likelihood ratio test against a reduced model, yielding a total of four GLMMs from each distribution. The enormous computational requirements of the GLMMs prevented us from evaluating these models in the full ground truth datasets; instead, we analyzed a series of downsampled datasets, each containing between 25 and 1,000 cells. To quantify the computational resources required by each DE method, we monitored peak memory usage using the 'peakRAM' R package, and the base R function 'system.time' to record wall time.

**Preprocessing and analysis of published single-cell datasets.** We assembled a compendium of 46 published single-cell or single-nucleus RNA-seq studies (Supplementary Fig. 3), and performed DE analyses across this compendium to establish the generality of our conclusions. For publications containing more than one comparison, only a single comparison was retained, as described in detail below. We retained the comparison involving the greatest number of cells, and used the most fine-grained cell type annotations provided by the authors of the original studies. When count matrices did not use gene symbols, the provided identifiers were mapped to gene symbols, and counts summed across genes mapping to identical symbols. Only cell types with at least three cells in each condition were subjected to DE analysis, and genes detected in less than three cells were removed.

*Angelidis et al., 2019*[14]. scRNA-seq data from young and aged mouse lung (3 m and 24 m, respectively), as well as matching bulk data from two purified cell types, was obtained from GEO (GSE124872). Metadata was obtained from GitHub (https://github.com/theislab/2018_Angelidis). Cells with missing cell type annotations were removed from the single-cell data. DE analysis was performed by comparing cells from young and old mice.

*Arneson et al., 2018*[75]. scRNA-seq data from the hippocampus of mice after a mild traumatic brain injury (mTBI), delivered using a mild fluid percussion injury model, and matched controls was obtained from GEO (GSE101901). Metadata, including cell type annotations, were provided by the authors. DE analysis was performed by comparing cells from mTBI and control mice.

*Avey et al., 2018*[76]. scRNA-seq data from the nucleus accumbens of mice treated with morphine for 4 h and saline-treated controls was obtained from GEO (GSE118918). Cells identified as doublets and non-unique barcodes were removed. Metadata, including cell type annotations, were provided by the authors. DE analysis was performed by comparing cells from morphine- and saline-treated mice.

*Aztekin et al., 2019*[77]. scRNA-seq data from regeneration-competent (NF stage 40-41) Xenopus laevis tadpoles was obtained from ArrayExpress (E-MTAB-7716). DE analysis was performed by comparing cells from tadpoles at 1 d post-amputation to control tadpoles.

*Bhattacherjee et al., 2019*[78]. scRNA-seq data from the prefrontal cortex of mice exposed to a cocaine withdrawal paradigm was obtained from GEO (GSE124952). DE analysis was performed by comparing cells at the 15 d post-withdrawal timepoint from cocaine- or saline-treated mice.

*Brenner et al., 2020*[79]. snRNA-seq data from the prefrontal cortex of alcoholic and control individuals was obtained from GEO (GSE141552). Metadata, including cell type annotations, were provided by the authors. DE analysis was performed by comparing nuclei from alcoholic and control individuals.

*Cano-Gamez et al., 2020*[13]. scRNA-seq data from naive and memory T cells, stimulated with anti-CD3/anti-CD28 coated beads in the presence or absence of various combinations of cytokines, was obtained from the supporting website (https://www.opentargets.org/projects/effectorness). Matching bulk RNA-seq and proteomics data was obtained from the same source. For the analyses presented as part of the compendium of 46 datasets, DE analysis was performed by comparing iTreg and control cells.

*Cheng et al., 2019*[80]. scRNA-seq data from intestinal crypt cells in wild-type and Hmgcs2 knockout mice was obtained directly from the authors of the original publication. DE analysis was performed by comparing wild type and KO mice.

*Co et al., 2020*[81]. scRNA-seq data of sorted cells from Drd1a-tdTomato+ control and Foxp2 KO mice was obtained from GEO (GSE130653). Cell type annotations were provided by the authors. Cell types annotated as 'Low quality' were removed prior to further analysis. DE analysis was performed by comparing WT and Foxp2 KO mice.

*Crowell et al., 2020*[10]. snRNA-seq data from the prefrontal cortex of mice peripherally stimulated with lipopolysaccharide (LPS) and control mice was obtained from the Bioconductor package 'muscData', using the 'Crowell19_4vs4' function. DE analysis was performed by comparing nuclei from LPS-treated and control mice.

*Davie et al., 2018*[82]. scRNA-seq data from the brains of flies of varying ages, sexes, and genotypes was obtained from the supporting website (http://scope.aertslab.org, file 'Aerts_Fly_AdultBrain_Filtered_57k.loom'). Cells marked as 'Unannotated' were removed. DE analysis was performed by comparing cells from DGRP-551 and W[1118] flies.

*Denisenko et al., 2020*[83]. scRNA-seq data from human kidneys subjected to varying dissociation methods and cell fixation techniques was obtained from GEO (GSE141115). Metadata, including cell type annotations, was obtained from the supporting information files accompanying the published manuscript. DE analysis was performed by comparing cells fixed with methanol and freshly dissociated cells, both at −20 °C.

*Der et al., 2019*[84]. scRNA-seq data of skin samples from patients with lupus nephritis (LN) and healthy controls was obtained from ImmGen (SDY997, EXP15077). Cell type annotations were obtained from the authors of the original manuscript. Other metadata, including biological replicate and experimental condition annotations for each individual cell, was obtained from the supporting information files accompanying the published manuscript. DE analysis was performed by comparing cells from patients with LN and healthy controls.

*Goldfarbmuren et al., 2020*[56]. scRNA-seq data of tracheal epithelial cells from smokers and non-smokers was obtained from GEO (GSE134174). Patients designated as 'excluded' were removed prior to downstream analysis. DE analysis was performed by comparing cells from smokers and non-smokers.

*Grubman et al., 2019*[52]. snRNA-seq data from the entorhinal cortex of patients with Alzheimer's disease and matched controls was obtained from the supporting website (http://adsn.ddnetbio.com). Nuclei annotated as 'undetermined' or 'doublet' were removed. DE analysis was performed by comparing nuclei from patients with Alzheimer's disease and controls.

*Gunner et al., 2019*[85]. scRNA-seq data from the mouse barrel cortex before or after whisker lesioning was obtained from GEO (GSE129150). Cell types not included in Supplementary Fig. 10 of the original publication were removed. DE analysis was performed by comparing cells from lesioned and control mice.

*Haber et al., 2017*[86]. scRNA-seq data from epithelial cells of the mouse small intestine in healthy mice and after ten days of infection with the parasitic helminth *Heligmosomoides polygyrus* was obtained from GEO (GSE92332), using the Drop-seq data collected by the original publication. DE analysis was performed by comparing cells from infected and uninfected mice.

*Hagai et al., 2018*[12]. scRNA-seq data of bone marrow-derived mononuclear phagocytes from four different species (mouse, rat, pig, and rabbit) exposed to lipopolysaccharide (LPS) or poly-I:C for two, four, or six h was obtained from ArrayExpress (E-MTAB-6754). Matching bulk RNA-seq data was also obtained from ArrayExpress (E-MTAB-6773). Finally, scRNA-seq data from human dermal fibroblasts stimulated with interferon-β for two or six h, in which the ERCC mixture of synthetic mRNAs was spiked in alongside every cell, was obtained from ArrayExpress (E-MTAB-7051). Counts were summed across technical replicates of the same biological samples. For the analyses presented as part of the compendium of 46 datasets, DE analysis was performed by comparing rabbit cells stimulated with LPS for 2 h and control cells. DE analysis of the spike-in dataset was performed by comparing cells stimulated for 2 h and 6 h.

*Hashimoto et al., 2019*[87]. scRNA-seq data of peripheral blood mononuclear cells from human supercentenarians and younger controls was obtained from the supporting website (http://gerg.gsc.riken.jp/SC2018). Metadata, including cell type annotations, were provided by the authors. DE analysis was performed by comparing cells from supercentenarians and younger controls.

*Hrvatin et al., 2018*[50]. scRNA-seq data from the visual cortex of mice housed in darkness, then exposed to light for 0 h, 1 h, or 4 h was obtained from GEO (GSE102827). Cell types labeled as 'NA' were removed from downstream analyses. DE analysis was performed by comparing cells from mice stimulated with light for 4 h to control mice.

*Hu et al., 2017*[88]. snRNA-seq data from the cerebral cortex of mice after pentylenetetrazole (PTZ)-induced seizure and saline-treated controls was obtained from the Google Drive folder accompanying the original publication (https://github.com/wulabupenn/Hu_MolCell_2017). DE analysis was performed by comparing cells from PTZ- and saline-treated mice.

*Huang et al., 2019*[58]. scRNA-seq data from the colon of pediatric patients with colitis and inflammatory bowel disease and matched controls was obtained from the supporting website (https://zhanglaboratory.com/research-data/). DE analysis was performed by comparing cells from patients with colitis and healthy controls.

*Jaitin et al., 2019*[89]. scRNA-seq data from white adipose tissue of mice fed either a high-fat diet or normal chow for six weeks were obtained from the Bitbucket repository accompanying the original publication (https://bitbucket.org/account/user/amitlab/projects/ATIC). Metadata, including cell type annotations, were provided by the authors. DE analysis was performed by comparing cells from high-fat diet and normal chow-fed mice.

*Jakel et al., 2019*[90]. snRNA-seq data of oligodendrocytes from patients with multiple sclerosis and matched controls was obtained from GEO (GSE118257). DE analysis was performed by comparing nuclei from individuals with multiple sclerosis versus matched controls.

*Kang et al., 2018*[5]. scRNA-seq data from peripheral blood mononuclear cells (PBMCs) stimulated with recombinant IFN-β for 6 h and unstimulated PBMCs was obtained from GEO (GSE96583). Doublets and unclassified cells were removed. DE analysis was performed by comparing IFN-stimulated and unstimulated cells.

*Kim et al., 2019*[91]. scRNA-seq data from the ventromedial hypothalamus of mice exposed to a range of behavioral stimuli and control mice was obtained from the Mendeley repository accompanying the original publication. Cell type annotations were provided directly by the authors. DE analysis was performed by comparing cells from animals engaging in aggressive behaviour to the common population of control animals.

*Kotliarov et al., 2020*[92]. scRNA-seq data of peripheral blood mononuclear cells from subjects who were subsequently given an influenza vaccination were obtained from Figshare (https://doi.org/10.35092/yhjc.c.4753772). DE analysis was performed by comparing cells from high and low responders to the influenza vaccination, as categorized by the authors.

*Madissoon et al., 2020*[93]. scRNA-seq data from esophagus, lung, and spleen samples after varying durations of cold storage was obtained from the study website (https://cellgeni.cog.sanger.ac.uk/tissue-stability/). DE analysis was performed by comparing cells from samples preserved for 12 h and fresh samples.

*Mathys et al., 2019*[6]. snRNA-seq data from the prefrontal cortex of patients with Alzheimer's disease and matched controls was obtained from Synapse (syn18681734). Patient data and additional metadata were also obtained from Synapse (syn3191087 and syn18642926, respectively). DE analysis was performed by comparing nuclei from patients with Alzheimer's disease and controls.

*Nagy et al., 2020*[57]. snRNA-seq data from the dorsolateral prefrontal cortex of patients with major depressive disorder (MDD) and matched controls was obtained from GEO (GSE144136). DE analysis was performed by comparing nuclei from patients with MDD and controls.

*Nault et al., 2021*[94]. snRNA-seq data from the livers of mice gavaged with 2,3,7,8-tetrachlorodibenzo-p-dioxin or sesame oil vehicle was obtained from GEO (GSE148339). DE analysis was performed by comparing nuclei from treated and vehicle livers.

*Ordovas-Montanes et al., 2018*[95]. scRNA-seq data from ethmoid sinus cells of patients with chronic rhinosinusitis (CRS), with and without nasal polyps, from Supplementary Table 2 of the original publication. DE analysis was performed by comparing cells from patients with polyposis and non-polyposis CRS.

*Reyes et al., 2020*[96]. scRNA-seq data of peripheral blood mononuclear cells from patients with sepsis and healthy controls was obtained from the Broad Institute's Single Cell Portal (SCP548). DE analysis was performed by comparing cells from individuals with bacterial sepsis and controls.

*Reyfman et al., 2019*[15]. scRNA-seq data from the lungs of patients with pulmonary fibrosis and healthy controls was obtained from GEO (GSE122960). Metadata, including cell type annotations, was provided by the authors. One sample ("Cryobiopsy_01") was removed as it was sequenced separately from the rest of the experiment. The results of DE analysis of bulk RNA-seq data, comparing purified AT2 cells or alveolar macrophages from patients with pulmonary fibrosis and healthy controls, were obtained from the supporting information accompanying the original publication. DE analysis was performed by comparing cells from patients with pulmonary fibrosis and controls.

*Rossi et al., 2019*[53]. scRNA-seq data from the hypothalamus of mice fed either a high-fat diet or normal chow for between 9-16 weeks was obtained directly from the authors, in the form of a processed Seurat object. Cells annotated as 'unclassified' were removed. DE analysis was performed by comparing cells from high-fat diet and normal chow-fed mice.

*Sathyamurthy et al., 2018*[51]. snRNA-seq data from the spinal cord parenchyma of adult mice exposed to formalin or matched controls was obtained from GEO (GSE103892). Cell types with blank annotations, or annotated as 'discarded', were

removed. DE analysis was performed by comparing cells from mice exposed to formalin and control animals.

*Schafflick et al., 2020*[97]. scRNA-seq data of peripheral blood mononuclear cells from individuals with multiple sclerosis and matched controls was obtained from GEO (GSE138266). Metadata, including cell type annotations, was obtained from Github (https://github.com/chenlingantelope/MSscRNAseq2019). DE analysis was performed by comparing cells from individuals with multiple sclerosis and controls.

*Schirmer et al., 2019*[98]. snRNA-seq data from cortical and subcortical areas from the brains of patients with multiple sclerosis and control tissue from unaffected individuals was obtained from the web browser accompanying the original publication (https://cells.ucsc.edu/ms). DE analysis was performed by comparing cells from multiple sclerosis and control patients.

*Skinnider et al., 2021*[27]. snRNA-seq data from the spinal cords of mice with a spinal cord injury, some of which were exposed to epidural electrical stimulation to restore locomotion after paralysis, was obtained from GEO (GSE142245). DE analysis was performed by comparing nuclei from paralyzed and walking mice.

*Tran et al., 2019*[55]. scRNA-seq data from the retinal ganglion of mice at various timepoints after an optic nerve crush injury, as well as uninjured controls, was obtained from GEO "GSE137398". Metadata, including cell type annotations, was obtained from the Broad Institute's Single-Cell Portal (SCP509). DE analysis was performed by comparing cells from mice at 12 h post-injury and uninjured mice.

*Wagner et al., 2018*[99]. scRNA-seq data from zebrafish embryos between 14-16 h post-fertilization, with either the chordin locus or a control locus (tyrosinase) disrupted by CRISPR-Cas9 knock- out, was obtained from GEO (GSE112294). DE analysis was performed by comparing cells from chordin- or tyrosinase-targeted embryos.

*Wang et al., 2020*[100]. scRNA-seq data from the ovaries of young and old cynomolgus monkeys was obtained from GEO (GSE130664). Metadata, including cell type annotations, was obtained from the supporting information accompanying the original publication. Spike-ins were removed. DE analysis was performed by comparing cells from young and old primates.

*Wilk et al., 2020*[59]. scRNA-seq data of peripheral blood mononuclear cells from patients with COVID-19 and healthy controls was obtained from the supporting website (https://www.covid19cellatlas.org/). DE analysis was performed by comparing patients with COVID-19 and controls.

*Wirka et al., 2019*[101]. scRNA-seq data from the aortic root of mice fed a high-fat diet or normal chow for eight weeks from GEO (GSE131776). Metadata, including cell type annotations, was provided by the authors, and unannotated cells were removed. DE analysis was performed by comparing cells from high-fat diet and normal chow-fed mice.

*Wu et al., 2017*[49]. scRNA-seq data from the amygdala of mice subjected to 45 min of immobilization stress and control mice was obtained from GEO (GSE103976). DE analysis was performed by comparing cells from stressed and control mice.

*Ximerakis et al., 2019*[102]. scRNA-seq data from whole brains of young (2–3 mo) and old (21–23 mo) mice from the Broad Institute's Single Cell Portal (SCP263). DE analysis was performed by comparing cells from young and old mice.

**Visualization**. Throughout the manuscript, box plots show the median (horizontal line), interquartile range (hinges) and smallest and largest values no more than 1.5 times the interquartile range (whiskers), and the error bars show the standard deviation.

**Reporting summary**. Further information on research design is available in the Nature Research Reporting Summary linked to this article.

## Data availability

Raw sequencing data and count matrices have been deposited to the Gene Expression Omnibus under accession code GSE165003. The 18 'ground truth' datasets, including single-cell RNA-seq, bulk RNA-seq and proteomics data, are available from Zenodo at https://doi.org/10.5281/zenodo.5048449. All other relevant data supporting the key findings of this study are available within the article and its Supplementary Information files or from the corresponding author upon reasonable request. The complete list of all 500 studies is provided as Source Data. Source data are provided with this paper.

## Code availability

We provide an R package, Libra, implementing all methods for DE analysis discussed in this study within a consistent interface. The Libra package is available from GitHub (https://github.com/neurorestore/Libra) and as Supplementary Software 1. In addition, the R source code used to perform data analysis is available from GitHub at https://github.com/neurorestore/DE-analysis.

## References

1. Wang, Z., Gerstein, M. & Snyder, M. RNA-Seq: a revolutionary tool for transcriptomics. *Nat. Rev. Genet.* **10**, 57–63 (2009).
2. Stark, R., Grzelak, M. & Hadfield, J. RNA sequencing: the teenage years. *Nat. Rev. Genet.* **20**, 631–656 (2019).
3. Srinivasan, K. et al. Untangling the brain's neuroinflammatory and neurodegenerative transcriptional responses. *Nat. Commun.* **7**, 11295 (2016).
4. Chen, X., Teichmann, S. A. & Meyer, K. B. From tissues to cell types and back: single-cell gene expression analysis of tissue architecture. *Annu. Rev. Biomed. Data Sci.* **1**, 29–51 (2018).
5. Kang, H. M. et al. Multiplexed droplet single-cell RNA-sequencing using natural genetic variation. *Nat. Biotechnol.* **36**, 89–94 (2018).
6. Mathys, H. et al. Single-cell transcriptomic analysis of Alzheimer's disease. *Nature* **570**, 332–337 (2019).
7. Finak, G. et al. MAST: a flexible statistical framework for assessing transcriptional changes and characterizing heterogeneity in single-cell RNA sequencing data. *Genome Biol.* **16**, 278 (2015).
8. Kharchenko, P. V., Silberstein, L. & Scadden, D. T. Bayesian approach to single-cell differential expression analysis. *Nat. Methods* **11**, 740–742 (2014).
9. Zimmerman, K. D., Espeland, M. A. & Langefeld, C. D. Pseudoreplication bias in single-cell studies; a practical solution. *BioRxiv* (2020) https://doi.org/10.1101/2020.01.15.906248.
10. Crowell, H. L. et al. muscat detects subpopulation-specific state transitions from multi-sample multi-condition single-cell transcriptomics data. *Nat. Commun.* **11**, 6077 (2020).
11. Mehta, T., Tanik, M. & Allison, D. B. Towards sound epistemological foundations of statistical methods for high-dimensional biology. *Nat. Genet.* **36**, 943–947 (2004).
12. Hagai, T. et al. Gene expression variability across cells and species shapes innate immunity. *Nature* **563**, 197–202 (2018).
13. Cano-Gamez, E. et al. Single-cell transcriptomics identifies an effectorness gradient shaping the response of CD4+ T cells to cytokines. *Nat. Commun.* **11**, 1801 (2020).
14. Angelidis, I. et al. An atlas of the aging lung mapped by single cell transcriptomics and deep tissue proteomics. *Nat. Commun.* **10**, 963 (2019).
15. Reyfman, P. A. et al. Single-cell transcriptomic analysis of human lung provides insights into the pathobiology of pulmonary fibrosis. *Am. J. Respir. Crit. Care Med.* **199**, 1517–1536 (2019).
16. Irizarry, R. A. et al. Multiple-laboratory comparison of microarray platforms. *Nat. Methods* **2**, 345–350 (2005).
17. Soneson, C. & Robinson, M. D. Bias, robustness and scalability in single-cell differential expression analysis. *Nat. Methods* **15**, 255–261 (2018).
18. Lun, A. T. L. & Marioni, J. C. Overcoming confounding plate effects in differential expression analyses of single-cell RNA-seq data. *Biostatistics* **18**, 451–464 (2017).
19. Rapaport, F. et al. Comprehensive evaluation of differential gene expression analysis methods for RNA-seq data. *Genome Biol.* **14**, R95 (2013).
20. Tarazona, S., García-Alcalde, F., Dopazo, J., Ferrer, A. & Conesa, A. Differential expression in RNA-seq: a matter of depth. *Genome Res.* **21**, 2213–2223 (2011).
21. Jiang, L. et al. Synthetic spike-in standards for RNA-seq experiments. *Genome Res.* **21**, 1543–1551 (2011).
22. Tung, P.-Y. et al. Batch effects and the effective design of single-cell gene expression studies. *Sci. Rep.* **7**, 39921 (2017).
23. Ståhl, P. L. et al. Visualization and analysis of gene expression in tissue sections by spatial transcriptomics. *Science* **353**, 78–82 (2016).
24. Maniatis, S. et al. Spatiotemporal dynamics of molecular pathology in amyotrophic lateral sclerosis. *Science* **364**, 89–93 (2019).
25. van den Brand, R. et al. Restoring voluntary control of locomotion after paralyzing spinal cord injury. *Science* **336**, 1182–1185 (2012).
26. Beauparlant, J. et al. Undirected compensatory plasticity contributes to neuronal dysfunction after severe spinal cord injury. *Brain* **136**, 3347–3361 (2013).
27. Skinnider, M. A. et al. Cell type prioritization in single-cell data. *Nat. Biotechnol.* **39**, 30–34 (2021).
28. Squair, J. W., Skinnider, M. A., Gautier, M., Foster, L. J. & Courtine, G. Prioritization of cell types responsive to biological perturbations in single-cell data with Augur. *Nat. Protoc.* **16**, 3836–3873 (2021).
29. Robinson, M. D., McCarthy, D. J. & Smyth, G. K. edgeR: a Bioconductor package for differential expression analysis of digital gene expression data. *Bioinformatics* **26**, 139–140 (2010).
30. Wang, F. et al. RNAscope: a novel in situ RNA analysis platform for formalin-fixed, paraffin-embedded tissues. *J. Mol. Diagn.* **14**, 22–29 (2012).
31. Samanta, D. & Semenza, G. L. Maintenance of redox homeostasis by hypoxia-inducible factors. *Redox Biol.* **13**, 331–335 (2017).
32. Zhang, C. et al. IGF binding protein-6 expression in vascular endothelial cells is induced by hypoxia and plays a negative role in tumor angiogenesis. *Int. J. Cancer* **130**, 2003–2012 (2012).

33. Li, Y. et al. Pericytes impair capillary blood flow and motor function after chronic spinal cord injury. *Nat. Med.* **23**, 733–741 (2017).

34. Zimmerman, K. D., Espeland, M. A. & Langefeld, C. D. A practical solution to pseudoreplication bias in single-cell studies. *Nat. Commun.* **12**, 738 (2021).

35. Stuart, T. et al. Comprehensive integration of single-cell data. *Cell* **177**, 1888–1902.e21 (2019).

36. Wolf, F. A., Angerer, P. & Theis, F. J. SCANPY: large-scale single-cell gene expression data analysis. *Genome Biol.* **19**, 15 (2018).

37. Svensson, V., da Veiga Beltrame, E. & Pachter, L. A curated database reveals trends in single-cell transcriptomics. *Database (Oxford)* **2020**, (2020).

38. Zhang, J. M., Kamath, G. M. & Tse, D. N. Valid post-clustering differential analysis for single-cell RNA-Seq. *Cell Syst.* **9**, 383–392.e6 (2019).

39. Ntranos, V., Yi, L., Melsted, P. & Pachter, L. A discriminative learning approach to differential expression analysis for single-cell RNA-seq. *Nat. Methods* **16**, 163–166 (2019).

40. McDavid, A. et al. Data exploration, quality control and testing in single-cell qPCR-based gene expression experiments. *Bioinformatics* **29**, 461–467 (2013).

41. Love, M. I., Huber, W. & Anders, S. Moderated estimation of fold change and dispersion for RNA-seq data with DESeq2. *Genome Biol.* **15**, 550 (2014).

42. Ritchie, M. E. et al. limma powers differential expression analyses for RNA-sequencing and microarray studies. *Nucleic Acids Res.* **43**, e47 (2015).

43. McCarthy, D. J., Chen, Y. & Smyth, G. K. Differential expression analysis of multifactor RNA-Seq experiments with respect to biological variation. *Nucleic Acids Res.* **40**, 4288–4297 (2012).

44. Lun, A. T. L., Chen, Y. & Smyth, G. K. It's DE-licious: a recipe for differential expression analyses of RNA-seq experiments using quasi-likelihood methods in edgeR. *Methods Mol. Biol.* **1418**, 391–416 (2016).

45. Law, C. W., Chen, Y., Shi, W. & Smyth, G. K. voom: Precision weights unlock linear model analysis tools for RNA-seq read counts. *Genome Biol.* **15**, R29 (2014).

46. Subramanian, A. et al. Gene set enrichment analysis: a knowledge-based approach for interpreting genome-wide expression profiles. *Proc. Natl Acad. Sci. USA* **102**, 15545–15550 (2005).

47. Sergushichev, A. An algorithm for fast preranked gene set enrichment analysis using cumulative statistic calculation. *BioRxiv* (2016) https://doi.org/10.1101/060012.

48. Zappia, L., Phipson, B. & Oshlack, A. Splatter: simulation of single-cell RNA sequencing data. *Genome Biol.* **18**, 174 (2017).

49. Wu, Y. E., Pan, L., Zuo, Y., Li, X. & Hong, W. Detecting activated cell populations using single-cell RNA-Seq. *Neuron* **96**, 313–329.e6 (2017).

50. Hrvatin, S. et al. Single-cell analysis of experience-dependent transcriptomic states in the mouse visual cortex. *Nat. Neurosci.* **21**, 120–129 (2018).

51. Sathyamurthy, A. et al. Massively parallel single nucleus transcriptional profiling defines spinal cord neurons and their activity during behavior. *Cell Rep.* **22**, 2216–2225 (2018).

52. Grubman, A. et al. A single-cell atlas of entorhinal cortex from individuals with Alzheimer's disease reveals cell-type-specific gene expression regulation. *Nat. Neurosci.* **22**, 2087–2097 (2019).

53. Rossi, M. A. et al. Obesity remodels activity and transcriptional state of a lateral hypothalamic brake on feeding. *Science* **364**, 1271–1274 (2019).

54. Smillie, C. S. et al. Intra- and inter-cellular rewiring of the human colon during ulcerative Colitis. *Cell* **178**, 714–730.e22 (2019).

55. Tran, N. M. et al. Single-cell profiles of retinal ganglion cells differing in resilience to injury reveal neuroprotective genes. *Neuron* **104**, 1039–1055.e12 (2019).

56. Goldfarbmuren, K. C. et al. Dissecting the cellular specificity of smoking effects and reconstructing lineages in the human airway epithelium. *Nat. Commun.* **11**, 2485 (2020).

57. Nagy, C. et al. Single-nucleus transcriptomics of the prefrontal cortex in major depressive disorder implicates oligodendrocyte precursor cells and excitatory neurons. *Nat. Neurosci.* **23**, 771–781 (2020).

58. Huang, B. et al. Mucosal profiling of pediatric-onset Colitis and IBD reveals common pathogenics and therapeutic pathways. *Cell* **179**, 1160–1176.e24 (2019).

59. Wilk, A. J. et al. A single-cell atlas of the peripheral immune response in patients with severe COVID-19. *Nat. Med.* **26**, 1070–1076 (2020).

60. Asboth, L. et al. Cortico-reticulo-spinal circuit reorganization enables functional recovery after severe spinal cord contusion. *Nat. Neurosci.* **21**, 576–588 (2018).

61. Wenger, N. et al. Spatiotemporal neuromodulation therapies engaging muscle synergies improve motor control after spinal cord injury. *Nat. Med.* **22**, 138–145 (2016).

62. Anderson, M. A. et al. Required growth facilitators propel axon regeneration across complete spinal cord injury. *Nature* **561**, 396–400 (2018).

63. Scheff, S. W., Rabchevsky, A. G., Fugaccia, I., Main, J. A. & Lumpp, J. E. Experimental modeling of spinal cord injury: characterization of a force-defined injury device. *J. Neurotrauma* **20**, 179–193 (2003).

64. Squair, J. W. et al. Integrated systems analysis reveals conserved gene networks underlying response to spinal cord injury. *elife* **7**, (2018).

65. Courtine, G. et al. Transformation of nonfunctional spinal circuits into functional states after the loss of brain input. *Nat. Neurosci.* **12**, 1333–1342 (2009).

66. Takeoka, A., Vollenweider, I., Courtine, G. & Arber, S. Muscle spindle feedback directs locomotor recovery and circuit reorganization after spinal cord injury. *Cell* **159**, 1626–1639 (2014).

67. Dominici, N. et al. Versatile robotic interface to evaluate, enable and train locomotion and balance after neuromotor disorders. *Nat. Med.* **18**, 1142–1147 (2012).

68. La Manno, G. et al. RNA velocity of single cells. *Nature* **560**, 494–498 (2018).

69. Hafemeister, C. & Satija, R. Normalization and variance stabilization of single-cell RNA-seq data using regularized negative binomial regression. *Genome Biol.* **20**, 296 (2019).

70. Zeisel, A. et al. Molecular architecture of the mouse nervous system. *Cell* **174**, 999–1014.e22 (2018).

71. Grimm, D. et al. In vitro and in vivo gene therapy vector evolution via multispecies interbreeding and retargeting of adeno-associated viruses. *J. Virol.* **82**, 5887–5911 (2008).

72. Anderson, M. A. et al. Astrocyte scar formation aids central nervous system axon regeneration. *Nature* **532**, 195–200 (2016).

73. Tomer, R., Ye, L., Hsueh, B. & Deisseroth, K. Advanced CLARITY for rapid and high-resolution imaging of intact tissues. *Nat. Protoc.* **9**, 1682–1697 (2014).

74. Voigt, F. F. et al. The mesoSPIM initiative: open-source light-sheet microscopes for imaging cleared tissue. *Nat. Methods* **16**, 1105–1108 (2019).

75. Arneson, D. et al. Single cell molecular alterations reveal target cells and pathways of concussive brain injury. *Nat. Commun.* **9**, 3894 (2018).

76. Avey, D. et al. Single-cell RNA-Seq uncovers a robust transcriptional response to morphine by Glia. *Cell Rep.* **24**, 3619–3629.e4 (2018).

77. Aztekin, C. et al. Identification of a regeneration-organizing cell in the Xenopus tail. *Science* **364**, 653–658 (2019).

78. Bhattacherjee, A. et al. Cell type-specific transcriptional programs in mouse prefrontal cortex during adolescence and addiction. *Nat. Commun.* **10**, 4169 (2019).

79. Brenner, E. et al. Single cell transcriptome profiling of the human alcohol-dependent brain. *Hum. Mol. Genet.* **29**, 1144–1153 (2020).

80. Cheng, C.-W. et al. Ketone body signaling mediates intestinal stem cell homeostasis and adaptation to diet. *Cell* **178**, 1115–1131.e15 (2019).

81. Co, M., Hickey, S. L., Kulkarni, A., Harper, M. & Konopka, G. Cortical foxp2 supports behavioral flexibility and developmental dopamine D1 receptor expression. *Cereb. Cortex* **30**, 1855–1870 (2020).

82. Davie, K. et al. A single-cell transcriptome Atlas aging Drosophila brain. *Cell* **174**, 982–998.e20 (2018).

83. Denisenko, E. et al. Systematic assessment of tissue dissociation and storage biases in single-cell and single-nucleus RNA-seq workflows. *Genome Biol.* **21**, 130 (2020).

84. Der, E. et al. Tubular cell and keratinocyte single-cell transcriptomics applied to lupus nephritis reveal type I IFN and fibrosis relevant pathways. *Nat. Immunol.* **20**, 915–927 (2019).

85. Gunner, G. et al. Sensory lesioning induces microglial synapse elimination via ADAM10 and fractalkine signaling. *Nat. Neurosci.* **22**, 1075–1088 (2019).

86. Haber, A. L. et al. A single-cell survey of the small intestinal epithelium. *Nature* **551**, 333–339 (2017).

87. Hashimoto, K. et al. Single-cell transcriptomics reveals expansion of cytotoxic CD4 T cells in supercentenarians. *Proc. Natl Acad. Sci. USA* **116**, 24242–24251 (2019).

88. Hu, P. et al. Dissecting cell-type composition and activity-dependent transcriptional state in mammalian brains by massively parallel single-nucleus RNA-seq. *Mol. Cell* **68**, 1006–1015.e7 (2017).

89. Jaitin, D. A. et al. Lipid-associated macrophages control metabolic homeostasis in a Trem2-dependent manner. *Cell* **178**, 686–698.e14 (2019).

90. Jäkel, S. et al. Altered human oligodendrocyte heterogeneity in multiple sclerosis. *Nature* **566**, 543–547 (2019).

91. Kim, D.-W. et al. Multimodal analysis of cell types in a hypothalamic node controlling social behavior. *Cell* **179**, 713–728.e17 (2019).

92. Kotliarov, Y. et al. Broad immune activation underlies shared set point signatures for vaccine responsiveness in healthy individuals and disease activity in patients with lupus. *Nat. Med.* **26**, 618–629 (2020).

93. Madissoon, E. et al. scRNA-seq assessment of the human lung, spleen, and esophagus tissue stability after cold preservation. *Genome Biol.* **21**, 1 (2019).

94. Nault, R., Fader, K. A., Bhattacharya, S. & Zacharewski, T. R. Single-nuclei RNA sequencing assessment of the hepatic effects of 2,3,7,8-Tetrachlorodibenzo-p-dioxin. *Cell. Mol. Gastroenterol. Hepatol.* **11**, 147–159 (2021).

95. Ordovas-Montanes, J. et al. Allergic inflammatory memory in human respiratory epithelial progenitor cells. *Nature* **560**, 649–654 (2018).

96. Reyes, M. et al. An immune-cell signature of bacterial sepsis. *Nat. Med.* **26**, 333–340 (2020).

97.  Schafflick, D. et al. Integrated single cell analysis of blood and cerebrospinal fluid leukocytes in multiple sclerosis. *Nat. Commun.* **11**, 247 (2020).
98.  Schirmer, L. et al. Neuronal vulnerability and multilineage diversity in multiple sclerosis. *Nature* **573**, 75–82 (2019).
99.  Wagner, D. E. et al. Single-cell mapping of gene expression landscapes and lineage in the zebrafish embryo. *Science* **360**, 981–987 (2018).
100. Wang, S. et al. Single-cell transcriptomic atlas primate ovarian aging. *Cell* **180**, 585–600.e19 (2020).
101. Wirka, R. C. et al. Atheroprotective roles of smooth muscle cell phenotypic modulation and the TCF21 disease gene as revealed by single-cell analysis. *Nat. Med.* **25**, 1280–1289 (2019).
102. Ximerakis, M. et al. Single-cell transcriptomic profiling of the aging mouse brain. *Nat. Neurosci.* **22**, 1696–1708 (2019).

## Acknowledgements

## Author contributions

J.W.S and M.A.S. performed computational analysis, with contributions from M.G. J.W.S., C.K., M.A.A., N.D.J., T.H. and Q.B. performed experimental validation, including RNAscope, immunohistochemistry, CLARITY, microscopy, and electrophysiology. J.W.S., M.G. and Q.B. analyzed experimental validation data. C.K., K.J.E.M. and A.J.L. performed nucleus extraction and single-nucleus RNA-seq. J.W.S., M.G., R.H., T.Q. and M.A.S. carried out the literature review. G.L.M. contributed to study design. M.A.S. and G.C. supervised the work. J.W.S., M.A.S. and G.C. wrote the manuscript. All authors contributed to its editing.

## Competing interests

G.C. is a founder and shareholder of Onward Medical, a company with no direct relationships with the present work. The remaining authors declare no competing interests.

## Additional information

**Supplementary information** The online version contains supplementary material available at https://doi.org/10.1038/s41467-021-25960-2.

**Correspondence** and requests for materials should be addressed to Michael A. Skinnider or Grégoire Courtine.

**Peer review information** *Nature Communications* thanks the anonymous reviewer(s) for their contribution to the peer review of this work.
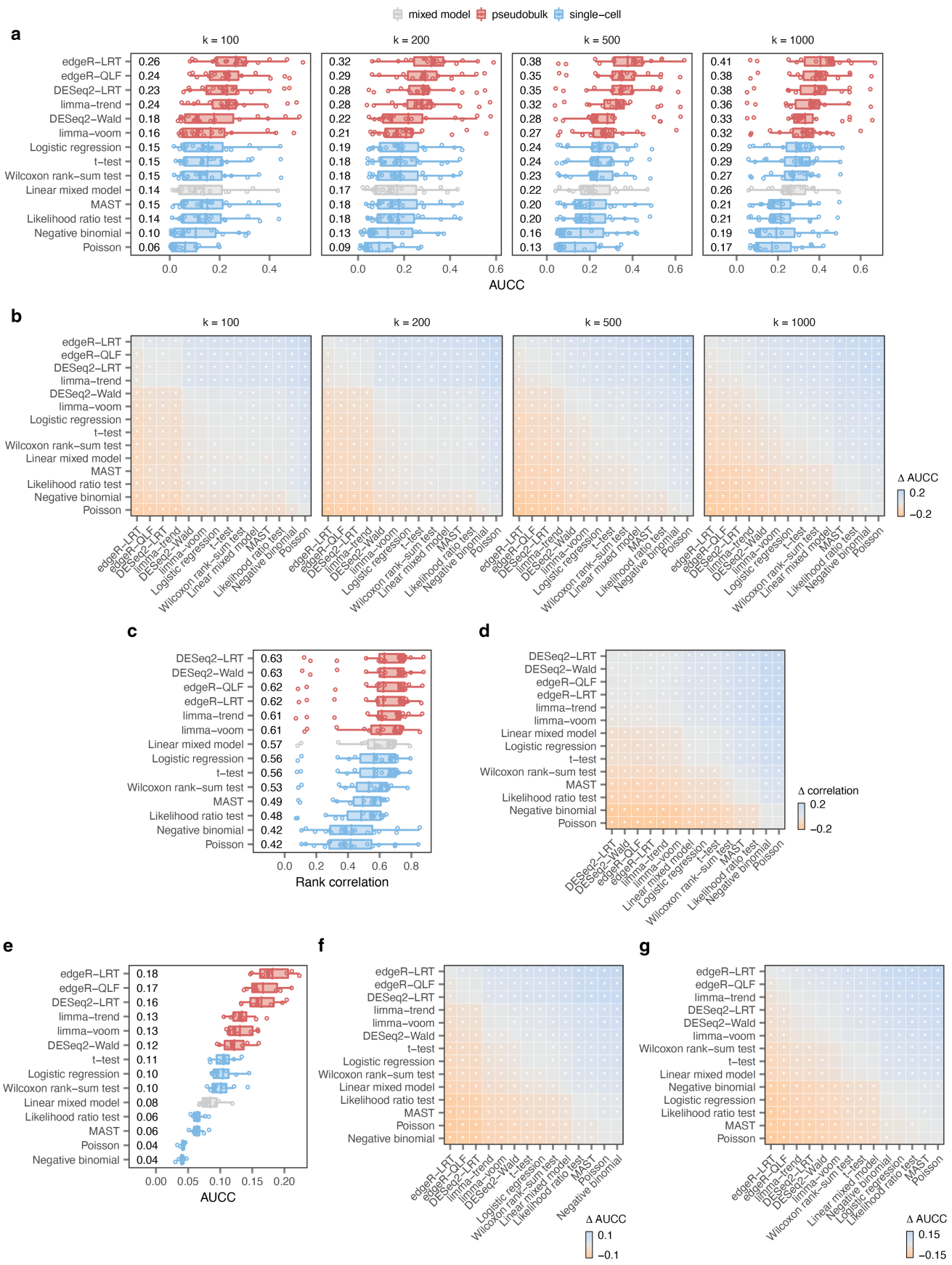
**Reprints and permission information** is available at http://www.nature.com/reprints

**Publisher's note** Springer Nature remains neutral with regard to jurisdictional claims in published maps and institutional affiliations.

**Supplementary Fig. 1 | A systematic benchmark of differential expression in single-cell transcriptomics.**

**a,** Impact of varying the parameter $k$ on the AUCC in the eighteen ground-truth datasets, as shown in **Fig. 1c** with $k = 500$.

**b,** Impact of varying the parameter k on the $\triangle$AUCC in the eighteen ground-truth datasets, as shown in **Fig. 1d** with $k = 500$.

**c,** Transcriptome-wide rank correlation between single-cell and bulk RNA-seq in the eighteen ground-truth datasets shown in **a**.

**d,** Mean difference in the transcriptome-wide rank correlation ($\triangle$correlation) between the fourteen DE methods shown in **c**. Asterisks indicate comparisons with a two-tailed t-test p-value less than 0.05.

**e,** AUCC in eight scRNA-seq datasets with matching bulk proteomics data[1].

**f,** Mean $\triangle$AUCC between the fourteen DE methods shown in **e**. Asterisks indicate comparisons with a two-tailed t-test p-value less than 0.05.

**g,** Mean $\triangle$AUCC of GO term enrichment between the fourteen DE methods shown in **Fig. 1e**. Asterisks indicate comparisons with a two-tailed t-test p-value less than 0.05.
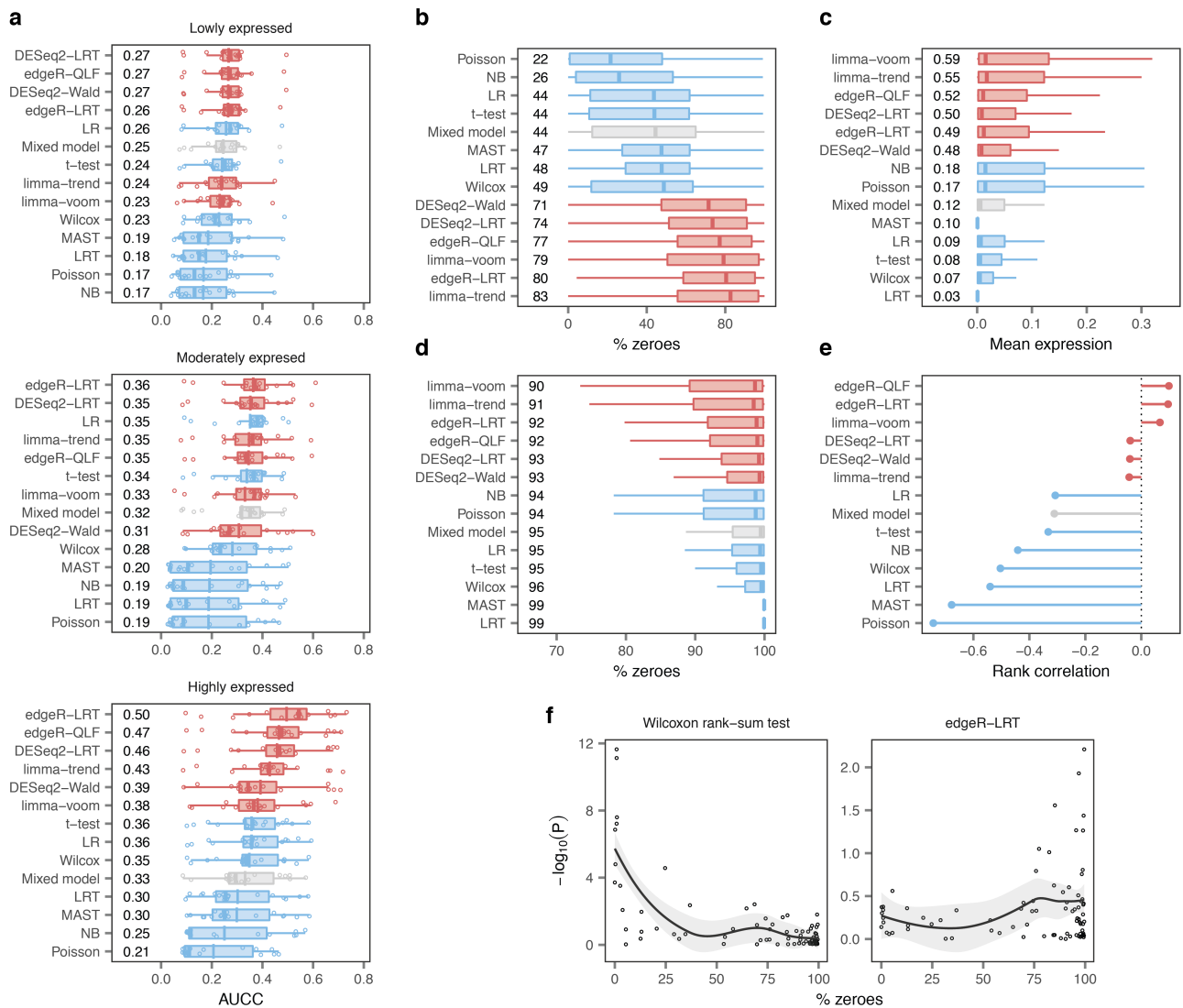
**Supplementary Fig. 2 | Single-cell DE methods are biased towards highly expressed genes.**

**a,** AUCCs across eighteen ground-truth datasets after dividing the transcriptome into terciles of lowly (top), moderately (middle), or highly (bottom) expressed genes, as shown in **Fig. 2b**.

**b,** Mean proportion of zero gene expression measurements for the 100 top-ranked false-positive genes from each DE method.

**c,** Mean expression levels of the 100 top-ranked false-negative genes from each DE method.

**d,** Mean proportion of zero gene expression measurements for the 100 top-ranked false-negative genes from each DE method.

**e,** Spearman correlation between the mean proportion of zero gene expression measurements for 80 ERCC spike-ins expressed in at least three cells and the $-\log_{10}$ p-value of differential expression assigned by each DE method.

**f,** Scatterplots of mean proportion of zero gene expression measurements vs. $-\log_{10}$ p-value for exemplary single-cell and pseudobulk DE methods. Trend lines and shaded areas show local polynomial regression and the 95% confidence interval, respectively.

**Supplementary Fig. 3 | Overview of single-cell transcriptomics datasets.**

**a,** Overview of $n$ = 46 published scRNA-seq datasets comparing two or more experimental conditions, used to systematically confirm the universality of the trends observed in analyses of individual datasets. Left, heatmap indicating the species of origin, the sequencing protocol, and whether cells or nuclei were sequenced. Right, properties of each dataset, including the total number of cell types identified in the original studies; the total number of cells sequenced; the number of cells per type (red bars indicate mean); and the mean number of reads for cells of each type. Datasets highlighted in grey contain matching bulk data and contributed to the 18 ground truth datasets shown in **b.**

**b,** Overview of $n$ = 18 ground-truth datasets with matching scRNA-seq and bulk data, used to evaluate the biological accuracy of single-cell DE methods. Left, heatmap indicating the species of origin, the cell type under investigation and the perturbation to which it was exposed, the sequencing protocol, and whether cells or nuclei were sequenced. Right, properties of each dataset, including the total number of cells and and the number of reads per cell.
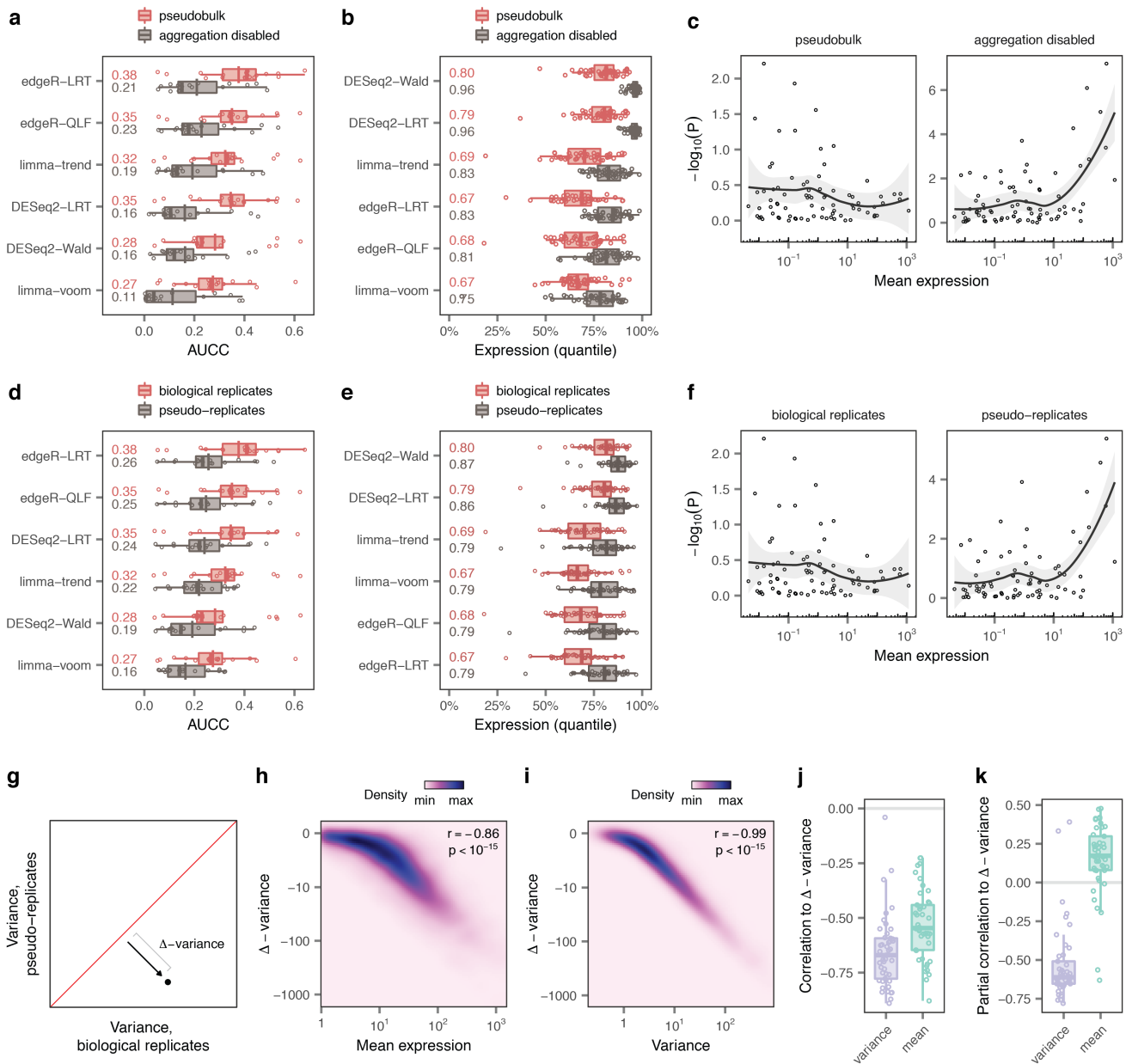
**Supplementary Fig. 4 | DE analysis in single-cell data must account for biological replicates.**

**a,** AUCC of the six pseudobulk methods applied to pseudobulks or individual cells in the eighteen ground-truth datasets.

**b,** Mean expression levels of the 200 top-ranked genes from six pseudobulk methods applied to pseudobulks or individual cells in a collection of 46 scRNA-seq datasets.

**c,** Scatterplots of mean ERCC expression vs. $-\log_{10}$ p-value for an exemplary pseudobulk method, edgeR-LRT, applied to pseudobulks (left) or individual cells (right). Trend lines and shaded areas show local polynomial regression and the 95% confidence interval, respectively.

**d,** AUCC of the six pseudobulk methods applied to pseudobulks or pseudo-replicates in the eighteen ground-truth datasets.

**e,** Mean expression levels of the 200 top-ranked genes from six pseudobulk methods applied to pseudobulks or pseudo-replicates in a collection of 46 scRNA-seq datasets.

**f,** Scatterplots of mean ERCC expression vs. $-\log_{10}$ p-value for an exemplary pseudobulk method, edgeR-LRT, applied to pseudobulks (left) or pseudo-replicates (right). Trend lines and shaded areas show local polynomial regression and the 95% confidence interval, respectively.

**g,** Schematic illustrating the calculation of the $\Delta$-variance between biological replicates and pseudo-replicates.

**h,** Correlation between mean expression and $\Delta$-variance for 10,448 genes with mean expression $\geq 1$ CPM in the dataset of mouse bone marrow mononuclear cells stimulated with poly-I:C. Mean expression is strongly correlated with $\Delta$-variance, such that the variance of highly expressed genes is disproportionately underestimated when ignoring information about biological replicates.

**i,** Correlation between expression variance and $\Delta$-variance for 10,448 genes with mean expression $\geq 1$ CPM in the dataset of mouse bone marrow mononuclear cells stimulated with poly-I:C. Variance is even more strongly correlated with $\Delta$-variance than mean expression, such that the most variable genes are disproportionately underestimated when ignoring information about biological replicate.

**j,** Correlation between mean expression levels or expression variance and $\Delta$-variance in 46 scRNA-seq datasets. Variance is even more strongly correlated with $\Delta$-variance than mean expression across a large compendium of datasets, corroborating the trends shown in **h-i**.

**k,** Partial correlation between mean expression and $\Delta$-variance, controlling for variance, or between variance and $\Delta$-variance, controlling for mean expression. The variance of gene expression is the primary determinant of $\Delta$-variance, implying that failing to account for biological replicates introduces a bias towards highly expressed genes because these genes are also more variable.
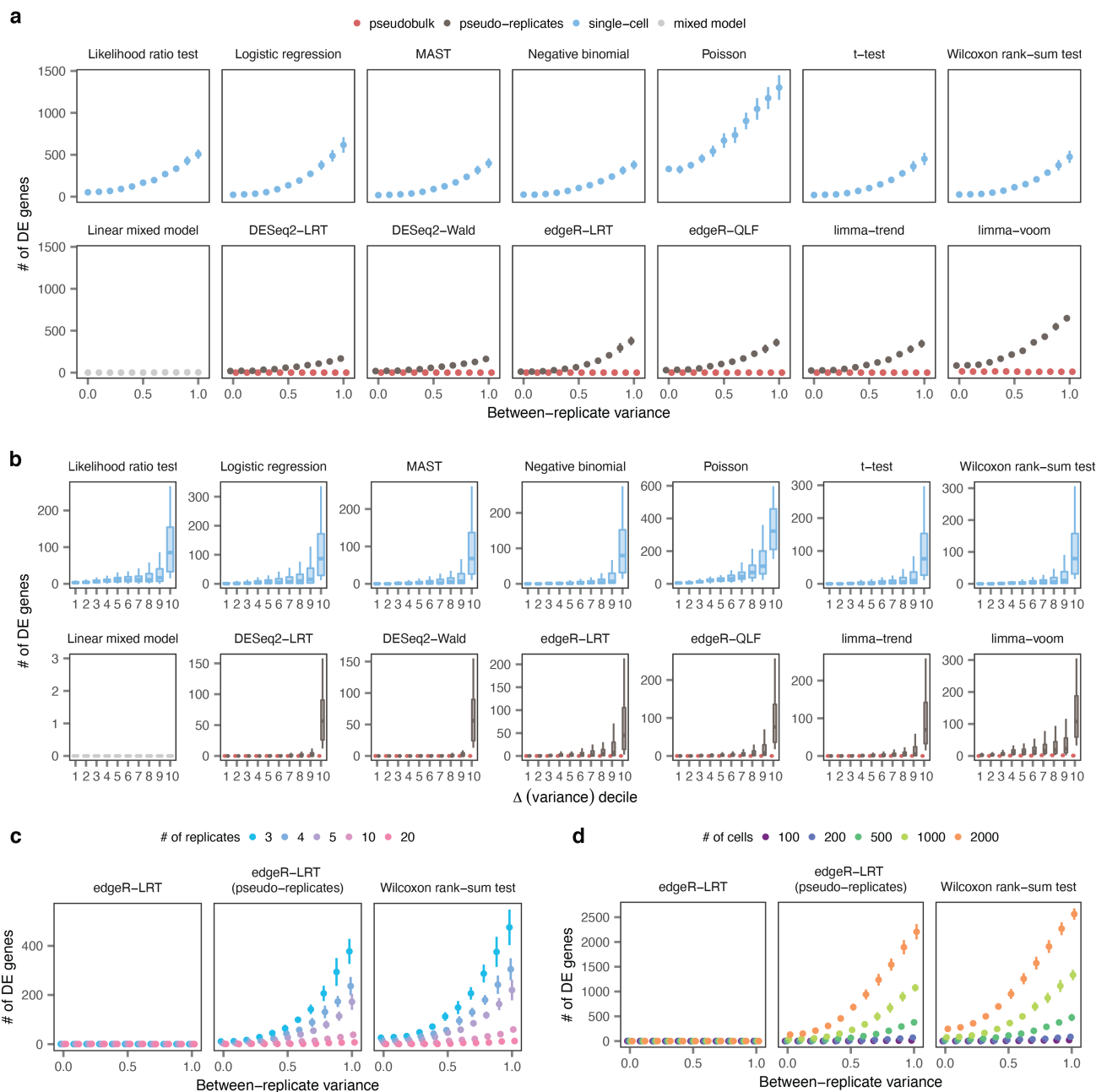
**Supplementary Fig. 5 | Simulation studies expose false discoveries in single-cell DE.**

**a,** Number of DE genes detected in stimulation experiments with varying degrees of heterogeneity between replicates by all DE methods. Points and error bars show the mean and standard deviation of ten independent simulations.

**b,** Number of DE genes detected by the tests shown in a for genes divided into deciles by the magnitude of the change in variance between biological replicates and pseudo-replicates (∆-variance).

**c,** Number of DE genes detected by a representative single-cell DE method, a representative pseudobulk method, and the same pseudobulk method applied to pseudo-replicates, when varying the total number of replicates in the simulated dataset. Points and error bars show the mean and standard deviation of ten independent simulations.

**d,** Number of DE genes detected by a representative single-cell DE method, a representative pseudobulk method, and the same pseudobulk method applied to pseudo-replicates, when varying the total number of cells in the simulated dataset. Points and error bars show the mean and standard deviation of ten independent simulations.
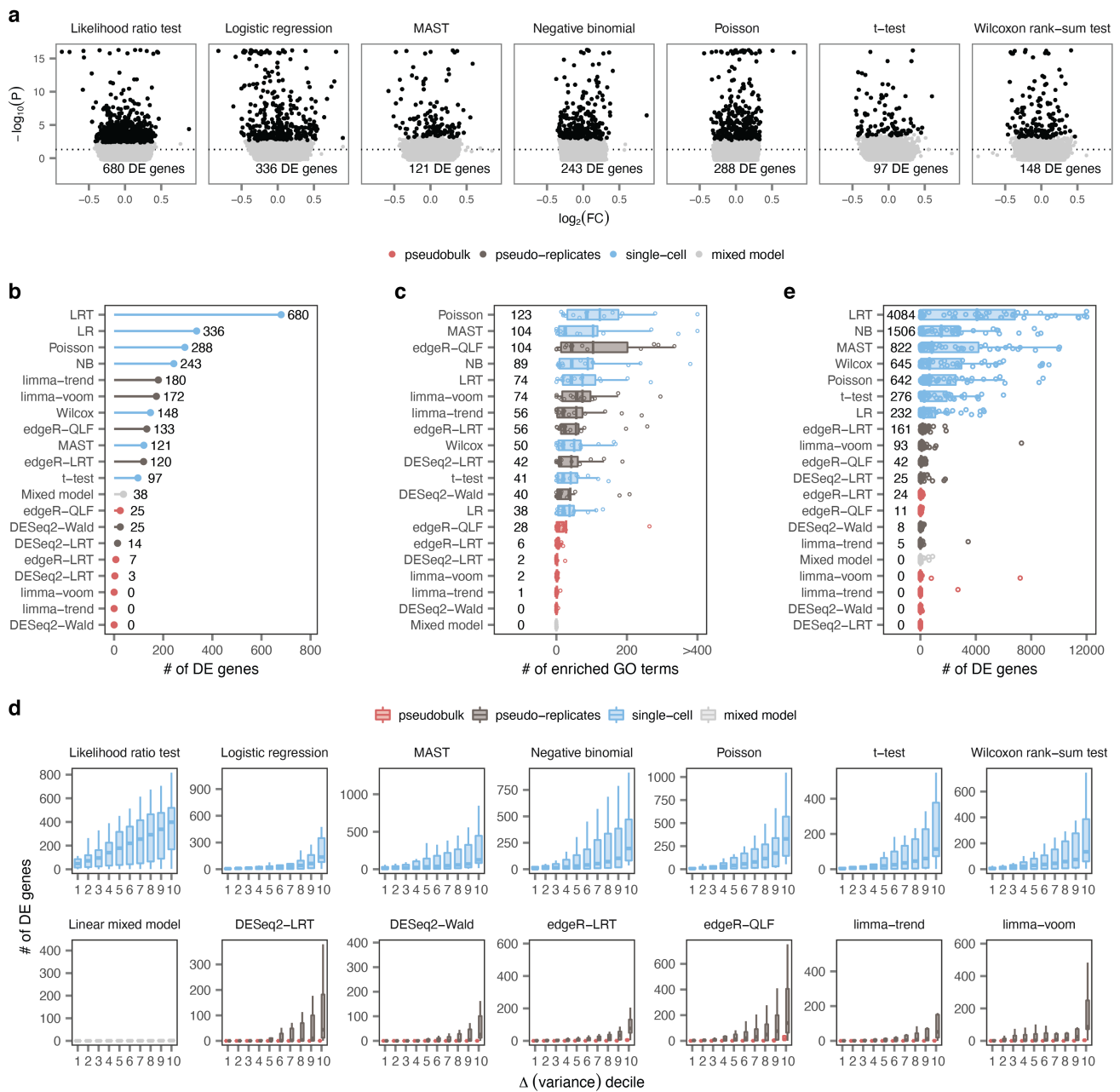
**Supplementary Fig. 6 | False discoveries in single-cell and spatial transcriptomics data.**

**a,** Volcano plots showing DE between T cells from random groups of unstimulated controls drawn from Kang et al.[2] using seven single-cell DE methods.

**b,** Number of DE genes detected by all DE methods in unstimulated T cells.

**c,** Number of GO terms enriched at 5% FDR among DE genes identified in comparisons of random groups of unstimulated controls from fourteen scRNA-seq studies with at least six control samples.

**d,** Number of DE genes in comparisons of random groups of unstimulated controls from fourteen scRNA-seq studies with at least six control samples, as shown in **Fig. 4e**, for genes divided into deciles by the magnitude of the change in variance between biological replicates and pseudo-replicates ($\Delta$-variance).

**e,** Number of DE genes detected by all DE methods within spinal cord regions from control mice profiled by spatial transcriptomics[3].

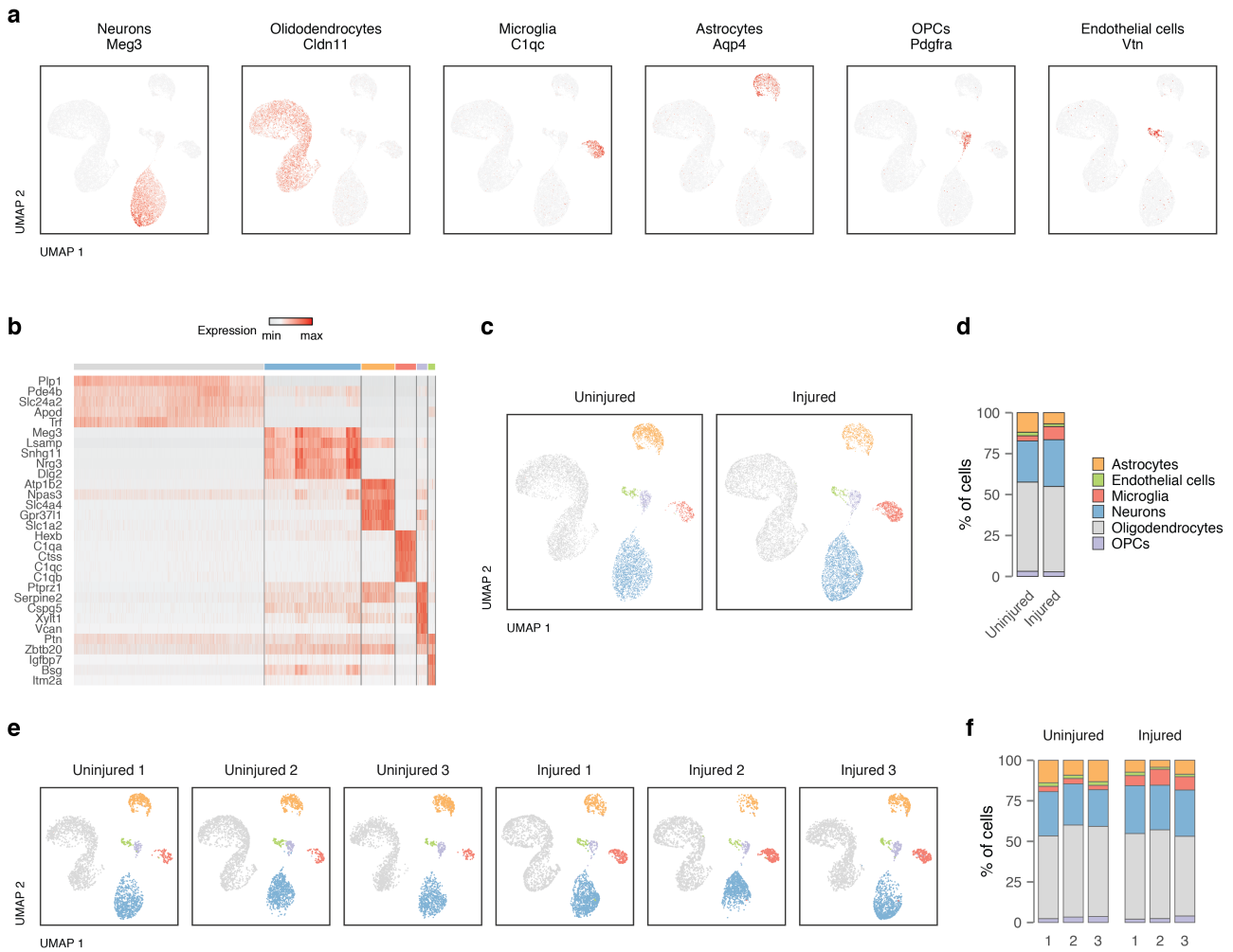**Supplementary Fig. 7 | Single-nucleus RNA-seq of the injured mouse lumbar spinal cord.**

**a,** Expression of key marker genes for the six major cell types of the lumbar spinal cord across 19,237 individual nuclei.

**b,** Top five marker genes for each major cell type of the lumbar spinal cord.

**c,** UMAP visualization of 19,237 nuclei, showing detection of the major cell types of the lumbar spinal cord across experimental conditions.

**d,** Proportion of cells of each major cell type detected in either experimental condition.

**e,** UMAP visualization of 19,237 nuclei, showing detection of the major cell types of the lumbar spinal cord across individual replicates.

**f,** Proportion of cells of each major cell type detected in each individual replicate.

**Supplementary Fig. 8 | Spasticity and hyperexcitability in the injured mouse lumbar spinal cord.**

**a,** Schematic illustration of electrophysiology experimental design. Inset demonstrates persistent amplitude at increasing frequency of the H-reflex in response to plantar stimulation, reflecting hyperexcitability.

**b,** Synapses and projections of *Vglut2*[ON] neurons in the mouse lumbar spinal cord before and after SCI.

**c,** Individual traces from representative injured and uninjured mice at each tested frequency, including 0.1, 0.5, 1, 2, and 5 Hz. We observed a persistent H-reflex in only injured animals, indicating hyperexcitability.

**d,** Quantification of electrophysiology traces as shown in **c,** demonstrating persistence of the H-reflex in the injured group. Points and error bars show mean and standard deviation, respectively, for $n$ = 6 biologically independent animals examined with 12 repeated measures for each condition.

Source data are provided as a Source Data file.

**Supplementary Fig. 9 | *In vivo* validation of single-cell DE analysis by RNAscope.**
**a,** Overlap between genes identified as DE within endothelial cells of the injured mouse lumbar spinal cord by edgeR-LRT and the Wilcoxon rank-sum test.
**b,** RNAscope quantification, left, and representative images, right, for nineteen genes identified as DE exclusively by edgeR-LRT or the Wilcoxon rank-sum test. Horizontal line and shaded area show the mean and standard deviation, respectively.
Source data are provided as a Source Data file.
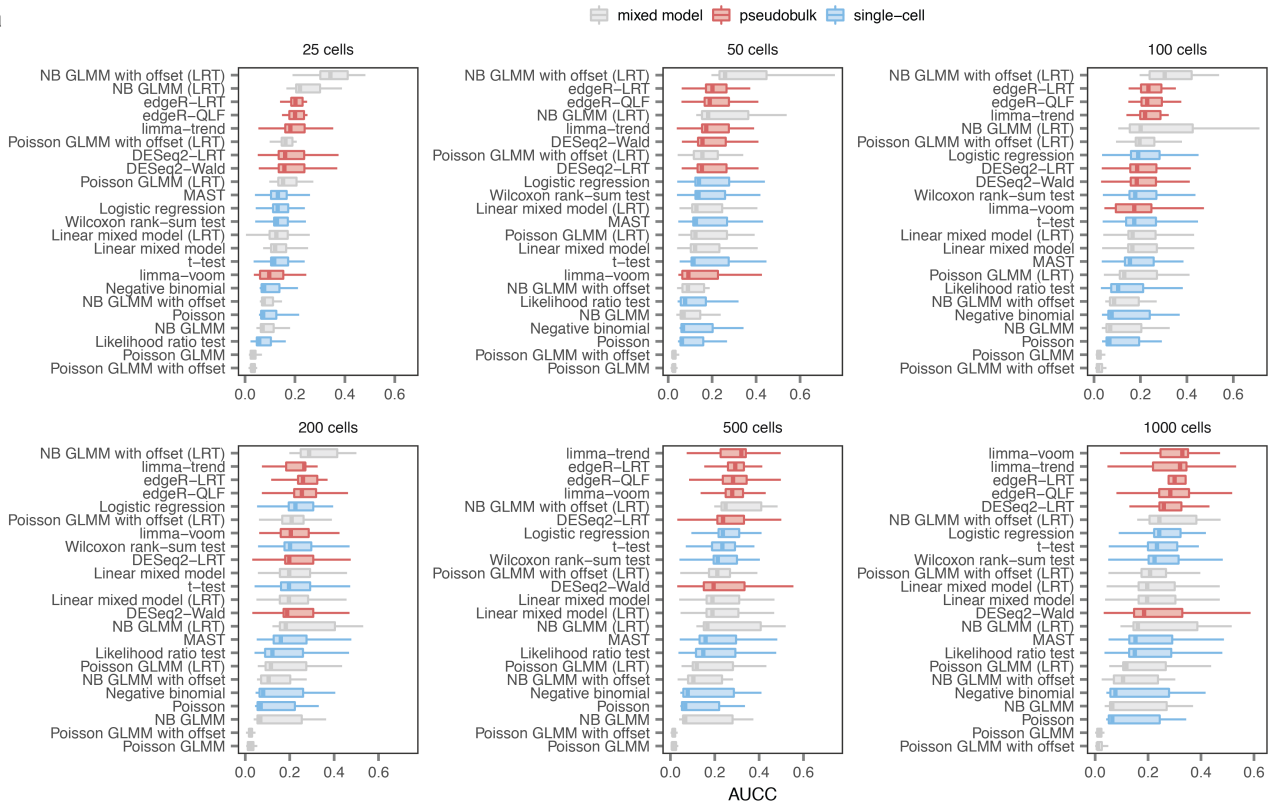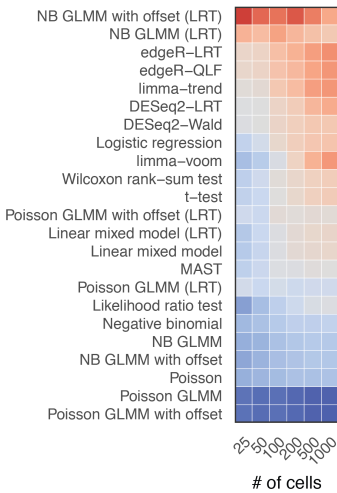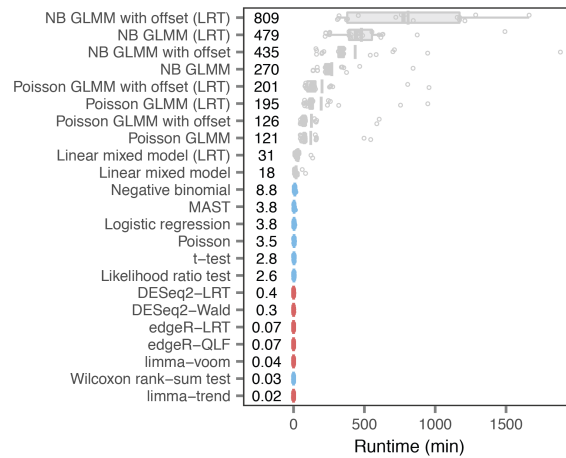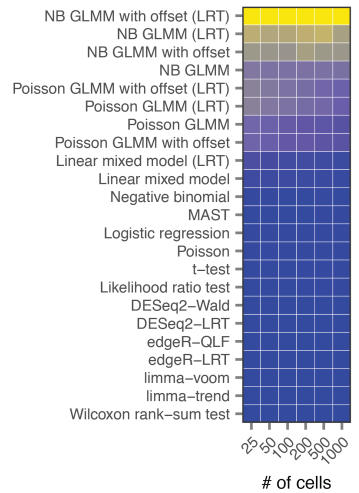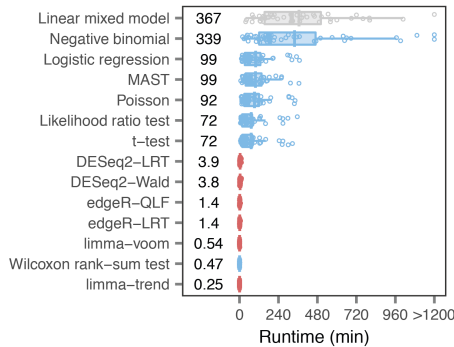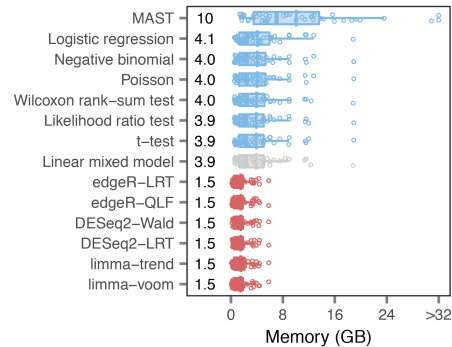
**Supplementary Fig. 10 | Single-cell DE analysis with generalized linear mixed models.**
**a,** AUCC for ten different generalized linear mixed models (GLMMs), varying in the choice of link function (identity, Poisson, or negative binomial, NB); method used to evaluate statistical significance (Wald test or likelihood ratio test, LRT), and presence of an offset term, in samples of between 25 and 1,000 cells from the eighteen ground-truth datasets shown in **Fig. 1c**, and compared to the fourteen DE methods shown in the same panel.
**b,** As in **a,** but showing the mean AUCC as a function of the number of cells sampled for each DE method.
**c,** Runtime in minutes for the ten GLMMs shown in a in samples of 1,000 cells. The top-performing GLMM required a mean of 13.5 h per cell type to perform DE analysis.
**d,** Runtime of the ten GLMMs and the fourteen DE methods shown in **Fig. 1c**, shown as a percentage of the maximum runtime, as a function of the number of cells sampled.
**e,** Runtime in minutes of the fourteen DE methods shown in **Fig. 1c** across 46 scRNA-seq datasets.
**f,** Maximum memory required in gigabytes by the fourteen DE methods shown in **Fig. 1c** across 46 scRNA-seq datasets.

# Chapter 4

# The *Tabulae paralytica*: Multimodal single-cell and spatial atlases of spinal cord injury

This last chapter represent the core of my work over the past 4 years. Here we establish four molecular and cellular atlases of spinal cord injury (SCI), comprising a single-nucleus transcriptome atlas of half a million cells, a multi-omic atlas pairing transcriptomic and epigenomic measurements within the same nuclei, and two spatial transcriptomic atlases of the injured spinal cord spanning four spatiotemporal dimensions. This resource allowed us to understand the biology of SCI at unprecedented resolution; to uncover new principles governing the responses to SCI; and to leverage these discoveries to develop a rejuvenative gene therapy that restored walking after paralysis in old mice. We believe this work represents a biological, technical, and therapeutic landmark in the fields of neuroscience and genomics.

My contribution as a co-first author : I contributed to all aspects of the work, conducting experiments, analysis of data and preparation of the manuscript.

# The *Tabulae Paralytica*: Multimodal single-cell and spatial atlases of spinal cord injury

Michael A. Skinnider[1,2,8], Matthieu Gautier[1,2,8], Alan Yue Yang Teo[1,2], Claudia Kathe[1,2], Thomas H. Hutson[1,2,3], Achilleas Laskaratos[1,2], Alexandra de Coucy[1,2], Nicola Regazzi[1,2], Viviana Aureli[1,2,4,5], Nicholas D. James[1,2], Bernard Schneider[1,6], Michael V. Sofroniew[7], Quentin Barraud[1,2], Jocelyne Bloch[1,2,4,5], Mark A. Anderson[1,2,3,5,9 ✉], Jordan W. Squair[1,2,4,9 ✉], and Grégoire Courtine[1,2,4,5,9 ✉]

[1] NeuroX Institute, School of Life Sciences, Swiss Federal Institute of Technology (EPFL), Lausanne, Switzerland
[2] Defitech Center for Interventional Neurotherapies (.NeuroRestore), EPFL/CHUV/UNIL, Lausanne, Switzerland
[3] Wyss Center for Bio and Neuroengineering, Geneva, Switzerland
[4] Department of Neurosurgery, Lausanne University Hospital (CHUV) and University of Lausanne (UNIL), Lausanne, Switzerland
[5] Department of Clinical Neuroscience, Lausanne University Hospital (CHUV) and University of Lausanne (UNIL), Lausanne, Switzerland
[6] Bertarelli Platform for Gene Therapy, Swiss Federal Institute of Technology (EPFL), Lausanne, Switzerland
[7] Department of Neurobiology, David Geffen School of Medicine, University of California Los Angeles, Los Angeles, CA USA
[8] These authors contributed equally
[9] These authors jointly supervised this work
✉ e-mail: gregoire.courtine@epfl.ch, jordan.squair@epfl.ch, mark.anderson@epfl.ch

**Here, we introduce the *Tabulae Paralytica*—a compilation of four atlases of spinal cord injury (SCI) comprising a single-nucleus transcriptome atlas of half a million cells; a multiome atlas pairing transcriptomic and epigenomic measurements within the same nuclei; and two spatial transcriptomic atlases of the injured spinal cord spanning four spatial and temporal dimensions. We integrated these atlases into a common framework to dissect the molecular logic that governs the responses to injury within the spinal cord. The *Tabulae Paralytica* exposed new biological principles that dictate the consequences of SCI, including conserved and divergent neuronal responses to injury; the priming of specific neuronal subpopulations to become circuit-reorganizing neurons after injury; an inherent trade-off between neuronal stress responses and the activation of circuit reorganization programs; the necessity of reestablishing a tripartite neuroprotective barrier between immune-privileged and extra-neural environments after SCI; and a catastrophic failure to form this barrier in old mice. We leveraged the *Tabulae Paralytica* to develop a rejuvenative gene therapy that reestablished this tripartite barrier, and restored the natural recovery of walking after paralysis in old mice. The *Tabulae Paralytica* provides an unprecedented window into the pathobiology of SCI, while establishing a framework for integrating multimodal, genome-scale measurements in four dimensions to study biology and medicine.**

Spinal cord injury (SCI) irreversibly damages neural tissues, leading to permanent and devastating loss of neurological functions[1,2]. Advances in medical management[3] and neurotechnologies[4–9] have improved survival and allow clinicians to address many aspects of neurological dysfunction after SCI. However, decades of investigations culminating in large-scale clinical trials have yet to identify safe and effective therapies to repair the injured spinal cord[1,10].

A SCI triggers a cascade of molecular and cellular responses involving inflammatory cell infiltration and cytokine release, apoptosis, demyelination, excitotoxicity, ischemia, and the formation of a fibrotic scar surrounded by an astrocyte border[2,10–16]. Altering the course of this cascade to repair the injured spinal cord will require a complete understanding of how neural and non-neural cells coordinate the response to SCI over time and throughout the lesion microenvironment[2,17,18]. Previous attempts to delineate the molecular logic governing this response initially turned to bulk transcriptomics and proteomics of the entire lesion[15,19–26]. However, these attempts were technically limited in their ability to resolve cell-type-specific molecular programs triggered by injury, or else focused on isolated aspects of the injury response.

Emerging genome-scale technologies are poised to overcome these limitations. First, single-cell transcriptomics could unveil the molecular programs triggered by SCI within hundreds of thousands of cells composing the injured spinal cord[27–30]. Second, multi-omic methods that couple single-cell transcriptomics to chromatin accessibility profiling within the same cell could access the regulatory programs that govern the response to injury[31–34]. Third, spatial transcriptomics could circumscribe these transcriptional and regulatory programs within the complex cytoarchitecture of the lesion microenvironment[35–42].

Here, we leveraged single-cell transcriptomics, multiomics, and spatial transcriptomics in mice to establish the *Tabulae Paralytica*, or 'atlases of spinal cord injury' (**Fig. 1a** and **Supplementary Video 1**). Together, these atlases,
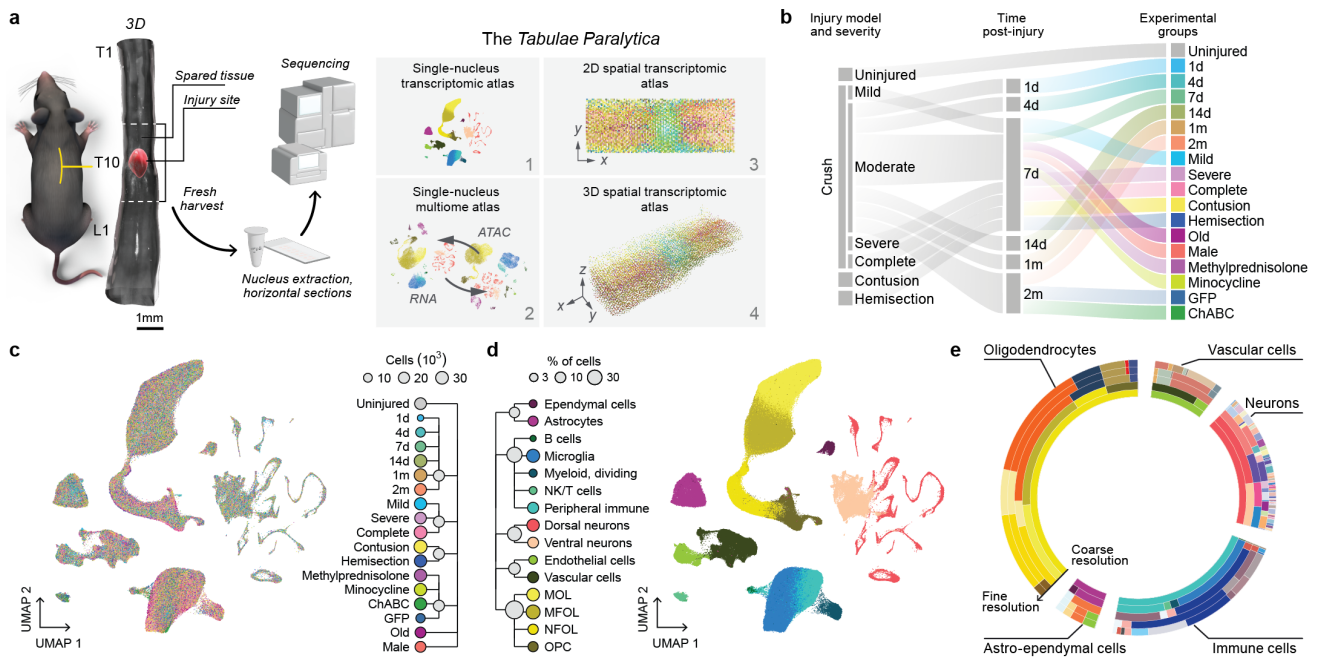
**Fig. 1 | Overview of the *Tabulae Paralytica* and the snRNA-seq atlas.**

**a,** Schematic overview of the *Tabulae Paralytica*.

**b,** Schematic overview of the snRNA-seq atlas.

**c,** UMAP visualizations of the 435,099 cells in the snRNA-seq atlas, colored by experimental condition. Dendrogram shows major groups of experimental conditions.

**d,** As in **c,** but colored by cell type. Dendrogram shows the first two levels of the clustering tree of spinal cord cell types.

**e,** Sunburst plot showing cell type proportions in the snRNA-seq atlas at each level of the clustering tree, from broadest (innermost ring) to most granular (outermost ring).

comprising 482,825 individual cells spanning 18 experimental conditions and 71,499 spatial barcodes mapped onto the three-dimensional architecture of the injured spinal cord, provide an unprecedented window into the pathobiology of SCI. We provide an interactive web application to explore these atlases at http://tabulaeparalytica.com.

## Results

### Single-nucleus RNA-seq of the injured spinal cord

Single-cell transcriptomics of injured spinal cord tissues presents unique challenges: many cell types do not survive harsh dissociation protocols, and surviving cells express a dissociation-induced stress signature[43–46]. To overcome these limitations, we optimized single-nucleus RNA-sequencing (snRNA-seq) protocols for the injured spinal cord. We acquired high-quality transcriptomes from all the major cell types from injured and uninjured spinal cords (**Supplementary Fig. 1a-i**). Comparison with 16 published datasets[47–62] confirmed that our protocol recovered the complete repertoire of spinal cord cell types, even when applied to injured spinal cord tissues (**Supplementary Fig. 1j-q**).

### A comprehensive set of experiments for large-scale snRNA-seq

We next leveraged these optimized protocols to conduct snRNA-seq profiling of the injured spinal cord across a comprehensive set of experimental conditions and injury models that aimed to capture the multifaceted responses to SCI and

how pharmacological interventions may alter these responses (**Fig. 1b-c** and **Supplementary Figs. 2** and **3**).

The pathobiological responses activated in the injured spinal cord depend on the severity and mechanism of the initial insult, and evolve over the following days, weeks, and months[1,3,18]. To capture these responses, we profiled the spinal cord of uninjured mice at 1, 4, 7, 14, 30, and 60 days after mid-thoracic SCI. Next, we devised a progression of injury severities that led to mild, moderate, severe, and complete functional impairments. Finally, we profiled the spinal cord following SCI induced by different mechanisms of injury, including crush[15,63], contusion[64,65], and dorsal hemisection[12].

In humans, immune responses differ across the lifespan and between males and females, with broad implications for disease initiation and progression[66–69]. To evaluate the impact of sex and age on the cell-type-specific molecular programs activated by SCI, we profiled injured spinal cords from male and female mice, and from young and old mice.

Finally, we asked whether single-cell techniques could provide insights into the molecular mechanisms of pharmacotherapies for SCI. To address this question, we profiled the spinal cord of mice treated with three of the most extensively investigated clinical and experimental interventions: methylprednisolone[70–72], minocycline[73–76], and chondroitinase ABC (ChABC)[77–84].

## A single-nucleus transcriptomic atlas of SCI

We exploited this progression of 18 experimental conditions to establish a single-cell atlas of SCI, profiling the spinal cords of mice from each condition by snRNA-seq. We obtained high-quality transcriptomes for a total of 435,099 nuclei from 54 mice (**Fig. 1c-d** and **Supplementary Fig. 4**).

To identify both coarse cell types and more granular subtypes, we subjected the entire dataset to multiple rounds of clustering at increasingly fine-grained resolutions. This procedure identified all the major cell types of the spinal cord and allowed us to establish a comprehensive catalog of 175 more granular subpopulations. We organized these subpopulations into a clustering tree[85] that recapitulated the known cellular hierarchy of the spinal cord (**Fig. 1e** and **Supplementary Fig. 5**)[2,9,47–62,86–88].

Coarse clustering identified cells originating from immune, astroependymal, vascular, oligodendrocyte, and neuronal lineages (**Supplementary Fig. 6**). Within each of these lineages, we first explored the evolution of each subpopulation over time and with increasing injury severity.

The immune compartment comprised 106,619 immune cells spanning both central nervous system-resident and infiltrating immune cells, which are known to coordinate sequential phases of the acute response to SCI (**Fig. 2a** and **Supplementary Fig. 7a-c**)[11]. *P2ry12*-expressing homeostatic microglia were transcriptionally distinguishable from reactive microglia, which expressed *Tgfbr1*. Peripheral lymphocytes comprised B cells, NK cells, and CD8 T cells, whereas myeloid cells subdivided into proliferating and fate-committed subpopulations, as well as neutrophils, macrophages, and dendritic cells. Macrophages encompassed border-associated macrophages (expressing *H2-Aa*) that mediate immune responses in perivascular spaces[89], as well as distinct inflammatory (*Ifi211*), chemotaxis-inducing (*Cd300a*), and thrombospondin-sensing (*Htr2b*) subpopulations[58].

Our single-cell atlas recapitulated the known evolution of the immune response over the first two months following SCI[11]. Extensive infiltration of peripheral immune cells peaked between 7 and 14 days, paralleling the initiation and slow stabilization of microglial activation (**Fig. 2b**). The relative proportion of homeostatic microglia decreased gradually with injury severity, whereas the proportions of chemotaxis-inducing and inflammatory macrophages expanded (**Supplementary Fig. 7d**). These shifts in the composition of the immune compartment reflected an increasingly profound disruption of the blood-brain barrier.

When a SCI occurs, astrocytes form a barrier that surrounds the fibrotic lesion core to protect viable neural tissue from infiltrating immune cells[15,90–92]. In our single-cell atlas, the astroependymal compartment comprised 25,211 nuclei, spanning grey matter-resident protoplasmic astrocytes (*Nwd1*, *Gfap*[low]), white matter-resident fibrous astrocytes (*Slc4a4*, *Gfap*[high]), reactive subpopulations that we subdivided based on the expression of *Aldoc*, *Tmem47*, and *Gja1*, and ependymal cells (*Dnah12*) (**Fig. 2c** and **Supplementary Fig. 8a-c**).

The proportion of protoplasmic astrocytes declined gradually over the first few days after injury (**Supplementary Fig. 8d**). The extent of this loss correlated with the severity of the injury (**Supplementary Fig. 8e-f**). This loss contrasted with the reactive astrocyte compartment, which expanded immediately after injury, and persisted into the chronic stage (**Supplementary Fig. 8g**). These responses coincided with the entry of astrocytes into the cell cycle starting at 1 day, with peak proliferation observed at 4 days (**Fig. 2d**). By 7 days, astrocytes had returned to G1/G0, indicating that this proliferation was completed.

The cerebrovasculature comprises an arteriovenous axis of arteries, arterioles, capillaries, venules, and veins[51,93,94]. Together, these vessels form the blood-brain barrier that separates the immune-privileged spinal cord parenchyma from the extra-neural environment[95–99]. In our single-cell atlas, the vascular compartment comprised 40,620 cells, which subdivided into endothelial cells, vascular leptomeningeal cells (VLMCs, *Pdgfra*[high])[51,93] and pericytes (**Fig. 2e** and **Supplementary Fig. 9a-c**). Endothelial cells were further subdivided by their arteriovenous zonation, with distinct arterial (*Emcn*), capillary (*Meox1*), and venous (*Slc38a5*) subpopulations. VLMCs, which are fibroblast-like cells located between astrocyte end-feet and endothelia that express fibril-forming collagens[51,93], were further separated into homeostatic and extracellular matrix-forming subpopulations, as well as arachnoid barrier cells (*Slc47a1*) that are involved in cerebrospinal fluid maintenance[51,100].

Our single-cell atlas revealed an immediate and severity-dependent disruption of the blood-brain barrier following SCI. This disruption encompassed a contraction of the endothelial and pericyte compartments, and a concomitant expansion in the proportion of VLMCs (**Fig. 2f** and **Supplementary Fig. 9d**). Moreover, vascular cells exhibited a severity-dependent increase in the expression of genes associated with blood-brain barrier dysfunction that increased over the first four days[101] (**Supplementary Fig. 9e-f**). By 7 days, proliferation of arachnoid barrier cells marked the onset of barrier formation from the cerebrospinal fluid space (**Fig. 2f**). The formation of the cerebrospinal fluid barrier was followed by the reestablishment of the blood-brain barrier, marked by the proliferation of endothelial cells and pericytes, and resolution of blood-brain barrier dysfunction. The resolution of peripheral immune cell invasion coincided with the reestablishment of these barriers.

The oligodendrocyte lineage comprised 182,334 cells that were distributed along a continuous developmental trajectory, spanning oligodendrocyte precursor cells (OPCs), differentiation-committed oligodendrocyte precursors (COPs), newly formed oligodendrocytes (NFOLs), myelin-forming oligodendrocytes (MFOLs), and mature oligodendrocytes (MOLs) (**Fig. 2g** and **Supplementary Fig. 10a-c**)[51,102]. The proportion of oligodendrocytes decreased at 1 day, consistent with the notion that they are sensitive to the ischemic environment that develops after SCI (**Supplementary Fig. 10d**)[103]. By 4 days, we observed a severity-dependent expansion in the proportion of OPCs,
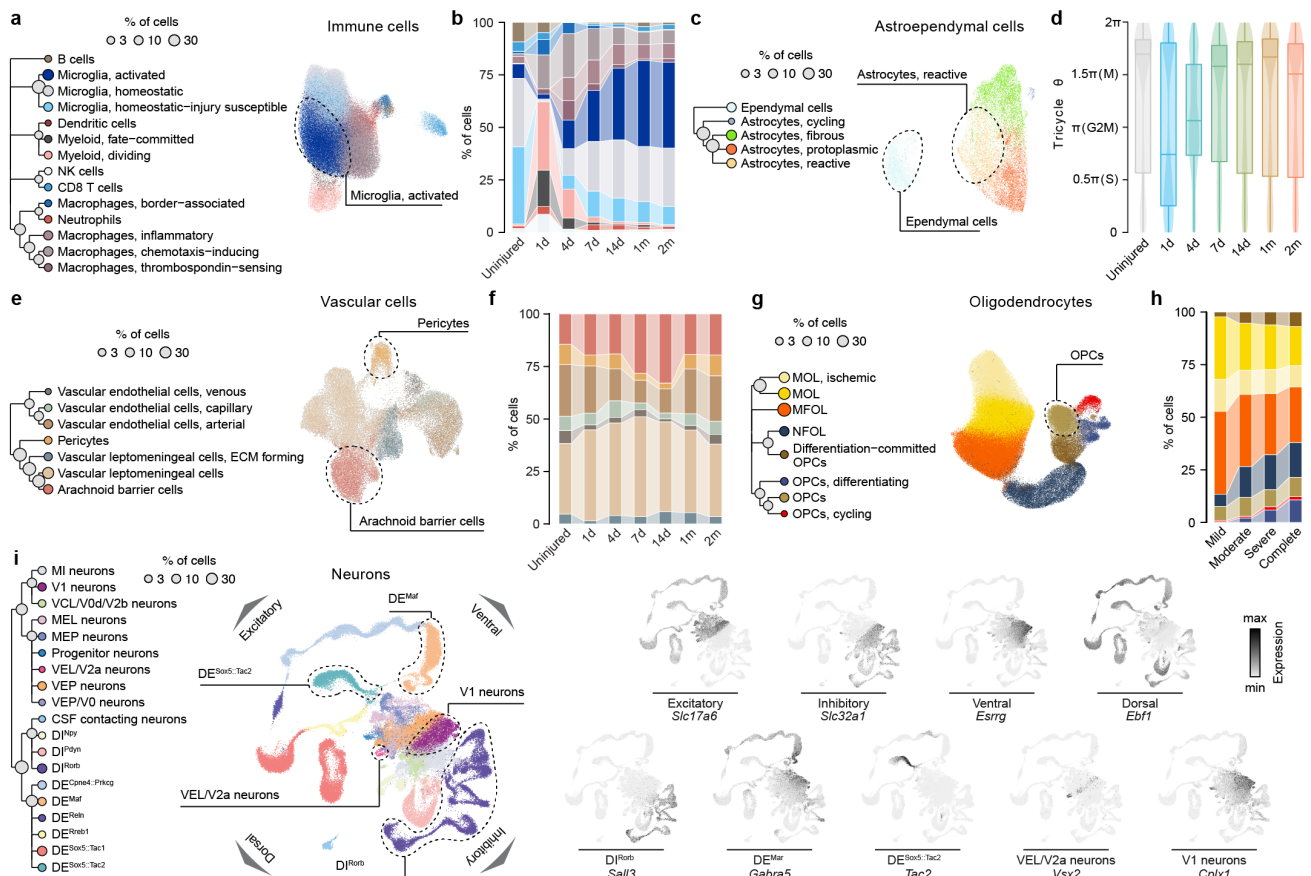
**Fig. 2 | Cell types and subtypes of the uninjured and injured mouse spinal cord.**

**a,** UMAP visualization of 106,619 immune cells in the snRNA-seq atlas, colored by cell type. Dendrogram shows the bottom four levels of the clustering tree, subset to show immune cell subtypes only.

**b,** Proportions of each immune cell subtype across timepoints.

**c,** As in **a**, but for 25,211 astroependymal cells.

**d,** Cell cycle stages assigned to astroependymal cells at each timepoint post-injury.

**e,** As in **a**, but for 40,620 vascular cells.

**f,** Proportions of each vascular cell subtype across timepoints.

**g,** As in **a**, but for 182,334 oligodendrocytes.

**h,** Proportions of each oligodendrocyte subtype across injury severities.

**i,** Left, as in **a**, but for 80,315 neurons. Right, UMAP visualization showing expression of key marker genes for select neuronal subtypes.

which preceded the reinstatement of a near-normal oligodendrocyte compartment by 7 days (**Fig. 2h** and **Supplementary Fig. 10d**).

The spinal cord encompasses dozens of anatomically, functionally, and transcriptionally distinct neuronal subpopulations[2,9,47–51,53,56,57,59,60,86–88]. The scale of our single-cell atlas, which comprised 80,315 single-neuron transcriptomes, allowed us to identify 60 distinct subpopulations of neurons (**Fig. 2i** and **Supplementary Fig. 11**). Neuronal subpopulations were parcellated into dorsal versus ventral, excitatory versus inhibitory, and local (*Nfib*) versus long-projecting (*Zfhx3*) populations[59]. We identified well-studied dorsal excitatory (*Tac1*, *Reln*, *Cck*) and inhibitory (*Rory*, *Npy*, *Gal*) subpopulations, as well as dI5/dIL deep dorsal subpopulations expressing *Lmx1b*[47,51,86,88]. A group of ventral neuron subpopulations included developmentally defined V0, V1, V2, V3 (*Sim1*) neurons[86,104]; Renshaw cells (*Calb1*, *Chrna2*, *Slco5a1*)[105,106]; cerebrospinal

fluid-contacting neurons (CSF-N; *Pdk1l2*)[51,107,108]; and motor neurons (*Isl1*)[109]. V0 neurons subclustered into V0c (*Chat*, *Pitx2*)[110], V0v (*Evx1*)[111,112], V0g (*Slc17a6*, *Pitx2*)[110], and V0d (*Chat*, *Evx1*OFF, *Gabra1*)[111,112] subpopulations. V1 (*En1*) neurons subclustered into four subpopulations expressing *Pou6f2*, *Foxp2*, *Mafa*, and *Sp8*, respectively[113]. Within V2 neurons, we identified one inhibitory subpopulation of V2b neurons expressing *Gata2* and *Gata3*[114,115], as well as multiple subpopulations of developmentally defined V2a neurons (*Vsx2*)[39,86,116–118] that could be separated into local (*Nfib*) and long-projecting (*Zfhx3*) subpopulations[59].

Together, this atlas establishes a single-cell taxonomy of the mouse spinal cord, and delineates the impact of injury severity and time on the repertoire of cell types within the injured spinal cord.

## Conserved and divergent neuronal responses to SCI

A common feature of many insults to the nervous system is that specific neuronal subpopulations exhibit disproportionate susceptibility or resilience to the insult[119–125]. However, whether different neuronal subtypes within the spinal cord respond differentially to injury remains unknown.

To address this possibility, we compared the proportions of neurons from each subpopulation between injured and uninjured spinal cords. Our single-cell atlas confirmed the expected severity-dependent loss of neurons after injury (**Fig. 3a** and **Supplementary Fig. 12a**). However, there were minimal changes in the relative proportions of each neuronal subpopulation, suggesting that spinal cord neurons are, in general, equally vulnerable to SCI (**Supplementary Fig. 12b**).

The sole exception arose from cerebrospinal fluid-contacting neurons[51,107,108], which exhibited a unique resilience to SCI (**Fig. 3b** and **Supplementary Fig. 12c**). This resilience was consistent across every comparison of injured and uninjured spinal cords, and became more pronounced with increasingly severe injuries (**Supplementary Fig. 12d-e**). Immunohistochemistry validated this resilience of cerebrospinal fluid-contacting neurons (**Supplementary Fig. 12f-g**).

We asked whether cerebrospinal fluid-contacting neurons express unique transcriptional programs in response to injury that could explain this resilience (**Supplementary Fig. 12h**). Relative to other neuronal subpopulations, these neurons upregulated genes associated with cell adhesion (*Cntnap5c*), angiogenesis (*Rhoj*), and acute tissue remodeling (*Timp3*).

In contrast, other neuronal subpopulations exhibited a homogenous degree of vulnerability to SCI. We hypothesized that this homogeneity may coincide with the activation of shared transcriptional programs in response to injury. Indeed, we found that SCI initially triggered molecular responses that were broadly conserved across all neuronal subpopulations (**Fig. 3c** and **Supplementary Fig. 13a**). These responses gradually diverged over the following two months, as individual neuronal subpopulations activated increasingly distinct transcriptional programs (**Fig. 3c**).

This homogeneity compelled us to characterize this conserved early response of neurons to SCI (**Supplementary Fig. 13b**). We found that upregulation of immune response pathways (*Fkbp3*, *Stat3*), apoptotic programs (*Pdcd5*, *Bex3*, *Parp3*), and mitochondrial membrane disruption (*Atpif1*, *Ndufa7*, *Fis1*) were the hallmarks of this response. Conversely, neurons downregulated core neuronal functions, including neurotransmitter release (*Lyn*), ion channel expression (*Kcqn1*, *Slc24a5*), and cell adhesion (*Ctnn1*, *Calr*, *Add3*, *Ctnna3*).

We next explored the gradual divergence of neuronal responses at later time points. This divergence coincided with the known timescale at which circuit reorganization mediates the natural recovery of neurological functions after SCI[2]. We therefore reasoned that this divergence might reflect subpopulation-specific circuit reorganization. Indeed, we found that only a few neuronal subpopulations upregulated genes associated with projection growth and morphogenesis, which occurred between 14 days and 2 months after injury (**Fig. 3d** and **Supplementary Fig. 13c**).

Within these subpopulations, local *Vsx2*[ON] (*Nfib*) neurons exhibited the greatest upregulation of genes associated with circuit reorganization (**Fig. 3d** and **Supplementary Fig. 13d-e**). To link this transcriptional response to neurological recovery, we ablated *Vsx2*[ON] neurons in the thoracic spinal cord two weeks prior to a moderate SCI. Ablating *Vsx2*[ON] neurons prevented the natural recovery of walking in these mice (**Fig. 3e-f**, **Supplementary Fig. 13f-h**, and **Supplementary Video 2**).

Local *Vsx2* neurons also exhibited the highest expression of genes associated with circuit reorganization in the uninjured spinal cord (**Supplementary Fig. 13i**). This observation raised the intriguing possibility that specific neuronal subpopulations may be intrinsically primed to serve as circuit-reorganizing cells after injury[2]. To study this possibility, we correlated the expression of circuit reorganization programs in each subpopulation of uninjured neurons with the upregulation of the same programs after injury. We identified a striking correlation between basal and injury-induced circuit reorganization programs between 14 days and 1 month post-injury, when these programs were maximally upregulated (**Fig. 3g** and **Supplementary Fig. 13j**). This time course coincides precisely with the temporal window of opportunity for the circuit reorganization that mediates natural recovery after SCI[2,126]. Together, these findings imply that specific neuronal subpopulations are endowed with the inherent potential to become circuit-reorganizing cells that support neurological recovery.

Our analyses thus far exposed a temporal continuum between early-conserved and late-diverging neuronal responses following SCI. We sought to quantify the relative intensity of these time-dependent responses. To enable this quantification, we assessed the relative degree of transcriptional perturbation within each neuronal subpopulation over the course of recovery after SCI using Augur[60,127]. Augur is a machine-learning framework that quantifies the relative magnitude of the transcriptional response within any given cell type to an arbitrary perturbation, a procedure we refer to as cell type prioritization. This prioritization revealed a pronounced neuronal response at 1 day that decreased in intensity over the subsequent days, and thereafter remained constant (**Fig. 3h**).

Based on these observations, we propose a model in which all neurons undergo a profound and broadly conserved transcriptional response immediately after injury that leads to a dichotomous outcome of survival versus apoptosis. Over the subsequent weeks, the surviving neurons exhibit gradually divergent transcriptional responses to injury, whereby only specific subpopulations upregulate molecular programs associated with circuit reorganization. The degree of this injury-induced upregulation is encoded in the basal transcriptional state of each neuronal subpopulation, suggesting that specific subpopulations are primed to serve as circuit-reorganizing neurons following injury[2].

## Surviving neurons remain differentiated after CNS injury

Single-cell studies have shown that neurons in the injured peripheral nervous system undergo dedifferentiation and loss of transcriptional identity following axonal injury[128,129]. We asked whether similar biological principles dictate neuronal responses in the injured CNS.

Contrary to single-cell analyses of peripheral neurons, we failed to identify a separate cluster of dedifferentiated neurons within the injured spinal cord at any timepoint (**Fig. 2i**). We reasoned that differential expression (DE) of neuronal marker genes could identify more subtle loss of transcriptional identity. However, we found that the vast majority of subpopulation-specific marker genes were neither up- nor downregulated across the entire time course of SCI (**Fig. 3i** and **Supplementary Fig. 14a**). This observation was robust to the statistical threshold used to identify neuronal marker genes (**Supplementary Fig. 14b-c**).

Collectively, these observations raise the possibility that transient loss of neuron transcriptional identity after injury may be a mechanism by which the peripheral nervous system maintains the distinct capacity to regrow severed nerves[130,131]. However, the central nervous system fails to recruit this mechanism after injury.

## Growth-facilitating and inhibiting molecule expression

Following SCI, neural and non-neural cells express multiple families of molecules that can facilitate or inhibit axon growth and circuit reorganization[15,63,132–134]. These molecular pathways have historically been the main targets for interventions that aim to promote spinal cord repair[10], but the identities of the cells that produce these molecules are not well characterized.

Our single-cell atlas provides a resource to explore the production of inhibitory and facilitating molecules across the entire repertoire of cell types in the injured spinal cord. For example, we and others previously showed that laminins provide a permissive substrate for axon growth[15,63,135], but the

cells that express these molecules have not been identified. We found that laminins (*Lama1*, *Lama2*, *Lama4*, *Lama5*) were expressed primarily by VLMCs, identifying these cells as a target to upregulate the expression of axon growth-supporting molecules for spinal cord repair (**Supplementary Fig. 15a-d**). A second example comes from the family of chondroitin sulfate proteoglycans (CSPGs), which are known to play contrasting roles in inhibiting or supporting axon growth[15,63,77–79,136]. Among inhibitory CSPGs, we found that OPCs are responsible for the expression of *Acan*, *Vcan*, and *Ncan*, whereas astrocytes were the dominant producers of *Bcan* (**Supplementary Fig. 15e-h**). OPCs were also the dominant producer of axon growth-supportive CSPGs, such as *Cspg4* and *Cspg5* (**Supplementary Fig. 15i-j**).

Various studies reported that the enzyme ChABC can digest CSPGs[80,81,137–139], which are a main constituent of perineuronal nets[82,140], and that this digestion may open opportunities for circuit reorganization[10,80,81,141]. We employed cell type prioritization to identify the cell types that were most transcriptionally perturbed by ChABC treatment, which pointed to CSPG-producing cell types including OPCs and VLMCs (**Supplementary Fig. 15k**). We then asked how ChABC influences genes associated with circuit reorganization. After ChABC administration, neurons upregulated genes associated with focal adhesion, as previously described[142], including *Itgav*, *Sorbs3*, *Itgb5*, and *Ilk* (**Supplementary Fig. 15l-m**). Despite these changes, however, high-resolution kinematics showed no significant benefit for the recovery of walking (**Supplementary Fig. 3d**).

Collectively, these results illustrate how our single-cell atlas can be used as a resource to identify the cell-types that produce growth-promoting or inhibitory molecules following SCI, and dissect cell-type-specific responses to potential therapies that target these molecules.

## Immunomodulation does not confer neuroprotection after SCI

Early therapeutic approaches to SCI sought to inhibit immune responses to injury, with the aim of conferring neuroprotection[71]. Preclinical studies suggested neuroprotective actions of methylprednisolone[70] and minocycline[73–75], which led to large-scale clinical trials[71,76]. However, these trials failed to demonstrate the effectiveness of these treatments to mediate functional recovery[70,72,143].

We asked whether our single-cell atlas could reconcile the paradox between the established immunomodulatory activity of these drugs and their failure to ameliorate neurological function. Cell type prioritization[60,127] confirmed that both methylprednisolone and minocycline triggered a profound transcriptional perturbation of the entire immune lineage (**Supplementary Fig. 16a-b**). However, this immunomodulation did not coincide with an increase in the survival of neurons (**Supplementary Fig. 16c-e**). This failure to protect neurons from apoptosis coincided with the lack of detectable neurological recovery, despite high-resolution kinematic analyses.

Although these agents failed to improve the survival of neurons after SCI, we reasoned that they might induce more subtle transcriptional changes in the surviving neurons. Specifically, we hypothesized that these agents might repress the molecular programs activated by injury within neurons, thus promoting a shift towards an uninjured transcriptional phenotype. To test this hypothesis, we trained a machine-learning model to classify individual neurons as originating from injured versus uninjured spinal cords (**Supplementary Fig. 16f**). Applying this model to cells from mice treated with methylprednisolone or minocycline exposed a threefold increase in the proportion of neurons that were classified as uninjured (**Fig. 3j**). Consistent with this prediction, surviving neurons treated with methylprednisolone downregulated transcriptional programs associated with innate and adaptive immune responses and cellular stress (**Supplementary Fig. 16g-h**).

Together, these findings suggest that methylprednisolone and minocycline modulate the immune responses to SCI, which in turn shifts the surviving neurons towards their basal transcriptional states. However, these agents fail to alter the early, dichotomous outcome of survival versus apoptosis, and therefore fail to prevent neuronal death or improve neurological recovery.

## Sexually dimorphic responses to SCI are subtle

Sexual dimorphism in immune responses underlies differences in the prevalence of autoimmune disease between males and females[66,67]. Consequently, we hypothesized that transcriptional programs activated by SCI may also be sexually dimorphic. We applied cell type prioritization to evaluate whether specific cell types are differentially perturbed by SCI in male versus female mice. As anticipated, this analysis prioritized immune cell types as having the most prominent sex-dependent transcriptional differences (**Supplementary Fig. 17a**). Moreover, comparison of immune cell proportions revealed an increase in NK cells within female mice, consistent with established sex differences in the adaptive immune response to neurotrauma[66,144] (**Supplementary Fig. 17b-c**).

Despite these dimorphic immune responses, however, high-resolution kinematics failed to demonstrate any sexual dimorphism in neurological recovery (**Supplementary Fig. 3f**). Moreover, the average magnitude of the transcriptional perturbation between male and female mice was among the most subtle in our single-cell atlas (**Supplementary Fig. 17d**). Accordingly, we failed to detect sex differences in the overall proportion of surviving neurons (**Supplementary Fig. 17e-f**).

Taken together, these results suggest that sexual dimorphism does not impact early neuronal death or survival, and consequently, has no detectable influence on neurological recovery[145].

## Cellular divergence between animal models of SCI

Preclinical studies of SCI require the selection of a relevant paradigm from a large repertoire of potential injury models[146–148]. One important difference between these models is whether they explicitly open the meninges, which is thought to promote excessive immune cell infiltration. Unex-

pectedly, however, we found that the degree of peripheral immune invasion was broadly conserved across the injury models included in our single-cell atlas (**Fig. 3k** and **Supplementary Fig. 18a-c**). We validated this finding by morphometrically quantifying Cd45-expressing cells, finding the number of these to be essentially identical across injury models (**Supplementary Fig. 18d-e**). These observations suggest that crush and contusion injuries dismantle the blood-brain barrier and cause extensive peripheral immune invasion that is not contingent on explicit meningeal disruption caused by hemisection injuries.

A second potential difference between preclinical paradigms is their relevance to human injuries. The most common mechanism of spinal cord damage in humans occurs through burst fractures and distraction injuries that impact the ventral spinal cord[149]. To understand whether our profiled injury models lead to differential perturbations of neurons along the dorsoventral axis, we employed cell type prioritization to quantify transcriptional responses in each neuronal subpopulation. Compared to crush injury, we found that dorsal hemisection and contusion injuries preferentially perturbed neurons in the dorsal spinal cord (**Supplementary Fig. 18f**). Conversely, increasingly severe crush injuries induced balanced perturbations in neurons located in the dorsal and ventral spinal cord (**Supplementary Fig. 18g**). These differences between rodent models of SCI must be considered when selecting an injury paradigm for preclinical studies.

## Catastrophic failure of tripartite barrier formation in old mice

Aging causes multifaceted changes in gene expression that culminate in dysregulated transcriptional responses to disease and biological perturbations[150–155], but whose cellular and functional consequences after SCI remain poorly understood. Remarkably, we found that the transcriptional differences between young and old mice after SCI were nearly as profound as those between injured and uninjured mice (**Fig. 4a**). The magnitude of this transcriptional perturbation was mirrored by extensive functional impairments in old mice compared to young mice (**Fig. 4b-c**, **Supplementary Fig. 3e**, and **Supplementary Video 3**). We therefore sought to elucidate the mechanisms underlying these transcriptional and functional differences.

We first compared the proportions of cell types in the injured spinal cord of young and old mice. This comparison revealed a profound reduction in the proportion of neurons surviving the injury in old mice, which was accompanied by a dramatic increase in the proportion of immune cells (**Fig. 4d**). Anatomical assessments confirmed that old mice developed larger lesions compared to young mice, despite identical mechanisms of injury (**Fig. 4e**).

We next asked how age impacted the transcriptional responses to SCI within individual cell types. Cell type prioritization[60,127] revealed abnormal responses in infiltrating immune cells from old mice, including dividing myeloid progenitors, NK cells, and T cells (**Supplementary Fig.**

19a). However, Augur also detected abnormal responses within cell types involved in the formation of the blood-brain barrier and the astrocyte barrier, including extracellular matrix-forming VLMCs, capillary endothelial cells, and OPCs. Consistent with this observation, we detected an age-dependent decrease in the proportion of *Id3*-expressing astrocytes, which form the astrocyte lesion border[156], and of arachnoid barrier cells, which form the cerebrospinal fluid barrier (**Supplementary Fig. 19b-c**). Immunohistochemistry for Sox9 and Id3 confirmed these findings (**Fig. 4f-g**). Within the vascular compartment, we identified an age-dependent upregulation of gene programs associated with dysfunction of the blood-brain barrier, and downregulation of the specialized gene programs that enable vascular cells to establish the blood-brain barrier (**Fig. 4h** and **Supplementary Fig. 19d**).

To dissect the transcriptional programs that are dysregulated in old mice, we performed DE analysis[87] of all the cell types in the spinal cord. In contrast to young mice, we observed that many genes were DE within just a single cell type in old mice (**Fig. 4i**). Moreover, other genes were upregulated in some cell types, but downregulated in others (**Supplementary Fig. 19e-f**). To quantify the coordination of the transcriptional responses to SCI across cell types, we devised statistical measures that aimed to capture both the variability of DE and changes in the direction of DE across cell types. These quantifications revealed that transcriptional responses to injury were profoundly discoordinated across the cell types of the spinal cord in old mice, relative to every other experimental comparison (**Fig. 4j** and **Supplementary Fig. 19e-f**).

Together, these findings suggest that old mice fail to deploy the coordinated, multicellular response to SCI that naturally occurs in young mice. This failure manifests in the disruption of three essential neuroprotective barriers between the immune-privileged and extra-neural environments of the injured spinal cord: (i) the blood-brain barrier; (ii) the CSF-brain barrier; and (iii) the border-forming astrocyte barrier (**Fig. 4k**). The consequence of this tripartite barrier formation failure is a dramatic increase in peripheral immune cell invasion, which culminates in the uncontrolled expansion of the lesion, the catastrophic loss of neurons adjacent to the injury site, and a resulting inability to coordinate the recovery of neurological functions.

## A single-nucleus multi-omic atlas of the injured and uninjured spinal cord

Our snRNA-seq atlas exposed the transcriptional programs triggered by SCI across the entire repertoire of cells in the spinal cord. However, we recognized that this atlas was intrinsically limited in its ability to expose the regulatory mechanisms that underlie these transcriptional programs. To overcome this limitation, we compiled the second atlas of the *Tabulae Paralytica*: a multi-omic atlas of the injured spinal cord (**Fig. 5a**).

We deployed single-nucleus multi-omics to measure both RNA and accessible chromatin within the same individual
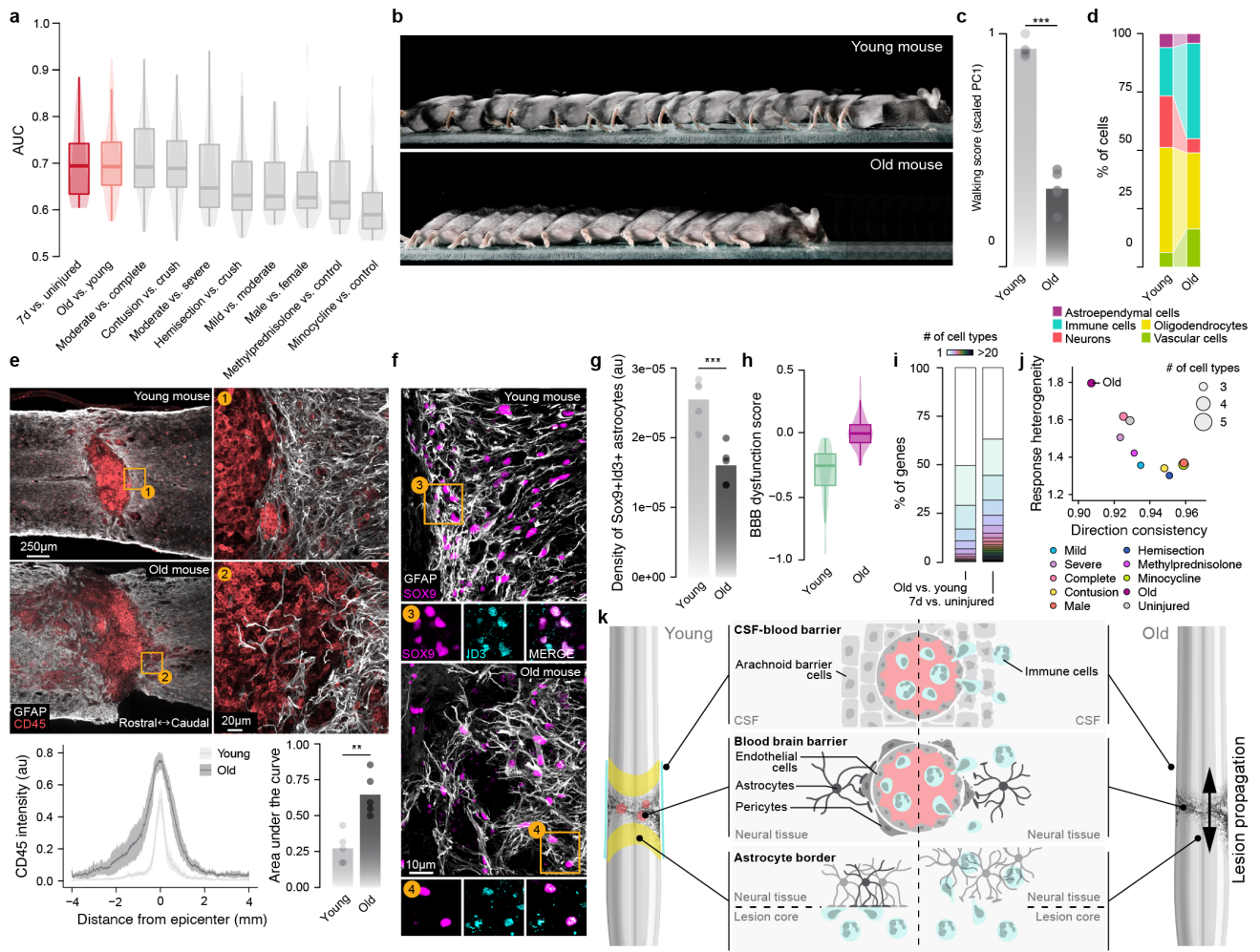
**Fig. 4 | Catastrophic failure to reestablish a tripartite neuroprotective barrier in old mice.**

**a,** Intensity of the transcriptional perturbation across all cell types of the spinal cord, as quantified by Augur, for all comparisons involving the injured spinal cord at 7 days post-injury. Comparisons between injured and uninjured mice, and old and young injured mice, are highlighted.

**b-c,** Chronophotography, **b,** and walking performance (*n* = 5 each), **c,** of young and old mice after spontaneous recovery from moderate crush SCI.

**d,** Proportions of each major spinal cord cell type in young versus old mice after SCI.

**e,** Composite tiled scans of GFAP and CD45 in horizontal sections from representative old and young mice. Bottom left, line graph demonstrates CD45 intensity at specific distances rostral and caudal to lesion centers. Bottom right, bar graph indicates the area under the curve (independent samples two-tailed t-test; *n* = 5 per group; t = 4.57; p = 0.002).

**f,** Horizontal sections from representative old and young mice identifying a lack of Sox9^ON^Id3^ON^ cells in the astrocyte border region in old mice compared to young mice.

**g,** Density of Sox9^ON^Id3^ON^ cells in the astrocyte border region (independent samples two-tailed t-test; *n* = 5 per group; t = 4.84; p = 0.001).

**h,** Expression of the BBB dysfunction module in capillary endothelial cells from young and old mice at seven days post-injury.

**i,** Cell type specificity of DE genes in comparisons of young vs. old mice or injured vs. uninjured mice.

**j,** Heterogeneity of cell-type-specific differential expression in experimental comparisons involving the injured spinal cord at seven days after SCI. Aging is characterized by greater discoordination of gene expression than any other condition in the snRNA-seq atlas, as reflected by increased response heterogeneity and decreased direction consistency.

**k,** Schematic overview of the cell types comprising the tripartite neuroprotective barrier.

cells, using the assay for transposase-accessible chromatin by sequencing (ATAC-seq). We leveraged these methodologies to profile the uninjured and injured spinal cords of mice at 7 days and 2 months post-injury. After quality control of both modalities[157], we obtained a dataset measuring gene expression and chromatin accessibility in 47,726 nuclei (**Fig. 5b** and **Supplementary Fig. 20**).

We aimed to link the multi-omic atlas to the cellular taxonomy of the spinal cord that our snRNA-seq atlas had established. To overcome challenges in cell type annotation

within snATAC-seq data, we adapted an automated cell type annotation approach[158] to hierarchically assign cell types and subtypes to each cell in the multiome atlas based on the RNA modality. We validated the accuracy of this approach through cross-validation in the snRNA-seq atlas, and established that cell types were recovered at similar frequencies in both atlases (**Supplementary Figs. 21-22**).

We then leveraged this taxonomy to call peaks within each cell type and subtype at increasingly granular resolutions on the clustering tree (**Supplementary Fig.**
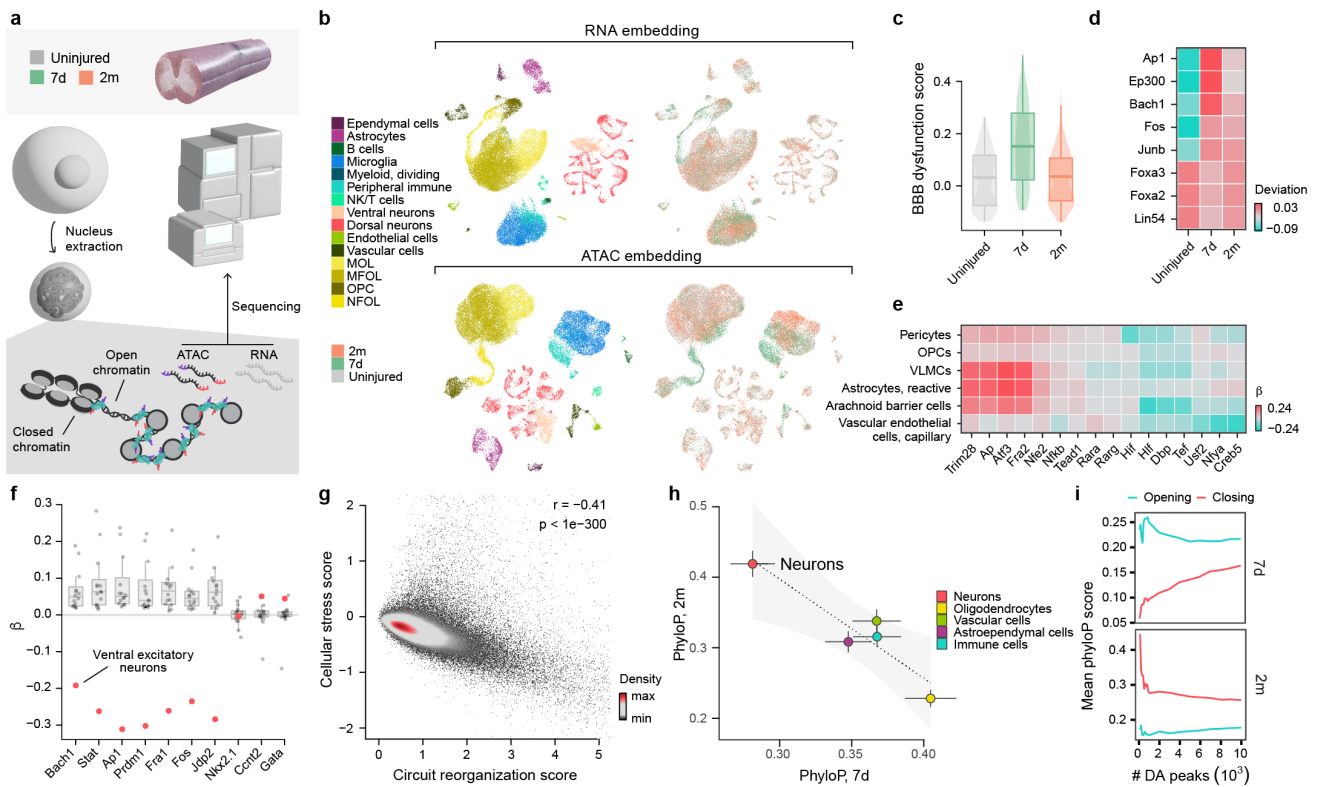
**Fig. 5 | A multi-omic atlas of SCI.**

**a,** Schematic overview of the multiome atlas.

**b,** UMAP visualizations of the 40,256 cells in the multiome atlas, based on the RNA, top, or ATAC, bottom, modalities, and colored by cell types, left, or experimental conditions, right.

**c,** Expression of the blood-brain barrier dysfunction module score in vascular cells across timepoints in the multiome atlas.

**d,** Transcription factors for which motif accessibility in the ATAC modality correlated with expression of the blood-brain barrier dysfunction module in the RNA modality across vascular cells in the multiome atlas.

**e,** Selected transcription factors with significant differences in motif accessibility at 7 days in cell types that establish the tripartite barrier.

**f,** Transcription factors exhibiting significant variability in transcription factor binding across neuron subtypes at 2 months. Motif accessibility in ventral excitatory interneurons is highlighted.

**g,** Anticorrelated expression of the circuit reorganization module, x-axis, versus that of the cellular stress module, y-axis, in 80,315 neurons from the snRNA-seq atlas.

**h,** Mean phyloP scores of differentially accessible peaks in major cell types of the spinal cord at 7 days, x-axis, and 2 months, y-axis. Error bars show the standard error of the mean for each comparison.

**i,** Mean phyloP scores of differentially accessible peaks that are opening or closing in neurons at 7 days or 2 months post-injury.

23)[157], and identified differentially accessible transcriptional factors within each subpopulation using chromVAR (**Supplementary Figs. 24-25**)[159]. This analysis highlighted well-studied transcriptional factors that play canonical roles in specifying the identity of spinal cord cell types, including astrocytes (*Nr1d1*, *Nfib*[160]), B cells (*Pax2*, *Pax5*[161]), Microglia (*Irf1*[162]), pericytes (*Ebf1*[163]), and endothelial cells (*Lef1*[164]). However, our data also pointed to less-characterized cell-type-specific TFs, including *Zbtb3* (ventral interneurons), *Nf1* (vascular leptomeningeal cells), *Zbtb7b* (oligodendrocyte precursor cells), *Rfx5* (ependymal cells), *Ccnt2* (CSF-contacting neurons), and *Mlx* (immune cells).

## Regulatory programs underlying tripartite neuroprotective barrier formation

Since our snRNA-seq atlas exposed a number of biological principles that dictate the multifaceted responses to SCI in different cell types of the spinal cord, we sought to leverage our multiome atlas to understand the regulatory programs that orchestrate these transcriptional responses.

We first aimed to dissect the gene regulatory programs involved in the reestablishment of the tripartite neuroprotective barrier after SCI. Because our multiome atlas recapitulated the upregulation of gene programs associated with blood-brain barrier dysfunction that we had observed in the snRNA-seq atlas (**Fig. 5c**), we leveraged the ATAC modality to identify the transcriptional factors that underlie this dysfunction. To exploit the link between RNA and ATAC modalities, we correlated the accessibility of transcriptional factor binding motifs to the expression of these gene programs within the same cell (**Supplementary Fig. 26a**). Within vascular cells, the expression of the blood-brain barrier dysfunction program[101] was correlated with the accessibility of transcription factors associated with cellular stress and inflammation (*Ap1*, *Junb*, *Bach1*, *Fos*) and hypoxia-induced VEGF stimulation (*EP300*), and anticorrelated with the accessibility

of transcription factors driving cellular proliferation (*Foxa2*, *Foxa3*, *Lin54*; **Fig. 5d** and **Supplementary Fig. 26b**).

These responses were mirrored by shared and cell-type-specific regulatory programs in the other cellular subpopulations that coordinate the formation of the tripartite barrier (**Fig. 5e** and **Supplementary Fig. 26c**). VLMCs, pericytes, and arachnoid barrier cells exhibited decreased accessibility of transcription factors known to modulate the permeability of the blood-brain or cerebrospinal fluid barriers (*Rarg*, *Hif1*), whereas arachnoid barrier cells and pericytes exhibited decreased accessibility of transcription factors that govern barrier efflux of metabolites and that regulate neuronal activity (*Dbp*, *Tef*). Finally, border-forming astrocytes exhibited increased motif accessibility of multiple transcription factors associated with acute responses to stress or hypoxia, including *Junb*, *Bach1*, *Fos*, and *EP300*[160].

## Evolutionary divergence in circuit reorganization

Our snRNA-seq atlas established that SCI triggers an immediate transcriptional response that is conserved across all neuronal subpopulations. Conversely, we found that transcriptional responses gradually diverged between neuronal subpopulations over time after SCI (**Fig. 3c**). We therefore next sought to understand the regulatory programs that govern neuronal responses to SCI as well as their associated functional consequences and potential origins.

In the multiome atlas, we observed that the early-conserved transcriptional response was mirrored by conserved regulatory programs that involved increased accessibility of transcription factors associated with cellular stress (*Myc*, *Nfe2*) and apoptosis (*Tfap2*) (**Supplementary Fig. 27a**). To characterize late-diverging regulatory programs, we devised a permutation-based statistical approach that evaluated variability in transcription factor binding across all subpopulations of neurons (**Supplementary Fig. 27b**). We found that this variability originated from divergent regulatory responses within a subpopulation of ventral excitatory interneurons (**Fig. 5f** and **Supplementary Fig. 27c**). Whereas every other subpopulation of neurons exhibited increased accessibility of transcription factors associated with cellular stress responses (*Ap1*, *Stat*, *Bach1*, *Fos*), this subpopulation of ventral excitatory interneurons instead exhibited decreased accessibility of these transcription factors.

The results from our snRNA-seq atlas revealed that ventral excitatory interneurons express genes implicated in circuit reorganization at high levels (**Supplementary Fig. 13c**). The distinctive lack of cellular stress responses within these neurons led us to hypothesize that, in general, neurons face an inherent trade-off between the expression of cellular stress response programs and transcriptional programs associated with circuit reorganization. To test this hypothesis, we re-examined our snRNA-seq atlas and confirmed the existence of an anticorrelation between the expression of programs related to stress response versus circuit reorganization (**Fig. 5g**). These observations suggest a model whereby the ability of different neuronal subpopulations to participate in circuit reorganization is intrinsically linked to the intensity of their response to cellular stress.

Neuronal responses to injury vary dramatically across the tree of life, to the extent that neurons from lower vertebrates can demonstrate spontaneous regeneration whereas neurons from adult mammals fail to regenerate after SCI[16]. This divergence compelled us to characterize the evolutionary conservation of the genomic regions that become differentially accessible following SCI. We used phyloP[165] to quantify the sequence conservation of these regions, and identified profound differences in the evolutionary conservation of differentially accessible peaks within neurons, as compared to glia (**Fig. 5h** and **Supplementary Fig. 28a-c**). Inspecting these differences more closely, we discovered dichotomous patterns of evolutionary conservation for peaks that opened versus closed in neurons after SCI (**Fig. 5i** and **Supplementary Fig. 28d-e**). In the acute phase of SCI, neurons displayed increased accessibility of evolutionarily conserved genomic regions, which was mirrored by decreased accessibility of evolutionarily accelerated genomic regions. These trends were reversed two months after SCI, when evolutionarily accelerated regions displayed increased accessibility.

These observations led us to ask whether the opening of evolutionarily accelerated regions is necessary for neurons to participate in the recovery of neurological functions. To test this possibility, we computed the mean evolutionary conservation of accessible genomic regions within individual neurons. Across all subpopulations of neurons, we found that the same subpopulation of ventral excitatory interneurons demonstrated the most pronounced opening of evolutionarily accelerated regions in response to injury (**Supplementary Fig. 28f**).

We conclude that neurons in the spinal cord face an inherent tradeoff between the activation of cellular stress responses, and the opening of evolutionarily accelerated genomic regions to express transcriptional programs associated with circuit reorganization.

## A spatial transcriptomic atlas of SCI

Interrogation of our snRNA-seq and multiome atlases identified cell-type-specific transcriptional and regulatory programs triggered by SCI. However, these transcriptional and regulatory programs were identified in dissociated cells, and therefore, could not be visualized within the complex microenvironment of the injury. To overcome this limitation, we resolved these programs within the cytoarchitecture of the spinal cord using spatial transcriptomics (**Fig. 6a**).

We profiled the spinal cords of uninjured and injured mice at 7 days and 2 months after SCI, and obtained 33,941 high-quality spatial barcodes from 36 coronal sections (**Supplementary Fig. 29**). To permit direct comparison across experimental conditions, we registered all 36 sections to a common coordinate system[166] (**Fig. 6a-b**).

The coordinated, multicellular response to SCI establishes a thin astrocyte barrier that separates the fibrotic lesion core from surrounding immune-privileged neural tissue[17,18]. The requirements to promote neural repair are known to differ between these distinct lesion compartments,
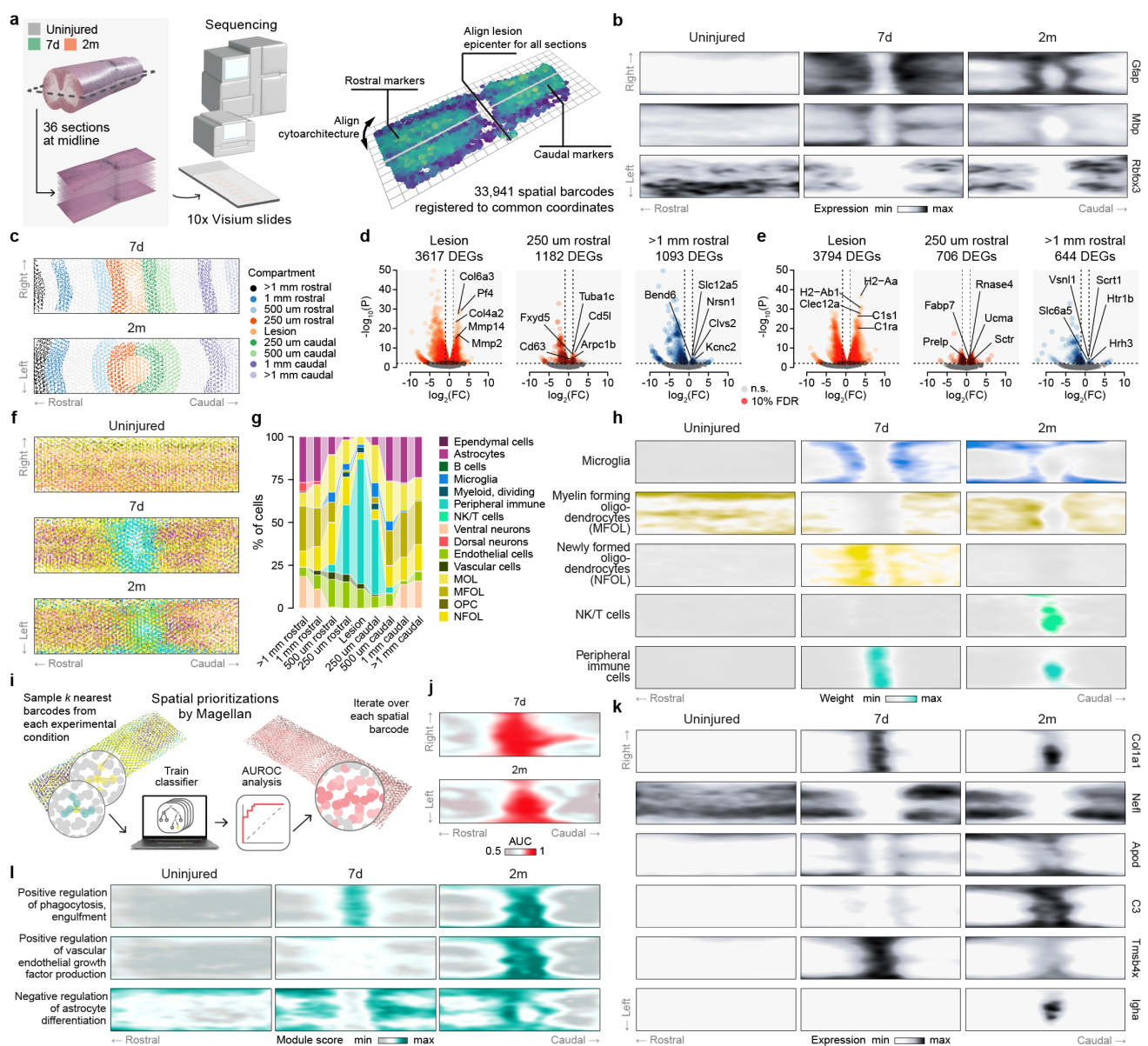
**Fig. 6 | A spatial transcriptomic atlas of SCI.**

**a,** Schematic overview of the 2D spatial transcriptomic atlas.

**b,** Computational histology of key marker genes on the two-dimensional common coordinate system of the spinal cord.

**c,** Legend showing the position of each lesion compartment on the coordinate system of the spinal cord.

**d-e,** Volcano plots showing compartment-specific genes at 7 days, **d,** and 2 months, **e,** for a subset of the lesion compartments discussed in the text.

**f,** Cell type deconvolution of spatial barcodes in the 2D spatial transcriptomic atlas.

**g,** Cellular composition of each lesion compartment, as determined by cell type deconvolution.

**h,** Deconvolution weights assigned by RCTD to selected cell types.

**i-j,** Spatial prioritizations assigned by Magellan to each spatial barcode at 7 days, **i,** and 2 months, **j.**

**k-l,** Expression of selected genes, **k,** and gene modules, **l,** prioritized by their correlation to spatial prioritizations assigned by Magellan at each spatial barcode.

but the underlying molecular logic remains incompletely understood[2,10]. We leveraged our spatial atlas to uncover the molecular programs that are shared between, or specific to, each of these compartments.

To identify molecular differences between lesion compartments, we demarcated spatial barcodes corresponding to the fibrotic scar, the astrocyte barrier, and the adjacent neural tissue (**Fig. 6c** and **Supplementary Fig. 30**). We then

performed DE analysis to identify genes specific to each lesion compartment (**Fig. 6d-e** and **Supplementary Fig. 31**). This analysis showed that the fibrotic scar was differentiated from other lesion compartments by upregulation of extracellular matrix molecules (*Col6a3*, *Col4a2*) and matrix metalloproteinases (*Mmp2*, *Mmp14*), and a sustained expression of cytokines (*Cd74*, *Pf4*) and complement proteins (*C1s1*, *C1ra*). The astrocyte barrier was differentiated by genes

associated with cytoskeletal organization (*Tuba1c*, *Arpc1b*) and cell proliferation (*Fxyd5*, *Id3*) at 7 days, and by genes related to radial glial fiber development (*Fabp7*), extracellular matrix molecules (*Ucma*, *Prelp*), synaptic reorganization (*Sctr*), and neuronal survival (*Rnase4*) at 2 months after SCI. Spared reactive neural tissue was differentiated by genes associated with neuronal functions, including solute transport (*Slc12a5*, *Kcnc2*), neuron growth and projection formation (*Nrsn1*, *Bend6*), and synapse maturation (*Scrt1*, *Nptx1*), whereas levels of growth factors and their receptors demonstrated little change.

We next sought to dissect the cellular composition of each lesion compartment by deconvolving the cell types within each spatial barcode[167] (**Fig. 6f-h** and **Supplementary Fig. 32**). We found that the fibrotic lesion core was composed almost exclusively of immune and vascular cells (**Fig. 6g**). The density of astroependymal cells abruptly increased towards the edge of the lesion, and thereafter gradually decreased with increasing distance from the lesion core. As the distance from the lesion core increased, the proportions of each cell type approximated those observed in uninjured spinal cords, mirroring immunohistochemical observations[17,18].

To quantify the relative degree of transcriptional perturbation throughout the lesion microenvironment, we applied Magellan (**Fig. 6i**)[9]. Magellan is a machine-learning framework that quantifies the relative magnitude of the transcriptional response at any given spatial locus to an arbitrary perturbation, a procedure we refer to as spatial prioritization (**Supplementary Fig. 33a**). This prioritization recovered the profound transcriptional perturbation occurring at the lesion core during the first 7 days after injury, with a gradient of decreasing intensity that spread radially throughout the spared but reactive neural tissue adjacent to the fibrotic scar (**Fig. 6j** and **Supplementary Fig. 33b**). Spatial prioritization also captured the contraction of the injury border after 2 months of recovery from SCI (**Fig. 6j** and **Supplementary Fig. 33c-d**).

These results illustrate how spatial prioritization accurately recovered the two-dimensional architecture of the evolving injury. We therefore asked whether spatial prioritization could also provide a resource to identify the molecular programs that elaborate this architecture, without any *a priori* definition of the lesion compartments. To answer this question, we tested for correlation between the spatial prioritization scores assigned to each barcode by Magellan and the expression of individual genes (**Supplementary Fig. 34a-c**). As anticipated, this approach recovered many of the genes associated with canonical lesion compartments, including extracellular matrix molecules at the lesion core (*Col1a1*, *Col13a1*) and neuronal genes (*Nefl*, *Nefh*) in spared but reactive neural tissue (**Fig. 6k** and **Supplementary Fig. 34d-f**). Similarly, we tested for correlation between the spatial prioritizations assigned by Magellan and the average expression of all genes associated with a given Gene Ontology (GO) term. This analysis recapitulated the multifaceted innate and adaptive immune responses within the lesion site (**Fig. 6l** and **Supplementary Fig. 35**).

We then asked whether the spatial transcriptomic atlas could identify genes whose correlation to the perturbation response differed between 7 days and 2 months after SCI. To answer this question, we tested for differential correlation between spatial prioritization scores and gene expression at 7 days and 2 months post-SCI (**Supplementary Fig. 36a**). This analysis highlighted genes (*Gfap*, *Aqp4*, *Apod*) coinciding with the location of the astrocyte barrier, reflecting the contraction of this border that takes place between 7 days and 2 months after injury (**Fig. 6k** and **Supplementary Fig. 36b**). Beyond the astrocyte barrier, differential prioritization also pointed to temporal evolution in the innate and adaptive immune responses, including immediate microglial activation (*Wfdc17*, *Spp1*) and lymphocyte homing (*Stab1*), which contrasted with delayed complement activation (*C3*) and monocyte maturation (*Ms4a7*) (**Fig. 6k** and **Supplementary Fig. 36b**). Repeating this differential prioritization at the level of GO terms highlighted the spatial evolution of astrocyte differentiation, vascular endothelial growth factor production, and phagocytosis (**Fig. 6l** and **Supplementary Fig. 37**).

Spatial prioritization also allowed us to uncover less appreciated aspects of the biology of an SCI. For example, we identified chronic activation of immunoglobulin factors (*Ighg2c*, *Jchain*, *Igha*) within the lesion core, which likely contribute to maintaining host defenses, and antigen binding within the fibrotic core (**Supplementary Fig. 36b**). Spatial prioritization also highlighted a robust expression of *Dbi*[168] along the lesion border (**Supplementary Fig. 36b**). Since *Dbi* modulates the activity of the neurotransmitter gamma-aminobutyric acid (GABA), the expression of this gene may be involved in the reported reduction of neuronal activity in the vicinity of lesion borders. Moreover, our analyses identified *Prdx6* as highly associated with the lesion border, suggesting the expression of this antioxidant enzyme may protect the surrounding reactive neural tissue from oxidative injury (**Supplementary Fig. 36b**). Last, spatial prioritization identified distinct subcompartments of the lesion core itself. We observed that genes associated with iron metabolism (*Flt1*) expressed diffusely throughout the lesion, but genes associated with fat metabolism (*Plin2*) confined to the innermost aspects of the lesion core, and genes associated with actin sequestration (*Tms4bx*) extending out along the lesion edges (**Fig. 6k** and **Supplementary Fig. 34f**).

Together, these results establish a resource to explore the multicellular responses to SCI across the cytoarchitecture of the spinal cord, and validate the ability of spatial prioritization to resolve both well-documented and novel aspects of these responses.

## A four-dimensional spatiotemporal atlas of SCI

The ability to visualize the central nervous system in three dimensions using tissue clearing technologies has opened new possibilities to study the anatomy and function of the nervous system[169]. Analogously, we reasoned that expanding our spatial transcriptomic atlas into a third spatial dimension would enable a more complete description of the biology of SCI. We further surmised that our snRNA-seq and multiome

atlases could be overlaid onto this three-dimensional model of the spinal cord in order to resolve the spatiotemporal distribution of the transcriptional and regulatory responses across the compendium of experimental conditions included in our *Tabulae*.

To develop a four-dimensional spatial atlas of the spinal cord, we collected 16 tissue sections that were equally spaced along the dorsoventral axis of spinal cords from uninjured and injured mice at 7 days and 2 months after SCI (**Fig. 7a**). The distance between each section was approximately 50 $\mu$m, which ensured a dense coverage of the third spatial dimension. After quality control and registration to a common three-dimensional coordinate system, we obtained a dataset comprising 37,558 spatial barcodes from 48 sections (**Supplementary Fig. 38**).

To validate the construction of our four-dimensional atlas, we first confirmed that our dataset resolved the established spatial distributions of cell types in the uninjured and injured spinal cord[17,18]. Three-dimensional projections of gene expression exposed the distinct lesion compartments, including the fibrotic scar (*Col4a2*), the astrocyte barrier (*Gfap*), and spared but reactive neural tissue (*Slc12a5*; **Fig. 7b** and **Supplementary Fig. 39**). Moreover, neurons and immune cells occupied their appropriate locations in the injured spinal cord, whereby the fibrotic scar was invaded by peripheral immune cells and devoid of neurons. We next inspected the expression of well-studied inhibitory and facilitating molecules (**Supplementary Fig. 40**), finding the inhibitory CSPG aggrecan (*Acan*) was expressed within spared neural tissue that surrounded the lesion core, whereas brevican (*Bcan*) was expressed in both the lesion core and neural tissue. The growth-permissive molecule *Cspg4* was expressed predominantly in the lesion core, whereas *Cspg5* was expressed within the astrocyte barrier. Finally, the permissive extracellular matrix molecule *Lama1* was upregulated both within the lesion core and by border-forming astrocytes.

To increase the resolution of this spatiotemporal atlas, we again leveraged our snRNA-seq atlas to deconvolve the cellular composition of each spatial barcode (**Supplementary Figs. 41-42**). This procedure resolved cellular subpopulations within highly specific locations, such as ependymal cells and border-forming macrophages. Moreover, dorsal and ventral neurons were appropriately separated along the coronal plane, and the locations of specific neuronal subpopulations such as cerebrospinal fluid-contacting neurons, *Vsx2*-expressing neurons, and motor neurons were correctly resolved (**Fig. 7c**).

We next aimed to integrate all of the *Tabulae* into a single, unified framework. Using Tangram[170], we embedded single-nucleus transcriptomes and epigenomes onto our four-dimensional atlas of the mouse spinal cord, generating a unified dataset of 554,324 single-nucleus or spatial barcodes that were each associated with a full transcriptome, an experimental condition, and x-, y-, and z-coordinates (**Fig. 7d**).

We then applied Magellan to the integrated spatial dataset. This spatial prioritization reflected the severity-dependent increase in transcriptional perturbation within in-creasing injury severity (**Fig. 7e**). Consistent with these observations, Magellan captured severity-dependent changes in peripheral immune cell invasion, astrocytic demarcation of the lesion, and neuronal death (**Supplementary Fig. 43**). Moreover, we spatialized the expression of conserved-early neuronal responses, as well as late-diverging expression of programs associated with circuit reorganization (**Supplementary Fig. 44**). We then linked these changes in cell type composition and gene expression to transcription factor accessibility by spatializing the accessibility of transcription factors involved in the establishment of the tripartite barrier (**Fig. 7f** and **Supplementary Fig. 45**).

Our snRNA-seq atlas identified a profound transcriptional perturbation across spinal cord cell types in old mice following SCI. We therefore sought to understand the spatial distribution of this perturbation. Magellan revealed that old mice developed an expanded and poorly circumscribed territory of transcriptional perturbation as compared to young mice, reflecting their failure to re-establish the tripartite neuroprotective barrier. This failure was reflected by global upregulation of blood-brain barrier dysfunction module score, and downregulation of gene expression programs associated with blood-brain barrier identity (**Fig. 7g** and **Supplementary Fig. 46**). Three-dimensional visualization of genes associated with peripheral immune invasion exposed the failure to demarcate the lesion in old mice (**Fig. 7h**).

Collectively, these results establish the feasibility of constructing an integrated transcriptomic and epigenomic atlas of healthy and perturbed tissues across four spatiotemporal dimensions.

## Reestablishing the tripartite barrier restores walking in old mice

The *Tabulae Paralytica* documented the spatially- and temporally-dependent activation of transcriptional and regulatory mechanisms that are triggered after SCI in order to reestablish a tripartite neuroprotective barrier. Conversely, the catastrophic failure to reestablish this tripartite barrier in old mice results in poorly circumscribed lesions, massive neuronal death, and impaired recovery of neurological functions (**Fig. 4**, **Supplementary Fig. 19**, and **Supplementary Video 3**). These observations led us to hypothesize that interventions that accelerate wound repair by promoting the formation of the tripartite barrier could restore neurological functions in old mice.

Because we found that the number of *Id3*-expressing, border-forming astrocytes was decreased in old mice (**Fig. 4f-g**), we reasoned that increasing their production would accelerate the formation of the astrocyte barrier, limiting lesion size and preserving neurological function. We previously found that the delivery of EGF and FGF2 increased both the proliferation and absolute number of border-forming astrocytes[63]. Moreover, it is established that the delivery of Vegf accelerates endothelial cell proliferation and reformation of vascular networks[171]. We therefore engineered lentiviruses to overexpress Egf, Fgf2, and Vegf and, as a proof-of-principle test, delivered these vectors to the lower
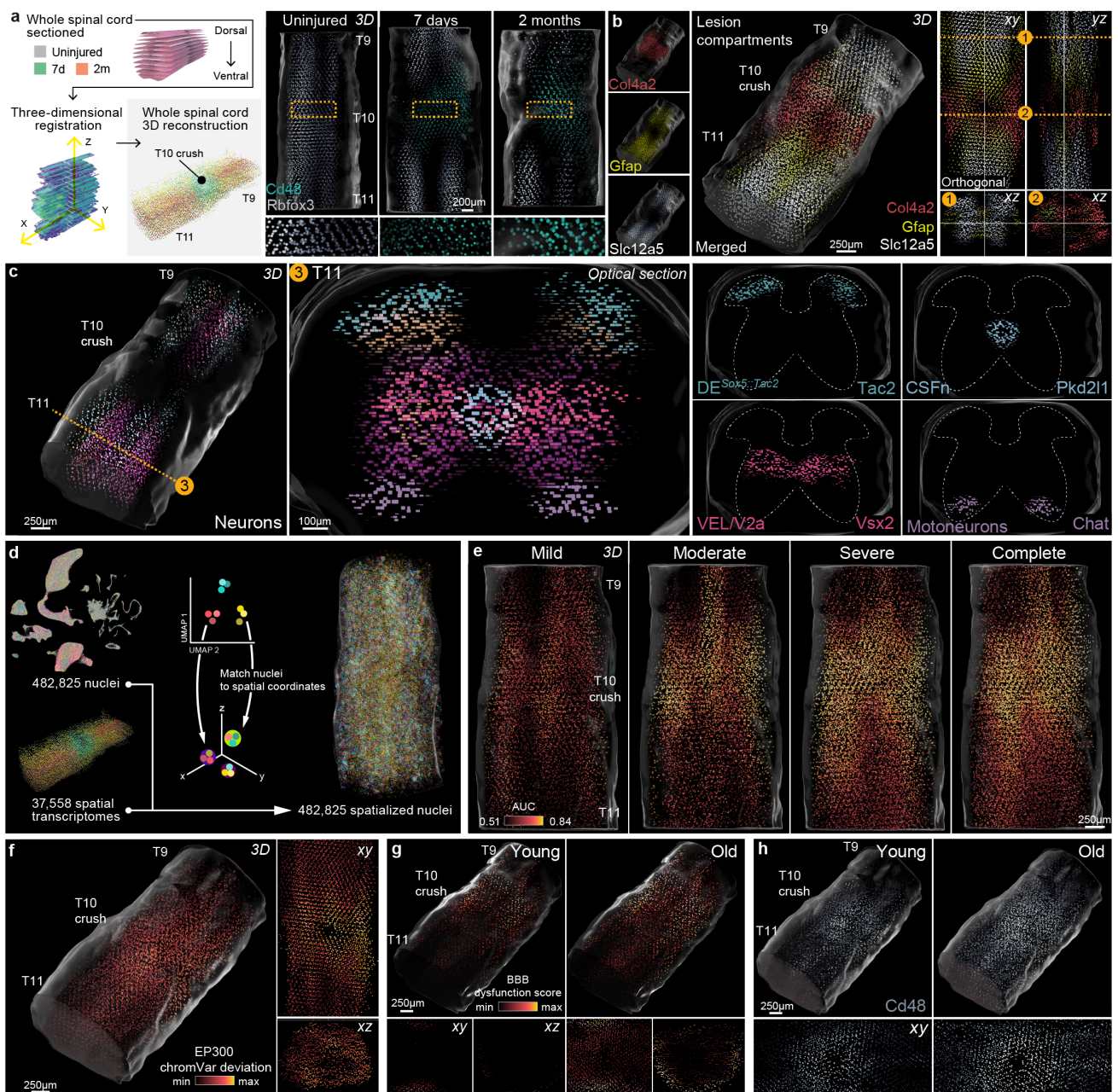
**Fig. 7 | A four-dimensional spatiotemporal atlas of SCI.**

**a,** Left, schematic overview of the 3D spatial transcriptomic atlas. Right, expression of marker genes for neurons (*Rbfox3*) and immune cells (*Cd48*) across three dimensions in the uninjured and injured mouse spinal cord.

**b,** Expression of marker genes associated with distinct lesion compartments across the 3D spatial transcriptomic atlas at 7 days, including the fibrotic scar (*Col4a2*), the astrocyte barrier (*Gfap*) and the surrounding spared but reactive neural tissue (*Slc12a5*).

**c,** Spatial localization of selected neuronal subpopulations defined by snRNA-seq across the 3D spatial transcriptomic atlas at 7 days.

**d,** Left, UMAP representation of 435,099 single-nucleus transcriptomes from the snRNA-seq atlases, colored by experimental condition. Right, spatial coordinates assigned to each single-nucleus transcriptome within the 3D spatial transcriptomic atlas.

**e,** Three-dimensional spatial prioritization of spatialized cells from the snRNA-seq atlas, across injury severities.

**f,** Accessibility of the EP300 binding motif within spatialized cells from the multiome atlas at 7 days, visualized on the 3D spatial transcriptomic atlas.

**g,** Expression of the blood-brain barrier dysfunction module in vascular cells from young and old mice at 7 days, visualized on the 3D spatial transcriptomic atlas.

**h,** Expression of *Cd48* in spatialized cells from young and old mice at 7 days, visualized on the 3D spatial transcriptomic atlas.

thoracic spinal cord two days prior to SCI (**Fig. 8a** and **Supplementary Fig. 47a**). This procedure increased the production of border-forming astrocytes, reduced the number of CD45+ infiltrating immune cells, and resulted in smaller and more circumscribed lesions (**Fig. 8b-c** and **Supplementary Fig. 47b-c**). In addition, and remarkably, treated old mice exhibited a natural recovery of walking resembling that of young mice subjected to the same severity of SCI (**Fig. 8d-f**,
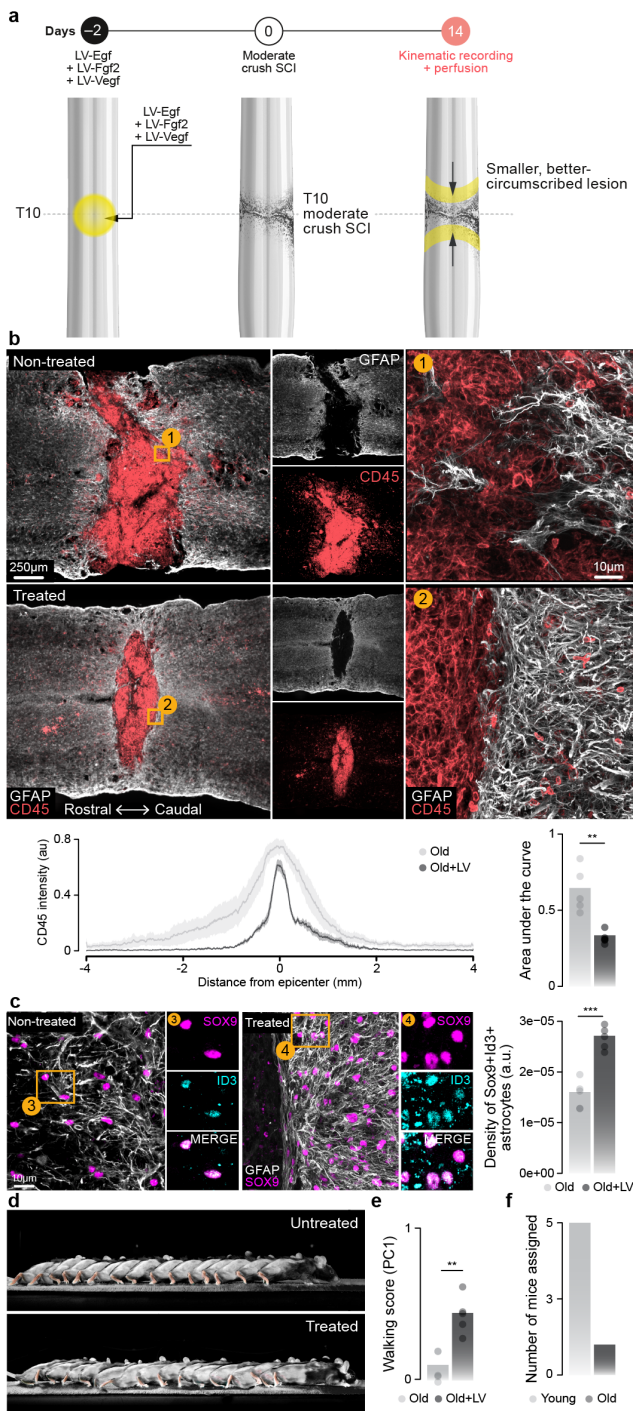
**Fig. 8 | A rejuvenative gene therapy reestablishes the tripartite barrier to restore walking.**
**a,** Experimental design of a gene therapy intervention to promote the formation of the tripartite barrier.
**b,** Composite tiled scans of GFAP and CD45 in horizontal sections from representative old and treated mice. Line graph demonstrates CD45 intensity at specific distances rostral and caudal to lesion centers. Bar graph shows the area under the curve (independent samples two-tailed t-test; $n = 5$ per group; $t = 4.57$; $p = 0.002$).
**c,** Horizontal sections from representative old and treated mice identifying a restoration of Sox9$^{ON}$Id3$^{ON}$ cells in the astrocyte border region in treated mice. Right, bar graph indicates the density of Sox9$^{ON}$Id3$^{ON}$ cells in the astrocyte border region (independent samples two-tailed t-test; $n = 5$ per group; $t = 6.84$; $p = 0.0002$).
**d,** Chronophotography of walking in old mice without (top) and with (bottom) a gene therapy intervention to promote the formation of the tripartite barrier.
**e,** Walking performance of old mice with and without treatment (independent samples two-tailed t-test; $n = 5$ per group; $t = 4.85$; $p = 0.001$).
**f,** Experimental conditions assigned to old mice that received gene therapy by a machine-learning model trained on kinematics data from untreated animals. Mice were almost exclusively assigned to the young mouse group, indicating that the walking patterns of treated old mice most resemble those of young mice.

far prevented the development of safe and effective therapies to repair the injured spinal cord. To help unravel this complexity, we established the *Tabulae Paralytica*—a resource comprising multimodal single-cell and spatial atlases of SCI. We profiled single-nucleus RNA expression in more than 400,000 cells, spanning 18 experimental conditions that captured the most commonly studied manipulations in basic and translational research on SCI that could be made accessible for these experiments. We simultaneously profiled the dynamics of chromatin accessibility and gene expression in a further 40,000 cells to expose the regulatory programs that direct the response to injury. To circumscribe these responses within the cytoarchitecture of the injured spinal cord, we generated a spatial transcriptomic atlas of the injury that we extended into four spatial and temporal dimensions. We merged these atlases into a combined atlas to provide an unprecedented window into the genome-wide molecular cascade that unfolds after an injury to the spinal cord—from epigenetic regulation, to transcriptional programs within individual cells, to spatially- and temporally-dependent multicellular responses—that we overlaid onto a four-dimensional model of the spinal cord.

The *Tabulae Paralytica* provide a resource that not only allowed us to resolve outstanding questions within the field of SCI, but also exposed previously unknown biological principles. For example, we revealed a dichotomy between the early-conserved and late-diverging neuronal responses to SCI, the latter of which reflect differential capacity for circuit reorganization across neuronal subpopulations. We found that this capacity is encoded in the basal transcriptional repertoires of each subpopulation prior to SCI, implying that specific neuronal subpopulations are primed to become circuit-reorganizing neurons after injury. Moreover, we show that the ability of neuronal subpopulations to contribute to recovery entails an inherent trade-off between the activation of cel-

**Supplementary Fig. 47d-e**, and **Supplementary Video 3**).

Together, these findings demonstrate that interventions that augment the tripartite neuroprotective barrier and thereby maintain the immune-privileged environment of the spinal cord can prevent the catastrophic neural damage resulting from SCI in aged subjects.

## Discussion

SCI triggers a coordinated cascade of cellular and molecular responses, whose spatiotemporal complexity has thus

lular stress responses versus that of transcriptional programs involved in circuit reorganization. We also demonstrate that the profound impairment of neurological recovery after SCI in old mice reflects a failure to coordinate the formation of a tripartite neuroprotective barrier between immune-privileged neural tissue and extra-neural lesion environments. This failure leads to overwhelming immune infiltration and catastrophic neuronal death into neural tissue, precluding neurological recovery. We built on this discovery to develop a new gene therapy strategy that reactivated border-forming cells, prevented lesion expansion, and improved neurological recovery in old mice. This mechanism-based therapeutic strategy opens new avenues to accelerate wound repair and increase neurological recovery in humans with SCI.

The *Tabulae Paralytica* embody a number of technological and conceptual advances that demonstrate how genome-wide single-cell and spatial technologies can deliver new insights into uninjured and perturbed tissues. On a conceptual level, we demonstrate how the increasing scale of single-cell technologies enables a comprehensive interrogation of the experimental manipulations relevant to any given disease within a single study. On a technical level, we establish the possibility of extending spatial transcriptomics into three and even four spatial and temporal dimensions within a common coordinate framework. Moreover, we show that the integration of multi-omic single-cell atlases allows us to overlay patterns of chromatin accessibility onto a four-dimensional spatial model. Finally, our findings illustrate the power of cell type and spatial prioritization, as implemented by Augur and Magellan, to resolve the molecular basis of diseases or biological perturbations using single-cell and spatial genomics.

The *Tabulae Paralytica*, or 'atlases of spinal cord injury,' will serve as (i) a foundational resource to understand the pathobiology of SCI; (ii) a reference of cellular and molecular responses to predict and interrogate the consequences of new therapeutic strategies; (iii) a conceptual and technical framework to advance spatially resolved single-cell studies of disease and biological perturbations; and (iv) a translational resource to uncover new biological mechanisms of SCI that can be exploited to develop therapies to repair the injured human spinal cord.

# Methods

**Mouse model and experimental conditions.** Adult male or female C57BL/6 mice (15-25 g body weight, 8-15 weeks of age) or transgenic mice were used for all experiments. Aged mice were purchased from JAX at 60 weeks of age (stock no. 000664). Vsx2$^{Cre}$ (MMMRRC 36672, also called Chx10$^{Cre}$) transgenic mouse strain was bred and maintained on a mixed genetic background (C57BL/6). Housing, surgery, behavioral experiments and euthanasia were all performed in compliance with the Swiss Veterinary Law guidelines. Manual bladder voiding and all other animal care was performed twice daily throughout the entire experiment. All procedures and surgeries were approved by the Veterinary Office of the Canton of Geneva (Switzerland; authorizations GE/145/2). Spinal cord crushes were performed as previously described[15,63]. For time-course experiments, animals were euthanised at 1 day, 4 days, 7 days, 14 days, 1 month, or 2 months post-injury. Crush injuries were performed at multiple severities by including spacers within No. 5 Dumont forceps (Fine Science Tools) such that when closed, there was a maximal distance of 1 mm, 0.5 mm, 0.25 mm, or 0 mm (no spacer) with a tip width of 0.5 mm. Dorsal hemisection SCIs were performed as previously described[12]. For dorsal hemisection SCI, a laminectomy was made at the mid-thoracic level (T10) and the dorsal half of the spinal cord was cut using a microscapel. Contusion SCIs were performed as previously described[9,64].

Minocycline was administered with intraperitoneal injections as previously described[73–75], with a loading dose of 50 mg/kg at 1 h post-injury and 24 h post-injury, followed by maintenance doses of 25 mg/kg every 24 h for the next five days. Methylprednisolone was administered intramuscularly as previously described[172], with a loading dose of 60 mg/kg at 1 h post-injury then an additional 30 mg/kg dose every 6 h for 24 h. Chondroitinase ABC was delivered via lentiviral injections as previously described[173]. Briefly, the *Proteus vulgaris* ChABC gene was previously modified to make a mammalian-compatible engineered ChABC gene[138]. The modified ChABC cDNA was subcloned into a lentiviral transfer vector (termed LV-ChABC) with the mouse phosphoglycerate kinase promoter[138]. The final viral titer was 479 $\mu$g/mL of P24, corresponding to ~10$^6$ TU/$\mu$L. A control lentiviral vector (termed LV-GFP) was generated from the same transfer vector containing the cDNA coding for GFP, with a viral titer of 346 $\mu$g/mL of P24.

**Viral vectors and vector production.** Viruses used in this study were either acquired commercially or produced at the EPFL core facility. The following AAV plasmids were used and detailed sequence information is available as detailed or upon request: AAV-CAG-flex-human Diphtheria Toxin Receptor (DTR, plasmid gifted by Prof. S. Arber), and produced as AAV5 at the EPFL Bertarelli Foundation Platform in Gene Therapy and SIN-cPPT-PGK-FGF2-WPRE,SIN-cPPT-PGK-EGF-WPRE SIN-cPPT-PGK-VEGF-WPRE, SIN-cPPT-GFAP-GDNF-WPRE, and LV-PGK-ChABC (gifted by Prof. E. Bradbury). Injection volumes, coordinates and experimental designs are described below.

**Biological repair intervention in aging mice.** General surgical procedures have been previously described in detail[15,63,64]. Surgeries were performed at EPFL under aseptic conditions and under 1-2% isoflurane in 0.5-1 L/min flow of oxygen as general anesthesia, using an operating microscope (Zeiss) and rodent stereotaxic apparatus (David Kopf) as previously described[63,64]. LV injections were made two days before SCI to allow time for expression, and were targeted over the intended spinal cord segment to be injured. LVs were injected into four sites (two sets of bilateral injections, 0.30 $\mu$L/injection [all vectors diluted to 600 $\mu$g P24/mL in sterile saline]) 0.6 mm below the surface at 0.15 $\mu$L per minute using glass micropipettes connected via high-pressure tubing (Kopf) to 10 $\mu$L syringes under the control of a microinfusion pump. Moderate crush SCIs were introduced at the level of T10/T11 after laminectomy of a single vertebra by using No. 5 Dumont forceps (Fine Science Tools) with a spacer so that when closed a 0.5 mm space remained, and with a tip width of 0.5 mm to completely compress the entire spinal cord laterally from both sides for 5 s. After surgeries, mice were allowed to wake up in an incubator. Analgesia, buprenorphine (Essex Chemie AG, Switzerland, 0.01-0.05 mg/kg s.c.) or carprofen (5 mg/kg s.c.), was given twice daily for 2-3 days after surgery. Animals were randomly assigned numbers and thereafter were evaluated blind to experimental conditions. Fourteen days after SCI, all mice were evaluated in an open field and all animals exhibiting any hindlimb movements were not studied further.

**Neuron subpopulation-specific ablation.** For ablation experiments with diphtheria toxin, Vsx2$^{Cre}$ mice were subjected to crush SCI as described above. Three sets of bilateral injections of AAV5-CAG-FLEX-DTR[174] were made over the T9, T10, and T11 spinal segments (0.25 $\mu$L per injection) at a depth of 0.6 mm below the dorsal surface and separated by 1 mm. Two weeks after spinal infusions, mice received intraperitoneal injections of diphtheria toxin (Sigma, D0564) diluted in saline (100 $\mu$g/kg) to ablate Vsx2 neurons. Kinematics were evaluated in all mice before ablation, one week, and two-weeks post-ablation.

**Behavioural assessments.** Behavioral procedures have been previously described in detail[64,174,175]. Briefly, during overground walking, bilateral leg kinematics were captured with twelve infrared cameras of a Vicon Motion Systems (Oxford, UK) that tracked reflective markers attached to the crest, hip, knee, ankle joints, and distal toes. The limbs were modelled as an interconnected chain of segments and a total of 80 gait parameters were calculated from the recordings. To evaluate differences between experimental conditions, as well as to identify the most relevant parameters to account for these differences, we implemented a multistep multifactorial analysis based on principal component analysis, as previously described in detail[9,64,174], and coupled to automated, markless tracking software[176].

**Perfusions.** Mice were perfused at the end of the experiments. Mice were deeply anesthetized by an intraperitoneal injection of 0.2 mL sodium pentobarbital (50 mg/mL). Mice were transcardially perfused with PBS followed by 4% paraformaldehyde in PBS. Tissue was removed and post-fixed overnight in 4% paraformaldehyde before being transferred to PBS or cryoprotected in 30% sucrose in PBS.

**Immunohistochemistry.** Immunohistochemistry was performed as previously described[15,63,64]. Perfused post-mortem tissue was cryoprotected in 30% sucrose in PBS for 48 h before being embedded in cryomatrix (Tissue Tek O.C.T., Sakura Finetek Europe B.V.) and freezing. 30 $\mu$m thick transverse or horizontal sections of the spinal cord were cut on a cryostat (Leica), immediately mounted on glass slides and dried or in free floating wells containing PBS plus 0.03% sodium azide. Primary antibodies were: rabbit anti-GFAP (1:1000; Dako); guinea pig anti-NeuN (1:300; Millipore); chicken anti-RFP (1:500, Novus Biologicals); rabbit anti-Chx10 (also known as Vsx2) (1:500, Novus Biologicals); rat anti-CD45 (1:100, BD Biosciences); goat anti-Sox9 (1:200, Novus Biologicals); rabbit anti-Id3 (1:500; Cell Signalling Technology); rabbit anti-PKD1L2 (1:1000; Merck Millipore); mouse anti-GFAP (1:1000; MARK). Fluorescent secondary antibodies were conjugated to Alexa 488 (green), or Alexa 405 (blue), or Alexa 555 (red), or Alexa 647 (far red) (ThermoFisher Scientific, USA). The nuclear stain was 4',6'-diamidino-2-phenylindole dihydrochloride (DAPI; 2 ng/mL; Molecular Probes). Sections were imaged digitally using a slide scanner (Olympus VS-120 Slide scanner) or confocal microscope (Zeiss LSM880 + Airy fast module with ZEN 2 Black software). Images were digitally processed using ImageJ (ImageJ NIH) software or Imaris (Bitplane, version 9.0.0).

**Tissue clearing (CLARITY).** Samples were incubated in X-CLARITY hydrogel solution (Logos Biosystems Inc., South Korea) for 24 h at 4°C with gentle shaking. Samples were then degassed and polymerized using the X-CLARITY Polymerisation System (Logos Biosystems Inc., South Korea), followed by washes in 0.001 M PBS for 5 minutes at room temperature. Samples were next placed in the X-CLARITY Tissue Clearing System (Logos Biosystems Inc., South Korea), set to 1.5 A, 100 RPM, 37°C, for 29 h. Clearing solution was made in-house with 4% sodium dodecyl sulfate (SDS), 200 mM boric acid with dH$_2$O, pH adjusted to 8.5. Following this, samples were washed for at least 24 h at room temperature with gentle shaking in 0.1 M PBS solution containing 0.1% Triton X-100 to remove excess SDS. Finally, samples were incubated in 40 g of Histodenz dissolved in 30 mL of 0.02 M PB, pH 7.5, 0.01% sodium azide (refractive index 1.465) for at least 24 h at room temperature with gentle shaking prior to imaging.

**3D imaging.** Imaging of cleared tissue was performed using a customized mesoSPIM[177] and CLARITY-optimized light-sheet microscope (COLM)[178]. A custom-built sample holder was used to secure the central nervous system in a chamber filled with RIMS. Samples were imaged using either a 1.25× or 2.5× objective at the mesoSPIM and a 4× or 10× objective at the COLM with one or two light sheets illuminating the sample from both the left and right sides. The voxel resolution in the x-, y- and z directions was 5.3 $\mu$m × 5.3 $\mu$m × 5 $\mu$m for the 1.25× acquisition and 2.6 $\mu$m × 2.6 $\mu$m × 3 $\mu$m for the 2.5× acquisition. The voxel resolution of the COLM was 1.4 $\mu$m × 1.4 $\mu$m by 5 $\mu$m. Images were generated as

16-bit TIFF files and then stitched using Arivis Vision4D (Arivis AG, Munich, Germany). 3D reconstructions and optical sections of raw images were generated using Imaris (Bitplane, version 9.0.0) software.

**Histological analysis.** To quantify immune invasion after different models of SCI, we measured the percentage of CD45 immunopositive area after binarizing the fluorescent signal using the image analysis software Fiji. To assess the formation of astrocyte scar borders after SCI in young and old mice, we counted the number of Sox9$^{ON}$ cells using the image analysis software QuPath and the cell detection functionality with default settings (version 0.4.3). We then classified Sox9$^{ON}$ cells as either Id3$^{ON}$ or Id3$^{OFF}$ by setting a mean signal intensity threshold. We used the same approach to count the number of NeuN$^{ON}$ and PKD1L2$^{ON}$ neurons, to assess the resilience of CSF-contacting neurons after SCI. To quantify the number of Vsx2$^{ON}$ neurons after neuronal subpopulation-specific ablation with DTR we used the image analysis software Imaris (Bitplane, version 9.0.0).

**Chronophotography.** Chronophotography was used to generate a representative series of still pictures arranged in a single photograph to illustrate the locomotor abilities of mice. Videos at 25 fps or photographs at 15 fps were recorded while mice were performing locomotor tasks such as quadrupedal walking on the runway. Images from these recordings were chosen to best illustrate the different consecutive phases of walking of the hindlimbs, i.e. stance phases and swing phases. The frequency of chosen pictures varied due to the varying velocity of the mice. The series of pictures were assembled in Photoshop while blending out non-essential details.

**snRNA sequencing library preparation.** Single-nucleus dissociation of the mouse lumbar spinal cord was performed according to our established procedures[9,60]. Following euthanasia by isoflurane inhalation and cervical dislocation, the lumbar spinal cord site was immediately dissected and frozen on dry ice. We denounced spinal cords in 250 $\mu$L sucrose buffer (0.32 M sucrose, 10 mM HEPES [pH 8.0], 5 mM CaCl$_2$, 3 mM Mg acetate, 0.1 mM EDTA, 1 mM DTT) and 0.1% Triton X-100 with the Kontes Dounce Tissue Grinder. 1.1 mL of sucrose buffer was then added and filtered through a 40 $\mu$m cell strainer. The lysate was centrifuged at 3200 g for 5 min at 4°C. The supernatant was decanted, and 1 mL of sucrose buffer added to the pellet and incubated for 1 min. The pellet was homogenized using an Ultra-Turrax and 3 mL of density buffer (1 M sucrose, 10 mM HEPES [pH 8.0], 3 mM Mg acetate, 1 mM DTT) was added below the nuclei layer. The tube was centrifuged at 3200 g at 4°C for 10 min and supernatant was immediately poured off. Nuclei on the bottom half of the tube wall were resuspended in 100 $\mu$L PBS with 1% BSA for subsequent single-nucleus RNA sequencing or in 10x Nuclei Buffer (catalog no. 2000153, 10x Genomics) for subsequent single-nucleus multiome sequencing. Resuspended nuclei were filtered through a 30 $\mu$m strainer, and adjusted to 1,000 nuclei/$\mu$L. We carried out snRNA-seq library preparation using the 10x Genomics Chromium Single Cell Gene Expression Kit Version 3.1. The nuclei suspension was added to the Chromium RT mix to achieve loading numbers of 10,000 nuclei. For downstream cDNA synthesis, library preparation and sequencing, the manufacturer's instructions were followed.

**Multiome sequencing library preparation.** We carried out snRNA- and ATAC library preparation using the 10x Genomics Chromium Single Cell Multiome ATAC + Gene Expression Kit. First, the transposition mix was added to the resuspended nuclei followed by a 60 min incubation at 37°C. The transposed nuclei were added to the Chromium RT mix to achieve loading numbers of 10,000 nuclei. The manufacturer's instructions were followed for downstream cDNA synthesis, library construction, indexing and sequencing.

**Spatial transcriptomics library preparation.** We carried out two separate experiments to study the cytoarchitecture of the lesion microenvironment after SCI. First, we prepared sections from uninjured mice, 7 days and 2 months after crush SCI (performed with a 0.5 mm spacer as described above). For each experimental condition, we prepared sections from the lesion epicenter of three independent biological replicates. Second, to prepare our four-dimensional spatiotemporal atlas, we collected sections throughout the entire spinal cord of mice from each of the three experimental conditions. The spinal cord injury sites of mice were embedded in OCT and cryosections were generated at 10 $\mu$m at −20°C. For the four-dimensional atlas, every fifth section was collected throughout the entire dorsoventral axis of each spinal cord. Sections were immediately placed on chilled Visium Tissue Optimization Slides (catalog no. 1000193, 10x Genomics) or Visium

Spatial Gene Expression Slides (catalog no. 1000184, 10x Genomics). Tissue sections were then fixed in chilled methanol and stained according to the Visium Spatial Gene Expression User Guide (catalog no. CG000239 Rev A, 10x Genomics) or Visium Spatial Tissue Optimization User Guide (catalog no. CG000238 Rev A, 10x Genomics). For gene expression samples, tissue was permeabilized for 12 min, which was selected as the optimal time based on tissue optimization time-course experiments. Brightfield histology images were taken using a 10× objective on a slide scanner (Olympus VS-120 Slide scanner). For tissue optimization experiments, fluorescent images were taken with a TRITC filter using a 10× objective and 400 ms exposure time. Libraries were prepared according to the Visium Spatial Gene Expression User Guide.

**Read alignment.** Following sequencing on our HiSeq4000 (EPFL Gene Expression Core Facility), snRNA-seq reads were aligned to the latest Ensembl release of the mouse genome (GRCm38.101), and a matrix of unique molecular identifier (UMI) counts was obtained using CellRanger (10x Genomics, version 4.0.0)[30]. For spatial transcriptomics, a spatial expression UMI count matrix was obtained using SpaceRanger (10x Genomics, version 1.0.0). For the multiome dataset, RNA-seq and ATAC-seq data were aligned to the reference genome using CellRanger-ARC (10x Genomics, version 2.0.0), and a matrix of UMI counts was obtained for the RNA modality. The ATAC modality was then processed further using ArchR, as described below.

**snRNA-seq preprocessing and quality control.** Droplet-based snRNA-seq experiments are known to be affected by ambient RNA contamination, whereby freely floating RNA molecules are encapsulated along with a cell or nucleus in a single droplet and spuriously attributed to the endogenous expression profile of the encapsulated cell[179]. The presence of ambient RNA is a potential source of batch effects and spurious differential expression. To mitigate this possibility, we used CellBender[180] to remove ambient RNA molecules and filter empty droplets. CellBender remove-background was run for 50 epochs with a learning rate of 5e-5. Corrected count matrices were then imported into Seurat[181] for further quality control. Quality control metrics included the number of UMIs per cell, the number of genes detectably expressed per cell, and the proportion of UMI counts arising from mitochondrial genes. For the pilot dataset, cells with between 200 and 40,000 UMIs, and less than 7,500 genes expressed, were retained. For the snRNA-seq and multiome datasets, cells with at least 200 UMIs were retained. Additional quality control was performed for the multiome dataset on the basis of the ATAC modality, as described further below. Low-quality libraries were identified as those with distributions of number of UMIs, number of genes expressed, or proportion of mitochondrial counts that differed markedly from the remainder of the libraries in the dataset, and a total of three low-quality libraries (two from the snRNA-seq dataset and one from the multiome dataset) were removed.

Putative doublets then were identified and filtered using a combination of approaches. We tested the performance of four computational methods for doublet detection in our pilot dataset, including DoubletFinder[182], scDblFinder[183], scds[184], and Scrublet[185]. On the basis of this analysis, we selected scDblFinder and scds as the two methods that (i) did not display an overt bias towards doublet detection for cells of any particular type, (ii) which showed the highest agreement with one another, and (iii) which were also found to be among the top-performing methods in an independent benchmark[186]. We adopted a conservative approach by filtering barcodes from the union of those called doublets by either scDblFinder or scds in both the pilot and snRNA-seq datasets. For the multiome dataset, doublets were instead identified and filtered using ArchR, as described below.

**Integration and cell type annotation.** Prior to clustering and cell type annotation, we first performed batch effect correction and data integration across experimental conditions using Harmony[158]. Gene expression counts were normalized to counts per 10,000 and log-transformed, and the top 2,000 variable genes were identified using the 'vst' method in Seurat. Gene expression values were then scaled and centered and provided as input to Harmony, which was run with 50 principal components. The integrated Harmony embeddings were then provided as input to k-nearest neighbor graph construction and Leiden clustering using the default Seurat workflow[181], as in our previous studies[9,60,87]. Cell types were then manually annotated on the basis of marker gene expression, guided by previous studies of the mouse spinal cord[47–57,59–61,87] and other relevant cell atlases of major cell types[93,102]. Local and projecting neuronal subpopulations were annotated on the basis of

*Nfib* and *Zfhx3* expression, respectively[59]. Clusters corresponding to damaged cells or doublets that had survived initial quality control were removed at this stage. In the pilot dataset, we performed an initial round of clustering to identify coarse cell types with a resolution of 0.05, followed by subclustering of neurons (resolution = 0.5) and glia (resolution = 0.1) to annotate more fine-grained subtypes. In the snRNA-seq dataset, we repeated the clustering analysis for multiple values of the resolution parameter (0.01, 0.05, 0.2, 0.5, 2) in order to annotate cell types across multiple resolutions (e.g. neurons → ventral neurons → ventral excitatory interneurons). We then used the clustree package[85] to link clusters across adjacent resolutions into a hierarchical clustering tree, as previously described[7,9,60].

**Pilot dataset and meta-analysis of published spinal cord snRNA-seq datasets.** We conducted an initial pilot experiment to confirm that our dissociation procedures enabled the recovery of all the cell types comprising the mouse spinal cord. snRNA-seq libraries were prepared from one uninjured mouse and one mouse 7 days after crush SCI, and deeply sequenced to a target depth of 100,000 reads per nucleus. After preprocessing and quality control as described above, we retained 9,170 nuclei from the injured sample and 9,099 nuclei from the uninjured sample. Following data integration and cell type annotation as described above, we confirmed that we recovered the major cell types of the spinal cord in both the injured and uninjured spinal cords, and that changes in cell type proportions across experimental conditions were concordant with the established pathophysiology of SCI. We then compared the cell type proportions in our pilot dataset to those in 16 published single-cell datasets from the mouse spinal cord[47-62]. Automated cell type annotation of published datasets was performed using the label transfer workflow in Seurat, with our own previously published dataset from the uninjured lumbar spinal cord[60] used as the reference. We confirmed that the label transfer workflow yielded reliable predictions by comparing automated cell type annotations to manual annotations from a published dataset[50]. This analysis established that our dissociation protocols allowed us to recover the major cell types of the spinal cord in proportions consistent with published single-nucleus RNA-sequencing studies of the whole adult spinal cord. Finally, we took advantage of our deeply sequenced pilot dataset to calibrate our target sequencing depth of our main experiments, and selected a target depth of 75,000 reads per nucleus on the basis of downsampling analysis of the pilot dataset.

**snRNA-seq atlas.** For the snRNA-seq dataset, preprocessing, quality control, data integration, and cell type annotation were performed as described above, yielding a dataset comprising 435,099 nuclei from 54 mice spanning 18 experimental conditions. Marker genes were identified for each cluster using the FindMarkers function in Seurat. We visualized the distribution of cell types, experimental conditions, and the expression of marker genes with UMAP embeddings of both the entire dataset as well as each major cell type. Marker gene dotplots were constructed using the DotPlot function in Seurat. Cell type proportions were visualized using sunburst plots[187] and Sankey diagrams. The cell cycle positions of astroependymal cells were estimated using tricycle[188]. The expression of a previously described gene module[101] associated with BBB dysfunction was estimated using the Seurat function AddModuleScore. Unless otherwise stated, all cell subtype analyses were performed at level 5 of the clustering tree (corresponding to a resolution of 2).

**Cell type proportions.** Testing for differences in cell type proportions within single-cell data can lead to false discoveries because the data is compositional in nature, and consequently, increases the proportion of one cell type can cause an artefactual decrease in the proportions of every other cell type[189]. To avoid this pitfall, we used the propeller method[190], as implemented in the speckle R package, to test for differences in cell type proportions between experimental conditions, as an independent benchmark showed this to be among the most accurate methods in balancing control of the false discovery rate with statistical power[191]. The details of individual cell type proportion analyses are described below.

**Differential expression.** To identify genes differentially expressed between experimental conditions, we performed differential expression (DE) analysis by aggregating expression from all cells of a given type within each replicate into a 'pseudobulk' profile, as previously described[87] and implemented in the Libra R package, (https://github.com/neurorestore/Libra). In our previous work[87], we demonstrated that this approach allowed us to overcome false discoveries caused by variability between biological replicates[192]. We showed that widely-used single-cell DE methods can con-

flate this variability with the effect of a biological perturbation, leading to hundreds or even thousands of false discoveries. We therefore instead used the likelihood ratio test implemented in edgeR[193] to identify DE genes between pseudobulks from each cell type. The details of individual DE analyses are described below.

**GO enrichment analysis.** GO term annotations for mouse were obtained from the Gene Ontology Consortium website. GO terms annotated to less than five genes were excluded. The average expression level of genes associated with each GO term in individual cells was calculated using the Seurat function AddModuleScores, which controls for the average expression of randomly selected control features. Linear mixed models were then used to test for differences in GO module scores test across experimental conditions, using the 'lmerTest' R package to optimize the restricted maximum likelihood and obtain p-values from the Satterthwaite approximation for degrees of freedom. The details of individual GO enrichment analyses are described below.

**Cell type prioritization.** To identify cell types activated in response to each biological perturbation captured in the *Tabulae Paralytica*, we employed a machine-learning method for cell type prioritization that we previously developed, named Augur[9,60,127]. Briefly, Augur seeks to rank cell types based on the intensity of their transcriptional response to a biological perturbation. The key assumption underlying Augur is that cell types undergoing a profound response to a perturbation should become more separable, within the highly multidimensional space of gene expression, than less affected cell types. To quantify this separability, we framed this problem as a classification task. Augur first withholds a proportion of experimental condition labels, then trains a random forest classifier to predict the condition from which each cell was obtained (for instance, SCI or uninjured). The accuracy with which this prediction can be made from single-cell gene expression measurements is then evaluated in cross-validation, and quantified using the area under the receiver operating characteristic curve (AUC). This process is repeated separately for each cell type. The AUC then provides a quantitative measure of separability that can be used to rank cell types based on the relative magnitude of their response to an arbitrary perturbation. We refer to this process as cell type prioritization. Augur was run with default parameters directly on the UMI count matrix for all comparisons. To evaluate the robustness of cell type prioritizations to the resolution at which neuronal subtypes were defined in the snRNA-seq data, we applied Augur at various clustering resolutions, and visualized the resulting cell type prioritizations both on a hierarchical clustering tree[85] of cell types and as a progression of UMAPs[9]. The details of individual cell type prioritization analyses are described below.

**Conserved and divergent neuronal responses to SCI.** To identify spinal cord neurons that were resilient or susceptible to SCI, we computed the $\log_2$-odds ratio between the uninjured spinal cord and each experimental condition in which the injured spinal cord was profiled at 7 days post-injury, using neuron subtypes defined at level 4 of the clustering tree (corresponding to a resolution of 0.5), then identified resilient or susceptible neuron subtypes using a t-test on the $\log_2$-odds ratios. To identify DE genes specific to CSF-contacting neurons at the most acute phase of the injury response, we used edgeR to test for an interaction term between neuronal subtype and experimental condition at 1 day post-injury, using pseudobulk gene expression profiles.

To quantify the degree to which transcriptional responses to injury were conserved across neuron subtypes, we computed the Spearman correlation between log-fold changes estimated by edgeR between each pair of level 4 neuron subtypes. For genes that were not quantified in one of the two subtypes, missing log-fold change values were replaced with zeros.

To characterize the conserved early response of neurons to SCI, we first filtered to genes that were differentially expressed within individual level 4 neuron subtypes at a 10% false discovery rate. We then sorted these genes first by the number of neuron subtypes in which they were DE, and second by the mean absolute log-fold change estimated by edgeR.

To quantify the expression of transcriptional programs associated with projection growth and morphogenesis, we used the average expression of genes associated with the GO term "GO:0031175" (neural projection development) to construct a circuit reorganization score, as described above. We then computed the basal expression of this circuit reorganization score as the median GO module score in the uninjured spinal cord for each level 4 neuron subtype. To quantify upregulation of the circuit reorganization score after injury, we subtracted the basal expression score from the GO module

score at each timepoint post-injury to yield induced expression scores. We then calculated the Pearson correlation between basal and induced circuit reorganization scores. We carried out similar analyses for the GO terms "GO:0061564" (axon development) and "GO:0016358" (dendrite development).

Cell type prioritization was performed by comparing neurons from each level 4 subtype at each timepoint post-injury to neurons from the uninjured spinal cord.

**Neurons remain differentiated after CNS injury.**    Individual marker genes for each neuron subtype were manually curated from literature after cross-referencing with other atlases, as described above. DE analysis was performed by comparing neurons from each level 4 subtype at each timepoint post-injury to neurons from the uninjured spinal cord using edgeR as described above, with a 5% false discovery rate. We also constructed unbiased lists of the top-$n$ marker genes for each level 4 neuron subtype (for $n = 5$, 10, or 50) using the FindMarkers function in Seurat. We used the AddModuleScore function to summarize the average expression of the top-$n$ marker genes in each individual neuron, then used a linear mixed model to test for differences across experimental conditions as described above for GO enrichment analyses.

**Facilitating and inhibiting molecule expression in the injured spinal cord.**    We visualized the expression of key facilitating and inhibiting molecules across the cell types and subtypes of the spinal cord using clustering trees, with the scaled mean expression for each cell type or subtype calculated as in the Seurat function DotPlot. To identify genes coordinately up- or downregulated across level 4 neuron subtypes in response to ChABC treatment, we used edgeR to perform DE analysis as described above, and performed a one-sample t-test on log-fold change estimates from edgeR[9]. We then used linear mixed models to perform GO enrichment analysis of ChABC treatment for each level 4 neuron subtype, as described above, and performed a one-sample t-test on coefficients estimated by the mixed models.

**Cellular divergence between animal models of SCI.**    Cell type proportions were compared using propeller, as described above, both for coarse cell types and for the most fine-grained subtypes of immune cells. Cell type prioritization was performed by comparing neurons from each level 4 subtype between each pair of animal models (crush, contusion, or hemisection). Separately, we tested for differences in the AUCs of dorsal and ventral level 4 neuron subtypes by comparing neurons from mild, moderate, severe, or complete injuries to neurons from the uninjured spinal cord.

**Immunomodulation does not confer neuroprotection after spinal cord injury.**    Cell type prioritization was performed by comparing cell types at each resolution of the clustering tree from drug-treated and untreated but injured spinal cords. The proportions of coarse cell types were compared using propeller as described above.

To dissect more subtle transcriptional effects of neuroprotective agents on surviving neurons, we developed a machine-learning approach to identify neurons displaying an uninjured transcriptional phenotype. For each experimental condition involving injured and untreated mice (i.e., excluding the uninjured and drug-treated conditions), we trained a random forest model on scaled and log-normalized gene expression data to distinguish cells from that condition ("injured" cells) to cells from the uninjured spinal cord ("uninjured" cells). We then applied each of these models in turn to neurons from the methylprednisolone and minocycline conditions, in order to predict whether they displayed an injured or uninjured phenotype. The modal prediction across all models was then assigned to each neuron. To further characterize the transcriptional programs induced by neuroprotective agents, we then used linear mixed models to perform GO enrichment analysis of methylprednisolone or minocycline treatment for each level 4 neuron subtype, as described above, and performed a one-sample t-test on coefficients estimated by the mixed models.

**Sexually dimorphic responses to SCI are subtle.**    Cell type prioritization was performed by comparing cell types at each resolution of the clustering tree from male and female spinal cords. The range of AUC values assigned by Augur in cross-validation was then compared to that observed in other comparisons involving the injured spinal cord at 7 days post-injury. Cell type proportions were compared using propeller, as described above, both for coarse cell types and for the most fine-grained subtypes of immune cells.

**Catastrophic failure of tripartite barrier formation in old mice.**    Cell type prioritization was performed by comparing cell types at each resolution of the clustering tree from young and old mice, and the range of AUC values assigned by Augur in cross-validation was again compared to that observed in other comparisons involving the injured spinal cord at 7 days post-injury. The proportion of *Id3*-expressing astrocytes was compared between young and old mice using a $\chi^2$ test. Gene modules associated with blood-brain barrier endothelial cell identity and peripheral endothelial cell identity were obtained from the literature[101], and their expression in individual vascular cells was calculated using the Seurat function AddModuleScore.

DE analysis was performed as described above by comparing cells from young and old mice after SCI, for cell subtypes at level 4 of the clustering tree (resolution = 0.5) and with a false discovery rate of 5%. To quantify the heterogeneity of gene expression across cell types, we calculated two summary statistics. First, we defined the direction consistency as the proportion of cell types in which the sign of the log-fold change was the same as the modal sign. For example, if a gene was upregulated in eight of ten cell types and downregulated in the other two, the direction consistency would be 80%. Second, we defined the response heterogeneity as the standard deviation of the log-fold change across cell types.

**snATAC-seq preprocessing and quality control.**    Preprocessing and quality control of the ATAC modality within our multiome dataset was carried out using CellRanger-ARC and ArchR[157]. Reads were mapped to the reference genome with CellRanger-ARC, and arrow files were created from the resulting fragment files. Nuclei were first filtered based on the RNA modality as described above, and subsequently additional quality control was performed in ArchR. We initially ran ArchR with very lenient filtering in order to determine optimal quality control parameters (minimum TSS enrichment score = 0, minimum fragments per cell = 100), and selected optimal parameters based on the joint distribution of these parameters. Arrow files were subsequently regenerated after filtering nuclei to those with a minimum TSS enrichment score of 4 and a minimum of 4,000 fragments per cell. Doublet detection and filtering was performed using the ArchR functions addDoubletScores and filterDoublets, both with default parameters. These steps afforded matrices of 40,526 nuclei that passed quality control in both the RNA and ATAC modalities.

To link cell types in the multiome dataset to the cellular taxonomy derived from our snRNA-seq atlas, we devised a hierarchical label transfer strategy using Symphony[158]. Briefly, we first used Symphony to perform automated cell type assignment in the multiome dataset at the highest level of the clustering tree (level 1, resolution = 0.01). We then used Symphony to perform automated cell type assignment at the second level of the clustering tree (resolution = 0.05), considering only subtypes of the assigned coarse cell types as potential matches for each nucleus. This process was repeated iteratively for each level of the clustering tree. We validated the accuracy of this strategy using a leave-library-out cross-validation approach within the snRNA-seq atlas, in which entire libraries were withheld from the atlas and automated cell type assignment was compared to the manual cell type assignment derived from the entire dataset. We found that the hierarchical approach improved the accuracy of automated cell type assignment relative to a non-hierarchical version of the same approach, in which all cell subtypes at any given level were considered as potential matches, particularly at more granular levels of the clustering tree. For cell type assignment in the multiome dataset, we ran Symphony using the hierarchical approach with 100 soft cluster centroids, 100 principal components, and 20 nearest-neighbors, then made additional manual adjustments to cell type annotations for a handful of cell subtypes that showed discordant marker gene expression.

Peak calling in the snATAC-seq dataset was then carried out using the default ArchR workflow, including peak calling with MACS2[194] on pseudobulk replicates from each cell type, followed by peak merging across cell types using an iterative overlap removal procedure. We repeated this process for cell type definitions at each level of the clustering tree and found that peak calling at more granular resolutions allowed us to preferentially detect distal regulatory elements. Unless otherwise noted, downstream analyses were carried out on the peak matrix called with coarse cell type definitions (level 1, resolution = 0.01).

**Transcription factor activities.**    Transcription factor deviations were estimated by chromVAR[159], using motif sets from the chromVAR package (ENCODE, HOMER, and CisBP) as well as the 2020 version of JASPAR[195]. Transcription factor motifs associated with cell type identity were identified using a Wilcoxon rank-sum test, as in the Seurat function FindMarkers.

Linear mixed models were used to identify transcription factor motifs differentially active in cells from injured spinal cords, using the 'lmerTest' R package to optimize the restricted maximum likelihood and obtain p-values from the Satterthwaite approximation for degrees of freedom, and a false discovery rate of 10%.

To identify transcription factors that were up- or downregulated across all level 4 neuron subtypes at 7 days post-injury, we performed a one-sample t-test on coefficients estimated by the mixed models. To identify transcription factors with discordant patterns of up- or downregulation at 2 months post-injury, we devised a permutation-based statistical approach. Neuron subtype assignments at level 4 of the clustering tree were randomized within each experimental condition, and differential activity testing was performed using linear mixed models in the permuted data. This process was repeated 100 times, and the standard deviation of model coefficients was calculated for the observed and permuted datasets. The resulting z statistics were then converted to p-values using a standard normal distribution and significantly divergent motifs were identified using a 10% false discovery rate.

To identify transcription factors associated with dysfunction of the tripartite barrier after SCI, BBB dysfunction module scores[101] were first estimated from the RNA modality of the multiome data, as in the snRNA-seq atlas. chromVAR deviations in the ATAC modality were then correlated to the resulting module scores, using the Pearson correlation and restricting this analysis to vascular cells. Linear mixed models were then used to identify motifs that were differentially accessible at 7 days in level 4 subtypes associated with the tripartite barrier, including vascular leptomeningeal cells, capillary endothelial cells, pericytes, arachnoid barrier cells, reactive astrocytes, and OPCs. Analyses of differentially active transcription factors in neurons or blood-brain barrier cell types were carried out using chromVAR deviation matrices derived from peak matrices at the relevant resolution of the clustering tree, as described above.

**Differential accessibility.** To identify differentially accessible peaks, we extended the workflow for pseudobulk DE analysis in Libra to peak count matrices derived by ArchR. Cells of each type were aggregated within replicates to form pseudobulks, and then testing for differential accessibility was performed using the likelihood ratio test implemented in DESeq2[196]. The evolutionary conservation of each peak was quantified as the mean phyloP conservation score from the 60-way vertebrate data set[165] of all bases within the peak. The evolutionary conservation of all peaks open within a given cell was further summarized by taking the mean phyloP score across all accessible peaks in that cell.

**Evolutionary divergence in circuit reorganization.** The expression of cellular stress response programs in the snRNA-seq atlas was estimated by using the Seurat function AddModuleScore to summarize the mean expression of genes associated with the GO term GO:0033554 ("cellular response to stress"). The resulting score was then correlated with the circuit reorganization score described above across all neurons.

**Spatial transcriptomics preprocessing and quality control.** Following read alignment and count matrix generation with SpaceRanger as described above, Seurat[181] was used to calculate quality control metrics for each spatial barcode, including the number of genes detected, number of UMIs, and proportion of reads aligned to mitochondrial genes. Low-quality barcodes were filtered by removing those with less than 3,000 or more than 45,000 UMIs. Low-quality sections were identified as those with distributions of number of UMIs, number of genes expressed, or proportion of mitochondrial counts that differed markedly from the remainder of the sections in the dataset, and removed. In the two-dimensional spatial dataset, these steps afforded a UMI count matrix comprising 33,941 spatial barcodes from nine biological replicates (three from each experimental condition). In the three-dimensional spatial dataset, these steps afforded a UMI count matrix comprising 37,558 spatial barcodes from three biological replicates (one from each experimental condition).

**Registration to a common coordinate framework.** We aligned all spatial transcriptomics sections into a common coordinate system using a custom image analysis pipeline that includes preprocessing, registration and combination of histological images from different sections, aspects of which have been previously described[9]. In brief, we implemented image preprocessing in Fiji, and registration procedures in R, using the image analysis package 'imager'. Segmentation of the histological sections and associated spatial barcodes from background was achieved using a custom macro in Fiji. Segmented sections were then aligned using imager. Image registration

was performed manually using the tissue structure to guide registration, as captured by (i) histological images, (ii) quality control statistics (e.g., % of mitochondrial counts), (iii) marker genes for coarse cell types and dorsoventral or rostrocaudal transcription factors (e.g., *Ebf1*, *Esrrg*, *Hox* genes), and (iv) unsupervised clustering of the spatial barcodes, as implemented within Seurat.

**Visualization.** Quality control metrics and marker gene expression were smoothed prior to visualization on the two-dimensional spinal cord using locally weighted regression, as implemented in the RCTD package[167]. Visualization of the three-dimensional spinal cord was achieved with Imaris (Bitplane, version 9.0.0). Briefly, the three-dimensional spatial transcriptomics data was binned along the z-dimension into slices of 10 $\mu$m. Within each slice, quantitative values (quality control metrics, gene expression, gene module scores, and chromVAR deviations) were smoothed using three-dimensional locally weighted regression. When multiple quantitative values were assigned to a single spatial coordinate (for example, when performing spatial prioritization on snRNA-seq barcodes embedded via Tangram), the mean value at each coordinate was assigned, with the exception of the expression of individual genes, for which the maximum value at each coordinate was assigned instead. Each barcode was then assigned a size of 3 pixels, and the resulting slices were exported as 16 bit grayscale TIFF files using imager for import into Imaris. Separate reconstructions of the three-dimensional spinal cord volume were performed for each experimental condition in the spatiotemporal atlas (that is, uninjured, 7 days, and 2 months).

**Differential expression.** To identify genes differentially expressed between regions in the injured spinal cord within the two-dimensional spatial dataset, we extended the workflow for pseudobulk DE analysis in Libra to spatial count matrices derived by SpaceRanger. Cells from each region were aggregated within replicates to form pseudobulks, and then testing for DE was performed using the likelihood ratio test implemented in edgeR[193]. DE analysis was performed separately for spinal cord regions at 7 days and 2 months post-injury. DE gene expression was visualized on the two-dimensional spinal cord using two-dimensional locally weighted regression, as implemented in the RCTD package[167].

Cell type deconvolution. To integrate our snRNA-seq atlas with the two- and three-dimensional spatial atlases, we used RCTD[167] to deconvolve spatial barcodes into a mixture of one or more cell types, while accounting for technical differences between single-nucleus and spatial transcriptomes. RCTD was run with doublet mode disabled, allowing each barcode to potentially contain more than two cell types, separately for cell type definitions at level 1 and 2 of the clustering tree. We recovered smoothed patterns of cell type abundance by two-dimensional locally weighted regression of deconvolution weights, as described by the authors of RCTD[167]. Separately, a single cell type was assigned to each spatial barcode by taking the maximum deconvolution weight assigned by RCTD for that barcode. For cell type definitions at level 2 of the clustering tree, only subtypes of the assigned level 1 cell types were considered as potential matches for each spatial barcode.

**Spatial prioritization with Magellan.** To characterize the spatial response to SCI in an unbiased manner, we employed a machine-learning method spatial prioritization that we recently developed, named Magellan[9]. Magellan builds on the concept of transcriptional separability that provides a basis for cell type prioritization in Augur, as described above. However, in spatial transcriptomics data, the analytical level of interest is not necessarily a cell type, but rather a coordinate within a two- or three-dimensional tissue. To approach the data at this level, we sought to evaluate the transcriptional separability between barcodes from two experimental conditions at each point within a common coordinate system. We reasoned that we could achieve this by evaluating the separability of barcodes from each condition within small, overlapping tiles, layered across the spatial coordinate system. Briefly, for each barcode in a spatial transcriptomics dataset, Magellan selects the $k$ nearest neighbors from each experimental condition within common coordinate space, where $k$ is set to 20 by default. Then, Magellan withholds the experimental condition labels for a proportion of these neighbors, and trains a random forest classifier to predict the experimental condition given the remaining barcodes as input. The accuracy of these predictions is evaluated in the withheld barcodes, and the process is repeated in three-fold cross-validation. As in Augur, the accuracy is quantified using the AUC. The cross-validation is repeated several times (by default, 50 times) in order to converge at a robust estimate of the AUC. The entire procedure is

repeated for each barcode in the dataset, providing a spatial map of the AUC over the coordinate system of the spatial transcriptomes.

Magellan was used to perform spatial prioritization in the two-dimensional spatial dataset by comparing registered spatial transcriptomes from each pair of experimental conditions (uninjured, 7 days, 2 months). To visualize the intensity of the perturbation response, the spatial AUC was smoothed by two-dimensional locally weighted regression. In addition, we performed a one-dimensional locally weighted regression to visualize the intensity of the perturbation response along the rostrocaudal axis of the spinal cord.

To more carefully dissect the transcriptional basis of the perturbation response detected by Magellan, we tested for correlation between gene expression and the AUC of spatial prioritization. Briefly, we filtered the UMI count matrix within each comparison to include only genes detected in at least 100 spatial barcodes, and then computed Pearson correlations between scaled and log-normalized gene expression vectors and the AUCs returned for each barcode by Magellan. We further identified genes that were differentially correlated with the AUCs at 7 days and 2 months by testing for differential correlations using the Fisher z-transformation, adapting code from the DGCA R package[197]. We extended this concept by computing module scores for GO terms for each spatial barcode with the Seurat function AddModuleScore, as described above, and testing for significant correlations between GO module scores and the AUCs returned by Magellan. As in the DE analysis, the expression of genes or GO modules correlated or anticorrelated with the AUC of spatial prioritization was visualized on the two-dimensional spinal cord using two-dimensional locally weighted regression.

**Integration of the *Tabulae Paralytica*.** To integrate all of the four *Tabulae* into a single framework, we leveraged Tangram[170] to to embed single-nucleus transcriptomes and epigenomes onto the common coordinate system established by our four-dimensional atlas of the mouse spinal cord. Alignment of single-cell barcodes into the spatiotemporal atlas was performed separately for each experimental condition in the snRNA-seq and multiome atlases, using the most similar condition in the spatiotemporal atlas as a reference (e.g., aligning cells from 14 days to the spatiotemporal atlas at 7 days and cells from 1 month to the spatiotemporal atlas at 2 months). Tangram was run with the top 500 highly variable genes for each cell type and using cell type definitions at level 4 of the clustering tree.

This procedure assigned x-, y-, and z-coordinates to each nuclei in the snRNA-seq and multiome atlases. We then employed Magellan to perform three-dimensional spatial prioritization on the spatialized single-cell data, using the coordinates assigned by Tangram for each barcode. Spatialized cells from each injury severity were compared to those from uninjured mice. Separately, spatialized cells from old mice were compared to those from injured young mice at the same timepoint. Moreover, we again tested for correlation between gene expression in spatialized cells and the AUC of three-dimensional spatial prioritization.

Gene modules associated with blood-brain barrier endothelial cell identity and peripheral endothelial cell identity were obtained from the literature[101], and their expression in spatial barcodes was calculated using the Seurat function AddModuleScore. Similarly, we used the average expression of genes associated with the GO term "GO:0031175" (neural projection development) to construct a circuit reorganization score, as described above for the snRNA-seq atlas, and visualized the expression of this score in spatialized neurons from the snRNA-seq atlas. Last, to summarize the expression of the conserved early response module in neurons, we selected the top 25 genes that were upregulated in the greatest number of level 4 neuron subtypes and with the greatest mean log-fold change at 4 days post-injury, and used the Seurat function AddModuleScore to summarize the expression of this gene module.

Transcription factor accessibility at 7 days was visualized on the four-dimensional atlas by first embedding individual nuclei from multiome atlas onto the three-dimensional coordinate system of the spinal cord, and then visualizing chromVAR deviations from linked epigenomes for each nucleus.

**Statistics, power calculations, group sizes, reproducibility, visualization.** Statistical evaluations of repeated measures were conducted by one-way ANOVA with post hoc independent pairwise analysis as per Tukey's HSD. For all photomicrographs of histological tissue, staining experiments were repeated independently with tissue from at least four, and in most cases six, different animals with similar results.

**Data availability.** Sequencing data have been deposited to the Gene Expression Omnibus (GSE234774 [reviewer access token: adspcgiwrvwxnsf],

snRNA-seq and spatial transcriptomics, and GSE230765 [reviewer access token: gdalmmoiplcbtyt], multiome).

**Author contributions.** J.W.S., J.B., M.V.S., M.A.A., M.A.S., and G.C. conceived and designed experiments. J.W.S., M.A.A., C.K., M.G., T.H.H., A.L., A.d.C., N.R., V.A., and N.D.J. conducted experiments. J.W.S., M.A.S., M.G., Q.B., and Y.Y.T. analyzed the data. B.S. contributed essential resources. J.W.S., M.A.S., M.A.A., and G.C. wrote the manuscript. All authors contributed to the editing of the manuscript.

# References

1. Courtine, G. & Sofroniew, M. V. Spinal cord repair: advances in biology and technology. *Nat. Med.* **25,** 898–908 (2019).
2. Anderson, M. A. *et al.* Natural and targeted circuit reorganization after spinal cord injury. *Nat. Neurosci.* **25,** 1584–1596 (2022).
3. Ahuja, C. S. *et al.* Traumatic spinal cord injury. *Nat. Rev. Dis. Primers* **3,** 1–21 (2017).
4. Harkema, S. *et al.* Effect of epidural stimulation of the lumbosacral spinal cord on voluntary movement, standing, and assisted stepping after motor complete paraplegia: a case study. *Lancet* **377,** 1938–1947 (2011).
5. Gill, M. L. *et al.* Neuromodulation of lumbosacral spinal networks enables independent stepping after complete paraplegia. *Nat. Med.* **24,** 1677–1682 (2018).
6. Wagner, F. B. *et al.* Targeted neurotechnology restores walking in humans with spinal cord injury. *Nature* **563,** 65–71 (2018).
7. Squair, J. W. *et al.* Neuroprosthetic baroreflex controls haemodynamics after spinal cord injury. *Nature* **590,** 308–314 (2021).
8. Rowald, A. *et al.* Activity-dependent spinal cord neuromodulation rapidly restores trunk and leg motor functions after complete paralysis. *Nat. Med.* **28,** 260–271 (2022).
9. Kathe, C. *et al.* The neurons that restore walking after paralysis. *Nature* **611,** 540–547 (2022).
10. Sofroniew, M. V. Dissecting spinal cord regeneration. *Nature* **557,** 343–350 (2018).
11. Popovich, P. G., Wei, P. & Stokes, B. T. Cellular inflammatory response after spinal cord injury in Sprague-Dawley and Lewis rats. *J. Comp. Neurol.* **377,** 443–464 (1997).
12. Dusart, I. & Schwab, M. E. Secondary cell death and the inflammatory reaction after dorsal hemisection of the rat spinal cord. *Eur. J. Neurosci.* **6,** 712–724 (1994).
13. Bartholdi, D. & Schwab, M. E. Expression of pro-inflammatory cytokine and chemokine mRNA upon experimental spinal cord injury in mouse: An in situ hybridization study. *Eur. J. Neurosci.* **9,** 1422–1438 (1997).
14. Kerr, B. J. & Patterson, P. H. Potent pro-inflammatory actions of leukemia inhibitory factor in the spinal cord of the adult mouse. *Exp. Neurol.* **188,** 391–407 (2004).
15. Anderson, M. A. *et al.* Astrocyte scar formation aids central nervous system axon regeneration. *Nature* **532,** 195–200 (2016).
16. Squair, J. W., Gautier, M., Sofroniew, M. V., Courtine, G. & Anderson, M. A. Engineering spinal cord repair. *Curr. Opin. Biotechnol.* **72,** 48–53 (2021).
17. Burda, J. E. & Sofroniew, M. V. Reactive gliosis and the multicellular response to CNS damage and disease. *Neuron* **81,** 229–248 (2014).
18. O'Shea, T. M., Burda, J. E. & Sofroniew, M. V. Cell biology of spinal cord injury and repair. *J. Clin. Invest.* **127,** 3259–3270 (2017).
19. Squair, J. W. *et al.* Integrated systems analysis reveals conserved gene networks underlying response to spinal cord injury. *eLife* **7,** e39188 (2018).
20. De Biase, A. *et al.* Gene expression profiling of experimental traumatic spinal cord injury as a function of distance from impact site and injury severity. *Physiol. Genomics* **22,** 368–381 (2005).
21. Duan, H. *et al.* Transcriptome analyses reveal molecular mechanisms underlying functional recovery after spinal cord injury. *Proc. Natl. Acad. Sci. U. S. A.* **112,** 13360–13365 (2015).
22. Chen, K. *et al.* RNA-seq characterization of spinal cord injury transcriptome in acute/subacute phases: a resource for understanding the pathology at the systems level. *PloS ONE* **8,** e72567 (2013).
23. Chamankhah, M. *et al.* Genome-wide gene expression profiling of stress response in a spinal cord clip compression injury model. *BMC Genomics* **14,** 1–25 (2013).
24. Satzer, D. *et al.* T cell deficiency in spinal cord injury: altered locomotor recovery and whole-genome transcriptional analysis. *BMC Neurosci.* **16,** 1–13 (2015).
25. Duran, R. C.-D. *et al.* The systematic analysis of coding and long non-coding RNAs in the sub-chronic and chronic stages of spinal cord injury. *Sci. Rep.* **7,** 1–15 (2017).
26. Shi, L.-L. *et al.* Transcriptome profile of rat genes in injured spinal cord at different stages by RNA-sequencing. *BMC Genomics* **18,** 1–14 (2017).
27. Svensson, V., Vento-Tormo, R. & Teichmann, S. A. Exponential scaling of single-cell RNA-seq in the past decade. *Nat. Protoc.* **13,** 599–604 (2018).
28. Klein, A. M. *et al.* Droplet barcoding for single-cell transcriptomics applied to embryonic stem cells. *Cell* **161,** 1187–1201 (2015).
29. Macosko, E. Z. *et al.* Highly parallel genome-wide expression profiling of individual cells using nanoliter droplets. *Cell* **161,** 1202–1214 (2015).
30. Zheng, G. X. *et al.* Massively parallel digital transcriptional profiling of single cells. *Nat. Commun.* **8,** 14049 (2017).
31. Chen, S., Lake, B. B. & Zhang, K. High-throughput sequencing of the transcriptome and chromatin accessibility in the same cell. *Nat. Biotechnol.* **37,** 1452–1457 (2019).
32. Zhu, C. *et al.* An ultra high-throughput method for single-cell joint analysis of open chromatin and transcriptome. *Nat. Struct. Mol. Biol.* **26,** 1063–1070 (2019).
33. Cao, J. *et al.* Joint profiling of chromatin accessibility and gene expression in thousands of single cells. *Science* **361,** 1380–1385 (2018).
34. Ma, S. *et al.* Chromatin potential identified by shared single-cell profiling of RNA and chromatin. *Cell* **183,** 1103–1116 (2020).
35. Maniatis, S. *et al.* Spatiotemporal dynamics of molecular pathology in amyotrophic lateral sclerosis. *Science* **364,** 89–93 (2019).
36. Ståhl, P. L. *et al.* Visualization and analysis of gene expression in tissue sections by spatial transcriptomics. *Science* **353,** 78–82 (2016).
37. Vickovic, S. *et al.* High-definition spatial transcriptomics for in situ tissue profiling. *Nat. Methods* **16,** 987–990 (2019).
38. Rodriques, S. G. *et al.* Slide-seq: A scalable technology for measuring genome-wide expression at high spatial resolution. *Science* **363,** 1463–1467 (2019).
39. Liu, Y. *et al.* High-spatial-resolution multi-omics sequencing via deterministic barcoding in tissue. *Cell* **183,** 1665–1681 (2020).
40. Cho, C.-S. *et al.* Microscopic examination of spatial transcriptome using Seq-Scope. *Cell* **184,** 3559–3572 (2021).
41. Chen, A. *et al.* Spatiotemporal transcriptomic atlas of mouse organogenesis using DNA nanoball-patterned arrays. *Cell* **185,** 1777–1792 (2022).
42. Fu, X. *et al.* Polony gels enable amplifiable DNA stamping and spatial transcriptomics of chronic pain. *Cell* **185,** 4621–4633 (2022).
43. Lacar, B. *et al.* Nuclear RNA-seq of single neurons reveals molecular signatures of activation. *Nat. Commun.* **7,** 11022 (2016).
44. Van den Brink, S. C. *et al.* Single-cell sequencing reveals dissociation-induced gene expression in tissue subpopulations. *Nat. Methods* **14,** 935–936 (2017).
45. Wu, H., Kirita, Y., Donnelly, E. L. & Humphreys, B. D. Advantages of single-nucleus over single-cell RNA sequencing of adult kidney: rare cell types and novel cell states revealed in fibrosis. *J. Am. Soc. Nephrol.* **30,** 23–32 (2019).
46. Denisenko, E. *et al.* Systematic assessment of tissue dissociation and storage biases in single-cell and single-nucleus RNA-seq workflows. *Genome Biol.* **21,** 1–25 (2020).
47. Häring, M. *et al.* Neuronal atlas of the dorsal horn defines its architecture and links sensory input to transcriptional cell types. *Nat. Neurosci.* **21,** 869–880 (2018).
48. Hayashi, M. *et al.* Graded arrays of spinal and supraspinal V2a interneuron subtypes underlie forelimb and hindlimb motor control. *Neuron* **97,** 869–884 (2018).
49. Rosenberg, A. B. *et al.* Single-cell profiling of the developing mouse brain and spinal cord with split-pool barcoding. *Science* **360,** 176–182 (2018).
50. Sathyamurthy, A. *et al.* Massively parallel single nucleus transcriptional profiling defines spinal cord neurons and their activity during behavior. *Cell Rep.* **22,** 2216–2225 (2018).
51. Zeisel, A. *et al.* Molecular architecture of the mouse nervous system. *Cell* **174,** 999–1014.e22 (2018).
52. Baek, M., Menon, V., Jessell, T. M., Hantman, A. W. & Dasen, J. S. Molecular logic of spinocerebellar tract neuron diversity and connectivity. *Cell Rep.* **27,** 2620–2635 (2019).

53. Delile, J. *et al.* Single cell transcriptomics reveals spatial and temporal dynamics of gene expression in the developing mouse spinal cord. *Development* **146,** dev173807 (2019).

54. Hamel, R. *et al.* Time-resolved single-cell RNAseq profiling identifies a novel Fabp5-expressing subpopulation of inflammatory myeloid cells in chronic spinal cord injury. Preprint at https://doi.org/10.1101/2020.10.21.346635 (2020).

55. Li, Y. *et al.* Microglia-organized scar-free spinal cord repair in neonatal mice. *Nature* **587,** 613–618 (2020).

56. Alkaslasi, M. R. *et al.* Single nucleus RNA-sequencing defines unexpected diversity of cholinergic neuron types in the adult mouse spinal cord. *Nat. Commun.* **12,** 2471 (2021).

57. Blum, J. A. *et al.* Single-cell transcriptomic analysis of the adult mouse spinal cord reveals molecular diversity of autonomic and skeletal motor neurons. *Nat. Neurosci.* **24,** 572–583 (2021).

58. Milich, L. M. *et al.* Single-cell analysis of the cellular heterogeneity and interactions in the injured mouse spinal cord. *J. Exp. Med.* **218,** e20210040 (2021).

59. Osseward, P. J. *et al.* Conserved genetic signatures parcellate cardinal spinal neuron classes into local and projection subsets. *Science* **372,** 385–393 (2021).

60. Skinnider, M. A. *et al.* Cell type prioritization in single-cell data. *Nat. Biotechnol.* **39,** 30–34 (2021).

61. Wahane, S. *et al.* Diversified transcriptional responses of myeloid and glial cells in spinal cord injury shaped by HDAC3 activity. *Sci. Adv.* **7,** eabd8811 (2021).

62. Li, C. *et al.* Temporal and spatial cellular and molecular pathological alterations with single-cell resolution in the adult spinal cord after injury. *Sig. Transduct. Target. Ther.* **7,** 65 (2022).

63. Anderson, M. A. *et al.* Required growth facilitators propel axon regeneration across complete spinal cord injury. *Nature* **561,** 396–400 (2018).

64. Asboth, L. *et al.* Cortico–reticulo–spinal circuit reorganization enables functional recovery after severe spinal cord contusion. *Nat. Neurosci.* **21,** 576–588 (2018).

65. Scheff, S. W., Rabchevsky, A. G., Fugaccia, I., Main, J. A. & Lumpp Jr, J. E. Experimental modeling of spinal cord injury: characterization of a force-defined injury device. *J. Neurotrauma* **20,** 179–193 (2003).

66. Klein, S. L. & Flanagan, K. L. Sex differences in immune responses. *Nat. Rev. Immunol.* **16,** 626–638 (2016).

67. Gal-Oz, S. T. *et al.* ImmGen report: sexual dimorphism in the immune system transcriptome. *Nat. Commun.* **10,** 4295 (2019).

68. López-Otín, C., Blasco, M. A., Partridge, L., Serrano, M. & Kroemer, G. The hallmarks of aging. *Cell* **153,** 1194–1217 (2013).

69. Nikolich-Žugich, J. The twilight of immunity: emerging concepts in aging of the immune system. *Nat. Immunol.* **19,** 10–19 (2018).

70. Short, D., El Masry, W. & Jones, P. High dose methylprednisolone in the management of acute spinal cord injury–a systematic review from a clinical perspective. *Spinal Cord* **38,** 273–286 (2000).

71. Bracken, M. B. *et al.* A randomized, controlled trial of methylprednisolone or naloxone in the treatment of acute spinal-cord injury: results of the Second National Acute Spinal Cord Injury Study. *N. Engl. J. Med.* **322,** 1405–1411 (1990).

72. Hurlbert, R. J. Methylprednisolone for acute spinal cord injury: an inappropriate standard of care. *J. Neurosurg. Spine* **93,** 1–7 (2000).

73. Wells, J. E., Hurlbert, R. J., Fehlings, M. G. & Yong, V. W. Neuroprotection by minocycline facilitates significant recovery from spinal cord injury in mice. *Brain* **126,** 1628–1637 (2003).

74. Stirling, D. P. *et al.* Minocycline treatment reduces delayed oligodendrocyte death, attenuates axonal dieback, and improves functional outcome after spinal cord injury. *J. Neurosci.* **24,** 2182–2190 (2004).

75. Festoff, B. W. *et al.* Minocycline neuroprotects, reduces microgliosis, and inhibits caspase protease expression early after spinal cord injury. *J. Neurochem.* **97,** 1314–1326 (2006).

76. Casha, S. *et al.* Results of a phase II placebo-controlled randomized trial of minocycline in acute spinal cord injury. *Brain* **135,** 1224–1236 (2012).

77. Fawcett, J. W. & Asher, R. A. The glial scar and central nervous system repair. *Brain Res. Bull.* **49,** 377–391 (1999).

78. Fitch, M. T., Doller, C., Combs, C. K., Landreth, G. E. & Silver, J. Cellular and molecular mechanisms of glial scarring and progressive cavitation: in vivo and in vitroanalysis of inflammation-induced secondary injury after CNS trauma. *J. Neurosci.* **19,** 8182–8198 (1999).

79. Tuszynski, M. H. & Kordower, J. *CNS Regeneration: Basic Science and Clinical Advances* (Elsevier, 1998).

80. Bradbury, E. J. *et al.* Chondroitinase ABC promotes functional recovery after spinal cord injury. *Nature* **416,** 636–640 (2002).

81. Barritt, A. *et al.* Chondroitinase ABC promotes sprouting of intact and injured spinal systems after spinal cord injury. *J. Neurosci.* **26,** 10856–10867 (2006).

82. Massey, J. M. *et al.* Chondroitinase ABC digestion of the perineuronal net promotes functional collateral sprouting in the cuneate nucleus after cervical spinal cord injury. *J. Neurosci.* **26,** 4406–4414 (2006).

83. Carter, L. M. *et al.* The yellow fluorescent protein (YFP-H) mouse reveals neuroprotection as a novel mechanism underlying chondroitinase ABC-mediated repair after spinal cord injury. *J. Neurosci.* **28,** 14107–14120 (2008).

84. Bradbury, E. J. & Carter, L. M. Manipulating the glial scar: chondroitinase ABC as a therapy for spinal cord injury. *Brain Res. Bull.* **84,** 306–316 (2011).

85. Zappia, L. & Oshlack, A. Clustering trees: a visualization for evaluating clusterings at multiple resolutions. *GigaScience* **7,** giy083 (2018).

86. Jessell, T. M. Neuronal specification in the spinal cord: inductive signals and transcriptional codes. *Nat. Rev. Genet.* **1,** 20–29 (2000).

87. Squair, J. W. *et al.* Confronting false discoveries in single-cell differential expression. *Nat. Commun.* **12,** 1–15 (2021).

88. Russ, D. E. *et al.* A harmonized atlas of spinal cord cell types and their computational classification. *Nat. Commun.* **12,** 5722 (2021).

89. Kierdorf, K., Masuda, T., Jordao, M. J. C. & Prinz, M. Macrophages at CNS interfaces: ontogeny and function in health and disease. *Nat. Rev. Neurosci.* **20,** 547–562 (2019).

90. Sofroniew, M. V. & Vinters, H. V. Astrocytes: biology and pathology. *Acta Neuropathol.* **119,** 7–35 (2010).

91. Faulkner, J. R. *et al.* Reactive astrocytes protect tissue and preserve function after spinal cord injury. *J. Neurosci.* **24,** 2143–2155 (2004).

92. Wanner, I. B. *et al.* Glial scar borders are formed by newly proliferated, elongated astrocytes that interact to corral inflammatory and fibrotic cells via STAT3-dependent mechanisms after spinal cord injury. *J. Neurosci.* **33,** 12870–12886 (2013).

93. Vanlandewijck, M. *et al.* A molecular atlas of cell types and zonation in the brain vasculature. *Nature* **554,** 475–480 (2018).

94. Winkler, E. A. *et al.* A single-cell atlas of the normal and malformed human brain vasculature. *Science* **375,** eabi7377 (2022).

95. Chow, B. W. & Gu, C. The molecular constituents of the blood–brain barrier. *Trends Neurosci.* **38,** 598–608 (2015).

96. Armulik, A. *et al.* Pericytes regulate the blood–brain barrier. *Nature* **468,** 557–561 (2010).

97. Yang, A. C. *et al.* A human brain vascular atlas reveals diverse mediators of Alzheimer's risk. *Nature* **603,** 885–892 (2022).

98. Daneman, R., Zhou, L., Kebede, A. A. & Barres, B. A. Pericytes are required for blood–brain barrier integrity during embryogenesis. *Nature* **468,** 562–566 (2010).

99. Janzer, R. C. & Raff, M. C. Astrocytes induce blood–brain barrier properties in endothelial cells. *Nature* **325,** 253–257 (1987).

100. Yasuda, K. *et al.* Drug transporters on arachnoid barrier cells contribute to the blood–cerebrospinal fluid barrier. *Drug Metab. Dispos.* **41,** 923–931 (2013).

101. Munji, R. N. *et al.* Profiling the mouse brain endothelial transcriptome in health and disease models reveals a core blood–brain barrier dysfunction module. *Nat. Neurosci.* **22,** 1892–1902 (2019).

102. Marques, S. *et al.* Oligodendrocyte heterogeneity in the mouse juvenile and adult central nervous system. *Science* **352,** 1326–1329 (2016).

103. Dewar, D., Underhill, S. M. & Goldberg, M. P. Oligodendrocytes and ischemic brain injury. *J. Cereb. Blood Flow Metab.* **23,** 263–274 (2003).

104. Briscoe, J., Pierani, A., Jessell, T. M. & Ericson, J. A homeodomain protein code specifies progenitor cell identity and neuronal fate in the ventral neural tube. *Cell* **101,** 435–445 (2000).

105. Alvarez, F. J. *et al.* Postnatal phenotype and localization of spinal cord V1 derived interneurons. *J. Comp. Neurol.* **493,** 177–192 (2005).

106. Perry, S. *et al.* Firing properties of Renshaw cells defined by Chrna2 are modulated by hyperpolarizing and small conductance ion currents Ih and ISK. *Eur. J. Neurosci.* **41,** 889–900 (2015).

107. Petracca, Y. L. *et al.* The late and dual origin of cerebrospinal fluid-contacting neurons in the mouse spinal cord. *Development* **143,** 880–891 (2016).

108. Vigh, B. *et al.* The system of cerebrospinal fluid-contacting neurons. Its supposed role in the nonsynaptic signal transmission of the brain. *Histol. Histopathol.* **19,** 607–628 (2004).

109. Pfaff, S. L., Mendelsohn, M., Stewart, C. L., Edlund, T. & Jessell, T. M. Requirement for LIM homeobox gene Isl1 in motor neuron generation reveals a motor neuron–dependent step in interneuron differentiation. *Cell* **84,** 309–320 (1996).

110. Zagoraiou, L. *et al.* A cluster of cholinergic premotor interneurons modulates mouse locomotor activity. *Neuron* **64,** 645–662 (2009).

111. Pierani, A. *et al.* Control of interneuron fate in the developing spinal cord by the progenitor homeodomain protein Dbx1. *Neuron* **29,** 367–384 (2001).

112. Moran-Rivard, L. *et al.* Evx1 is a postmitotic determinant of V0 interneuron identity in the spinal cord. *Neuron* **29,** 385–399 (2001).

113. Bikoff, J. B. *et al.* Spinal inhibitory interneuron diversity delineates variant motor microcircuits. *Cell* **165,** 207–219 (2016).

114. Zhou, Y., Yamamoto, M. & Engel, J. D. GATA2 is required for the generation of V2 interneurons. *Development* **127,** 3829–3838 (2000).

115. Zhang, J. *et al.* V1 and V2b interneurons secure the alternating flexor-extensor motor activity mice require for limbed locomotion. *Neuron* **82,** 138–150 (2014).

116. Ericson, J. *et al.* Pax6 controls progenitor cell identity and neuronal fate in response to graded Shh signaling. *Cell* **90,** 169–180 (1997).

117. Kimura, Y., Okamura, Y. & Higashijima, S.-i. alx, a zebrafish homolog of Chx10, marks ipsilateral descending excitatory interneurons that participate in the regulation of spinal locomotor circuits. *J. Neurosci.* **26,** 5684–5697 (2006).

118. Stepien, A. E. & Arber, S. Probing the locomotor conundrum: descending the 'V' interneuron ladder. *Neuron* **60,** 1–4 (2008).

119. Welin, D., Novikova, L. N., Wiberg, M., Kellerth, J.-O. & Novikov, L. N. Survival and regeneration of cutaneous and muscular afferent neurons after peripheral nerve injury in adult rats. *Exp. Brain Res.* **186,** 315–323 (2008).

120. Saxena, S. & Caroni, P. Selective neuronal vulnerability in neurodegenerative diseases: from stressor thresholds to degeneration. *Neuron* **71,** 35–48 (2011).

121. Steencken, A. C., Smirnov, I. & Stelzner, D. Cell survival or cell death: differential vulnerability of long descending and thoracic propriospinal neurons to low thoracic axotomy in the adult rat. *Neuroscience* **194,** 359–371 (2011).

122. Fu, H., Hardy, J. & Duff, K. E. Selective vulnerability in neurodegenerative diseases. *Nat. Neurosci.* **21,** 1350–1358 (2018).

123. Tran, N. M. *et al.* Single-cell profiles of retinal ganglion cells differing in resilience to injury reveal neuroprotective genes. *Neuron* **104,** 1039–1055 (2019).

124. Leng, K. *et al.* Molecular characterization of selectively vulnerable neurons in Alzheimer's disease. *Nat. Neurosci.* **24,** 276–287 (2021).

125. Kamath, T. *et al.* Single-cell genomic profiling of human dopamine neurons identifies a population that selectively degenerates in Parkinson's disease. *Nat. Neurosci.* **25,** 588–595 (2022).

126. Courtine, G. *et al.* Recovery of supraspinal control of stepping via indirect propriospinal relay connections after spinal cord injury. *Nat. Med.* **14,** 69–74 (2008).

127. Squair, J. W., Skinnider, M. A., Gautier, M., Foster, L. J. & Courtine, G. Prioritization of cell types responsive to biological perturbations in single-cell data with Augur. *Nat. Protoc.* **16,** 3836–3873 (2021).

128. Renthal, W. *et al.* Transcriptional reprogramming of distinct peripheral sensory neuron subtypes after axonal injury. *Neuron* **108,** 128–144 (2020).

129. Nguyen, M. Q., Le Pichon, C. E. & Ryba, N. Stereotyped transcriptomic transformation of somatosensory neurons in response to injury. *eLife* **8,** e49679 (2019).

130. Ramón y Cajal, S. Degeneration and regeneration of the nervous system (1928).

131. Sperry, R. W. Chemoaffinity in the orderly growth of nerve fiber patterns and connections. *Proc. Natl. Acad. Sci. U. S. A.* **50,** 703–710 (1963).

132. Harel, N. Y. & Strittmatter, S. M. Can regenerating axons recapitulate developmental guidance during recovery from spinal cord injury? *Nat. Rev. Neurosci.* **7,** 603–616 (2006).

133. Mironova, Y. A. & Giger, R. J. Where no synapses go: gatekeepers of circuit remodeling and synaptic strength. *Trends Neurosci.* **36,** 363–373 (2013).

134. Lin, A. C. & Holt, C. E. Local translation and directional steering in axons. *EMBO J.* **26,** 3729–3736 (2007).

135. Plantman, S. *et al.* Integrin-laminin interactions controlling neurite outgrowth from adult DRG neurons in vitro. *Mol. Cell. Neurosci.* **39,** 50–62 (2008).

136. Silver, J. & Miller, J. H. Regeneration beyond the glial scar. *Nat. Rev. Neurosci.* **5,** 146–156 (2004).

137. Rosenzweig, E. S. *et al.* Chondroitinase improves anatomical and functional outcomes after primate spinal cord injury. *Nat. Neurosci.* **22,** 1269–1275 (2019).

138. Bartus, K. *et al.* Large-scale chondroitin sulfate proteoglycan digestion with chondroitinase gene therapy leads to reduced pathology and modulates macrophage phenotype following spinal cord contusion injury. *J. Neurosci.* **34,** 4822–4836 (2014).

139. Alilain, W. J., Horn, K. P., Hu, H., Dick, T. E. & Silver, J. Functional regeneration of respiratory pathways after spinal cord injury. *Nature* **475,** 196–200 (2011).

140. Wang, F. *et al.* RNAscope: a novel in situ RNA analysis platform for formalin-fixed, paraffin-embedded tissues. *J. Mol. Diagn.* **14,** 22–29 (2012).

141. Yang, S., Kwok, J. C. & Fawcett, J. W. Neural ECM in regeneration and rehabilitation. *Prog. Brain Res.* **214,** 179–192 (2014).

142. Orlando, C., Ster, J., Gerber, U., Fawcett, J. W. & Raineteau, O. Perisynaptic chondroitin sulfate proteoglycans restrict structural plasticity in an integrin-dependent manner. *J. Neurosci.* **32,** 18009–18017 (2012).

143. Bracken, M. B. *et al.* Efficacy of methylprednisolone in acute spinal cord injury. *J. Am. Med. Assoc.* **251,** 45–52 (1984).

144. Ankeny, D. P. & Popovich, P. G. Mechanisms and implications of adaptive immune responses after traumatic spinal cord injury. *Neuroscience* **158,** 1112–1121 (2009).

145. Pitonak, M. *et al.* Effects of biological sex mismatch on neural progenitor cell transplantation for spinal cord injury in mice. *Nat. Commun.* **13,** 5380 (2022).

146. Cheriyan, T. *et al.* Spinal cord injury models: a review. *Spinal Cord* **52,** 588–595 (2014).

147. Kwon, B. K., Oxland, T. R. & Tetzlaff, W. Animal models used in spinal cord regeneration research. *Spine* **27,** 1504–1510 (2002).

148. Tuszynski, M. H. & Steward, O. Concepts and methods for the study of axonal regeneration in the CNS. *Neuron* **74,** 777–791 (2012).

149. Mattucci, S. *et al.* Basic biomechanics of spinal cord injury—How injuries happen in people and how animal models have informed our understanding. *Clin. Biomech.* **64,** 58–68 (2019).

150. Bahar, R. *et al.* Increased cell-to-cell variation in gene expression in ageing mouse heart. *Nature* **441,** 1011–1014 (2006).

151. Somel, M., Khaitovich, P., Bahn, S., Pääbo, S. & Lachmann, M. Gene expression becomes heterogeneous with age. *Curr. Biol.* **16,** R359–R360 (2006).

152. Martinez-Jimenez, C. P. *et al.* Aging increases cell-to-cell transcriptional variability upon immune stimulation. *Science* **355,** 1433–1436 (2017).

153. Ximerakis, M. *et al.* Single-cell transcriptomic profiling of the aging mouse brain. *Nat. Neurosci.* **22,** 1696–1708 (2019).

154. Ma, S. *et al.* Caloric restriction reprograms the single-cell transcriptional landscape of rattus norvegicus aging. *Cell* **180,** 984–1001 (2020).

155. Wang, S. *et al.* Single-cell transcriptomic atlas of primate ovarian aging. *Cell* **180,** 585–600 (2020).

156. O'Shea, T. *et al.* Lesion environments direct transplanted neural progenitors towards a wound repair astroglial phenotype in mice. *Nat. Commun.* **13,** 5702 (2022).

157. Granja, J. M. *et al.* ArchR is a scalable software package for integrative single-cell chromatin accessibility analysis. *Nat. Genet.* **53,** 403–411 (2021).

158. Korsunsky, I. *et al.* Fast, sensitive and accurate integration of single-cell data with Harmony. *Nat. Methods* **16,** 1289–1296 (2019).

159. Schep, A. N., Wu, B., Buenrostro, J. D. & Greenleaf, W. J. chromVAR: inferring transcription-factor-associated accessibility from single-cell epigenomic data. *Nat. Methods* **14,** 975–978 (2017).

160. Burda, J. E. *et al.* Divergent transcriptional regulation of astrocyte reactivity across disorders. *Nature* **606,** 557–564 (2022).

161. Cobaleda, C., Schebesta, A., Delogu, A. & Busslinger, M. Pax5: the guardian of B cell identity and function. *Nat. Immunol.* **8,** 463–470 (2007).

162. Gao, T. *et al.* Transcriptional regulation of homeostatic and disease-associated-microglial genes by IRF1, LXR$\beta$, and CEBP$\alpha$. *Glia* **67,** 1958–1975 (2019).

163. Wang, Z. *et al.* Cell-type-specific gene regulatory networks underlying murine neonatal heart regeneration at single-cell resolution. *Cell Rep.* **33,** 108472 (2020).

164. Hübner, K. *et al.* Wnt signaling positively regulates endothelial cell fate specification in the Fli1a-positive progenitor population via Lef1. *Dev. Biol.* **430,** 142–155 (2017).

165. Pollard, K. S., Hubisz, M. J., Rosenbloom, K. R. & Siepel, A. Detection of nonneutral substitution rates on mammalian phylogenies. *Genome Res.* **20,** 110–121 (2010).

166. Rood, J. E. *et al.* Toward a common coordinate framework for the human body. *Cell* **179,** 1455–1467 (2019).

167. Cable, D. M. *et al.* Robust decomposition of cell type mixtures in spatial transcriptomics. *Nat. Biotechnol.* **40,** 517–526 (2022).

168. Christian, C. A. *et al.* Endogenous positive allosteric modulation of GABAA receptors by diazepam binding inhibitor. *Neuron* **78,** 1063–1074 (2013).

169. Chung, K. & Deisseroth, K. CLARITY for mapping the nervous system. *Nat. Methods* **10,** 508–513 (2013).

170. Biancalani, T. *et al.* Deep learning and alignment of spatially resolved single-cell transcriptomes with Tangram. *Nat. Methods* **18,** 1352–1362 (2021).

171. Olsson, A.-K., Dimberg, A., Kreuger, J. & Claesson-Welsh, L. VEGF receptor signalling — In control of vascular function. *Nat. Rev. Mol. Cell Biol.* **7,** 359–371 (2006).

172. Rabchevsky, A. G., Fugaccia, I., Sullivan, P. G., Blades, D. A. & Scheff, S. W. Efficacy of methylprednisolone therapy for the injured rat spinal cord. *J. Neurosci. Res.* **68,** 7–18 (2002).

173. Muir, E. M. *et al.* Modification of N-glycosylation sites allows secretion of bacterial chondroitinase ABC from mammalian cells. *J. Biotechnol.* **145,** 103–110 (2010).

174. Takeoka, A., Vollenweider, I., Courtine, G. & Arber, S. Muscle spindle feedback directs locomotor recovery and circuit reorganization after spinal cord injury. *Cell* **159,** 1626–1639 (2014).

175. Kathe, C. *et al.* Wireless closed-loop optogenetics across the entire spinal cord in ecological environments. *Nat. Biotechnol.* **40,** 198–208 (2021).

176. Mathis, A. *et al.* DeepLabCut: markerless pose estimation of user-defined body parts with deep learning. *Nat. Neurosci.* **21,** 1281–1289 (2018).

177. Voigt, F. F. *et al.* The mesoSPIM initiative: open-source light-sheet microscopes for imaging cleared tissue. *Nat. Methods* **16,** 1105–1108 (2019).

178. Tomer, R., Ye, L., Hsueh, B. & Deisseroth, K. Advanced CLARITY for rapid and high-resolution imaging of intact tissues. *Nat. Protoc.* **9,** 1682–1697 (2014).

179. Caglayan, E., Liu, Y. & Konopka, G. Neuronal ambient RNA contamination causes misinterpreted and masked cell types in brain single-nuclei datasets. *Neuron* **110,** 4043–4056 (2022).

180. Fleming, S. J. *et al.* Unsupervised removal of systematic background noise from droplet-based single-cell experiments using CellBender. Preprint at https://doi.org/10.1101/791699 (2019).

181. Stuart, T. *et al.* Comprehensive integration of single-cell data. *Cell* **177,** 1888–1902.e21 (2019).

182. McGinnis, C. S., Murrow, L. M. & Gartner, Z. J. DoubletFinder: doublet detection in single-cell RNA sequencing data using artificial nearest neighbors. *Cell Syst.* **8,** 329–337 (2019).

183. Germain, P.-L., Lun, A., Meixide, C. G., Macnair, W. & Robinson, M. D. Doublet identification in single-cell sequencing data using scDblFinder. *F1000Research* **10,** 979 (2021).

184. Bais, A. S. & Kostka, D. scds: computational annotation of doublets in single-cell RNA sequencing data. *Bioinformatics* **36,** 1150–1158 (2020).

185. Wolock, S. L., Lopez, R. & Klein, A. M. Scrublet: computational identification of cell doublets in single-cell transcriptomic data. *Cell Syst.* **8,** 281–291 (2019).

186. Xi, N. M. & Li, J. J. Benchmarking computational doublet-detection methods for single-cell RNA sequencing data. *Cell Syst.* **12,** 176–194 (2021).

187. Koopmans, F. *et al.* SynGO: an evidence-based, expert-curated knowledge base for the synapse. *Neuron* **103,** 217–234 (2019).

188. Zheng, S. C. *et al.* Universal prediction of cell-cycle position using transfer learning. *Genome Biol.* **23,** 1–27 (2022).

189. Buettner, M., Ostner, J., Mueller, C. L., Theis, F. J. & Schubert, B. scCODA is a Bayesian model for compositional single-cell data analysis. *Nat. Commun.* **12,** 6876 (2021).

190. Phipson, B. *et al.* propeller: testing for differences in cell type proportions in single cell data. *Bioinformatics* **38,** 4720–4726 (2022).

191. Simmons, S. Cell type composition analysis: comparison of statistical methods. Preprint at https://doi.org/10.1101/2022.02.04.479123 (2022).

192. Zimmerman, K. D., Espeland, M. A. & Langefeld, C. D. A practical solution to pseudoreplication bias in single-cell studies. *Nat. Commun.* **12,** 738 (2021).

193. Robinson, M. D., McCarthy, D. J. & Smyth, G. K. edgeR: a Bioconductor package for differential expression analysis of digital gene expression data. *Bioinformatics* **26,** 139–140 (2010).

194. Zhang, Y. *et al.* Model-based analysis of ChIP-Seq (MACS). *Genome Biol.* **9,** 1–9 (2008).

195. Fornes, O. *et al.* JASPAR 2020: update of the open-access database of transcription factor binding profiles. *Nucleic Acids Res.* **48,** D87–D92 (2020).

196. Love, M. I., Huber, W. & Anders, S. Moderated estimation of fold change and dispersion for RNA-seq data with DESeq2. *Genome Biol.* **15,** 1–21 (2014).

197. McKenzie, A. T., Katsyv, I., Song, W.-M., Wang, M. & Zhang, B. DGCA: a comprehensive R package for differential gene correlation analysis. *BMC Syst. Biol.* **10,** 1–25 (2016).

# Supplementary figures
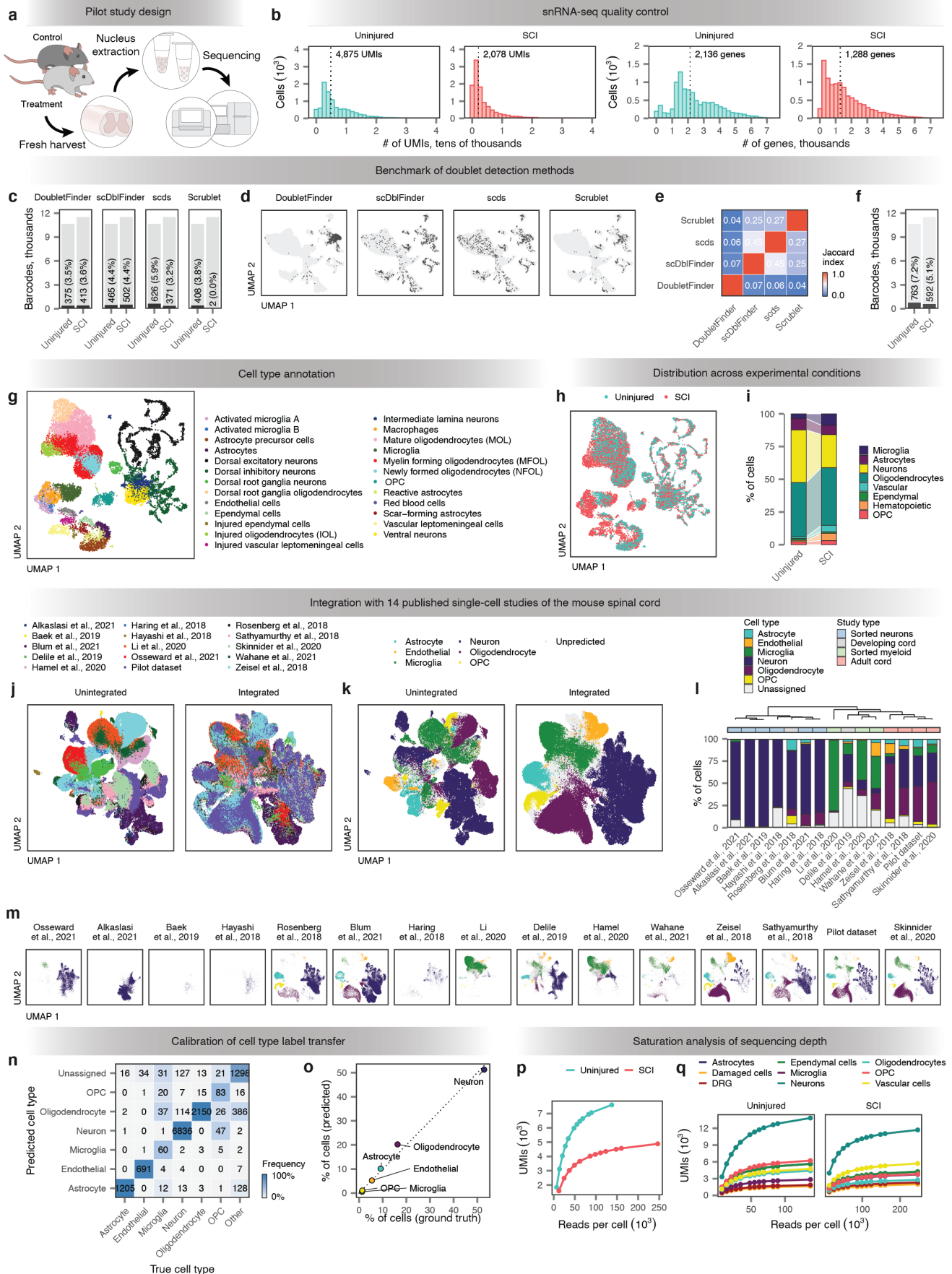
**Supplementary Fig. 1 | Pilot study of snRNA-seq in the injured mouse spinal cord.**

**a,** Schematic overview of experimental design.

**b,** Quality control (number of UMIs per cell and number of genes detected per cell) of single-cell libraries from injured and uninjured mouse spinal cords.

**c-f,** Detection and prevalence of cell doublets in the pilot study.

**c,** Number of doublets detected in each library by four computational methods for doublet detection.

**d,** Visualization of doublets detected by each of four computational methods on a UMAP plot of 22,157 cell barcodes from the mouse spinal cord.

**e,** Overlap between doublets identified by each method, as quantified by the Jaccard index. DoubletFinder calls a largely distinct set of cell barcodes as doublets, as compared to the other three methods.

**f,** Number and proportion of doublets detected in each library by the final method for doublet identification, comprising the union of doublet calls from scDblFinder and scds.

**g,** UMAP visualization of 18,269 cells, revealing 25 transcriptionally distinct clusters of cells in the injured and uninjured mouse spinal cord.

**h,** UMAP visualization of 18,269 cells, colored by the experimental condition of origin for each cell (uninjured or SCI).

**i,** Proportions of eight major cell types of the mouse spinal cord detected in either experimental condition.

**j,** UMAP visualization of 420,786 cells, including the pilot dataset and sixteen published single-cell studies of the mouse spinal cord, colored by the study of origin. Left, before data integration with Seurat; right, after data integration.

**k,** As in **j,** but showing major cell types inferred by label transfer with Seurat.

**l,** Proportions of six major cell types, and unassigned cells, recovered by sixteen published single-cell studies of the mouse spinal cord and the pilot dataset. Datasets are hierarchically clustered by cell type composition and annotated according to the study type.

**m,** As in **k,** but showing cells from each study individually.

**n-o,** Calibration of the label transfer functionality used to assign coarse cell types in published studies.

**n,** Concordance between cell types automatically assigned by label transfer and manually assigned by the authors of the original study in the Sathyamurthy et al. dataset.

**o,** Correlation between the cell type proportions recovered by label transfer and those manually assigned by the authors of the original study in the Sathyamurthy et al. dataset.

**p-q,** Analysis of the minimum sequencing depth required to detect cell-type-specific transcriptional changes in the injured mouse spinal cord.

**p,** Proportion of the complete UMI count matrix recovered after downsampling the number of reads in the injured and uninjured libraries, respectively, as compared to the complete dataset.

**q,** Proportion of the complete UMI count matrix recovered in each major cell type after downsampling the number of reads in the injured and uninjured libraries, respectively, as compared to the complete dataset.
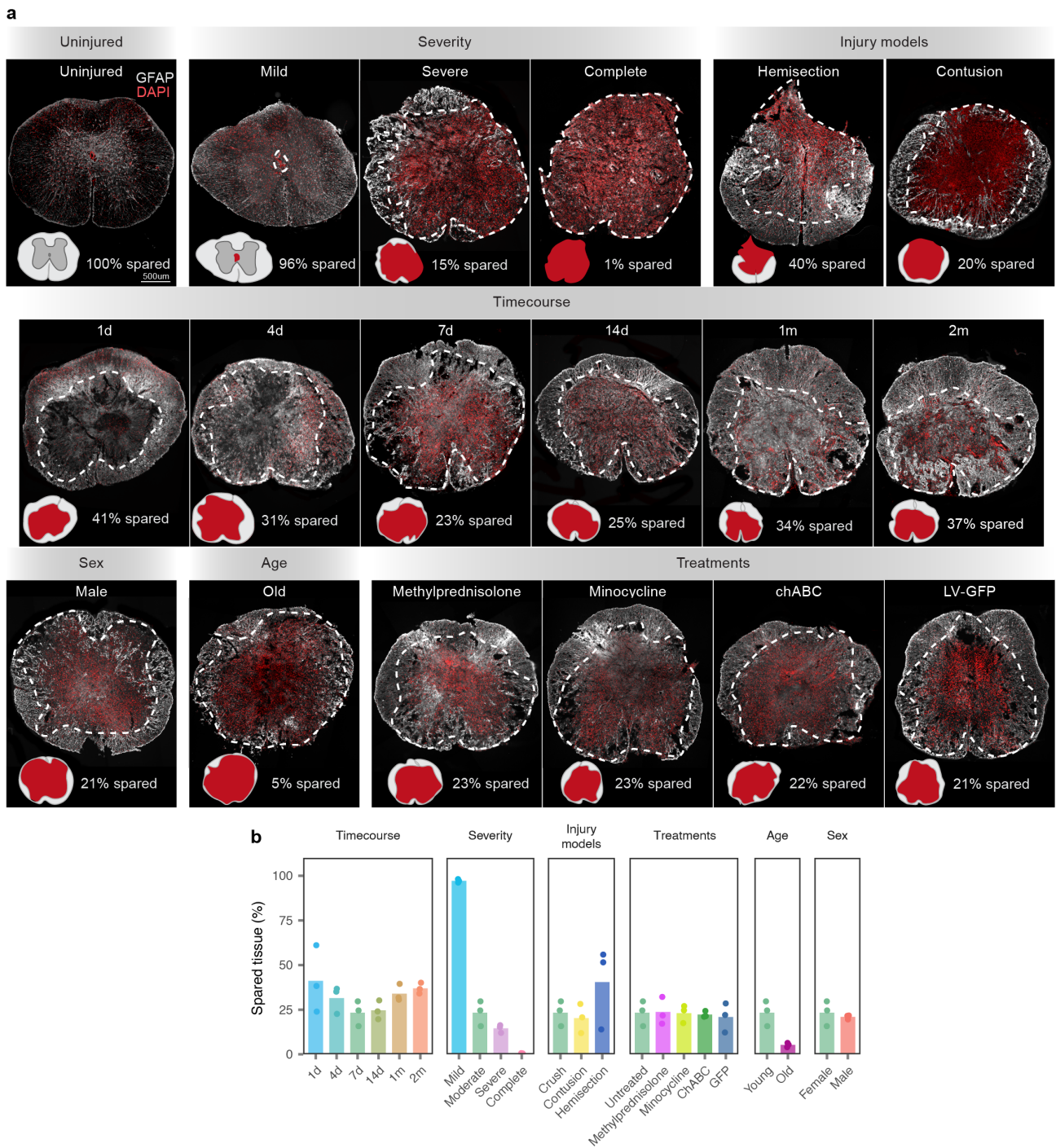
**Supplementary Fig. 2 | Representative histological images across experimental conditions.**

**a,** Histological photomicrographs show two-dimensional views of injured spinal cords stained with glial fibrillary acidic protein (GFAP).

**b,** Quantification of the SCI lesion epicentre. The extent of spared spinal cord tissue was quantified from coronal sections immunolabeled against GFAP.
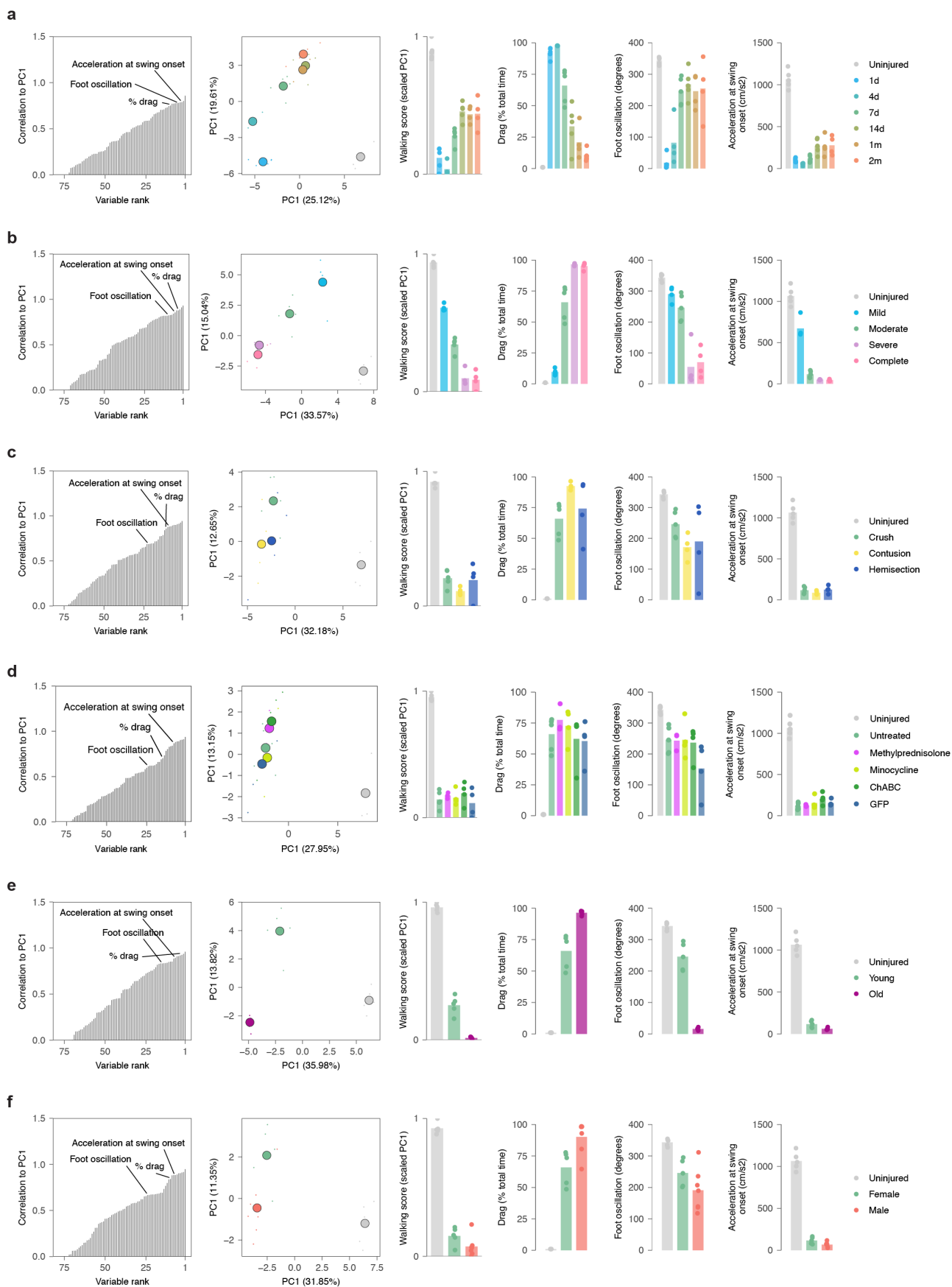
**Supplementary Fig. 3 | High-resolution kinematic analysis across experimental conditions.**

**a,** Locomotor performance of mice across timepoints after SCI. Locomotor performance was quantified using principal component analysis applied to 55 gait parameters calculated from kinematic recordings. Small points show individual gait cycles ($n > 10$ per mouse, $n = 4$-$7$ mice per group). Large points show the mean of each experimental group. The first principal component (PC1) distinguished gaits from mice across different experimental groups. Analysis of factor loadings on PC1 revealed that the percentage of paw dragging, the extent of foot oscillation, and acceleration of the limb at swing onset were among the parameters that showed the highest correlation with PC1. Bars report the mean values of these gait parameters.
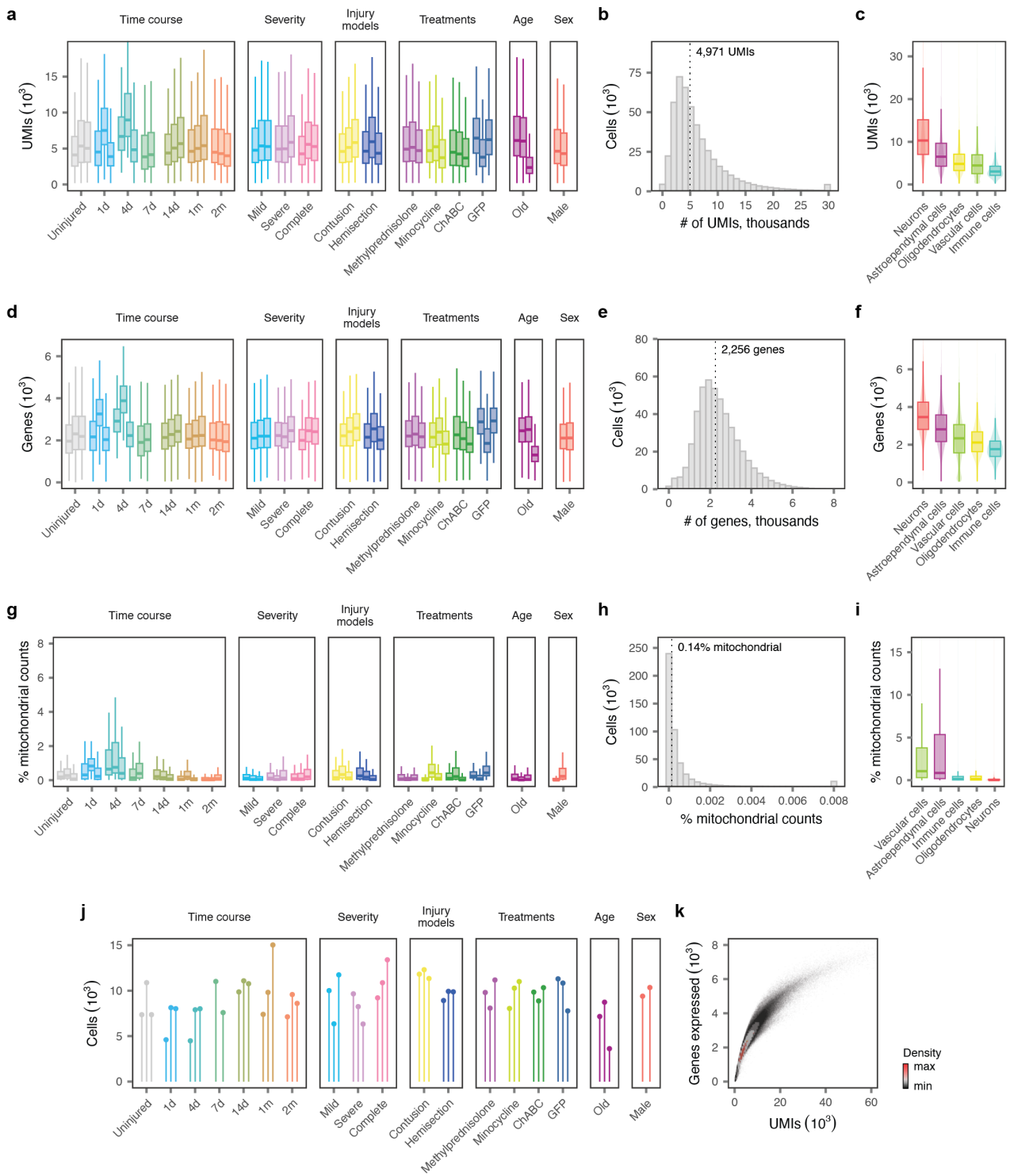
**b,** As in **a,** for mice subjected to different severities of crush SCI.

**c,** As in **a,** for mice subjected to different injury mechanisms.

**d,** As in **a,** for mice treated with various clinical and experimental interventions.

**e,** As in **a,** for old versus young mice.

**f,** As in **a,** for male versus female mice.

**Supplementary Fig. 4 | Quality control of the snRNA-seq atlas.**
**a-i,** Quality control statistics for 435,099 single-nucleus transcriptomes from the uninjured and injured mouse spinal cord.
**a,** Number of unique molecular identifiers (UMIs) per nucleus in individual libraries from each experimental condition.
**b,** Number of UMIs per nucleus, aggregated across all libraries. Inset text shows the median number of UMIs.
**c,** Number of UMIs per nucleus in each major cell type.
**d,** Number of genes detected per nucleus in individual libraries from each experimental condition.
**e,** Number of genes detected per nucleus, aggregated across all libraries. Inset text shows the median number of genes detected.
**f,** Number of genes detected per nucleus in each major cell type.
**g,** Proportion of mitochondrial counts per nucleus in individual libraries from each experimental condition.
**h,** Proportion of mitochondrial counts per nucleus, aggregated across all libraries. Inset text shows the median proportion of mitochondrial counts.
**i,** Proportion of mitochondrial counts per nucleus in each major cell type.
**j,** Number of nuclei passing quality control in each of the 54 libraries comprising the snRNA-seq atlas.
**k,** Relationship between the number of UMIs and the number of genes detected per nucleus across all 435,099 nuclei.

**a**       Level 3

Astroependymal cells
- Ependymal cells
- Astrocytes, cycling
- Astrocytes

Immune cells
- B cells
- Microglia
- NK, T cells
- Peripheral macrophages
- Infiltrating, bordering leukocytes
- Myeloid, dividing

Neurons
- VI
- VE
- DI
- DE

Vascular cells
- Vascular endothelial cells
- Vascular leptomeningeal cells
- Pericytes

Oligodendrocytes
- Mature oligodendrocytes (MOL), ischemic
- Mature oligodendrocytes (MOL)
- Myelin forming oligodendrocytes (MFOL)
- Newly formed oligodendrocytes (NFOL)
- Oligodendrocytes precursor cells (OPC)
- Oligodendrocytes precursor cells (OPC), differentiating

**b**       Level 4

Astroependymal cells
- Ependymal cells
- Astrocytes, cycling
- Astrocytes, fibrous
- Astrocytes, reactive
- Astrocytes, protoplasmic

Immune cells
- B cells
- Microglia
- Myeloid, dividing
- NK, T cells
- Infiltrating, bordering leukocytes
- Macrophages, inflammatory
- Macrophages, chemotaxis-inducing

Neurons
- MI
- VCL V0d/V2b
- V1
- MEL
- MEP
- Neural stem cells
- VEL/V2a neurons
- VEP
- VEP V0
- CSF contacting
- DI$^{Npy}$
- DI$^{Pdyn}$
- DI$^{Rorb}$
- DE$^{Cpne4::Prkcg}$
- DE$^{Maf}$
- DE$^{Reln}$
- DE$^{Rreb1}$
- DE$^{Sox5::Tac1}$
- DE$^{Sox5::Tac2}$

Vascular cells
- Vascular endothelial cells, venous
- Vascular endothelial cells
- Pericytes
- Vascular leptomeningeal cells
- Vascular leptomeningeal cells, ECM forming

Oligodendrocytes
- Mature oligodendrocytes (MOL), ischemic
- Mature oligodendrocytes (MOL)
- Myelin forming oligodendrocytes (MFOL)
- Differentiation-committed oligodendrocyte precursors (COPs)
- Newly formed oligodendrocytes (NFOL)
- Oligodendrocytes precursor cells (OPC), differentiating
- Oligodendrocytes precursor cells (OPC)
- Oligodendrocytes precursor cells (OPC), cycling

**c**       Level 5

Astroependymal cells
- Ependymal cells
- Astrocytes, cycling
- Astrocytes, fibrous
- Astrocytes, reactive
- Astrocytes, protoplasmic

Immune cells
- B cells
- Microglia, activated
- Microglia, homeostatic-injury susceptible
- Microglia, homeostatic
- Dendritic cells
- Myeloid, dividing
- Myeloid, fate-committed
- NK cells
- CD8 T cells
- Macrophages, border-associated
- Neutrophils
- Macrophages, inflammatory
- Macrophages, chemotaxis-inducing
- Macrophages, thrombospondin-sensing

Vascular cells
- Vascular endothelial cells, venous
- Vascular endothelial cells, capillary
- Vascular endothelial cells, arterial
- Pericytes
- Vascular leptomeningeal cells, ECM forming
- Arachnoid barrier cells
- Vascular leptomeningeal cells

Oligodendrocytes
- Mature oligodendrocytes (MOL), ischemic
- Mature oligodendrocytes (MOL)
- Myelin forming oligodendrocytes (MFOL)
- Newly formed oligodendrocytes (NFOL)
- Differentiation-committed oligodendrocyte precursors (COPs)
- Oligodendrocytes precursor cells (OPC), differentiating
- Oligodendrocytes precursor cells (OPC)
- Oligodendrocytes precursor cells (OPC), cycling

Neurons
- CSF contacting neurons
- DI$^{Npy::Qrfpr}$
- DI$^{Npy::Vgf}$
- DI$^{Gal}$
- DI$^{Pdyn::Gal}$
- DI$^{Maf::Adarb2}$
- DI$^{Nxph1::Npy}$
- DI$^{Rorb::Adamts5}$
- DI$^{Rorb::Kcnip2}$
- DI$^{Rorb::Nppc}$
- DI$^{Rorb::Rxfp2}$
- DE$^{Cck::Cpne4}$
- DE$^{Nts}$
- DE$^{Trh}$
- DE$^{Maf::Cpne4::Rorb}$
- DE$^{Maf::Kcnn8}$
- DE$^{Reln::Trhr}$
- DE$^{Rreb1::Zim1}$
- DE$^{Tac2::Nmu}$
- DE$^{Reln::Nmur2}$
- DE$^{Tac1}$
- DE$^{Sox5::Qrfpr}$
- MIL$^{Rorb}$
- MIL$^{Tlap2b}$
- MIP$^{Arhgap6}$
- MIP$^{Satb2}$
- MIP$^{Tlap2b}$
- Renshaw$^{Calb1}$
- VIL/V1$^{Foxp2::Nr4a2}$
- VIL/V1/Ia$^{Foxp2::Pvalb}$
- VIP/V1$^{Foxp2}$
- VIP/V1$^{Mafa}$
- VIP/V1$^{Pou6f2}$
- VCL$^{Lama2}$
- VCL$^{Nr5a2}$
- VCL$^{Sox6}$
- VIL/V0d$^{Bhlhe22::Pdm8}$
- VIL/V1$^{Sp8}$
- VIP/V2b$^{Gata2::Gata3}$
- MEL$^{Lmx1b::Myo5b}$
- MEL$^{Lmx1b::Satb1::Ankfn1}$
- VE$^{Gap43}$
- VEL$^{Syt10::Nr4a2}$
- MEP$^{Lmx1b::Ankfn1}$
- MEP$^{Lmx1b::Cep112}$
- Progenitor neurons
- VEL/V2a$^{Vsx2}$
- VEP/V2a$^{Vsx2::Shox2}$
- VEP/V0c$^{Chat::Pitx2}$
- VEP/V0g$^{Pitx2::Slc17a6}$
- VEP/V0v$^{Evx1}$
- MEL$^{Maf}$
- MEP$^{Lmx1b::Nms}$
- VEP$^{Bnc2::Pou6f2}$
- VEP$^{Bnc2::Rxfp1}$
- VEP/CCN$^{Gdnf}$
- VEP$^{Lhx9::Prlr}$
- VEP$^{Lhx9::Prlr::Mdga1}$
- VEP/V3$^{Sim1}$
- VEP/V2a$^{Vsx2}$

**Supplementary Fig. 5 | Clustering tree of 180 cell types and subtypes in the snRNA-seq atlas.**
**a,** Clustering tree of the mouse spinal cord, revealing the hierarchical relationships between spinal cord cell types across levels 1 to 3 in the taxonomy, with cell types at level 3 highlighted. Text at the top of the tree shows the clades of the clustering tree corresponding to the major cell types of the mouse spinal cord (i.e., level 1 in the taxonomy).
**b,** As in **a,** but showing level 4 in the taxonomy.
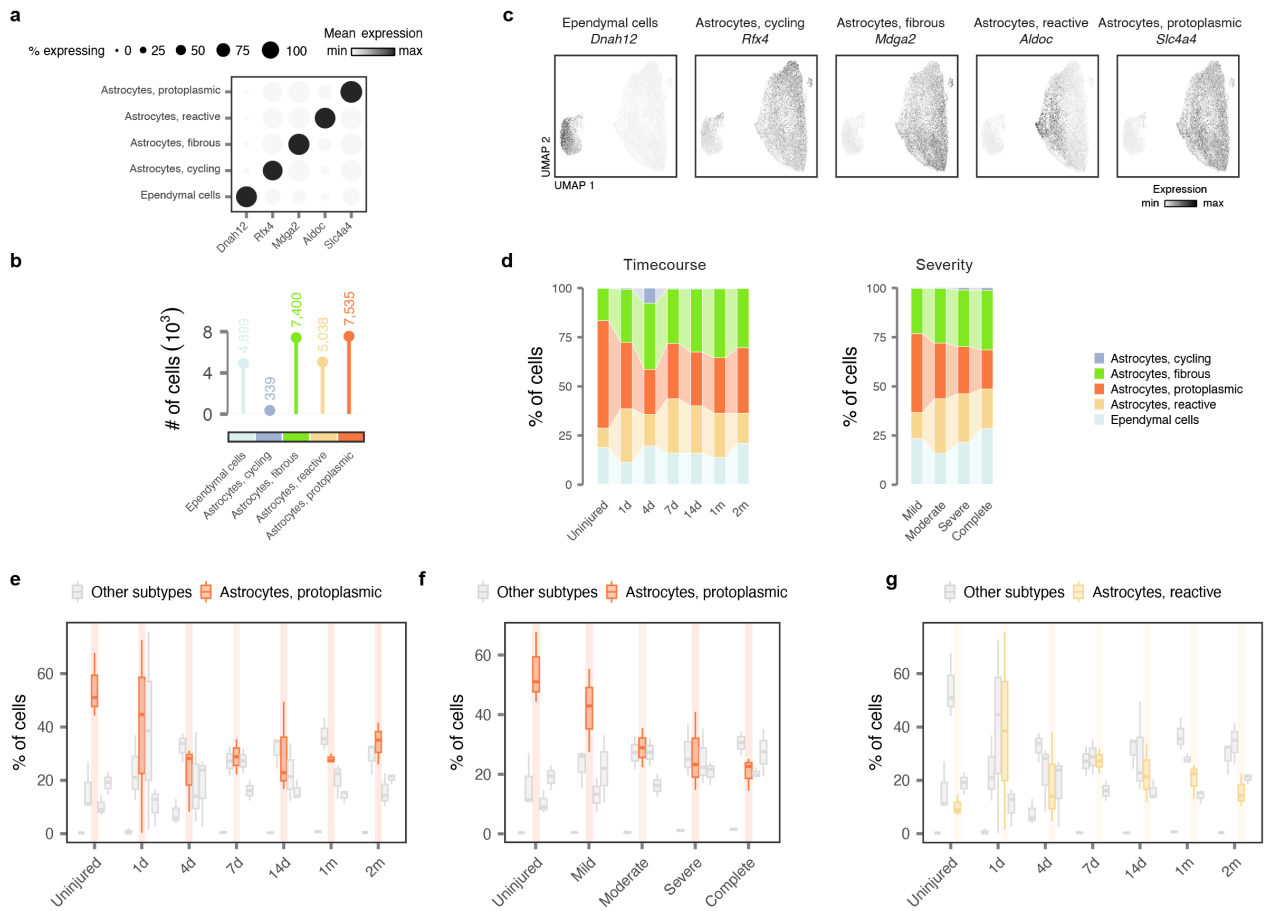**c,** As in **a,** but showing level 5 in the taxonomy.
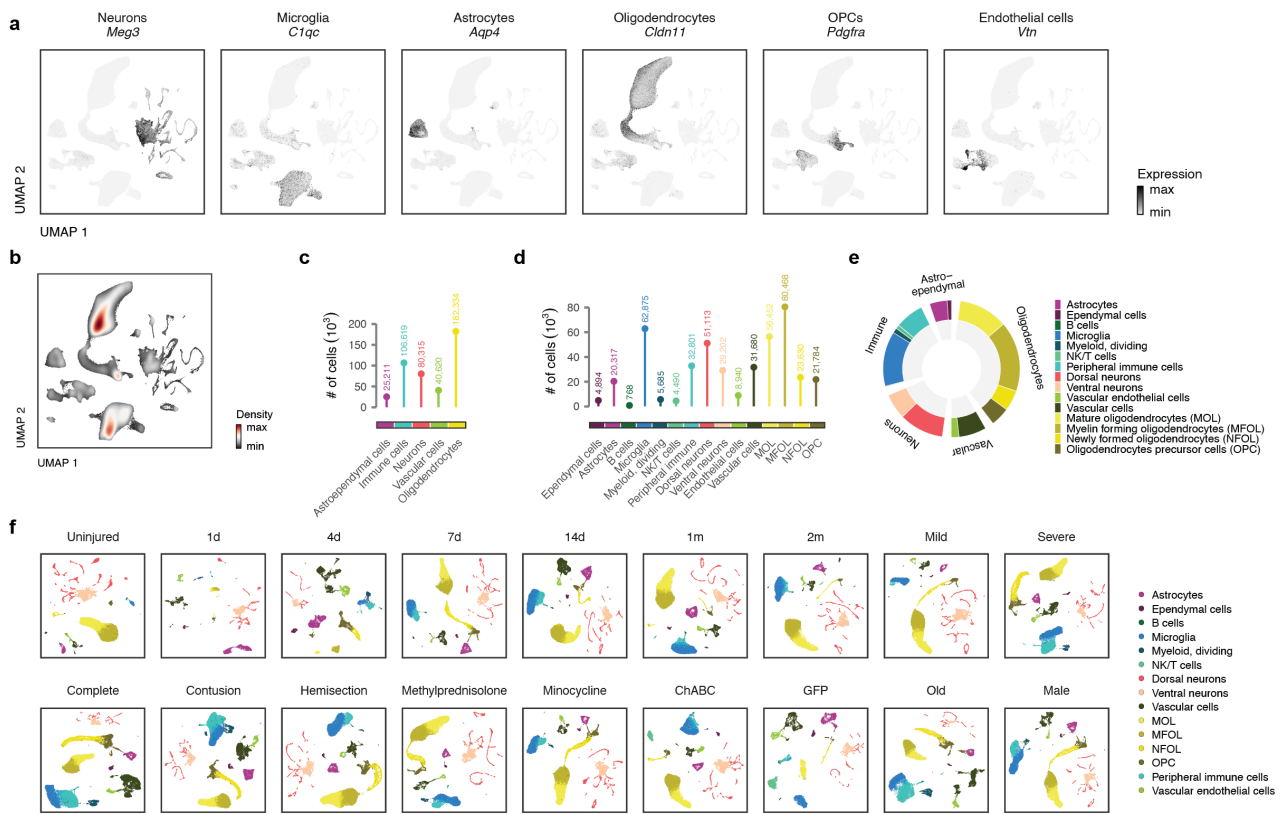
**Supplementary Fig. 6 | Annotation of major cell types in the snRNA-seq atlas.**
**a,** UMAP visualization showing expression of key marker genes for the major cell types of the mouse spinal cord.
**b,** UMAP visualization showing the density of individual nuclei within the UMAP embedding.
**c,** Number of nuclei from each major (level 1) cell type identified across all experimental conditions.
**d,** Number of nuclei from each level 2 cell type identified across all experimental conditions.
**e,** Proportions of nuclei from each level 1 (inner circle) and level 2 (outer circle) across all experimental conditions.
**f,** UMAP visualizations of each individual experimental condition in the snRNA-seq atlas, colored by level 2 cell type.
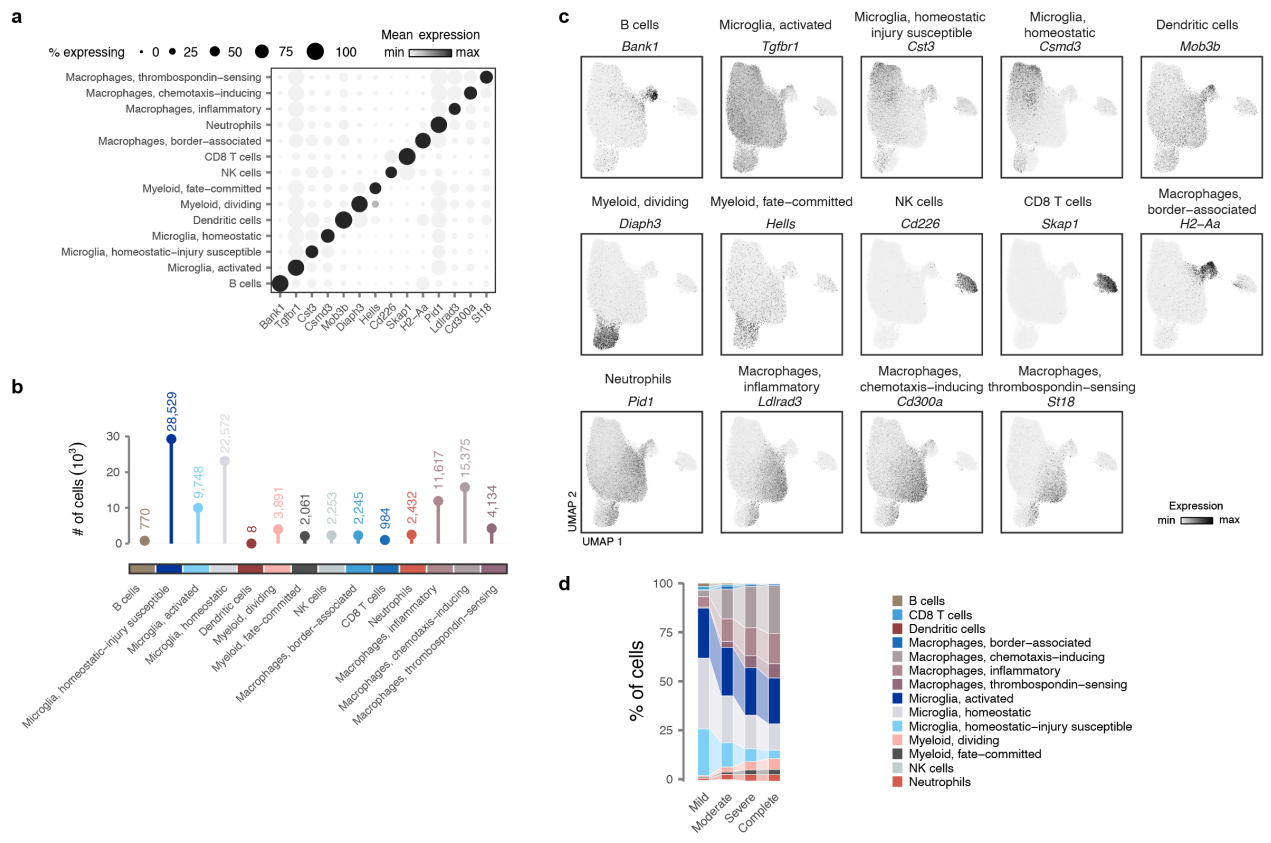
**Supplementary Fig. 7 | Annotation of immune cell subtypes in the snRNA-seq atlas.**
**a,** Dot plot showing expression of key marker genes for immune cell subtypes.
**b,** Number of nuclei from each immune cell subtype identified across all experimental conditions.
**c,** UMAP visualization showing expression of key marker genes for immune cell subtypes.
**d,** Sankey diagram showing the proportions of each astroependymal cell subtype across injury severities.

**Supplementary Fig. 8 | Annotation of astroependymal cell subtypes in the snRNA-seq atlas.**

**a,** Dot plot showing expression of key marker genes for astroependymal cell subtypes.

**b,** Number of nuclei from each astroependymal cell subtype identified across all experimental conditions.

**c,** UMAP visualization showing expression of key marker genes for astroependymal cell subtypes.

**d,** Sankey diagrams showing the proportions of each astroependymal cell subtype across timepoints, left, and injury severities, right.

**e,** Boxplot highlighting the proportions of protoplasmic astrocytes within individual libraries from the timecourse experiment, as compared to all other astroependymal cell subtypes.

**f,** Boxplot highlighting the proportion of protoplasmic astrocytes within individual libraries from the severity experiment, as compared to all other astroependymal cell subtypes.

**g,** Boxplot highlighting the proportion of reactive astrocytes within individual libraries from the timecourse experiment, as compared to all other astroependymal cell subtypes.
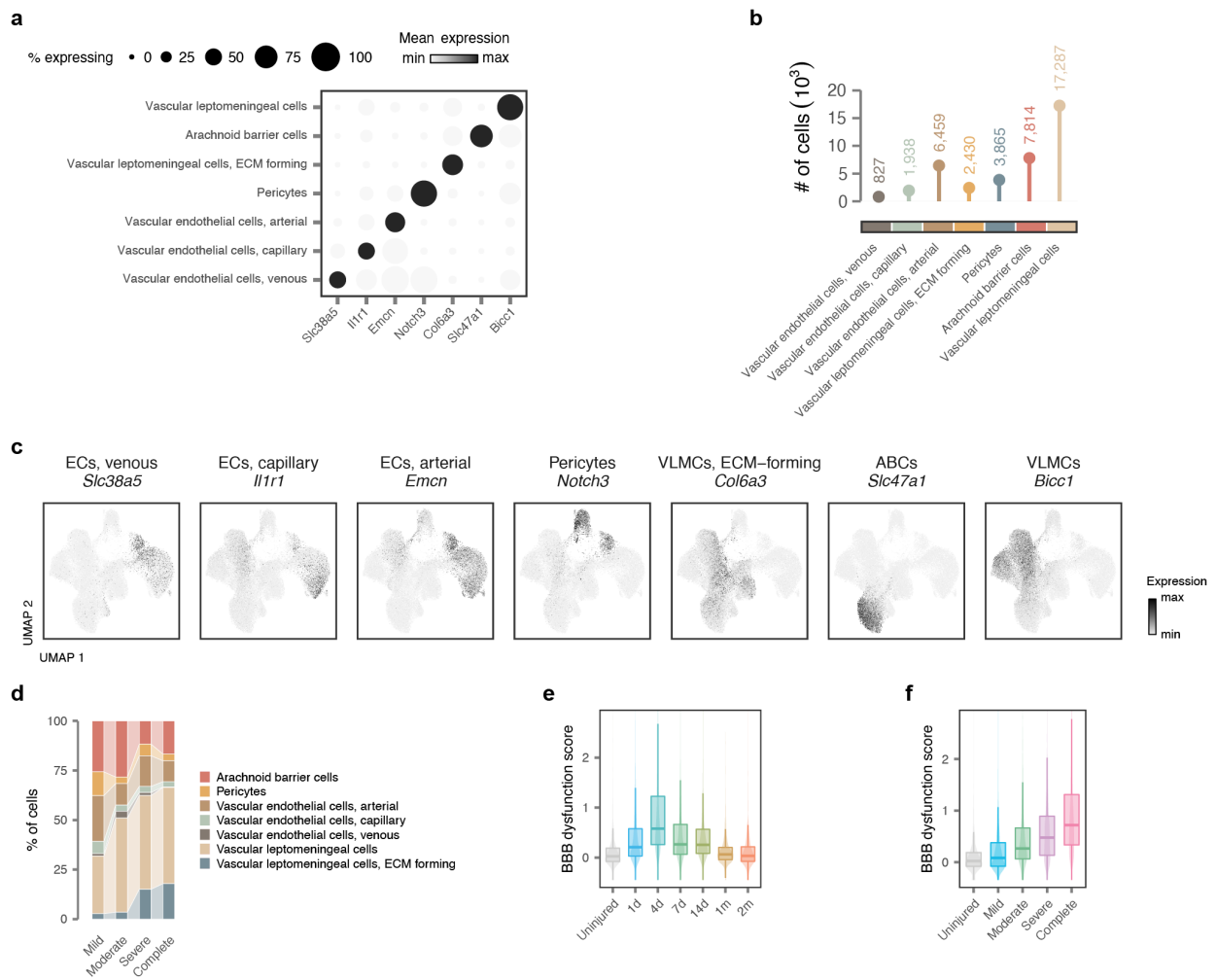
**Supplementary Fig. 9 | Annotation of vascular cell subtypes in the snRNA-seq atlas.**

**a,** Dot plot showing expression of key marker genes for vascular cell subtypes.

**b,** Number of nuclei from each vascular cell subtype identified across all experimental conditions.

**c,** UMAP visualization showing expression of key marker genes for vascular cell subtypes.

**d,** Sankey diagram showing the proportions of each vascular cell subtype across injury severities.

**e,** Average expression of the BBB dysfunction module in vascular cells across timepoints.

**f,** Average expression of the BBB dysfunction module in vascular cells across injury severities.
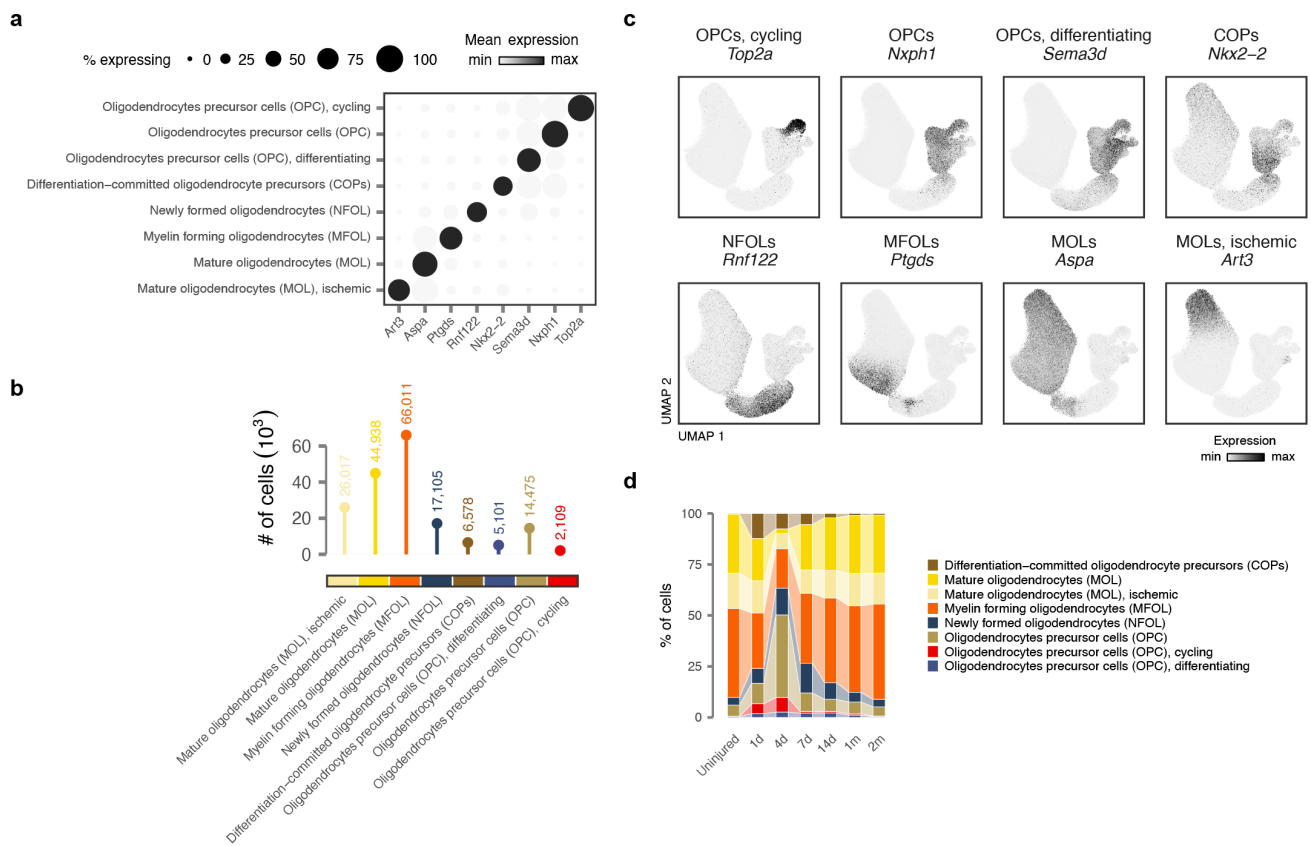
**Supplementary Fig. 10 | Annotation of oligodendrocyte subtypes in the snRNA-seq atlas.**

**a,** Dot plot showing expression of key marker genes for oligodendrocyte subtypes.

**b,** Number of nuclei from each oligodendrocyte subtype identified across all experimental conditions.

**c,** UMAP visualization showing expression of key marker genes for oligodendrocyte subtypes.

**d,** Sankey diagram showing the proportions of each oligodendrocyte subtype across timepoints.
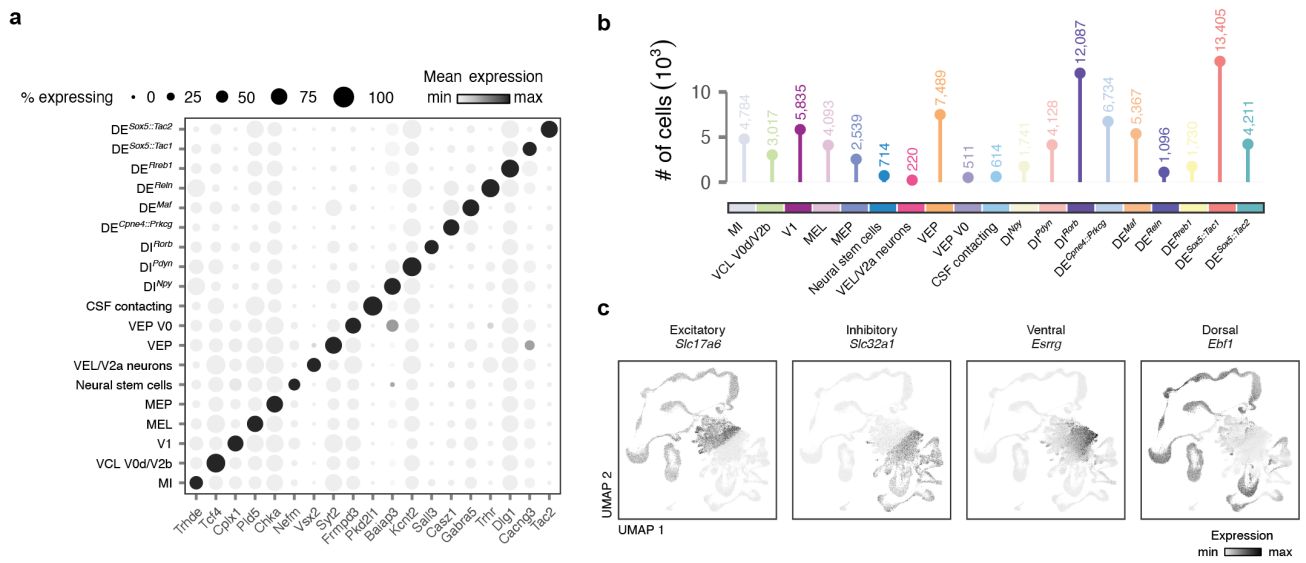
**Supplementary Fig. 11 | Annotation of neuron subtypes in the snRNA-seq atlas.**

**a,** Dot plot showing expression of one key marker gene for each level 4 neuron subtype in the mouse spinal cord.

**b,** Number of nuclei from each level 4 neuron subtype identified across all experimental conditions.

**c,** UMAP visualization showing expression of classical excitatory-inhibitory and dorsal-ventral marker genes within neurons in the mouse spinal cord.
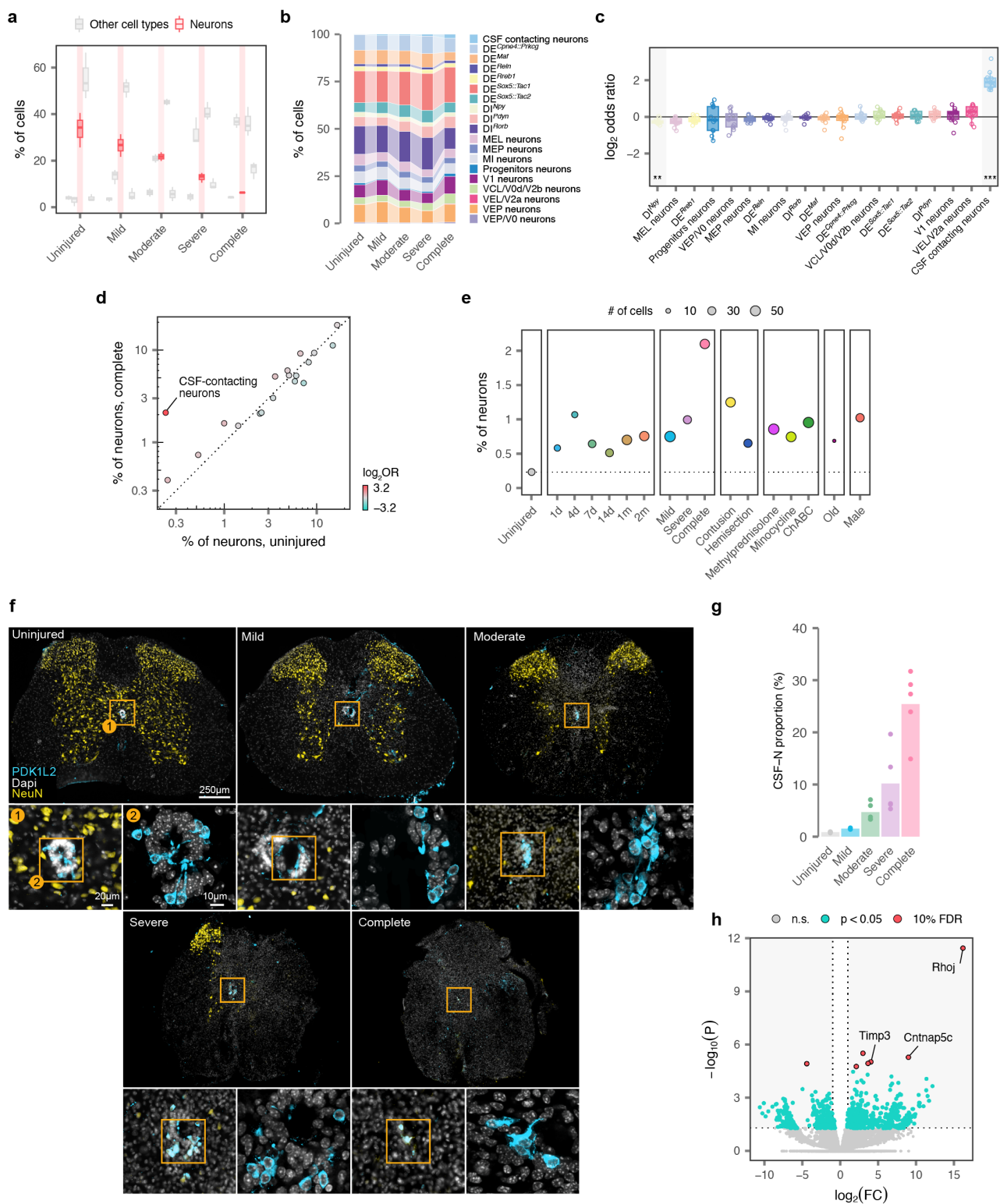
**Supplementary Fig. 12 | Neuronal susceptibility and resilience to SCI.**

**a,** Boxplot highlighting the proportion of neurons within individual libraries from the severity experiment, as compared to other major cell types.

**b,** Sankey diagram showing the proportions of each level 4 neuron subtype across injury severities.

**c,** Boxplot showing the $\log_2$-odds ratio comparing the proportions of neurons from each level 4 subtype between the uninjured spinal cord, for all comparisons involving the injured spinal cord at 7 days post-injury. Cerebrospinal fluid-contacting neurons are the lone subpopulation to exhibit statistically significant resilience following SCI. **, $p < 0.01$; ***, $p < 0.001$.

**d,** Scatterplot highlighting an individual comparison from **c,** showing the proportions of neurons from each level 4 subtype in the uninjured spinal cord, x-axis, and 7 days after a complete injury, y-axis. Color shows the $\log_2$-odds ratio. Cerebrospinal fluid-contacting neurons are highlighted.

**e,** Proportion, y-axis, and absolute number, point size, of cerebrospinal fluid-contacting neurons recovered from each experimental condition. Dotted line shows the proportion of cerebrospinal fluid-contacting neurons in the uninjured spinal cord.

**f,** Representative histological photomicrographs show injured spinal cords across injury severities after staining for NeuN and PKD1L2, a marker of cerebrospinal fluid-contacting neurons.

**g,** Quantification of histological data demonstrating increasing proportions of cerebrospinal fluid-contacting neurons across injury severities.

**h,** Volcano plot showing differentially expressed genes in cerebrospinal fluid-contacting neurons following spinal cord injury, as compared to other neuron subtypes.
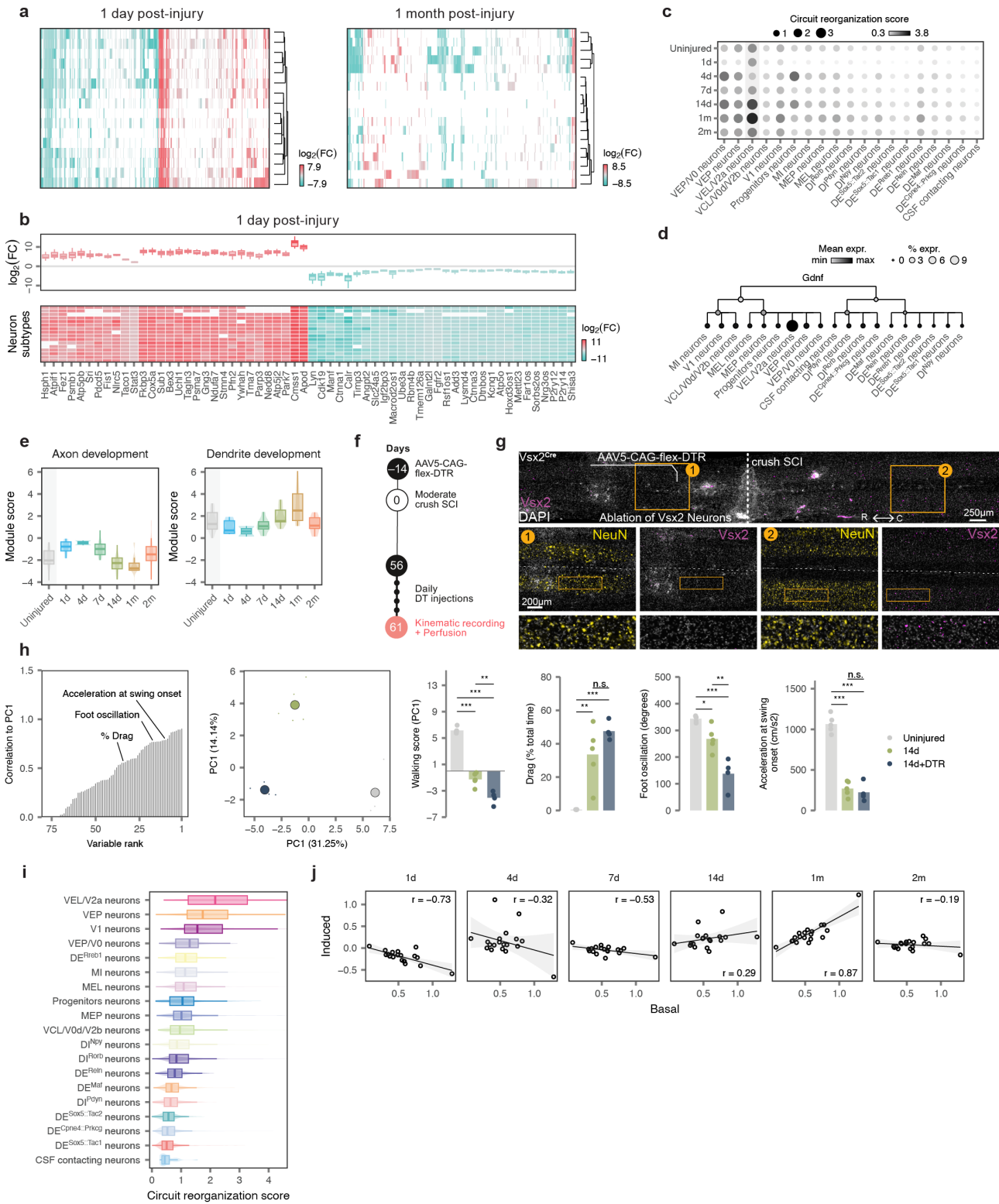
**Supplementary Fig. 13 | Conserved and divergent neuronal responses to SCI.**

**a,** Heatmap showing fold changes for all genes differentially expressed after SCI in at least one level 4 neuron subtype at 1 day, top, and 1 month, bottom, after injury. Patterns of differential expression are broadly conserved at 1 day, but more subtype-specific at 1 month.

**b,** Heatmap showing fold changes for selected genes with broadly conserved patterns of differential expression across level 4 neuron subtypes at 1 day post-injury.

**c,** Dot plot showing average expression of the circuit reorganization module in each level 4 neuron subtype across timepoints.

**d,** Dendrogram showing expression of the growth factor Gdnf across levels 1 to 4 of the neuron taxonomy. Point color shows mean expression in each neuron subtype, while point size reflects the proportion of neurons of that subtype with detectable expression.

**e,** Boxplots showing average expression of the axon development, left, and dendrite development, right modules in Vsx2-expressing neurons across timepoints.

**f,** Timeline of *Vsx2*$^{ON}$ neuron diphtheria toxin ablation experiments. Two weeks before complete crush SCI, animals received an injection of AAVs expressing DTR. At eight weeks, animals received daily injections of diphtheria toxin for 7 days. Kinematics were then recorded and tissue was collected for evaluation.

**g,** Histological verification of *Vsx2*$^{ON}$ neuron ablation in the lower thoracic region. Images show loss of *Vsx2*$^{ON}$ neurons in the thoracic spinal cord, above and below the level of the crush SCI. Bar graph shows the number of *Vsx2*$^{ON}$ neurons found in each animal ($n$ = 4 mice per group, independent samples two-tailed t-test, t = 11.7, p = 2.4 × 10$^{-5}$).

**h,** Locomotor performance in the *Vsx2*$^{ON}$ ablation experiment, as quantified in **Supplementary Fig. 2** ($n$ > 10 gait cycles per mouse, $n$ = 4 mice per group; statistics indicate Tukey HSD tests following one-way ANOVA). n.s., not significant; *, p < 0.05; **, p < 0.01; ***, p < 0.001.

**i,** Boxplot showing average expression of the circuit reorganization module in each level 4 neuron subtype within the uninjured spinal cord. Vsx2-expressing neurons display the highest expression of the circuit reorganization module in the uninjured spinal cord.

**j,** Scatterplots comparing basal expression of the circuit reorganization module in the uninjured spinal cord, x-axis, with the SCI-induced upregulation of this module at each timepoint after injury, y-axis, for each level 4 neuron subtype. Inset text shows the Pearson correlation. Basal and induced expression of the circuit reorganization module is maximally correlated at 1 month post-injury, coinciding with the temporal window of opportunity for natural recovery after SCI.
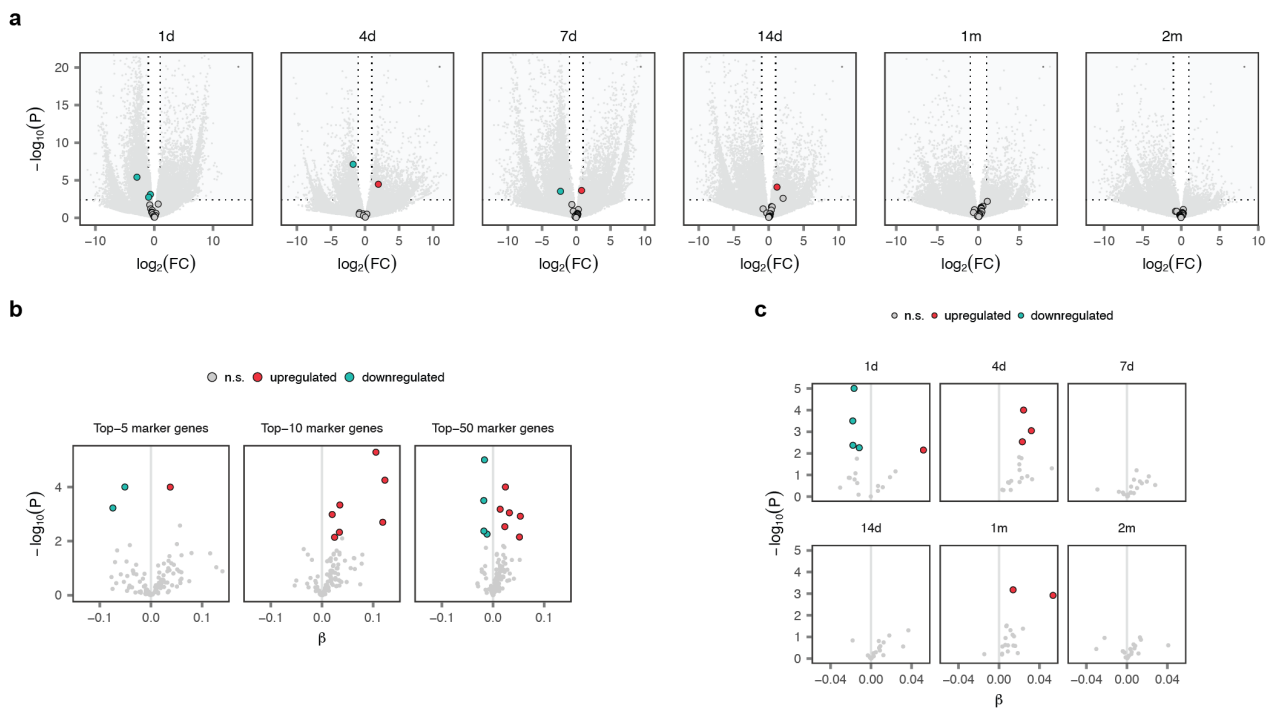
**Supplementary Fig. 14 | Neurons remain differentiated after SCI.**

**a,** Volcano plots showing differential expression for all level 4 neuron subtypes simultaneously across timepoints. Enlarged points represent the key marker genes for each neuron subtype shown in **Supplementary Fig. 11a**. Marker genes shown in grey show no evidence of differential expression after SCI in their respective neuron subtype.

**b,** Volcano plot showing differential expression for averaged gene expression modules comprising the top 5, top 10, or top 50 marker genes identified for each level 4 neuron subtype by unbiased comparisons with all other neurons, simultaneously across all timepoints. The vast majority of marker gene modules show no evidence of downregulation after SCI in their respective neuron subtype.

**c,** As in **b,** but showing differential expression for averaged gene expression modules comprising the top 50 marker genes for each level 4 neuron subtype, shown separately for each condition in the timecourse experiment.

**Expression of facilitating molecules in the injured spinal cord**
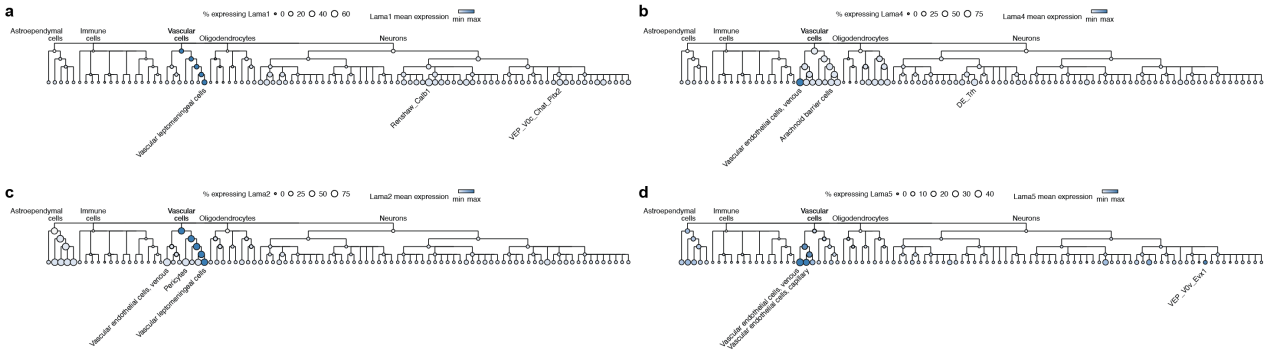
**Expression of inhibitory molecules in the injured spinal cord**
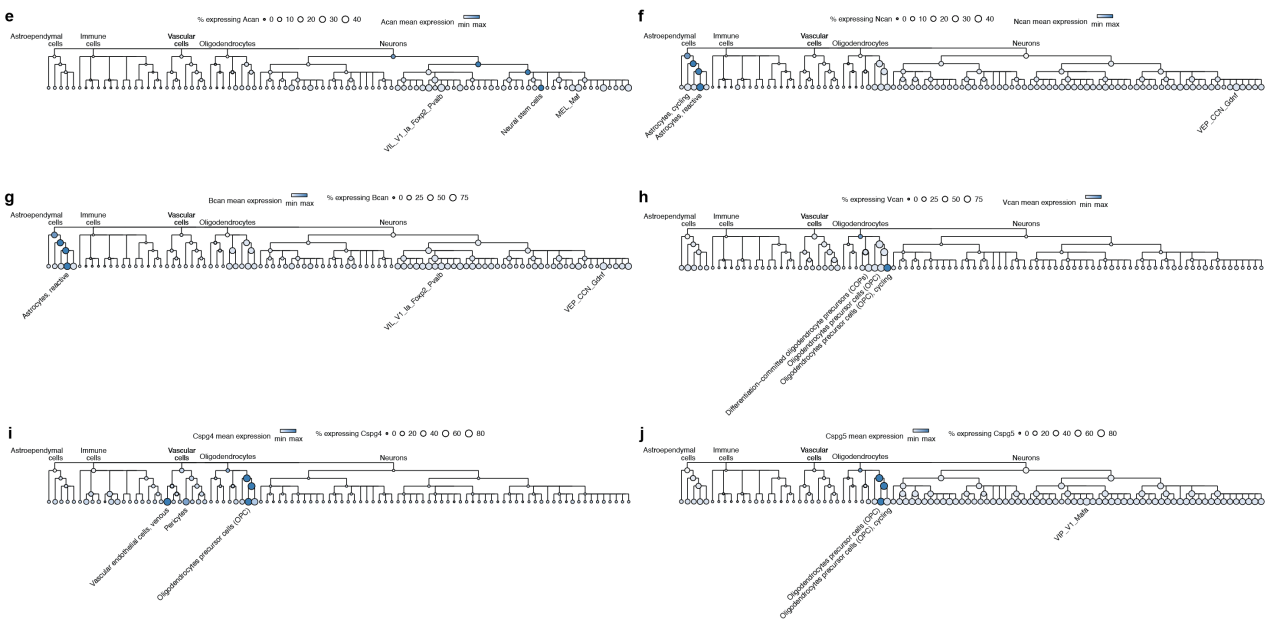
**Effects of ChABC on the injured spinal cord**
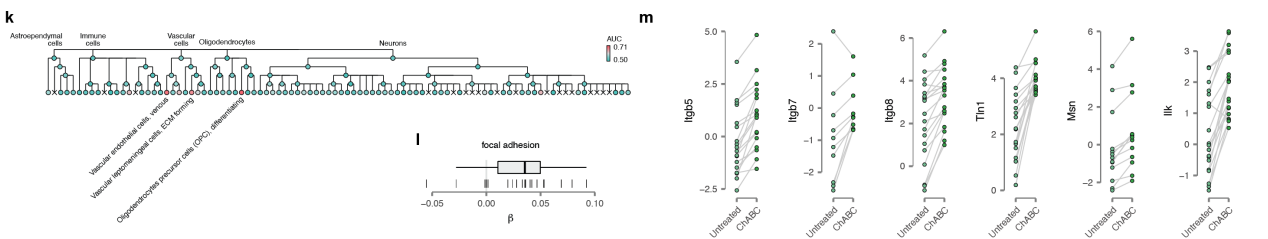
**Supplementary Fig. 15 | Facilitating and inhibiting molecule expression in the injured spinal cord.**

**a-j,** Dendrograms showing expression of selected facilitating and inhibiting molecules across the cellular taxonomy of the spinal cord. Point color shows mean expression in each cell type, while point size reflects the proportion of cells with detectable expression.

**k,** Dendrogram showing cell type prioritizations assigned by Augur across the cellular taxonomy of the spinal cord after treatment with ChABC. The three level 5 cell types with the highest AUCs are annotated.

**l,** Upregulation of genes associated with focal adhesion across level 4 neuron subtypes after ChABC treatment. Vertical lines show coefficients estimated by a linear mixed model within each neuron subtype.

**m,** Differential expression of individual genes associated with focal adhesion across level 4 neuron subtypes after ChABC treatment. Points show pseudobulk gene expression values in counts per million. Lines connect each neuron subtype across experimental conditions.
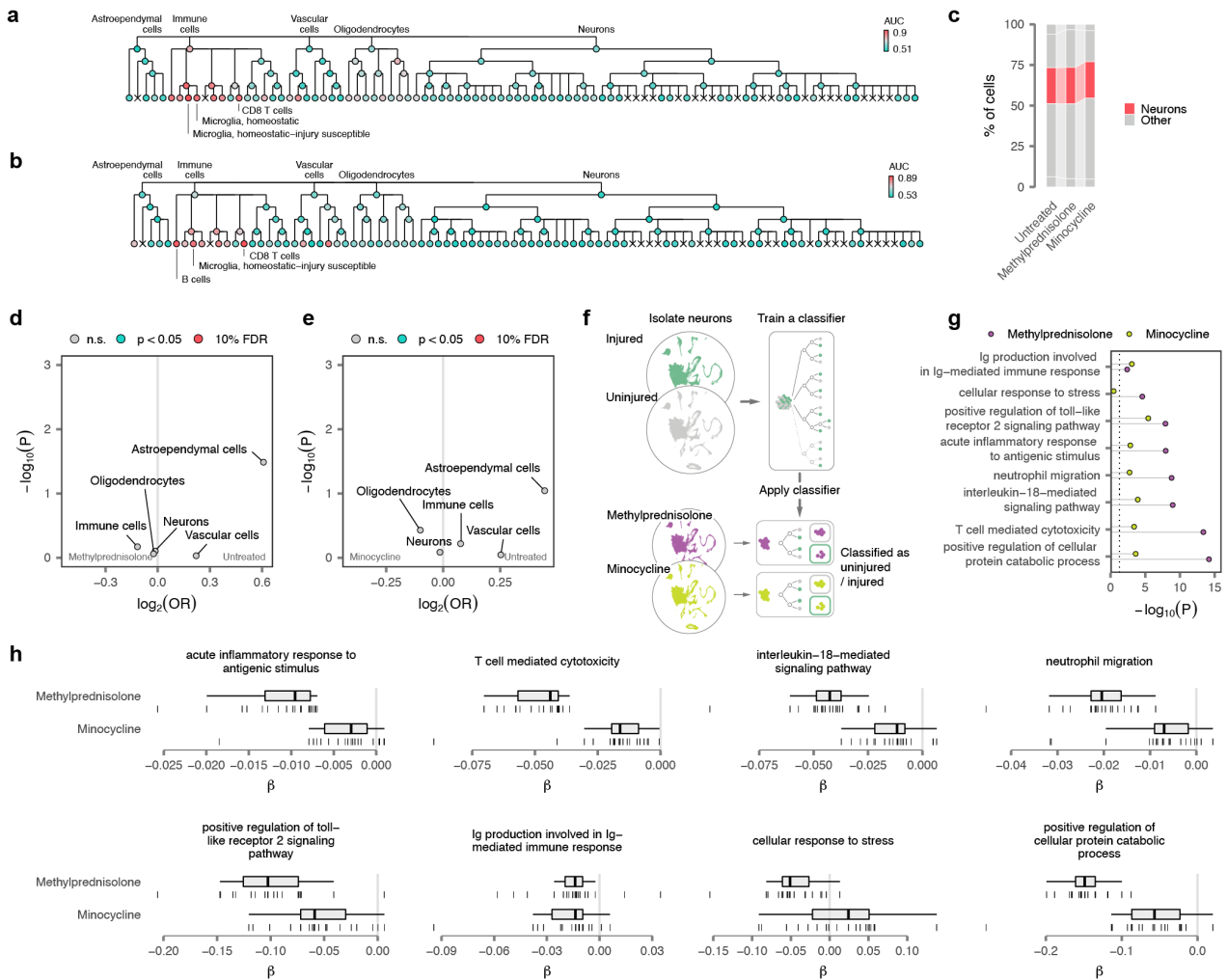
**Supplementary Fig. 16 | Immunomodulation does not confer neuroprotection after spinal cord injury.**

**a,** Dendrogram showing cell type prioritizations assigned by Augur across the cellular taxonomy of the spinal cord after treatment with methylprednisolone. The three level 5 cell types with the highest AUCs are annotated.

**b,** Dendrogram showing cell type prioritizations assigned by Augur across the cellular taxonomy of the spinal cord after treatment with minocycline. The three level 5 cell types with the highest AUCs are annotated.

**c,** Sankey diagram showing the proportions of neurons recovered from the injured spinal cord after treatment with methylprednisolone or minocycline, as compared to untreated controls.

**d,** Volcano plot showing the statistical significance of changes in major cell type proportions after treatment with methylprednisolone, as compared to untreated controls. No statistically significant differences in cell type proportions are detected after treatment.

**e,** Volcano plot showing the statistical significance of changes in major cell type proportions after treatment with minocycline, as compared to untreated controls. No statistically significant differences in cell type proportions are detected after treatment.

**f,** Schematic depicting the procedure by which neurons are assigned to uninjured versus injured transcriptional phenotypes by a machine-learning classifier.
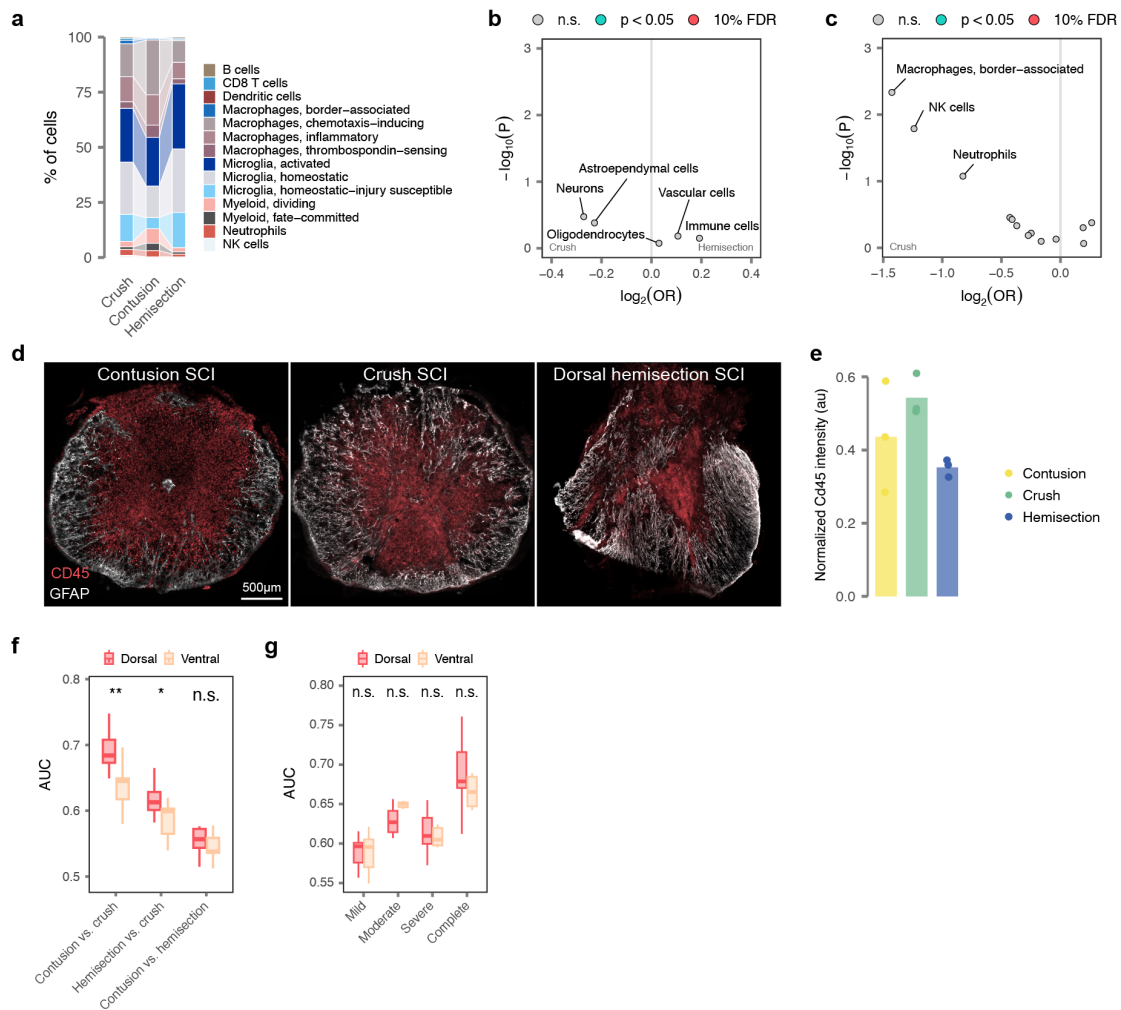
**g,** Lollipop plot showing the statistical significance of downregulation for each of the gene modules shown in in **h** after methylprednisolone or minocycline treatment.

**h,** Downregulation of gene modules associated with cellular stress across level 4 neuron subtypes after methylprednisolone or minocycline treatment. Vertical lines show coefficients estimated by a linear mixed model within each neuron subtype.
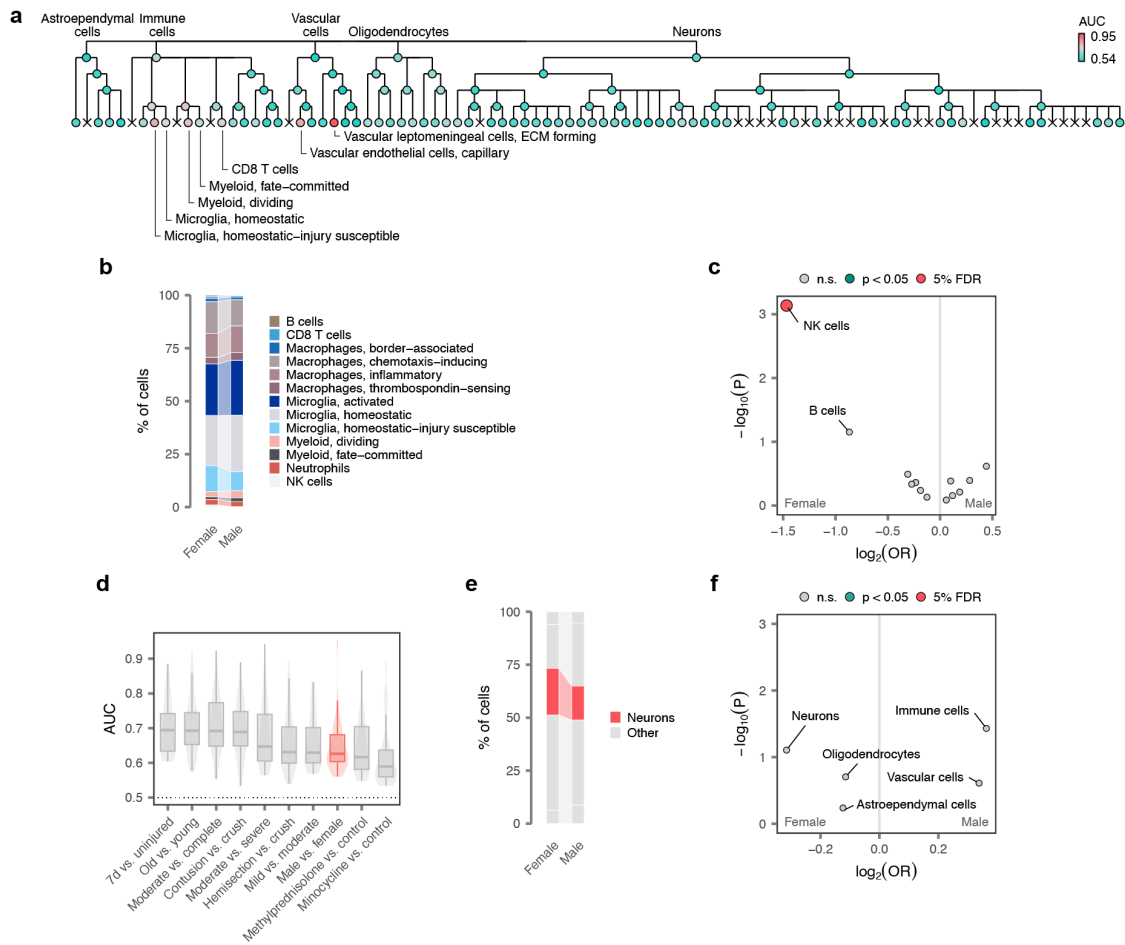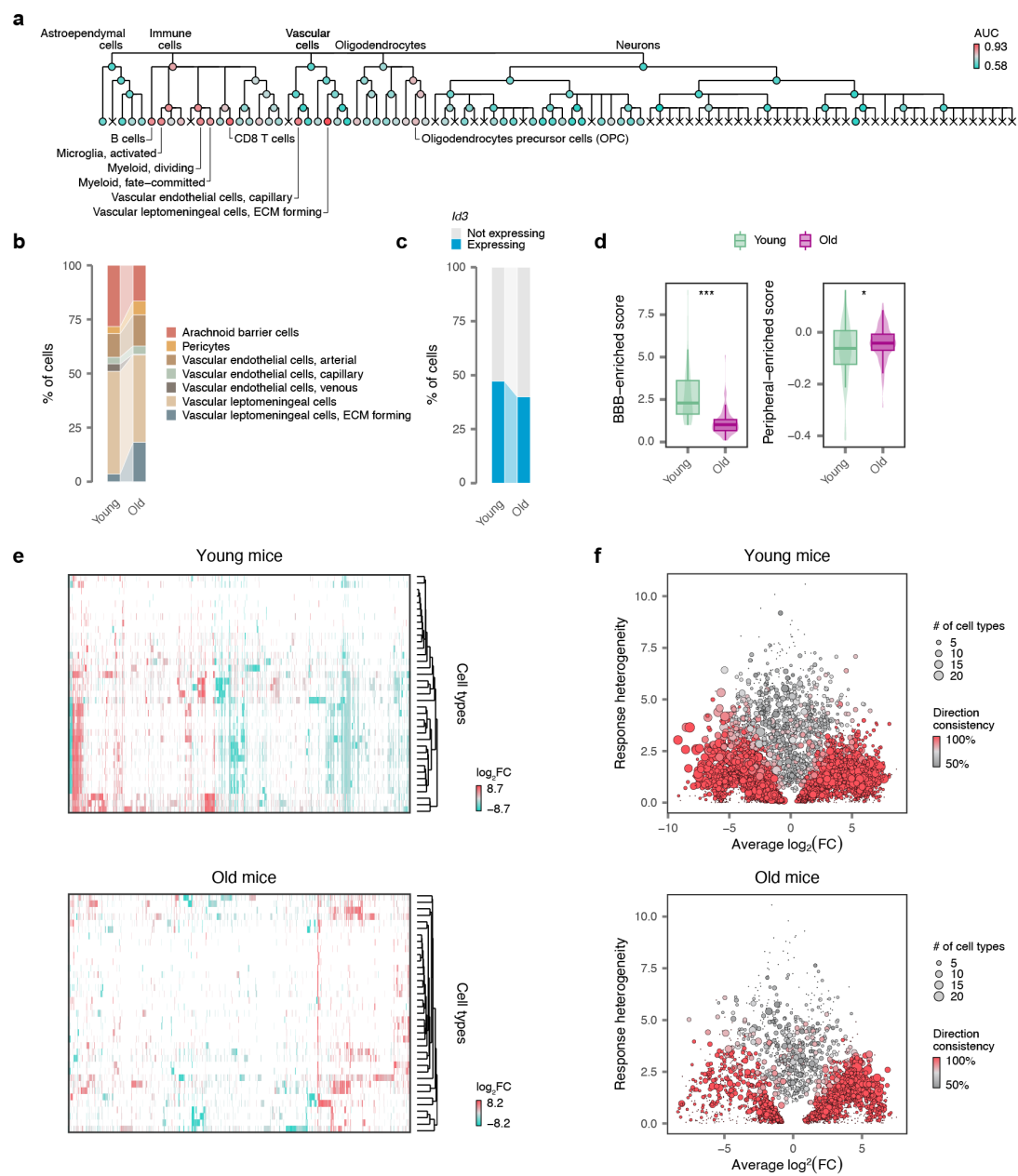
**Supplementary Fig. 17 | Sexual dimorphism in the response to SCI.**

**a,** Dendrogram showing cell type prioritizations assigned by Augur across the cellular taxonomy of the spinal cord in comparisons of male and female mice. The seven level 5 cell types with the highest AUCs are annotated.

**b,** Sankey diagram showing the proportions of immune cell subtypes recovered from the spinal cords of male versus female mice.

**c,** Volcano plot showing the statistical significance of changes in immune cell subtype proportions between male and female mice.

**d,** Boxplot showing the intensity of transcriptional perturbations within level 4 cell types, as quantified by Augur, in all comparisons involving the injured spinal cord at 7 days post-injury. The transcriptional perturbation between male and female mice is among the most subtle in the snRNA-seq atlas.

**e,** Sankey diagram showing the proportions of major cell types recovered from the spinal cords of male versus female mice.

**f,** Volcano plot showing the statistical significance of changes in major cell type proportions between male and female mice. No statistically significant differences in cell type proportions are detected.

**Supplementary Fig. 18 | Cellular divergence between animal models of SCI.**

**a,** Sankey diagram showing the proportions of immune cell subtypes across crush, contusion, and hemisection injury models.

**b,** Volcano plot showing the statistical significance of changes in major cell type proportions between crush and hemisection injuries. No statistically significant differences in cell type proportions are detected.

**c,** Volcano plot showing the statistical significance of changes in immune cell subtype proportions between crush and hemisection injuries. No statistically significant differences in cell type proportions are detected.

**d,** Histological photomicrographs show injured spinal cords across injury models after staining for GFAP and CD45.

**e,** Quantification of immune infiltration at the lesion epicentre across injury models. The extent of immune infiltration was quantified from coronal sections immunolabeled for CD45. No comparisons were significant (all p > 0.05, Tukey HSD tests following one-way ANOVA).

**f,** Boxplots showing the average intensity of transcriptional perturbations in dorsal versus ventral neurons, as quantified by Augur, in comparisons of mice subjected to crush, contusion, and hemisection injuries. *, p < 0.05; **, p < 0.01; n.s., not significant.

**g,** Boxplots showing the average intensity of transcriptional perturbations in dorsal versus ventral neurons, as quantified by Augur, in comparisons of mice subjected to crush injuries of increasing severity. n.s., not significant.

**Supplementary Fig. 19 | Catastrophic failure of tripartite barrier formation in old mice.**

**a,** Dendrogram showing cell type prioritizations assigned by Augur across the cellular taxonomy of the spinal cord in comparisons of young and old mice at seven days post-injury. The eight level 5 cell types with the highest AUCs are annotated.

**b,** Sankey diagram showing the proportions of vascular cell subtypes in young and old mice at seven days post-injury.

**c,** Sankey diagram showing the proportions of astroependymal cells expressing *Id3* in young and old mice at seven days post-injury.

**d,** Average expression of the BBB identity module, left, and the peripheral vascular identity module, right, in capillary endothelial cells from young and old mice at seven days post-injury.

**e,** Heatmap showing log-fold changes for all genes differentially expressed in at least one level 4 cell type in comparisons of injured versus uninjured mice, top, and old versus young mice, bottom.

**f,** Heterogeneity of differential expression in comparisons of injured versus uninjured mice, top, and old versus young mice, bottom. Each point shows a gene differentially expressed in at least one level 4 cell type. The x-axis shows the average log2-fold change across all cell types; the y-axis shows the standard deviation of the $\log_2$-fold change across cell types ("response heterogeneity"); point size reflects the total number of cell types in which the gene is differentially expressed; and point color reflects the proportion of cell types in which the sign of the log2-fold change was the same as the modal sign ("direction consistency").
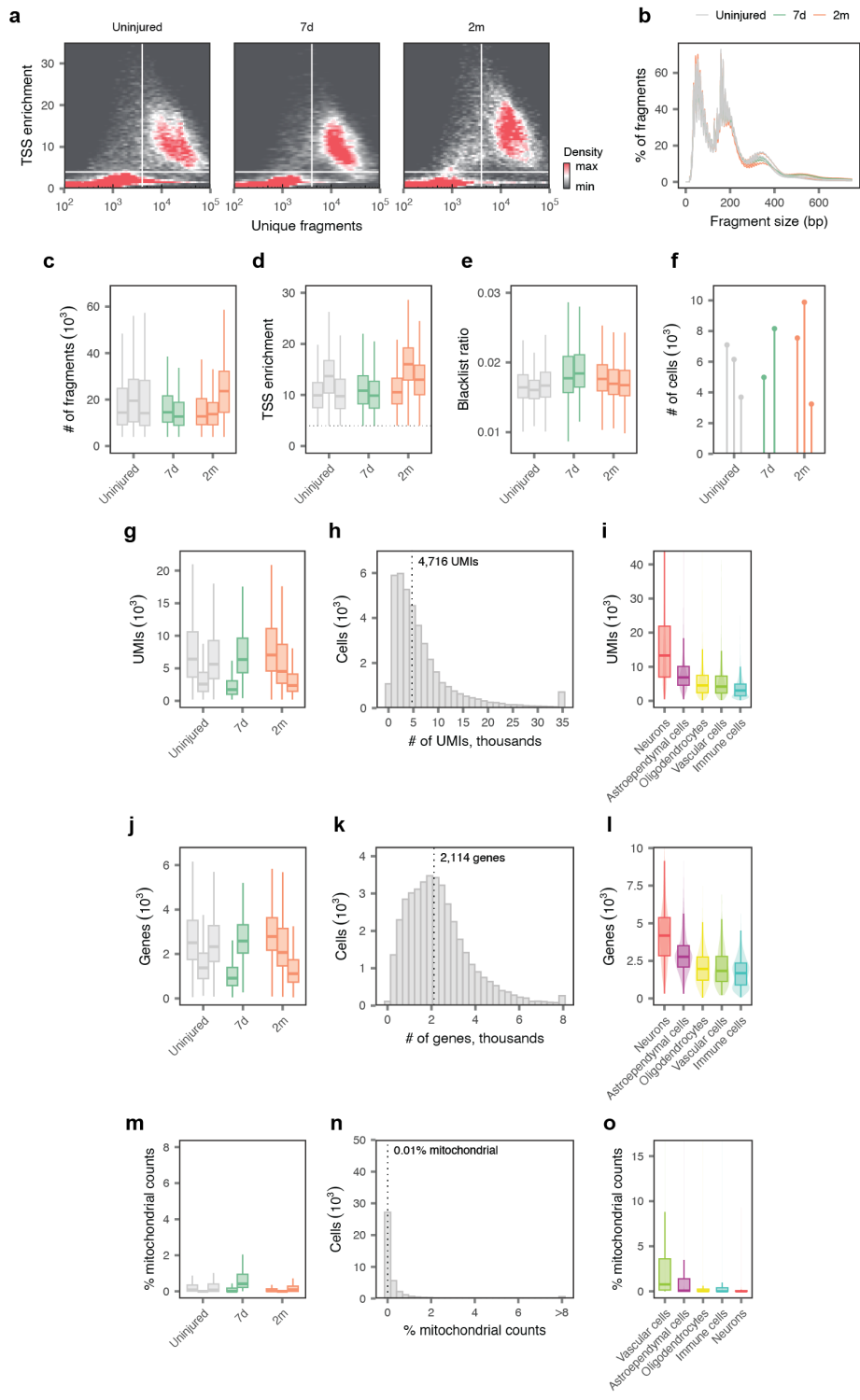
**Supplementary Fig. 20 | Quality control of the multiome atlas.**
**a-f,** Quality control of the ATAC modality.
**a,** TSS enrichment score versus the number of unique fragments per cell in barcodes from each experimental condition. Solid lines show the thresholds used for initial quality control of the ATAC modality in the multiome atlas.
**b,** Aggregate fragment size distributions for barcodes passing initial quality control thresholds in the ATAC modality of the multiome atlas.
**c,** Number of fragments per nucleus in individual libraries from each experimental condition.
**d,** TSS enrichment scores per nucleus in individual libraries from each experimental condition.
**e,** Proportion of reads mapping to blacklist regions per nucleus in individual libraries from each experimental condition.
**f,** Number of nuclei passing quality control for each individual library in the multiome atlas.
**g-o,** Quality control of the RNA modality.
**g,** Number of unique molecular identifiers (UMIs) per nucleus in individual libraries from each experimental condition.
**h,** Number of UMIs per nucleus, aggregated across all libraries. Inset text shows the median number of UMIs.
**i,** Number of UMIs per nucleus in each major cell type.
**j,** Number of genes detected per nucleus in individual libraries from each experimental condition.
**k,** Number of genes detected per nucleus, aggregated across all libraries. Inset text shows the median number of genes detected.
**l,** Number of genes detected per nucleus in each major cell type.
**m,** Proportion of mitochondrial counts per nucleus in individual libraries from each experimental condition.
**n,** Proportion of mitochondrial counts per nucleus, aggregated across all libraries. Inset text shows the median proportion of mitochondrial counts.
**o,** Proportion of mitochondrial counts per nucleus in each major cell type.
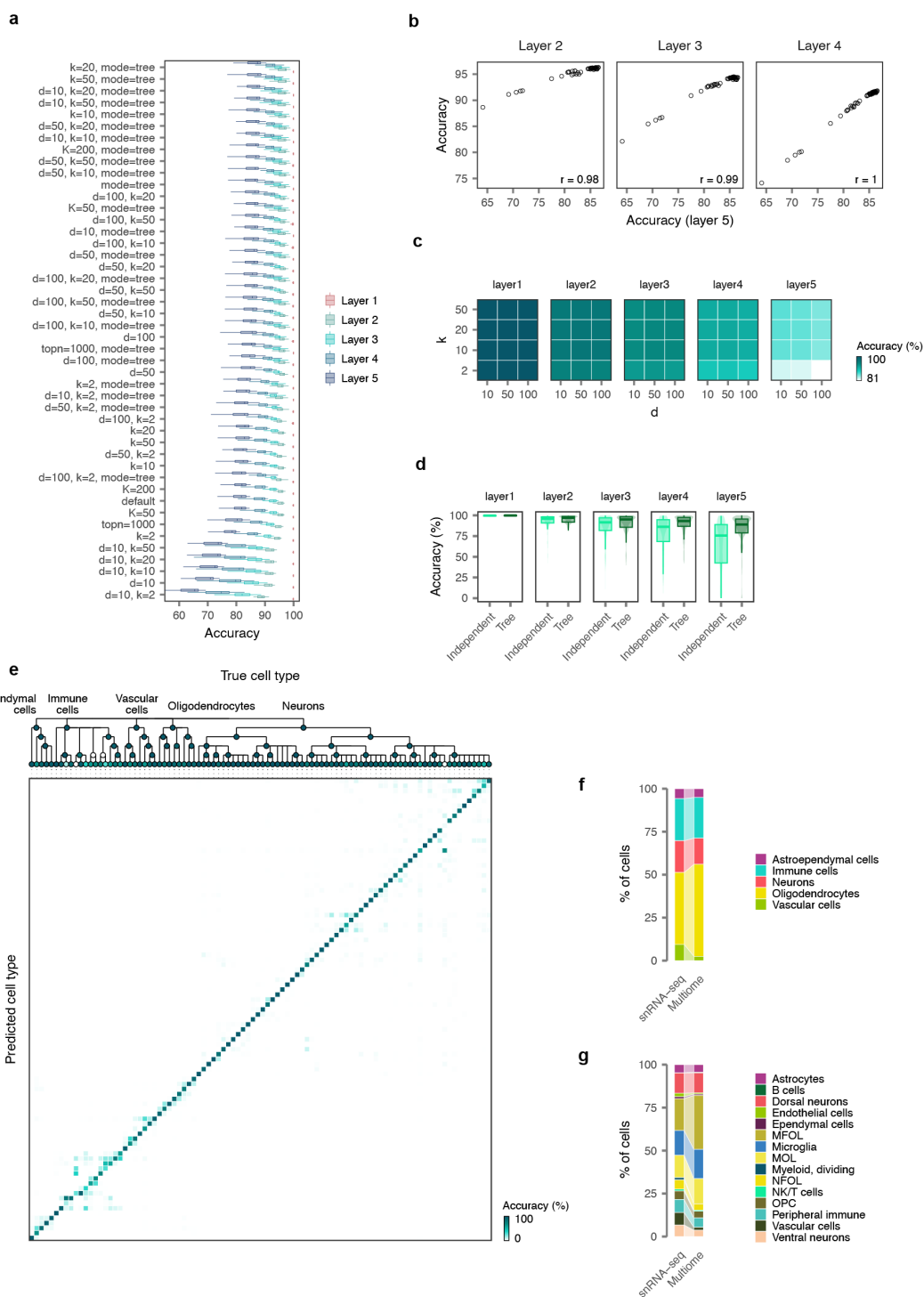
**Supplementary Fig. 21 | Hierarchical transfer of cell type annotations from the snRNA-seq atlas to the multiome atlas.**

**a,** Benchmarking the accuracy of automated cell type assignment by leave-library-out cross-validation on the snRNA-seq atlas. Boxplot shows per-cell-type accuracies in each held-out library after systematically varying the number of nearest-neighbors, k; the number of principal components, d; and the number of soft cluster centroids, K. In addition, we experimented with constraining the potential matches at finer levels of our cellular taxonomy on the basis of cell types assigned at higher levels ("mode=tree").
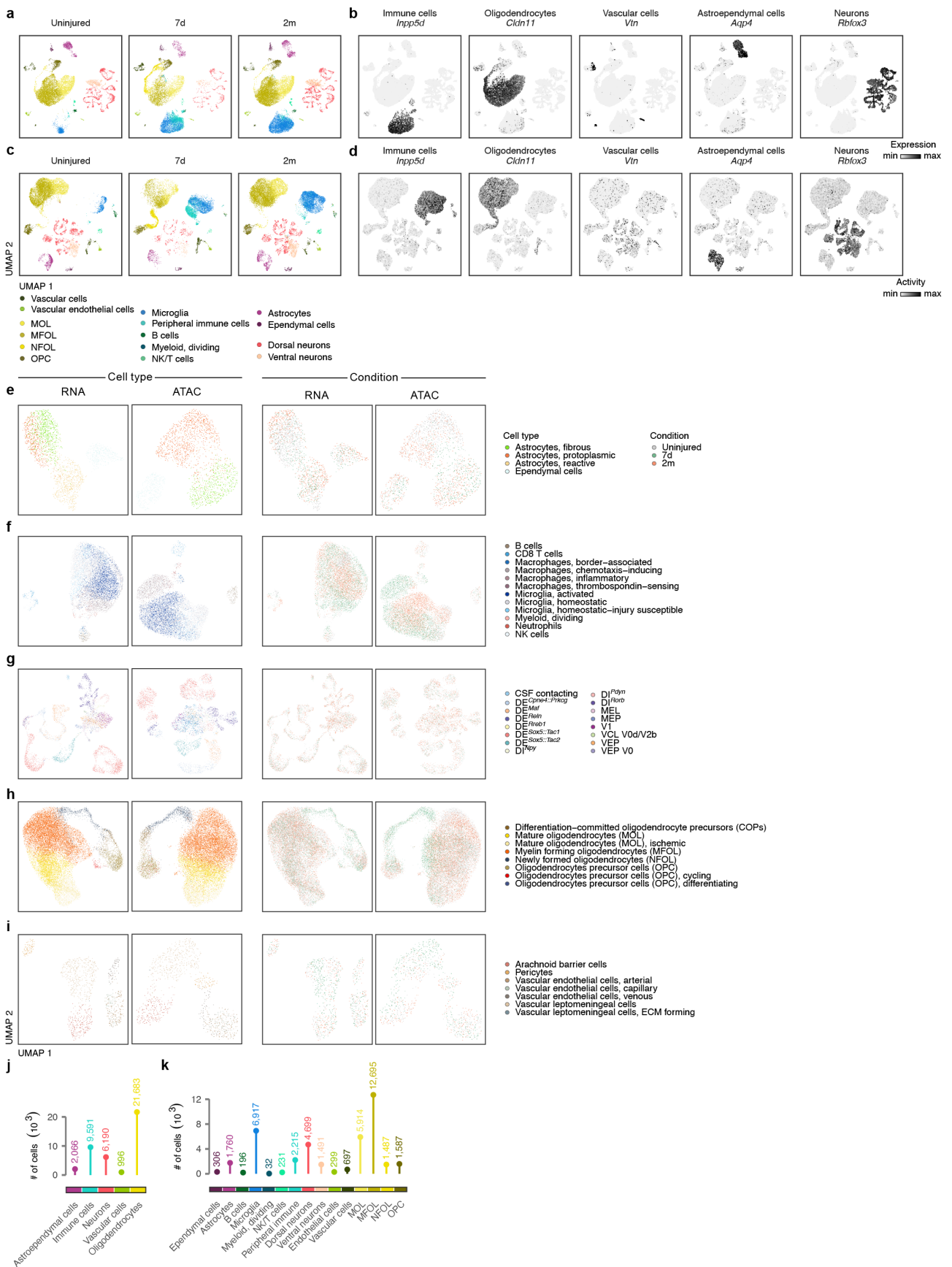
**b,** Correlation between the accuracy of cell type annotation at the finest level of the clustering tree (level 5) and levels 2, 3, and 4, for each hyperparameter combination shown in a. The results for level 1 are not shown because accuracy at this level approximated 100**c,** Impact of varying the the number of nearest-neighbors, k, and the number of principal components, d, on the accuracy of automated cell type assignment in leave-library-out cross-validation.

**d,** Impact of the hierarchical adaptation of cell type annotation transfer, whereby all possible cell types are considered as potential matches at a given resolution ("independent"), or potential matches are constrained based on the cell type annotation at the previous resolution of the clustering tree ("tree"). The hierarchical approach consistently improves accuracy, particularly for lower levels of the clustering tree.

**e,** Performance of automated cell type annotation under the specific parameters used for cell type annotation in the multiome dataset. Top, dendrogram showing the average accuracy of cell type annotation for the complete cellular taxonomy in leave-library-out cross-validation on the snRNA-seq atlas. Bottom, confusion matrix at level 5 of the cellular taxonomy.

**f,** Sankey diagram showing the proportions of major (level 1) cell types in the snRNA-seq versus multiome atlases.

**g,** Sankey diagram showing the proportions of level 2 cell types in the snRNA-seq versus multiome atlases.

**a**

Uninjured    7d    2m

**b**

Immune cells    Oligodendrocytes    Vascular cells    Astroependymal cells    Neurons
*Inpp5d*    *Cldn11*    *Vtn*    *Aqp4*    *Rbfox3*

**c**

Uninjured    7d    2m

**d**

Immune cells    Oligodendrocytes    Vascular cells    Astroependymal cells    Neurons
*Inpp5d*    *Cldn11*    *Vtn*    *Aqp4*    *Rbfox3*

Expression
min ▭ max

UMAP 2

UMAP 1

Activity
min ▭ max

● Vascular cells
● Vascular endothelial cells
● MOL
● MFOL
● NFOL
● OPC

● Microglia
● Peripheral immune cells
● B cells
● Myeloid, dividing
● NK/T cells

● Astrocytes
● Ependymal cells
● Dorsal neurons
● Ventral neurons

── Cell type ──    ── Condition ──

**e**

RNA    ATAC    RNA    ATAC

Cell type
● Astrocytes, fibrous
● Astrocytes, protoplasmic
● Astrocytes, reactive
● Ependymal cells

Condition
● Uninjured
● 7d
● 2m

**f**

● B cells
● CD8 T cells
● Macrophages, border–associated
● Macrophages, chemotaxis–inducing
● Macrophages, inflammatory
● Macrophages, thrombospondin–sensing
● Microglia, activated
● Microglia, homeostatic
● Microglia, homeostatic–injury susceptible
● Myeloid, dividing
● Neutrophils
● NK cells

**g**

● CSF contacting
● DE$^{Cpne4::Prkcg}$
● DE$^{Maf}$
● DE$^{Reln}$
● DE$^{Rreb1}$
● DE$^{Sox5::Tac1}$
● DE$^{Sox5::Tac2}$
● DI$^{Npy}$

● DI$^{Pdyn}$
● DI$^{Rorb}$
● MEL
● MEP
● V1
● VCL V0d/V2b
● VEP
● VEP V0

**h**

● Differentiation–committed oligodendrocyte precursors (COPs)
● Mature oligodendrocytes (MOL)
● Mature oligodendrocytes (MOL), ischemic
● Myelin forming oligodendrocytes (MFOL)
● Newly formed oligodendrocytes (NFOL)
● Oligodendrocytes precursor cells (OPC)
● Oligodendrocytes precursor cells (OPC), cycling
● Oligodendrocytes precursor cells (OPC), differentiating

**i**

● Arachnoid barrier cells
● Pericytes
● Vascular endothelial cells, arterial
● Vascular endothelial cells, capillary
● Vascular endothelial cells, venous
● Vascular leptomeningeal cells
● Vascular leptomeningeal cells, ECM forming

UMAP 2

UMAP 1

**j**    **k**

**Supplementary Fig. 22 | Cell types and subtypes in the multiome atlas.**

**a,** UMAP visualization showing nuclei separately for each experimental condition in the multiome atlas, based on gene expression in the RNA modality and colored by level 2 cell type.

**b,** UMAP visualization showing expression of key marker genes for major cell types in the RNA modality of the multiome atlas.

**c,** UMAP visualization showing nuclei separately for each experimental condition in the multiome atlas, based on chromatin accessibility in the ATAC modality and colored by level 2 cell type.

**d,** UMAP visualization showing gene activity scores of key marker genes for major cell types in the ATAC modality of the multiome atlas.

**e,** UMAP visualization of immune cells in the multiome atlas based on gene expression in the RNA modality or chromatin accessibility in the ATAC modality, and colored by level 2 cell type or experimental condition.

**f,** As in **e,** but for astroependymal cells.

**g,** As in **e,** but for vascular cells.

**h,** As in **e,** but for oligodendrocytes.

**i,** As in **e,** but for neurons.

**j,** Number of nuclei from each major (level 1) cell type identified in the multiome atlas.

**k,** Number of nuclei from each level 2 cell type identified in the multiome atlas.
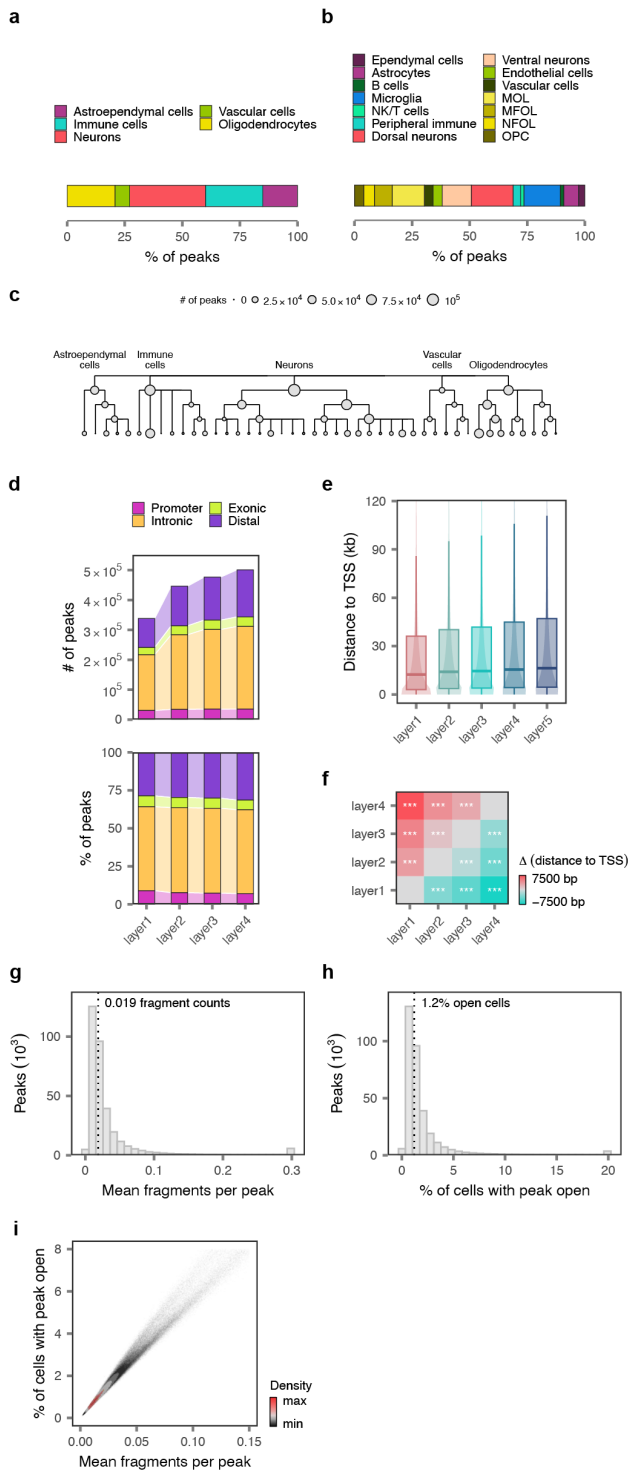
**Supplementary Fig. 23 | Peak calling in the multiome atlas.**

**a,** Number of peaks attributed to each major (level 1) cell type by the iterative overlap-merging procedure in ArchR.

**b,** Number of peaks attributed to each level 2 cell type by the iterative overlap-merging procedure in ArchR.

**c,** Number of peaks attributed to each cell type throughout the cellular taxonomy of the spinal cord by the iterative overlap-merging procedure in ArchR.

**d,** Number, top, and proportion, bottom, of promoter, exonic, intronic, or distal peaks when calling peaks at levels 1 to 4 of the cellular taxonomy.

**e,** Distance to the nearest TSS for peaks called at levels 1 to 4 of the cellular taxonomy.

**f,** Statistical comparison of distance to the nearest TSS for peaks called at levels 1 to 4 of the cellular taxonomy, as shown in **e.** Calling peaks for cell subtypes defined at more granular resolutions leads to improved detection of distal regulatory elements.

**g,** Distribution of the mean fragment counts per cell, for all peaks called at level 4 of the cellular taxonomy.

**h,** Distribution of the mean proportion of cells in which each peak is accessible, for all peaks called at level 4 of the cellular taxonomy.

**i,** Scatterplot showing the relationship between the mean fragment counts per cell and the mean, for all peaks called at level 4 of the cellular taxonomy.
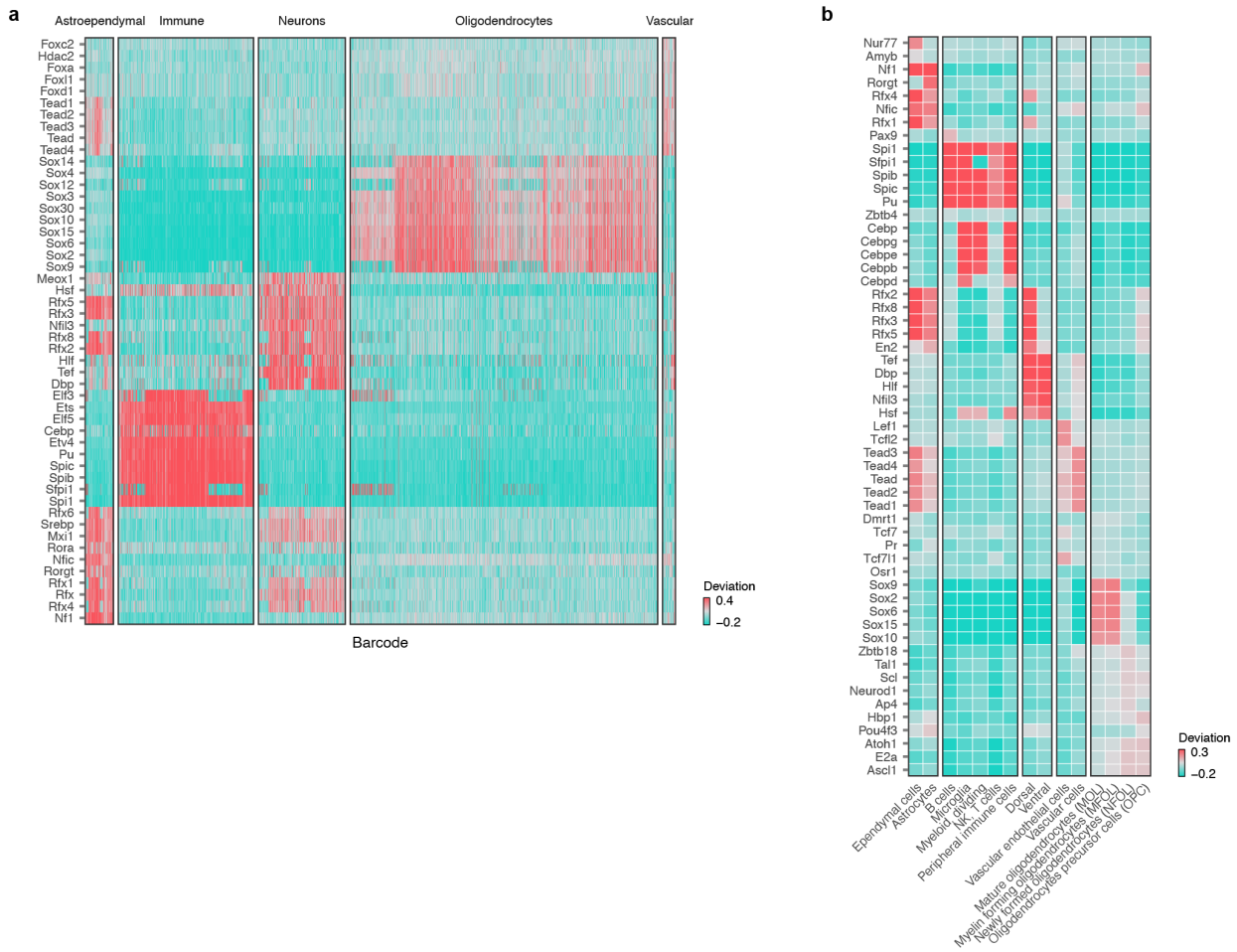
**Supplementary Fig. 24 | Cell-type-specific transcription factors in the multiome atlas.**

**a,** Deviations of the top ten cell-type-specific transcription factors for major (level 1) cell types identified by chromVAR, shown for each individual barcode in the multiome atlas.

**b,** Median deviations of the top five cell-type-specific transcription factors for level 2 cell types identified by chromVAR.

a  Nr1d1_844

b  Nfib_859

c  RFX5_1486

d  PAX2_1442

e  PAX5_1446

f  IRF1.IRF_136

g  EBF1_1325

h  Lef1_734

i  NF1.FOXA1.CTF.Forkhead_174

j  Zbtb7b_174

k  ZBTB3_1055

l  CCNT2_105

m  MLX_1577
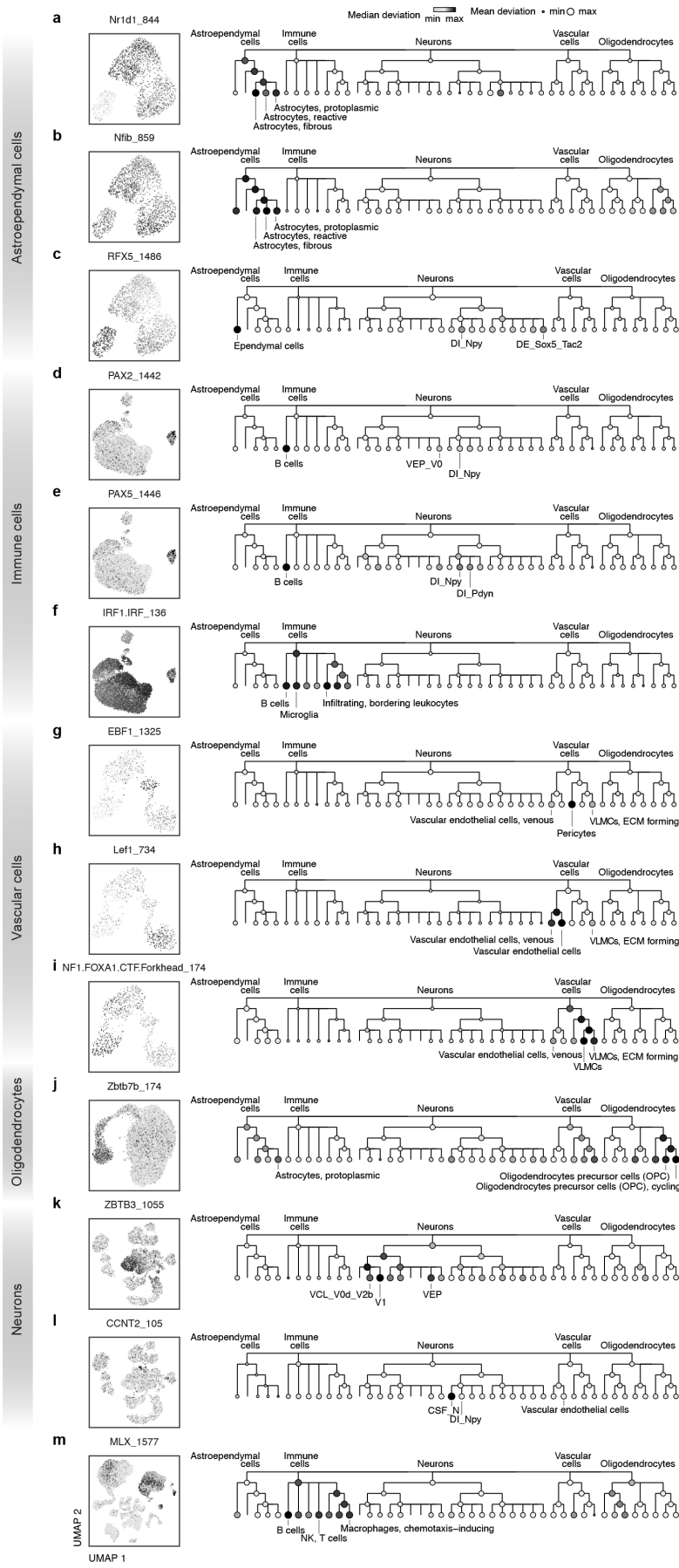
**Supplementary Fig. 25 | Cell type- and subtype-specific transcription factors in the multiome atlas.**
Cell-type-specific transcription factors discussed in the main text. Left, UMAP visualizations of chromVAR motif deviations for cells subset to the relevant major (level 1) cell type, **a-l,** or for all cells in the dataset, **m.** Right, dendrograms showing mean and median chromVAR motif deviations per cell type for levels 1-4 of the clustering tree.
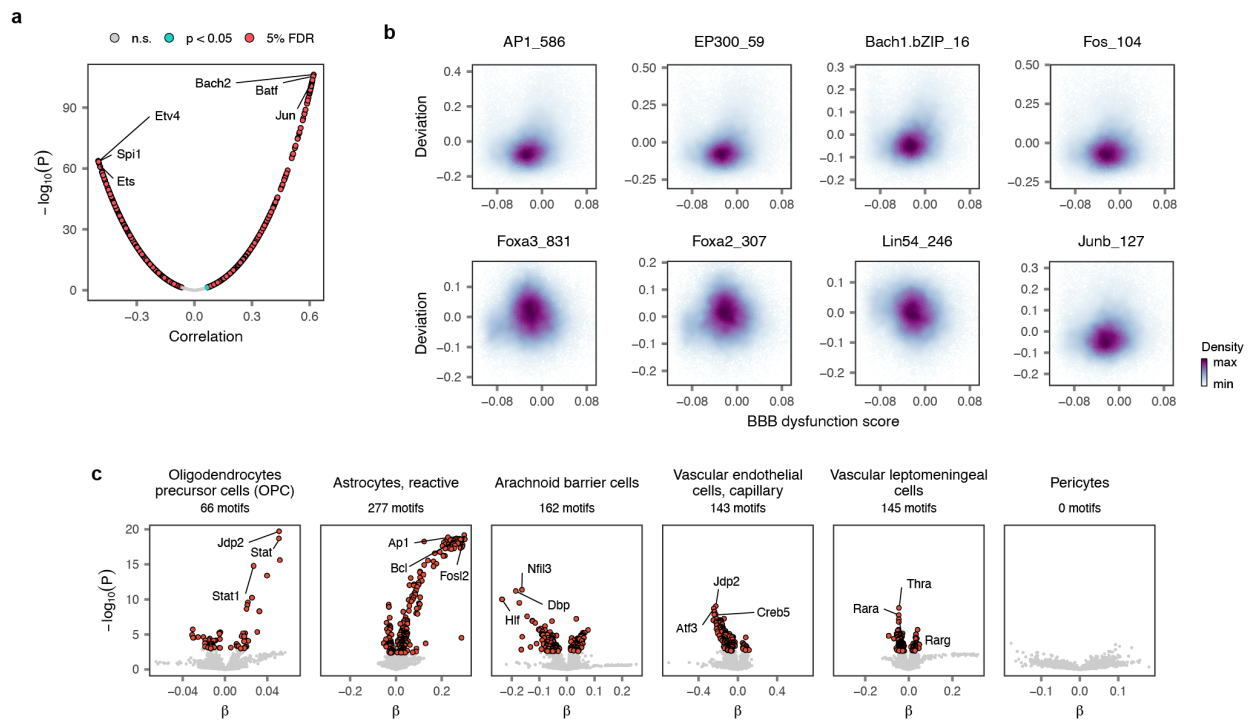
**Supplementary Fig. 26 | Regulatory programs underlying tripartite barrier formation.**

**a,** Volcano plot showing correlations between transcription factor binding motif accessibility, in the ATAC modality, and expression of the blood-brain barrier dysfunction score, in the RNA modality, across all vascular cells. The top three correlated and anti-correlated motifs are annotated.

**b,** Scatterplots highlighting relationships between expression of the blood-brain barrier dysfunction score and transcription factor binding motif accessibility for selected motifs discussed in the main text. Points are colored by the density of individual nuclei.

**c,** Volcano plots showing differentially accessible transcription factor binding motifs in the other cell types that establish the tripartite barrier.
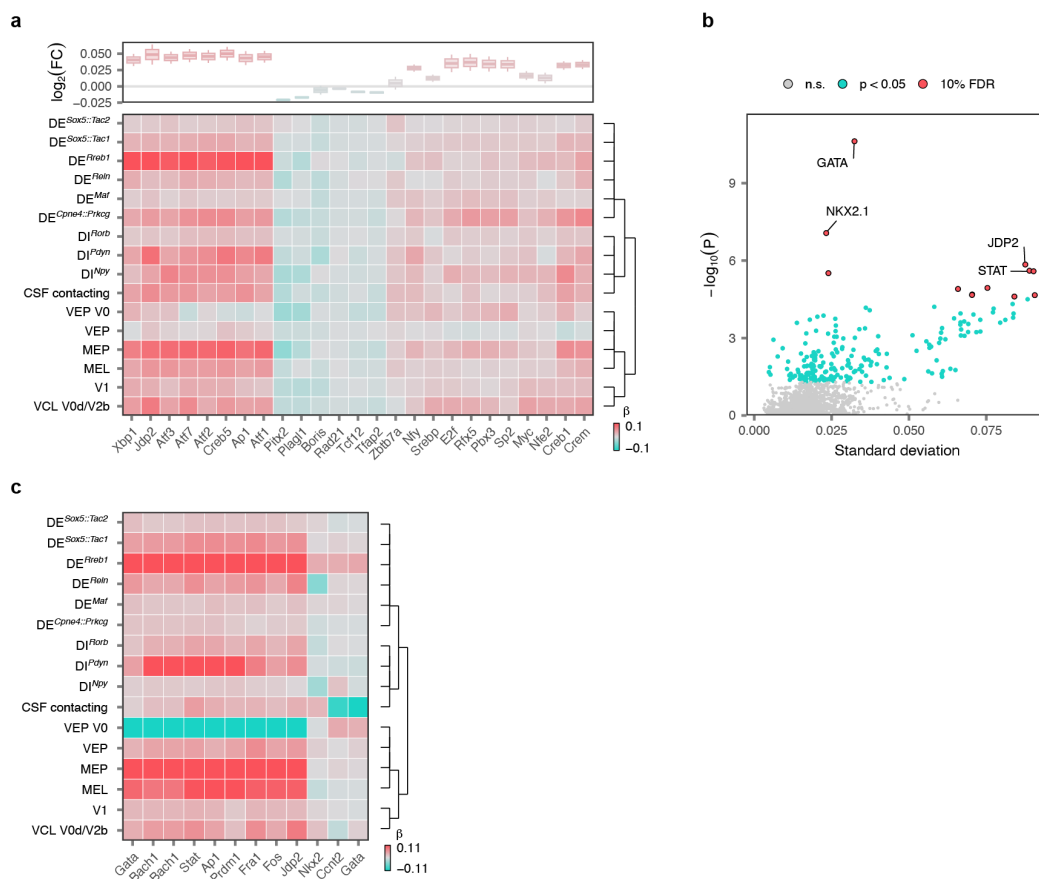
**Supplementary Fig. 27 | Conserved and divergent regulatory programs in injured neurons.**

**a,** Top 25 transcription factor binding motifs with conserved patterns of up- or downregulation across level 4 neuron subtypes at 7 days post-injury. Top, boxplot showing the estimated effect of SCI on transcription factor binding motif accessibility across all level 4 neuron subtypes. Bottom, heatmap showing the estimated effect of SCI on transcription factor binding motif accessibility within each level 4 neuron subtype individually.

**b,** Identification of transcription factor binding motifs with significant variation across neuron subtypes in their patterns of accessibility at 2 months post-injury. The x-axis shows the standard deviation of coefficients estimated by linear mixed models for each neuron subtype independently, while the y-axis shows the statistical significance of the standard deviation compared to linear mixed models fit with randomized neuron subtype assignments.

**c,** Heatmap showing the estimated effect of SCI on transcription factor binding motif accessibility across level 4 neuron subtypes for the significantly variable motif shown in **b.**
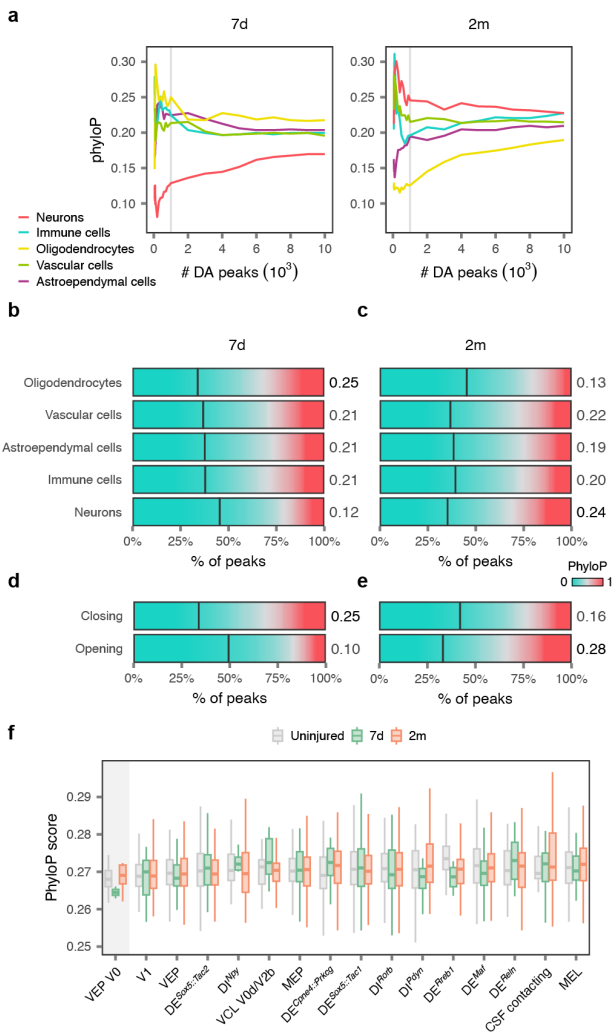
**Supplementary Fig. 28 | Evolutionary conservation and acceleration of differentially accessible regions.**
**a,** Line charts showing the median phyloP score of the top-*n* differentially accessible peaks, for values of *n* between 50 and 10,000, within major cell types of the spinal cord at 7 days and 2 months after SCI. Vertical lines highlight the top-1,000 differentially accessible peaks within each cell type.
**b-c,** Mean phyloP scores over all nucleotides within each of the top 1,000 differentially accessible peaks in each major cell type at 7 days, **b,** and 2 months, **c,** after SCI. Vertical line shows the median phyloP score for all peaks in the dataset.
**d-e,** Mean phyloP scores over all nucleotides within each of the top 1,000 peaks that are opening versus closing in neurons at 7 days, **d,** and 2 months, **e,** after SCI. Vertical line shows the median phyloP score for all peaks in the dataset.
**f,** Mean phyloP score over all accessible peaks in nuclei from each level 4 neuron subtype in the multiome atlas, split by experimental condition. Ventral excitatory projection neurons are highlighted.
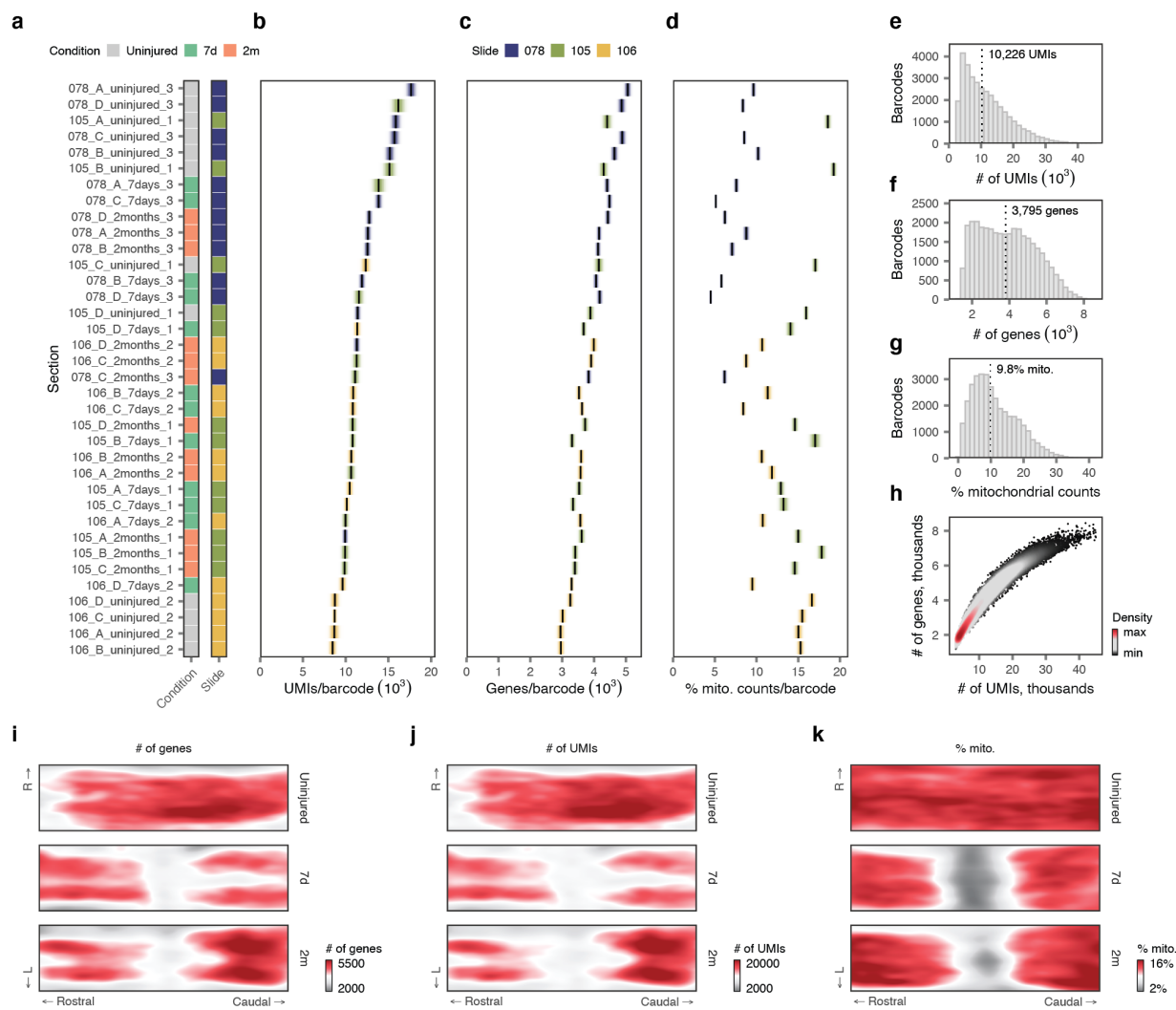
**Supplementary Fig. 29 | Quality control of the 2D spatial atlas.**
**a-d,** Quality control statistics for 36 sections profiled by spatial transcriptomics (**a,** legend showing the experimental condition and slide number for each section; **b,** mean number of UMIs per barcode; **c,** mean number of genes detected per barcode; **d,** mean proportion of mitochondrial counts per barcode). Shaded areas show the standard deviation. Sections are colored by the slide on which each section was sequenced.
**e-g,** Aggregate distributions of quality control statistics over all sections (**e,** number of UMIs per barcode; **f,** number of genes detected per barcode; **g,** proportion of mitochondrial counts per barcode).
**h,** Relationship between the number of UMIs and number of genes detected per spatial barcode.
**i-k,** Quality control statistics visualized on the common coordinate system of the spinal cord, separately for each experimental condition (**i,** mean number of UMIs per barcode; **j,** mean number of genes detected per barcode; **k,** mean proportion of mitochondrial counts per barcode).
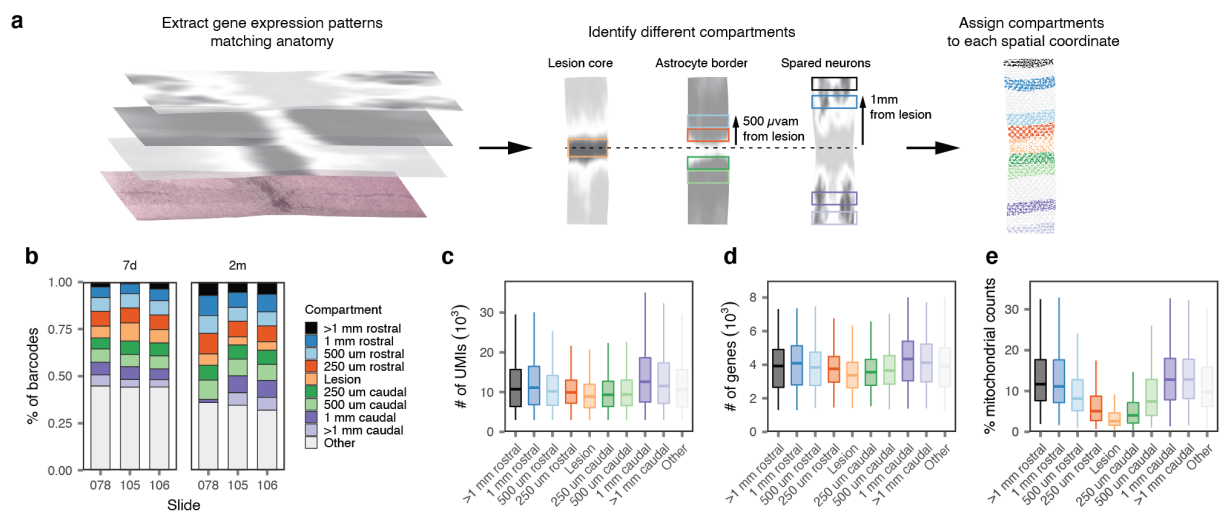
**Supplementary Fig. 30 | Definition and quality control of lesion compartments.**

**a,** Schematic overview of the procedure for definition of lesion compartments on the common coordinate system of the spinal cord.

**b,** Proportion of spatial barcodes assigned to each lesion compartment within each slide.

**c-e,** Distributions of quality control statistics (**c,** number of UMIs per barcode; **d,** number of genes detected per barcode; **e,** proportion of mitochondrial counts per barcode) for spatial barcodes within each lesion compartment.
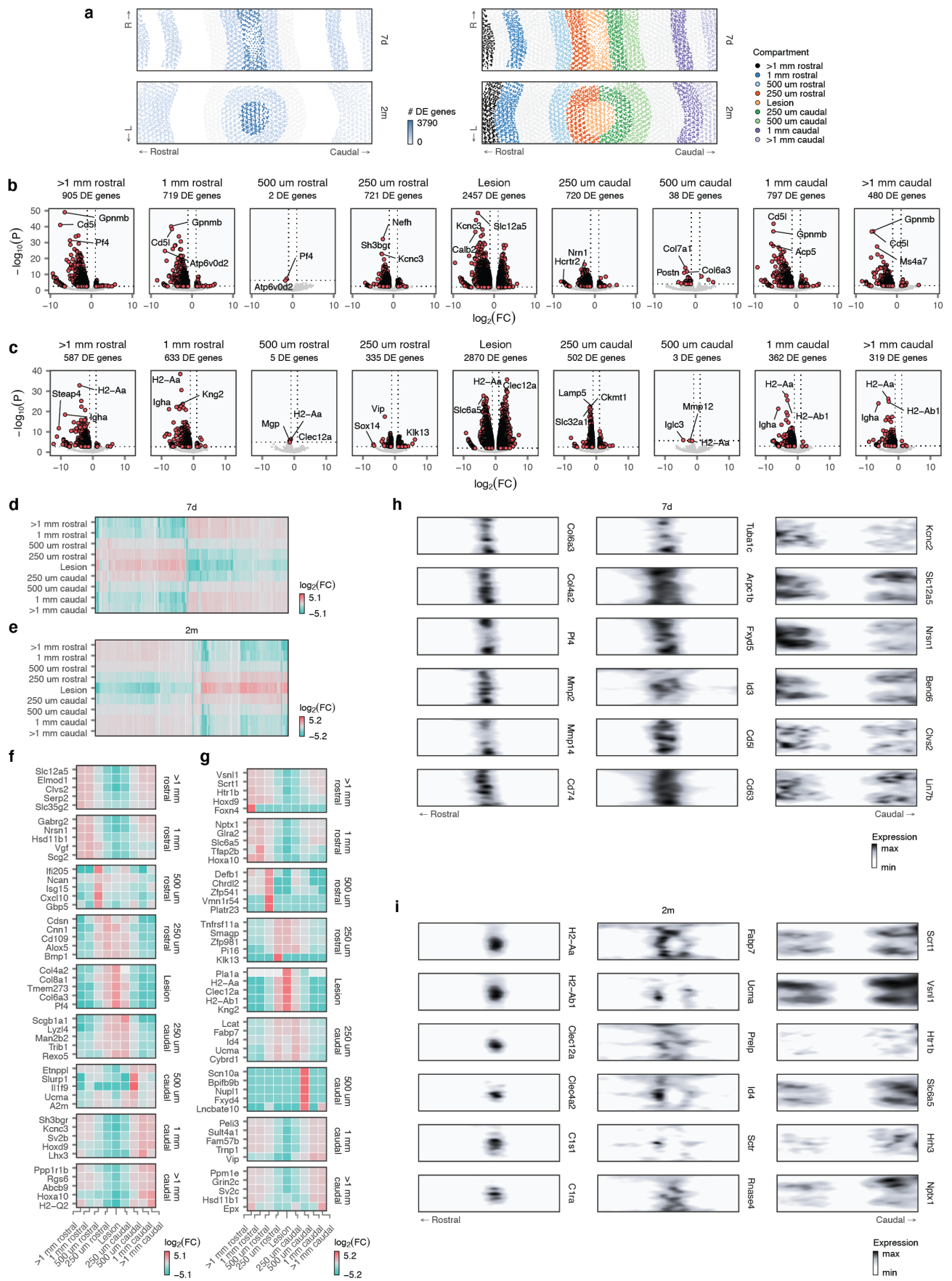
**Supplementary Fig. 31 | Shared and distinct programs of gene expression across lesion compartments.**

**a,** Left, total number of differentially expressed genes detected within each lesion compartment at 7 days and 2 months after SCI. Right, legend showing the position of each lesion compartment, as in **Fig. 6c.**

**b-c,** Volcano plots showing differentially expressed genes for all lesion compartments at 7 days, **b,** and 2 months, **c.** The top three genes per lesion compartment, as ranked by the product of the $\log_2$-fold change and the $-\log_{10}$ p-value, are annotated.

**d-e,** Heatmap showing $\log_2$-fold changes for all genes differentially expressed in at least one lesion compartment at 7 days, **d,** and 2 months, **e.**

**f-g,** Heatmap showing $\log_2$-fold changes for the top five genes differentially expressed in each lesion compartment at 7 days, **f,** and 2 months, **g.**

**h-i,** Visualization of selected differentially expressed genes specific to individual lesion compartments at 7 days, **h,** and 2 months, **i,** on the two-dimensional coordinate system of the injured spinal cord.
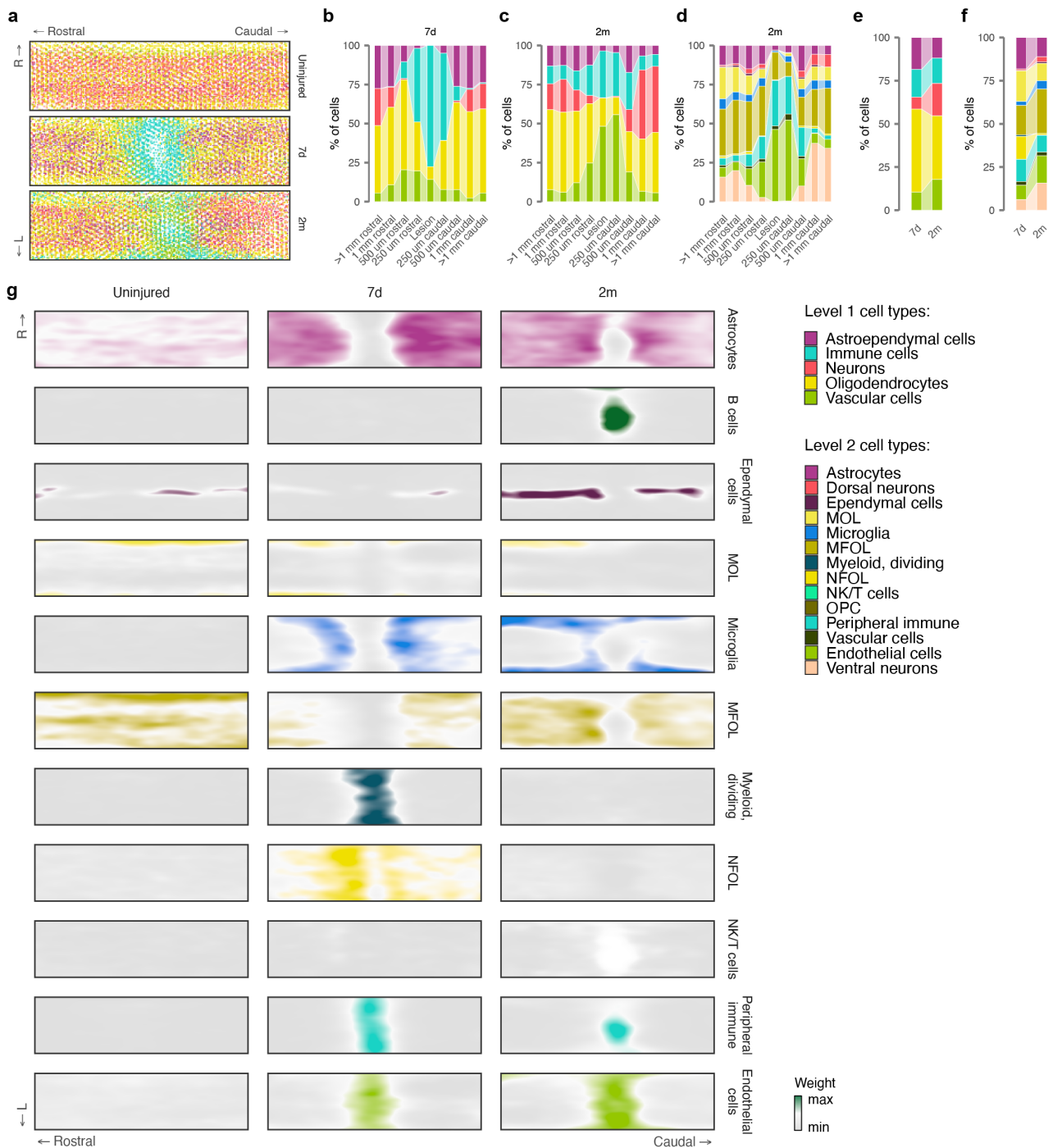
**Supplementary Fig. 32 | Cell type deconvolution of the 2D spatial atlas.**

**a,** Major cell types assigned to each spatial barcode, visualized for each experimental condition on the two-dimensional coordinate system of the injured spinal cord.

**b,** Sankey diagram showing the cellular composition of each lesion compartment at 7 days, for major (level 1) cell types.

**c,** Sankey diagram showing the cellular composition of each lesion compartment at 2 months, for level 1 cell types.

**d,** Sankey diagram showing the cellular composition of each lesion compartment at 2 months, for level 2 cell types.

**e,** Sankey diagram showing the evolution of the cellular composition of the entire injured spinal cord between 7 days and 2 months, for level 1 cell types.

**f,** Sankey diagram showing the evolution of the cellular composition of the entire injured spinal cord between 7 days and 2 months, for level 2 cell types.

**g,** Visualization of the deconvolution weights assigned by RCTD for selected level 2 cell types at each timepoint, on the two-dimensional coordinate system of the injured spinal cord.
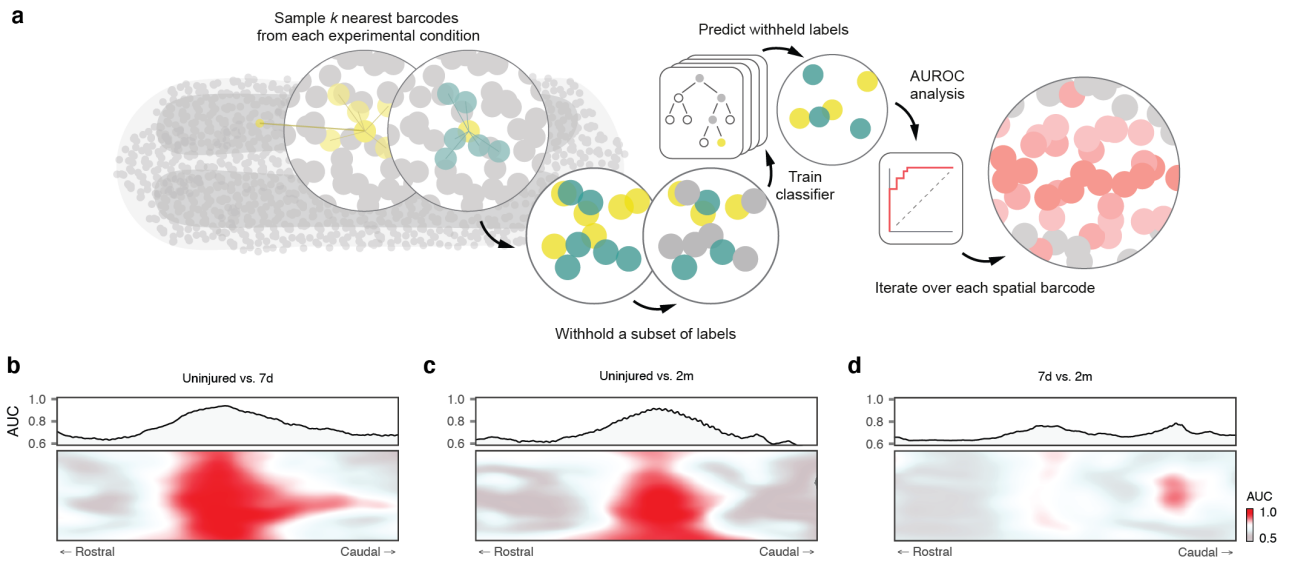
**Supplementary Fig. 33 | Spatial prioritization of the 2D spatial atlas.**

**a,** Schematic overview illustrating the concept of spatial prioritization, as captured in Magellan.

**b-d,** Spatial prioritizations assigned by Magellan to each pairwise comparison of experimental conditions in the 2D spatial atlas (**b,** 7 days versus uninjured; **c,** 2 months versus uninjured, **d,** 7 days versus 2 months). Bottom, AUCs of spatial prioritization visualized on the two-dimensional coordinate system of the injured spinal cord. Top, average AUCs of spatial prioritization along the rostrocaudal axis, highlighting prioritization of the lesion site.
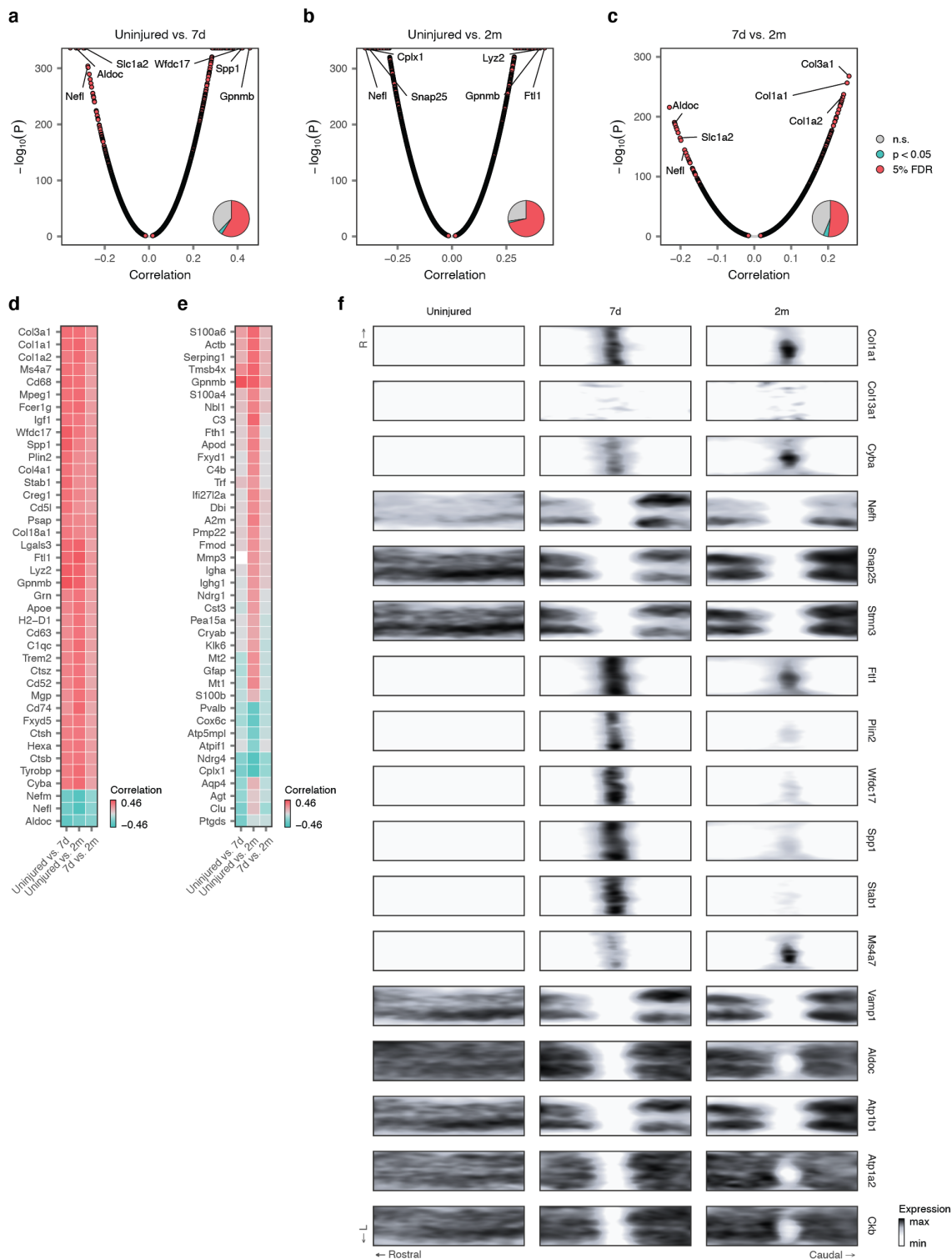
**Supplementary Fig. 34 | Molecular basis of spatial prioritization at the gene level.**

**a-c,** Volcano plots showing correlations between the AUCs assigned by Magellan at each spatial barcode and transcriptome-wide gene expression across the same spatial barcodes (**a,** 7 days versus uninjured; **b,** 2 months versus uninjured; **c,** 7 days versus 2 months). Inset pie charts show the proportions of all tested genes that are significantly correlated with the spatial prioritizations.

**d,** Heatmap showing Pearson correlations between spatial prioritizations and gene expression for each pairwise comparison of experimental conditions, for the top 40 most recurrently correlated genes across all comparisons.

**e,** Heatmap showing Pearson correlations between spatial prioritizations and gene expression for each pairwise comparison of experimental conditions, for the top 40 most variably correlated genes across all comparisons.

**f,** Visualization of selected genes prioritized by their correlation to spatial prioritizations on the two-dimensional coordinate system of the injured spinal cord.
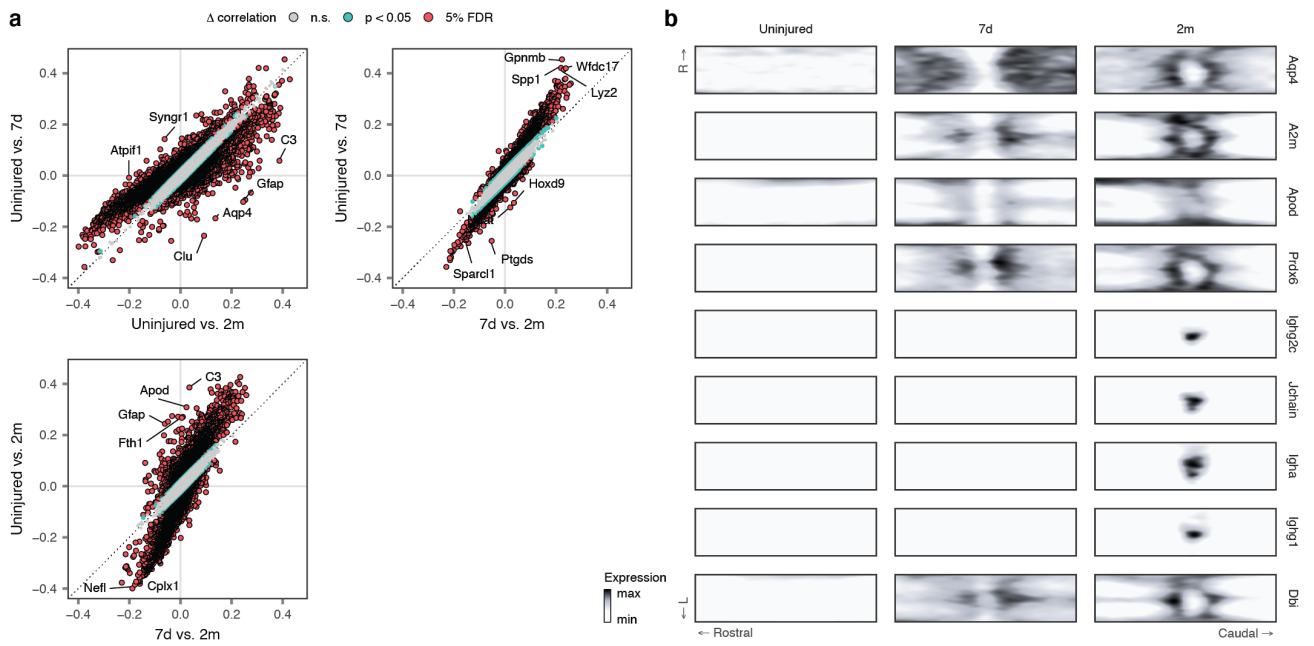
**Supplementary Fig. 35 | Molecular basis of spatial prioritization at the gene module level.**
**a-c,** Volcano plots showing correlations between the AUCs assigned by Magellan at each spatial barcode and the average expression of genes associated with a given GO term ("GO modules") across the same spatial barcodes (**a,** 7 days versus uninjured; **b,** 2 months versus uninjured; **c,** 7 days versus 2 months). Inset pie charts show the proportions of all tested GO modules that are significantly correlated with the spatial prioritizations.
**d,** Heatmap showing Pearson correlations between spatial prioritizations and GO module scores for each pairwise comparison of experimental conditions, for the top 40 most recurrently correlated GO modules across all comparisons.
**e,** Heatmap showing Pearson correlations between spatial prioritizations and GO module scores for each pairwise comparison of experimental conditions, for the top 40 most variably correlated GO modules across all comparisons.
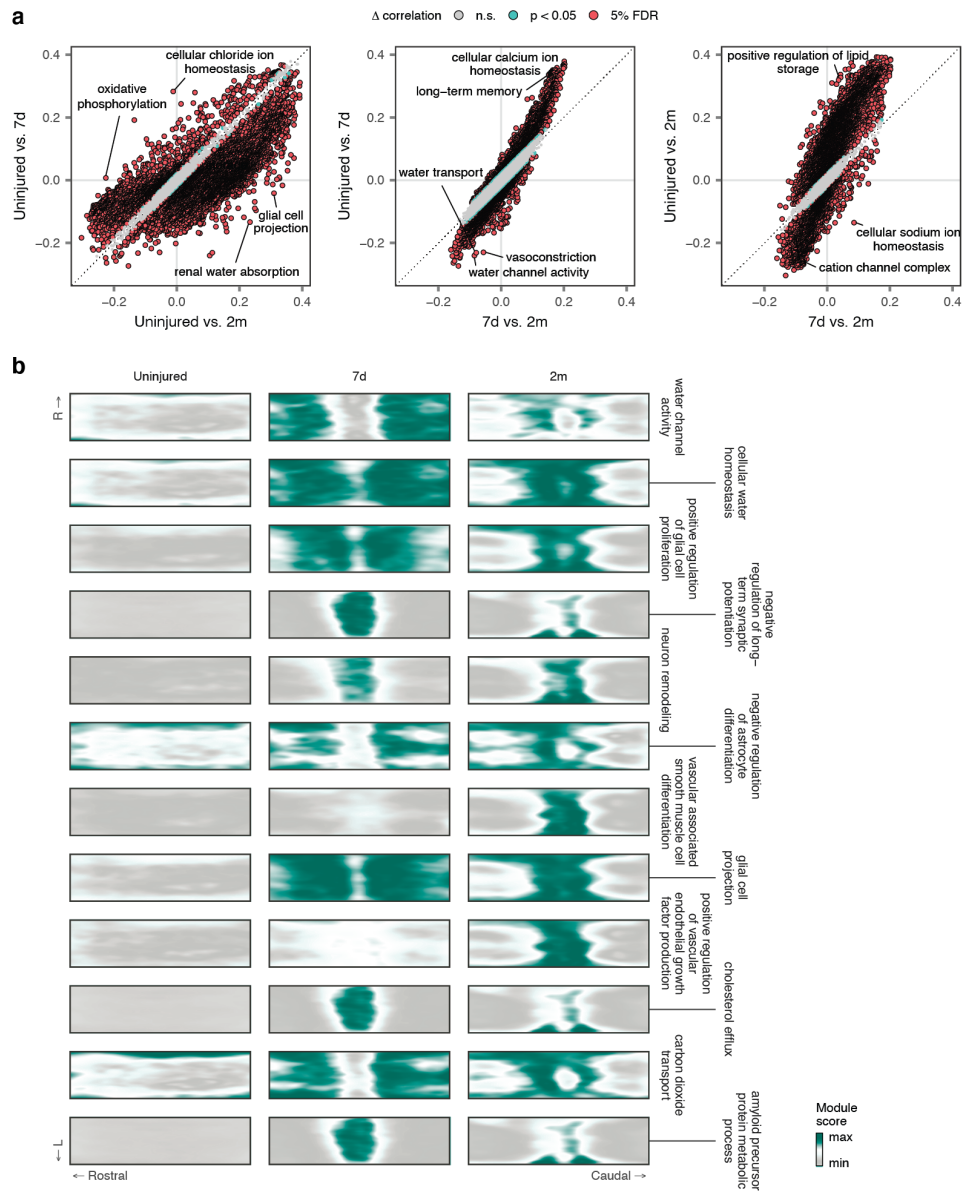**f,** Visualization of selected GO modules prioritized by their correlation to spatial prioritizations on the two-dimensional coordinate system of the injured spinal cord.

**Supplementary Fig. 36 | Molecular basis of differential spatial prioritization at the gene level.**
**a,** Scatterplots highlighting genes with differential correlations to spatial prioritizations between pairwise comparisons of experimental conditions.
**b,** Visualization of selected genes prioritized by their differential correlation to spatial prioritizations between comparisons on the two-dimensional coordinate system of the injured spinal cord.

**Supplementary Fig. 37 | Molecular basis of differential spatial prioritization at the gene module level.**
**a,** Scatterplots highlighting GO modules with differential correlations to spatial prioritizations between pairwise comparisons of experimental conditions.
**b,** Visualization of selected GO modules prioritized by their differential correlation to spatial prioritizations between comparisons on the two-dimensional coordinate system of the injured spinal cord.
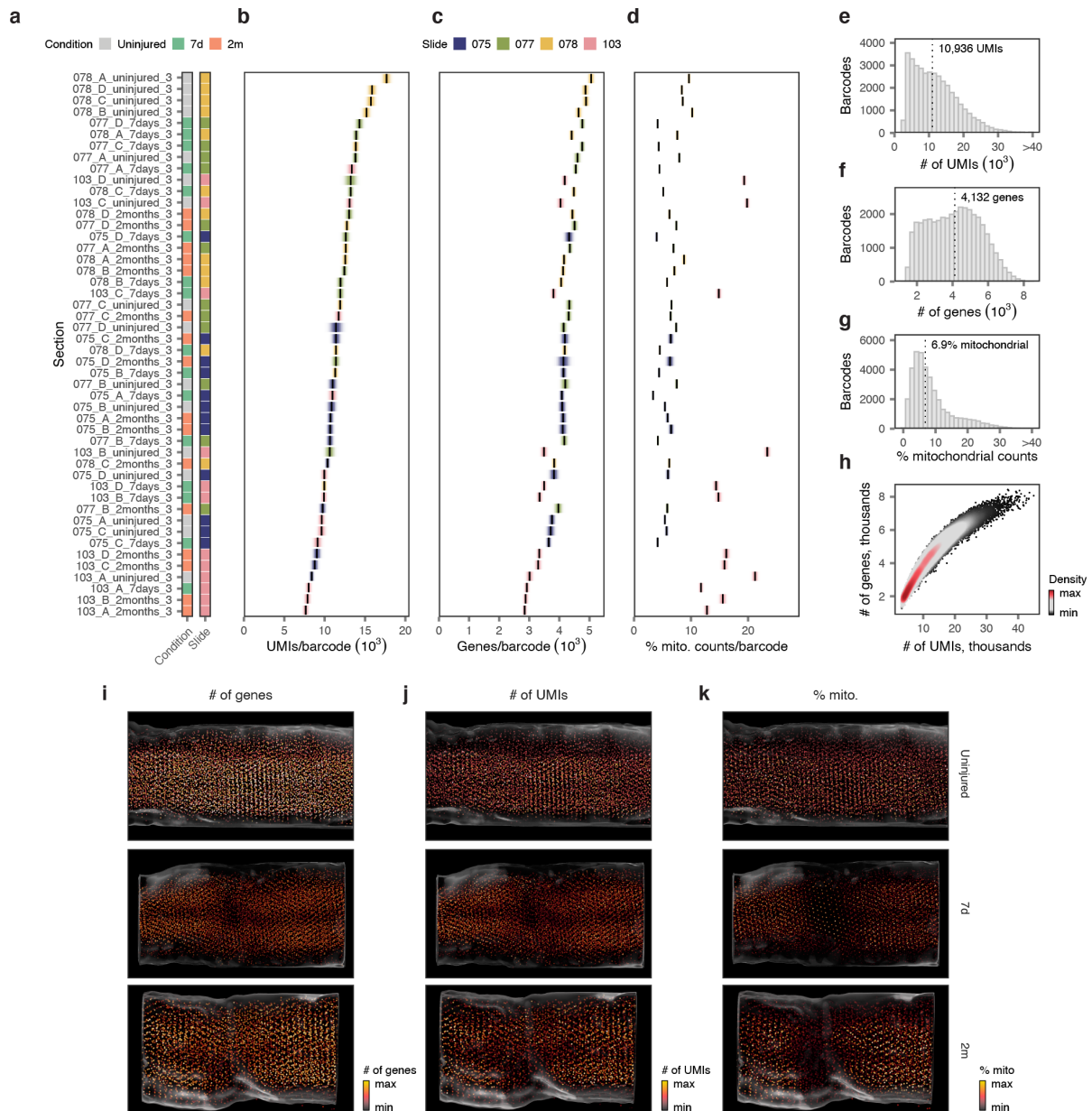
**Supplementary Fig. 38 | Quality control of the 3D spatial atlas.**

**a-d,** Quality control statistics for 16 sections profiled by three-dimensional spatial transcriptomics (**a,** legend showing the experimental condition and slide number for each section; **b,** mean number of UMIs per barcode; **c,** mean number of genes detected per barcode; **d,** mean proportion of mitochondrial counts per barcode). Shaded areas show the standard deviation. Sections are colored by the slide on which each section was sequenced.

**e-g,** Aggregate distributions of quality control statistics over all sections in the 3D spatial atlas (**e,** number of UMIs per barcode; **f,** number of genes detected per barcode; **g,** proportion of mitochondrial counts per barcode).

**h,** Relationship between the number of UMIs and number of genes detected per spatial barcode in the 3D spatial atlas.

**i-k,** Quality control statistics visualized on the three-dimensional common coordinate system of the spinal cord, separately for each experimental condition (**i,** mean number of UMIs per barcode; **j,** mean number of genes detected per barcode; **k,** mean proportion of mitochondrial counts per barcode).
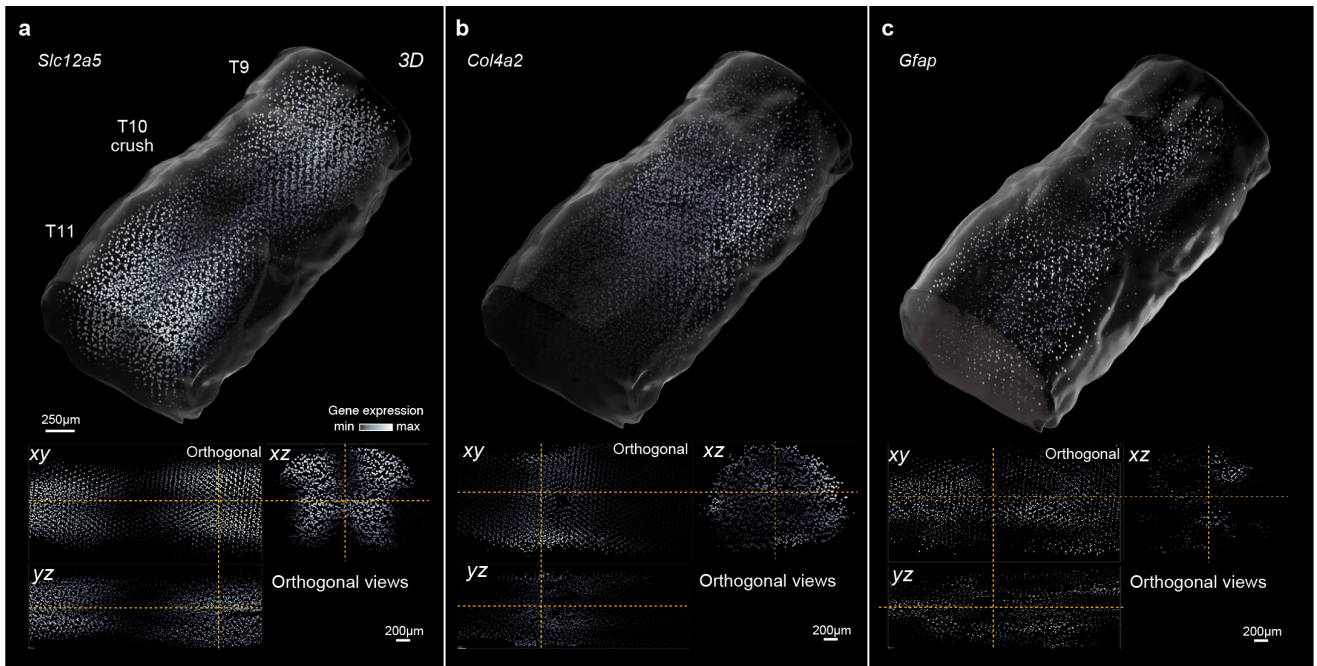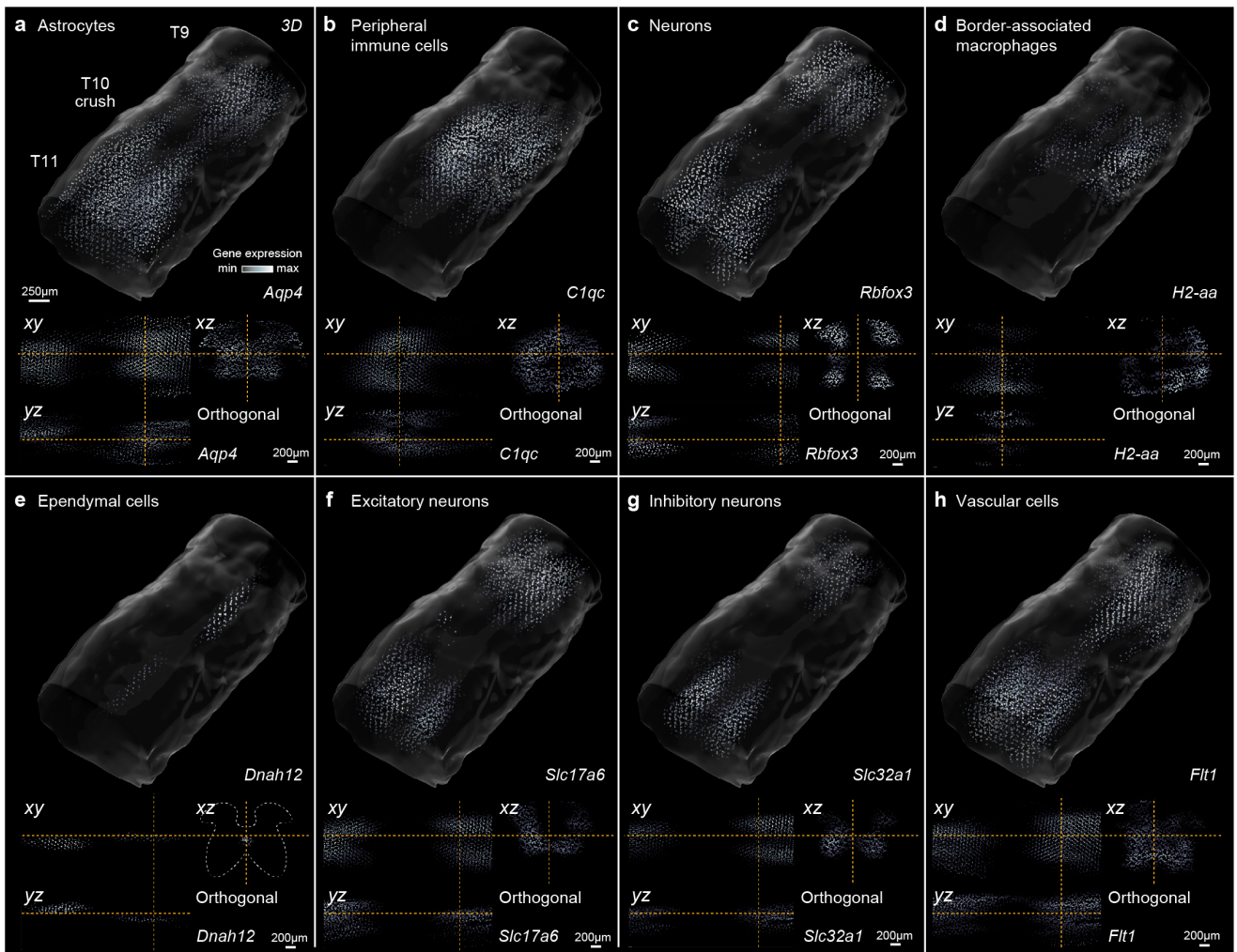
**Supplementary Fig. 39 | Lesion compartments in the 3D spatial atlas.**
Expression of marker genes associated with distinct lesion compartments across the 3D spatial transcriptomic atlas at 7 days, including spared but reactive neural tissue (*Slc12a5*, **a**) the fibrotic scar (*Col4a2*, **b**), and the astrocyte barrier (*Gfap*, **c**), as shown in **Fig. 8b** but here visualized separately for each gene.
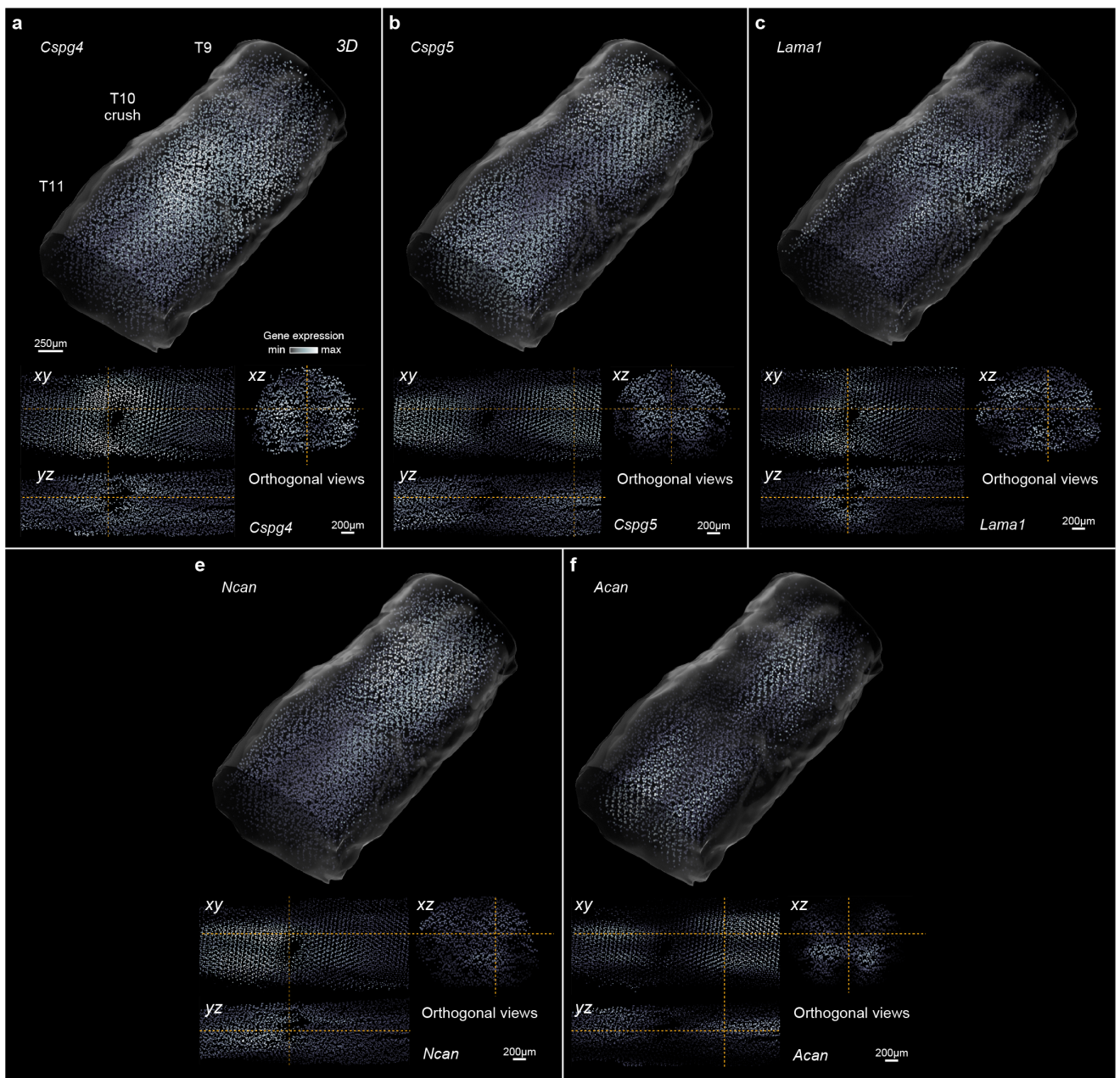
**Supplementary Fig. 40 | Inhibitory and facilitating molecules in the 3D spatial atlas.**
Expression of selected inhibitory and facilitating molecules across the 3D spatial transcriptomic atlas at 7 days. **a,** *Cspg4*; **b,** *Cspg5*; **c,** *Ncan*; **d,** *Acan*; **e,** *Lama1*.

**Supplementary Fig. 41 | Cell type marker gene expression in the 3D spatial atlas.**
Expression of selected cell type marker genes across the 3D spatial transcriptomic atlas at 7 days. **a,** *Aqp4* (astrocytes); **b,** *C1qc* (peripheral immune cells); **c,** *Rbfox3* (neurons); **d,** *H2-aa* (border-associated macrophages); **e,** *Dnah12* (ependymal cells); **f,** *Slc17a6*, excitatory neurons; **g,** *Slc32a1* (inhibitory neurons); **h,** *Flt1* (vascular cells).
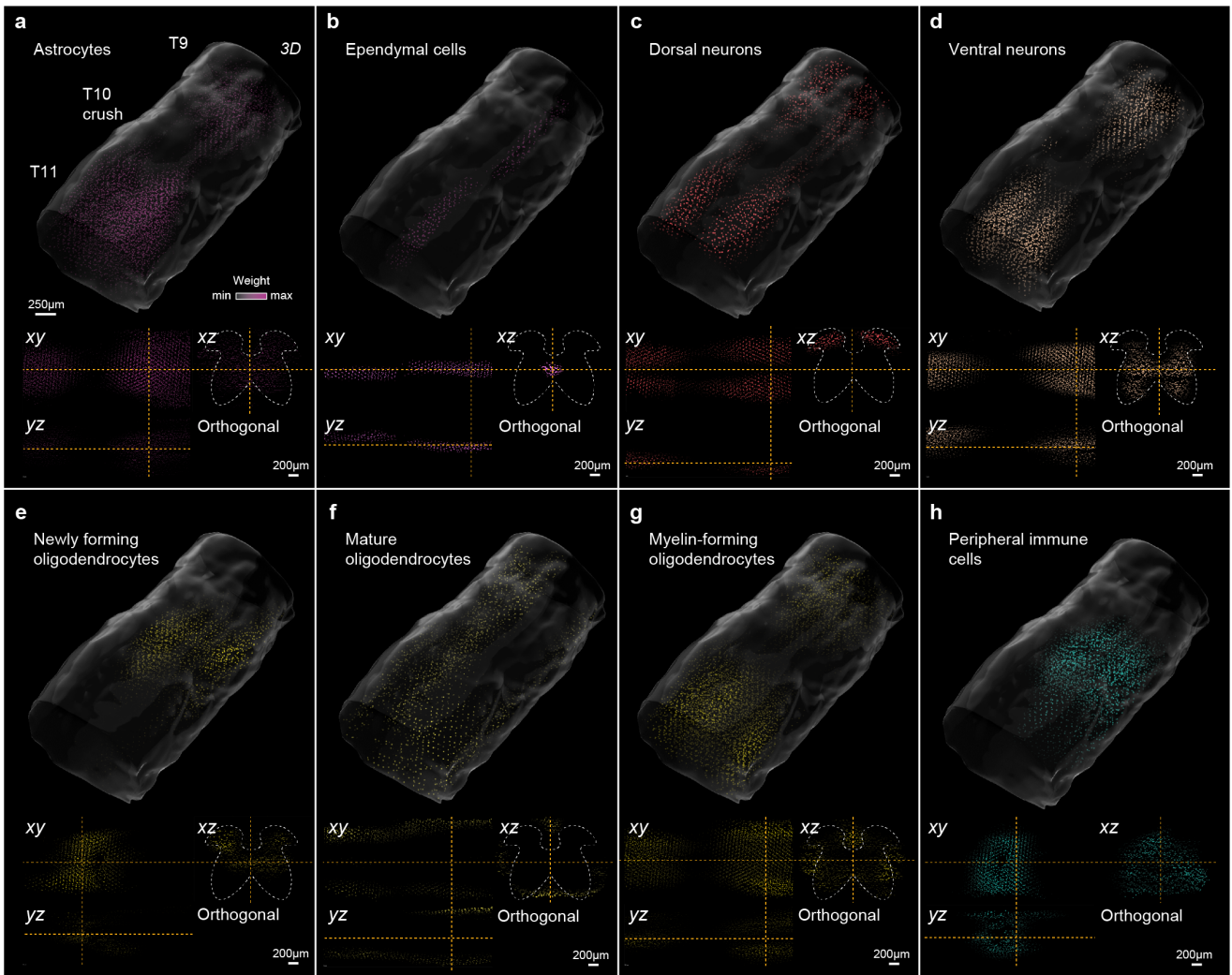
**Supplementary Fig. 42 | Cell type deconvolution of the 3D spatial atlas.**
Visualization of the deconvolution weights assigned by RCTD for selected level 2 cell types at 7 days, on the two-dimensional coordinate system of the injured spinal cord. **a,** Astrocytes; **b,** ependymal cells; **c,** dorsal neurons; **d,** ventral neurons; **e,** newly forming oligodendrocytes (NFOL); **f,** mature oligodendrocytes (MOL); **g,** myelin-forming oligodendrocytes (MFOL); **h,** peripheral immune cells.
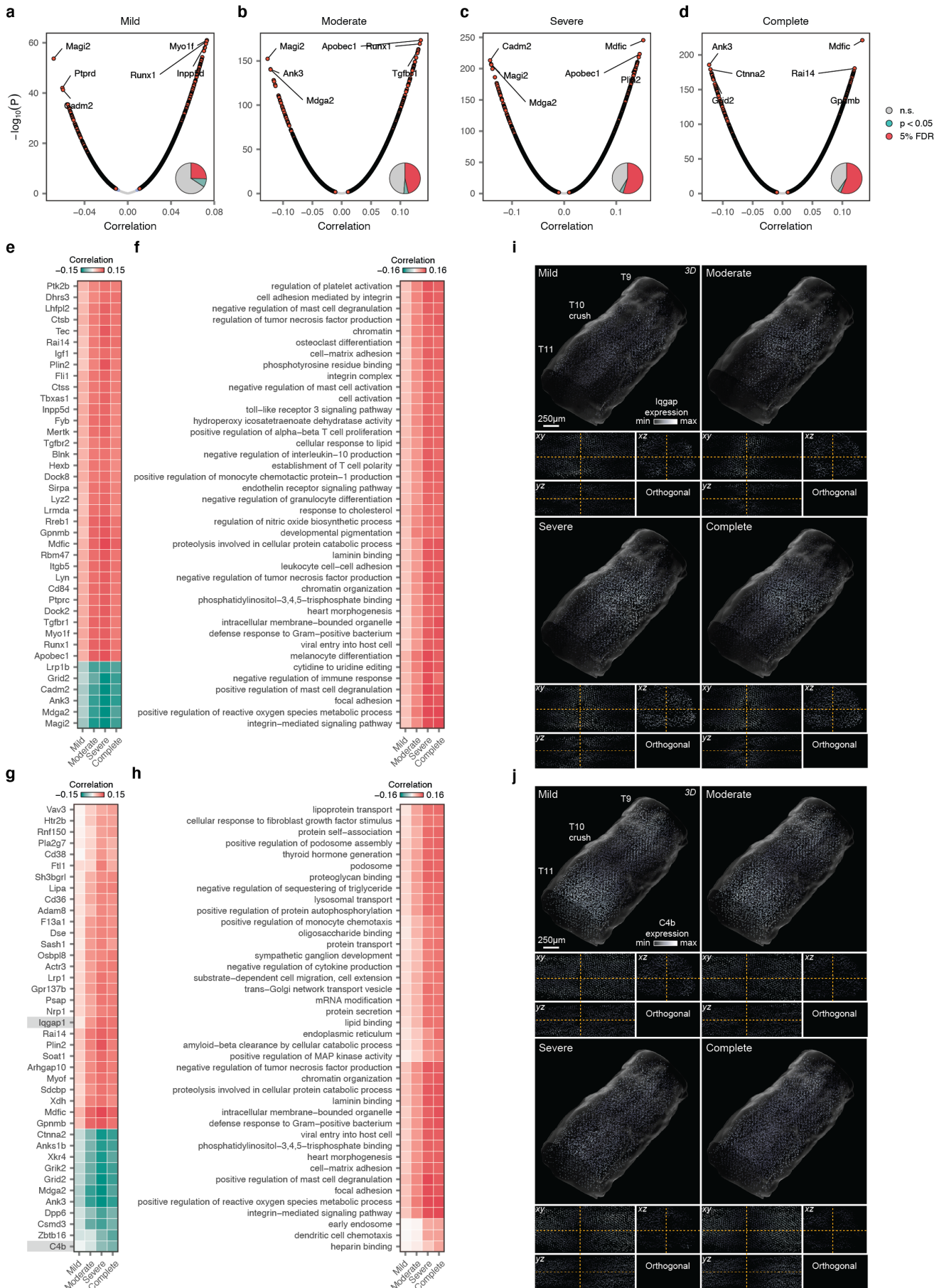
**Supplementary Fig. 43 | Molecular basis of three-dimensional spatial prioritization at the gene and gene module levels.**

**a-d,** Volcano plots showing correlations between the AUCs assigned by Magellan to each spatialized barcode from the snRNA-seq and transcriptome-wide gene expression across the same snRNA-seq barcodes (**a,** mild; **b,** moderate; **c,** severe; **d,** complete). Inset pie charts show the proportions of all tested genes that are significantly correlated with the spatial prioritizations.

**e,** Heatmap showing Pearson correlations between spatial prioritizations and gene expression for the top 40 most recurrently correlated genes across injury severities.

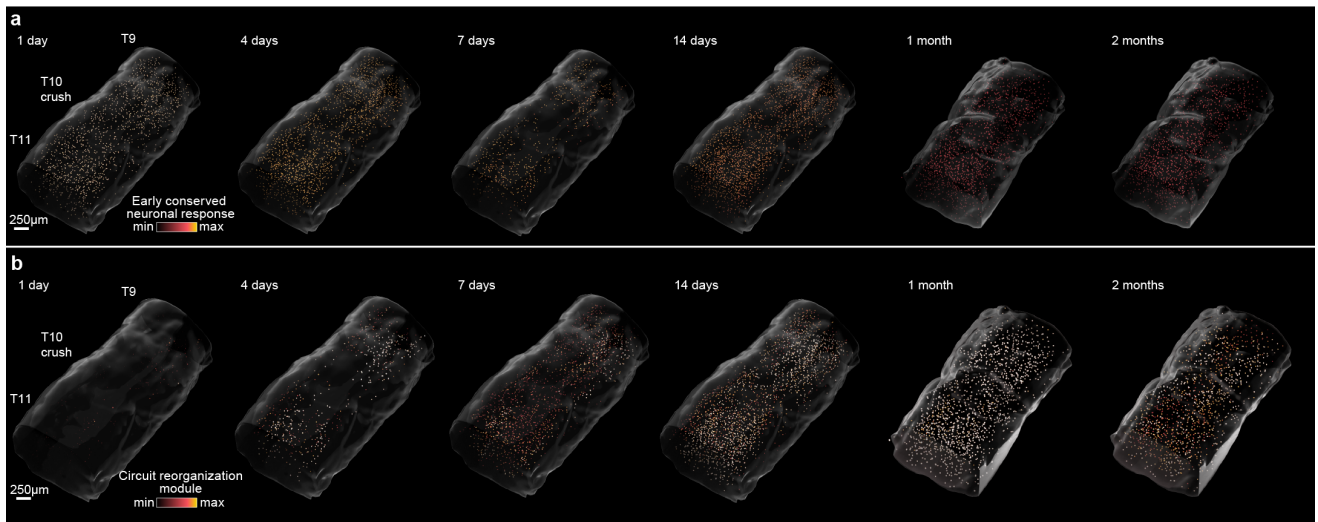**f,** Heatmap showing Pearson correlations between spatial prioritizations and gene expression for the top 40 most variably correlated genes across injury severities.

**g,** As in **e,** but for gene modules.

**h,** As in **f,** but for gene modules.

**i,** Expression of selected genes from **f** across injury severities, visualized on the 3D spatial transcriptomic atlas (**i,** *Iqgap*; **j,** *C4b*).

**Supplementary Fig. 44 | Early-conserved and late-diverging neuronal responses to SCI in the 3D spatial atlas.**
**a,** Expression of the early conserved neuronal response module in spatialized neurons from the snRNA-seq atlas, visualized on the coordinate system of the 3D spatial transcriptomic atlas.
**b,** Expression of the circuit reorganization module in spatialized neurons from the snRNA-seq atlas, visualized on the coordinate system of the 3D spatial transcriptomic atlas.
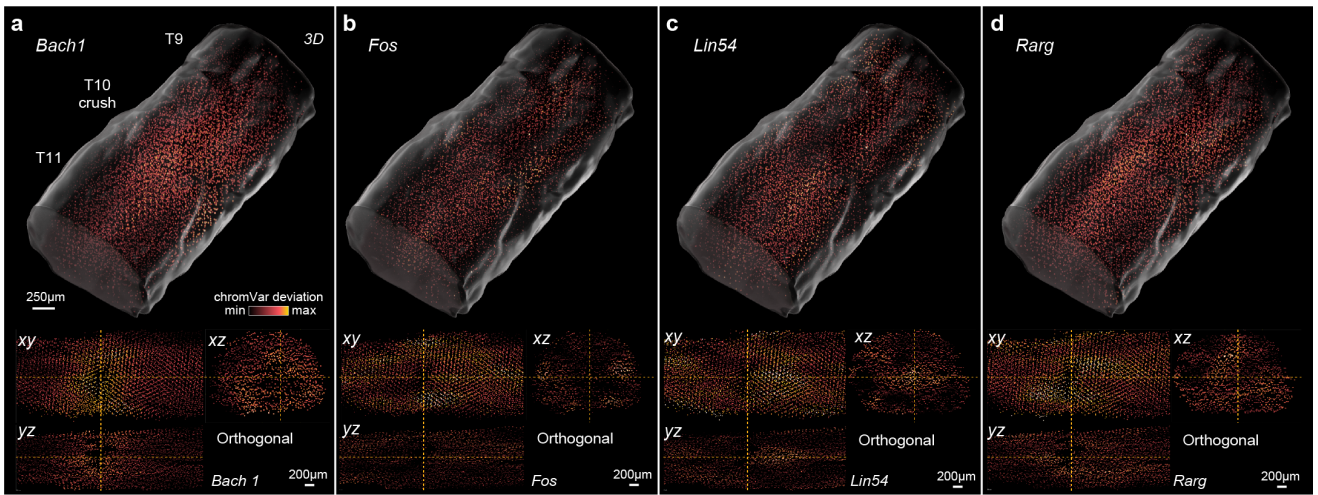
**Supplementary Fig. 45 | Three-dimensional mapping of chromatin accessibility.**
Accessibility of motifs associated with tripartite barrier formation in spatialized vascular cells from the multiome atlas, visualized on the coordinate system of the 3D spatial transcriptomic atlas. **a,** *Bach1*; **b,** *Fos*; **c,** *Lin54*; **d,** *Rarg*.
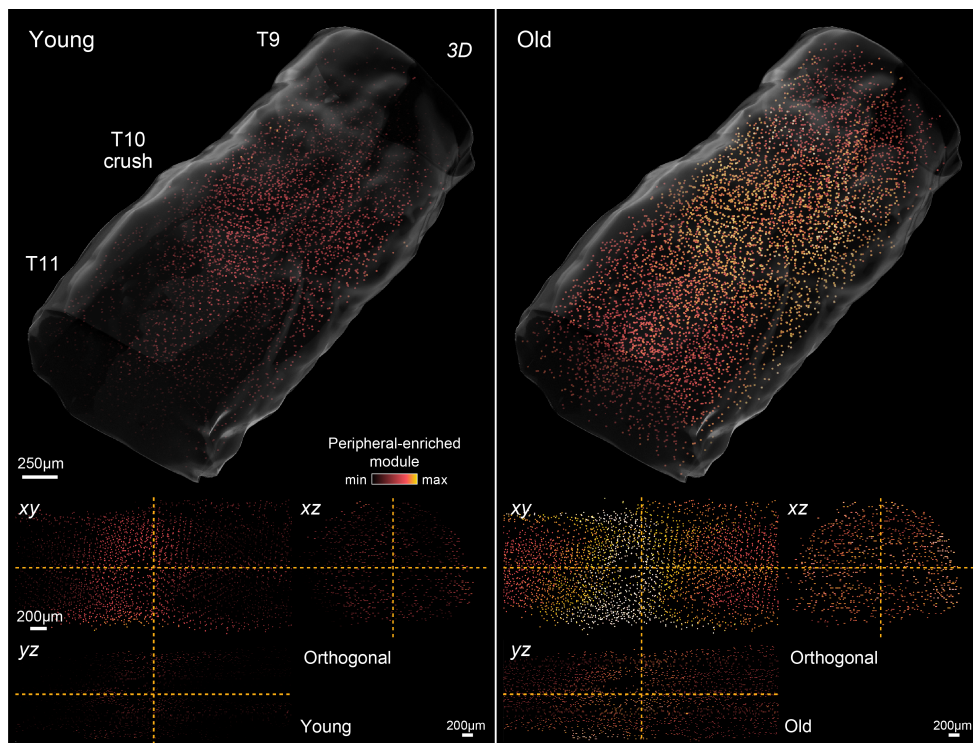
**Supplementary Fig. 46 | Loss of blood-brain barrier transcriptional identity in old mice.**
Expression of genes that distinguish peripheral endothelial cells from cells of the blood-brain barrier in spatialized vascular cells from young versus old mice, visualized on the coordinate system of the 3D spatial transcriptomic atlas.
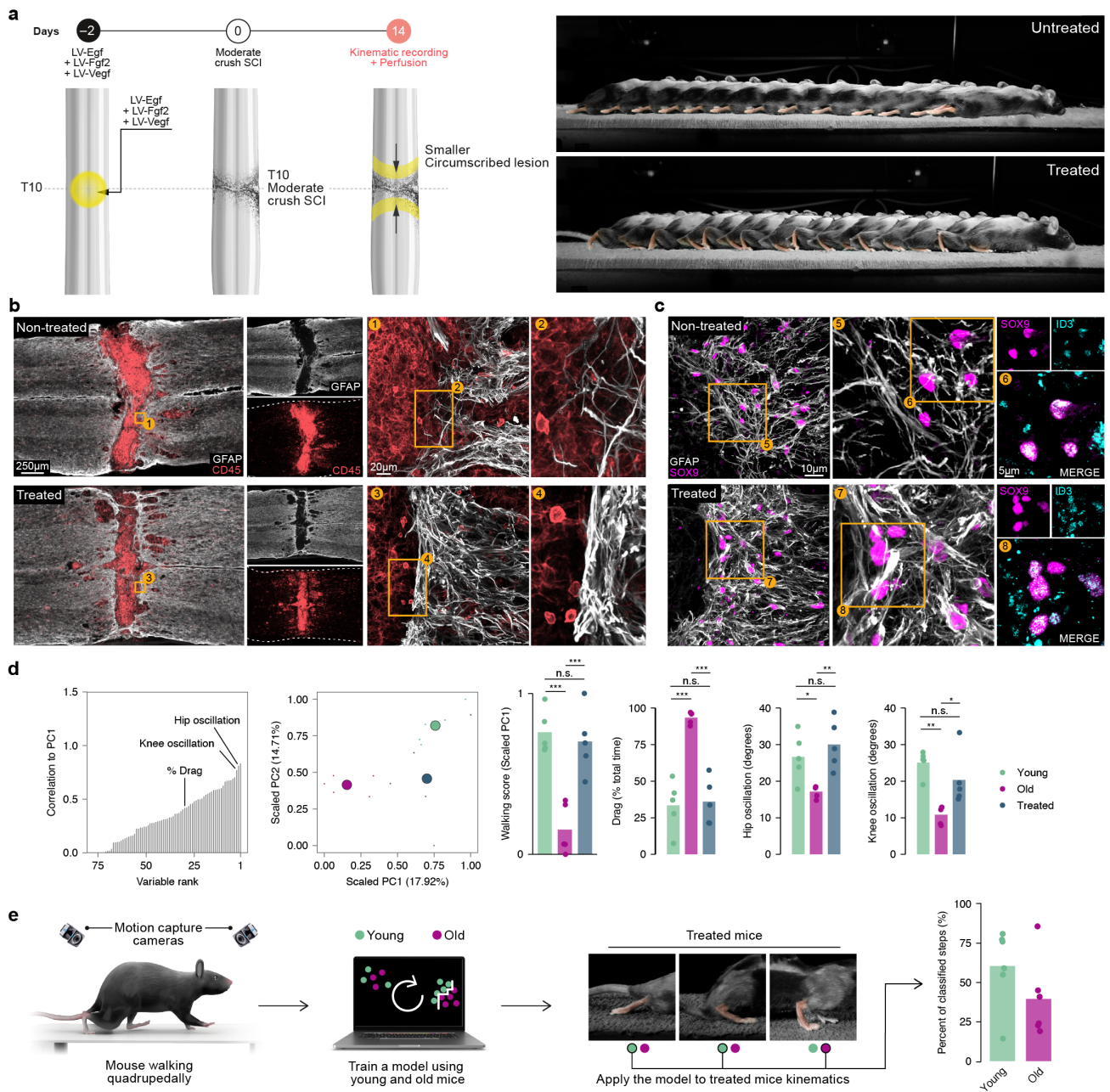
**Supplementary Fig. 47 | A rejuvenative gene therapy reestablishes the tripartite barrier to restore walking.**

**a,** Left, experimental design of a gene therapy intervention to promote the formation of the tripartite barrier, reproduced from **Fig. 8a**. Right, a second chronophotography series showing walking in old mice without (top) and with (bottom) a gene therapy intervention to promote the formation of the tripartite barrier.

**b,** Composite tiled scans of GFAP and CD45 in horizontal sections from representative old and treated mice.

**c,** Horizontal sections from representative old and treated mice identifying a restoration of Sox9[ON]Id3[ON] cells in the astrocyte border region in treated mice.

**d,** Locomotor performance in the gene therapy experiment, as quantified in **Supplementary Fig. 2** ($n > 10$ gait cycles per mouse, ($n = 5$ mice per group; statistics indicate Tukey HSD tests following one-way ANOVA). *, $p < 0.05$; **, $p < 0.01$; ***, $p < 0.001$.

**e,** Left, schematic overview of the classification pipeline using high-resolution kinematics data from young and old mice. Right, experimental conditions assigned to individual steps in old mice that received gene therapy by a machine-learning model trained on kinematics data from untreated animals.

# Chapter 5

# Discussion

## 5.1 A Novel Method for Single-Cell Data Analysis

We introduced a groundbreaking method for the analysis of single-cell data. Our developed tool, named "Augur," offers the ability to prioritize cell types based on their response to perturbations. Augur has played a pivotal role in our group's research, particularly in the context of spinal cord injury rehabilitation. With this tool, we identified key neuronal subpopulations that facilitate the recovery of walking following such injuries(Kathe et al., 2022). Additionally, Augur guided the development of a regenerative strategy to restore walking after a complete spinal cord injury by identifying neurons with a high propensity to regrow past the lesion center(Squair et al., 2023).

## 5.2 Benchmarking Bioinformatics Methods for Gene Expression Analysis

We conducted a comprehensive benchmark of bioinformatics methods used to detect differentially expressed genes in single-cell data. Our findings revealed a concerning rate of false positives when using the default methods commonly employed in the field. To validate this discovery, we screened genes that were erroneously identified as differentially expressed in RNAscope experiments. We emphasized that the performance of statistical methods in single-cell data analysis is strongly dependent on their ability to account for the intrinsic variability of biological replicates. This principle is critical in determining the biological accuracy of differential expression methods.

## 5.3 Establishment of the *Tabulae Paralytica* - Atlases of Spinal Cord Injury

Building on the knowledge gained in Chapters 1 and 2, Chapter 3 presents the creation of the "Tabulae Paralytica." This comprehensive resource comprises four molecular and cellular atlases of spinal cord injury (SCI). These atlases include a single-nucleus transcriptome atlas of over half a million cells, a multi-omic atlas that combines transcriptomic and epigenomic measurements within the same nuclei, and two spatial transcriptomic atlases that capture the spatiotemporal dimensions of the injured spinal cord.

These atlases have been instrumental in advancing our understanding of SCI at an unprecedented level of resolution. They have enabled us to uncover several new principles governing responses to SCI. We uncovered an inherent trade-off faced by neurons, wherein they must choose between the activation of cellular stress responses and circuit-reorganizing transcriptional programs in response to injury. Along with this finding we highlighted the intrinsic capacity of a specific neuronal subpopulation to transform into circuit-reorganizing neurons after injury, offering new possibilities for regenerative strategies.

We highlight the necessity to coordinate the formation of a tripartite neuroprotective barrier between immune-privileged neural tissue and extra-neural lesion environments for neurological recovery from SCI. This requirement becomes even more critical in the process of aging, where a catastrophic failure of the tripartite barrier leads to overwhelming immune infiltration and catastrophic neuronal death into neural tissue, precluding neurological recovery. Following this discovery we devised a gene therapy strategy that reactivated border-forming cells and improved the neurological recovery in old mice.

## 5.4 Future directions

The work presented in this thesis is a critical resource that will serve as a cornerstone for our future and present research. The Tabulae Paralytica establishes a comprehensive understanding of spinal cord cell populations and their responses to injury that has been instrumental in guiding our exploration into various aspects of spinal cord injury, including hemodynamic instability and specific regions such as the cervical area.

Future work will focus on identifying biomarkers which can be used as a tool to identify lesion severity to guide the design of personalized regenerative strategies to repair the injured spinal cord. Towards this, we plan to extend our comprehensive atlases using a combinatorial approach, varying different injury severities and timepoints at the hyperacute phase post injury.

Additionally, we are now focusing our efforts to develop a cross species atlas that can be used to

identify conserved and divergent transcriptional programs across a range of animal species ranging from animals which possess the spontaneous capacity to regenerate (e.g. zebrafish, salamanders), to species which possess extremely poor regenerative capabilities (non-human primates, humans). We anticipate that this comparative atlas will identify novel potential therapeutic targets which can be leveraged to harness the regenerative capability of the injured mammalian nervous system.

# Bibliography

Alizadeh, A., Dyck, S. M., & Karimi-Abdolrezaee, S. (2019). Traumatic spinal cord injury: An overview of pathophysiology, models and acute injury mechanisms. *Frontiers in neurology*, *10*, 282. https://doi.org/10.3389/fneur.2019.00282

Ahuja, C. S., Wilson, J. R., Nori, S., Kotter, M. R. N., Druschel, C., Curt, A., & Fehlings, M. G. (2017). Traumatic spinal cord injury. *Nature reviews. Disease primers*, *3*, 17018. https://doi.org/10.1038/nrdp.2017.18

Dobkin, B., Barbeau, H., Deforge, D., Ditunno, J., Elashoff, R., Apple, D., Basso, M., Behrman, A., Harkema, S., Saulino, M., Scott, M., & Group, S. C. I. L. T. (2007). The evolution of walking-related outcomes over the first 12 weeks of rehabilitation for incomplete traumatic spinal cord injury: The multicenter randomized spinal cord injury locomotor trial. *Neurorehabilitation and Neural Repair*, *21*(1), 25–35. https://doi.org/10.1177/1545968306295556

Krueger, H., Noonan, V. K., Trenaman, L. M., Joshi, P., & Rivers, C. S. (2013). The economic burden of traumatic spinal cord injury in canada. *Chronic diseases and injuries in Canada*, *33*(3), 113–122. https://doi.org/10.24095/hpcdp.33.3.01

Lorach, H., Galvez, A., Spagnolo, V., Martel, F., Karakas, S., Intering, N., Vat, M., Faivre, O., Harte, C., Komi, S., Ravier, J., Collin, T., Coquoz, L., Sakr, I., Baaklini, E., Hernandez-Charpak, S. D., Dumont, G., Buschman, R., Buse, N., . . . Courtine, G. (2023). Walking naturally after spinal cord injury using a brain-spine interface. *Nature*, *618*(7963), 126–133. https://doi.org/10.1038/s41586-023-06094-5

van den Brand, R., Heutschi, J., Barraud, Q., DiGiovanna, J., Bartholdi, K., Huerlimann, M., Friedli, L., Vollenweider, I., Moraud, E. M., Duis, S., Dominici, N., Micera, S., Musienko, P., & Courtine, G. (2012). Restoring voluntary control of locomotion after paralyzing spinal cord injury. *Science*, *336*(6085), 1182–1185. https://doi.org/10.1126/science.1217416

Wagner, F. B., Mignardot, J.-B., Le Goff-Mignardot, C. G., Demesmaeker, R., Komi, S., Capogrosso, M., Rowald, A., Seáñez, I., Caban, M., Pirondini, E., Vat, M., McCracken, L. A., Heimgartner, R., Fodor, I., Watrin, A., Seguin, P., Paoles, E., Van Den Keybus, K., Eberle, G., . . . Courtine, G. (2018). Targeted neurotechnology restores walking in humans with spinal cord injury. *Nature*, *563*(7729), 65–71. https://doi.org/10.1038/s41586-018-0649-2

Squair, J. W., Gautier, M., Mahe, L., Soriano, J. E., Rowald, A., Bichat, A., Cho, N., Anderson, M. A., James, N. D., Gandar, J., Incognito, A. V., Schiavone, G., Sarafis, Z. K., Laskaratos, A., Bartholdi, K., Demesmaeker, R., Komi, S., Moerman, C., Vaseghi, B., . . . Phillips, A. A. (2021). Neuro-

prosthetic baroreflex controls haemodynamics after spinal cord injury. *Nature, 590*(7845), 308–314. https://doi.org/10.1038/s41586-020-03180-w

Amar, A. P., & Levy, M. L. (1999). Pathogenesis and pharmacological strategies for mitigating secondary damage in acute spinal cord injury. *Neurosurgery, 44*(5), 1027–39, discussion 1039. https://doi.org/10.1097/00006123-199905000-00052

Bartholdi, D., & Schwab, M. E. (1997). Expression of pro-inflammatory cytokine and chemokine mRNA upon experimental spinal cord injury in mouse: An in situ hybridization study. *The European Journal of Neuroscience, 9*(7), 1422–1438. https://doi.org/10.1111/j.1460-9568.1997.tb01497.x

Dusart, I., & Schwab, M. E. (1994). Secondary cell death and the inflammatory reaction after dorsal hemisection of the rat spinal cord. *The European Journal of Neuroscience, 6*(5), 712–724. https://doi.org/10.1111/j.1460-9568.1994.tb00983.x

Kerr, B. J., & Patterson, P. H. (2004). Potent pro-inflammatory actions of leukemia inhibitory factor in the spinal cord of the adult mouse. *Experimental Neurology, 188*(2), 391–407. https://doi.org/10.1016/j.expneurol.2004.04.012

Popovich, P. G., Wei, P., & Stokes, B. T. (1997). Cellular inflammatory response after spinal cord injury in sprague-dawley and lewis rats. *The Journal of Comparative Neurology, 377*(3), 443–464. https://doi.org/10.1002/(sici)1096-9861(19970120)377:3\textless443::aid-cne10\textgreater3.0.co;2-s

Cuzzocrea, S., Riley, D. P., Caputi, A. P., & Salvemini, D. (2001). Antioxidant therapy: A new pharmacological approach in shock, inflammation, and ischemia/reperfusion injury. *Pharmacological Reviews, 53*(1), 135–159. Retrieved September 30, 2019, from https://www.ncbi.nlm.nih.gov/pubmed/11171943

Hall, E. D., & Braughler, J. M. (1993). Free radicals in CNS injury. *Research publications - Association for Research in Nervous and Mental Disease, 71*, 81–105. Retrieved October 10, 2023, from https://www.ncbi.nlm.nih.gov/pubmed/8380240

Delahaye-Duriez, A., Srivastava, P., Shkura, K., Langley, S. R., Laaniste, L., Moreno-Moral, A., Danis, B., Mazzuferi, M., Foerch, P., Gazina, E. V., Richards, K., Petrou, S., Kaminski, R. M., Petretto, E., & Johnson, M. R. (2016). Rare and common epilepsies converge on a shared gene regulatory network providing opportunities for novel antiepileptic drug discovery. *Genome Biology, 17*(1), 245. https://doi.org/10.1186/s13059-016-1097-7

Parikshak, N. N., Luo, R., Zhang, A., Won, H., Lowe, J. K., Chandran, V., Horvath, S., & Geschwind, D. H. (2013). Integrative functional genomic analyses implicate specific molecular pathways and circuits in autism. *Cell, 155*(5), 1008–1021. https://doi.org/10.1016/j.cell.2013.10.031

Voineagu, I., Wang, X., Johnston, P., Lowe, J. K., Tian, Y., Horvath, S., Mill, J., Cantor, R. M., Blencowe, B. J., & Geschwind, D. H. (2011). Transcriptomic analysis of autistic brain reveals convergent molecular pathology. *Nature, 474*(7351), 380–384. https://doi.org/10.1038/nature10110

Zhang, B., Gaiteri, C., Bodea, L.-G., Wang, Z., McElwee, J., Podtelezhnikov, A. A., Zhang, C., Xie, T., Tran, L., Dobrin, R., Fluder, E., Clurman, B., Melquist, S., Narayanan, M., Suver, C., Shah, H., Mahajan, M., Gillis, T., Mysore, J., . . . Emilsson, V. (2013). Integrated systems approach

identifies genetic nodes and networks in late-onset alzheimer's disease. *Cell*, *153*(3), 707–720. https://doi.org/10.1016/j.cell.2013.03.030

Svensson, V., Vento-Tormo, R., & Teichmann, S. A. (2018). Exponential scaling of single-cell RNA-seq in the past decade. *Nature Protocols*, *13*(4), 599–604. https://doi.org/10.1038/nprot.2017.149

Shalek, A. K., Satija, R., Shuga, J., Trombetta, J. J., Gennert, D., Lu, D., Chen, P., Gertner, R. S., Gaublomme, J. T., Yosef, N., Schwartz, S., Fowler, B., Weaver, S., Wang, J., Wang, X., Ding, R., Raychowdhury, R., Friedman, N., Hacohen, N., . . . Regev, A. (2014). Single-cell RNA-seq reveals dynamic paracrine control of cellular variation. *Nature*, *510*(7505), 363–369. https://doi.org/10.1038/nature13437

Treutlein, B., Brownfield, D. G., Wu, A. R., Neff, N. F., Mantalas, G. L., Espinoza, F. H., Desai, T. J., Krasnow, M. A., & Quake, S. R. (2014). Reconstructing lineage hierarchies of the distal lung epithelium using single-cell RNA-seq. *Nature*, *509*(7500), 371–375. https://doi.org/10.1038/nature13173

Klein, A. M., Mazutis, L., Akartuna, I., Tallapragada, N., Veres, A., Li, V., Peshkin, L., Weitz, D. A., & Kirschner, M. W. (2015). Droplet barcoding for single-cell transcriptomics applied to embryonic stem cells. *Cell*, *161*(5), 1187–1201. https://doi.org/10.1016/j.cell.2015.04.044

Macosko, E. Z., Basu, A., Satija, R., Nemesh, J., Shekhar, K., Goldman, M., Tirosh, I., Bialas, A. R., Kamitaki, N., Martersteck, E. M., Trombetta, J. J., Weitz, D. A., Sanes, J. R., Shalek, A. K., Regev, A., & McCarroll, S. A. (2015). Highly parallel genome-wide expression profiling of individual cells using nanoliter droplets. *Cell*, *161*(5), 1202–1214. https://doi.org/10.1016/j.cell.2015.05.002

Zeisel, A., Hochgerner, H., Lönnerberg, P., Johnsson, A., Memic, F., van der Zwan, J., Häring, M., Braun, E., Borm, L. E., La Manno, G., Codeluppi, S., Furlan, A., Lee, K., Skene, N., Harris, K. D., Hjerling-Leffler, J., Arenas, E., Ernfors, P., Marklund, U., & Linnarsson, S. (2018). Molecular architecture of the mouse nervous system. *Cell*, *174*(4), 999–1014.e22. https://doi.org/10.1016/j.cell.2018.06.021

La Manno, G., Siletti, K., Furlan, A., Gyllborg, D., Vinsland, E., Mossi Albiach, A., Mattsson Langseth, C., Khven, I., Lederer, A. R., Dratva, L. M., Johnsson, A., Nilsson, M., Lönnerberg, P., & Linnarsson, S. (2021). Molecular architecture of the developing mouse brain. *Nature*, *596*(7870), 92–96. https://doi.org/10.1038/s41586-021-03775-x

Delile, J., Rayon, T., Melchionda, M., Edwards, A., Briscoe, J., & Sagner, A. (2019). Single cell transcriptomics reveals spatial and temporal dynamics of gene expression in the developing mouse spinal cord. *Development*, *146*(12). https://doi.org/10.1242/dev.173807

Häring, M., Zeisel, A., Hochgerner, H., Rinwa, P., Jakobsson, J. E. T., Lönnerberg, P., La Manno, G., Sharma, N., Borgius, L., Kiehn, O., Lagerström, M. C., Linnarsson, S., & Ernfors, P. (2018). Neuronal atlas of the dorsal horn defines its architecture and links sensory input to transcriptional cell types. *Nature Neuroscience*, *21*(6), 869–880. https://doi.org/10.1038/s41593-018-0141-1

Osseward, P. J., Amin, N. D., Moore, J. D., Temple, B. A., Barriga, B. K., Bachmann, L. C., Beltran, F., Gullo, M., Clark, R. C., Driscoll, S. P., Pfaff, S. L., & Hayashi, M. (2021). Conserved

genetic signatures parcellate cardinal spinal neuron classes into local and projection subsets. *Science*, *372*(6540), 385–393. https://doi.org/10.1126/science.abe0690

Rosenberg, A. B., Roco, C. M., Muscat, R. A., Kuchina, A., Sample, P., Yao, Z., Graybuck, L. T., Peeler, D. J., Mukherjee, S., Chen, W., Pun, S. H., Sellers, D. L., Tasic, B., & Seelig, G. (2018). Single-cell profiling of the developing mouse brain and spinal cord with split-pool barcoding. *Science*, *360*(6385), 176–182. https://doi.org/10.1126/science.aam8999

Russ, D. E., Cross, R. B. P., Li, L., Koch, S. C., Matson, K. J. E., Yadav, A., Alkaslasi, M. R., Lee, D. I., Le Pichon, C. E., Menon, V., & Levine, A. J. (2021). A harmonized atlas of mouse spinal cord cell types and their spatial organization. *Nature Communications*, *12*(1), 5722. https://doi.org/10.1038/s41467-021-25125-1

Sathyamurthy, A., Johnson, K. R., Matson, K. J. E., Dobrott, C. I., Li, L., Ryba, A. R., Bergman, T. B., Kelly, M. C., Kelley, M. W., & Levine, A. J. (2018). Massively parallel single nucleus transcriptional profiling defines spinal cord neurons and their activity during behavior. *Cell reports*, *22*(8), 2216–2225. https://doi.org/10.1016/j.celrep.2018.02.003

Skinnider, M. A., Squair, J. W., Kathe, C., Anderson, M. A., Gautier, M., Matson, K. J. E., Milano, M., Hutson, T. H., Barraud, Q., Phillips, A. A., Foster, L. J., La Manno, G., Levine, A. J., & Courtine, G. (2021). Cell type prioritization in single-cell data. *Nature Biotechnology*, *39*(1), 30–34. https://doi.org/10.1038/s41587-020-0605-1

Arneson, D., Zhang, G., Ying, Z., Zhuang, Y., Byun, H. R., Ahn, I. S., Gomez-Pinilla, F., & Yang, X. (2018). Single cell molecular alterations reveal target cells and pathways of concussive brain injury. *Nature Communications*, *9*(1), 3894. https://doi.org/10.1038/s41467-018-06222-0

Avey, D., Sankararaman, S., Yim, A. K. Y., Barve, R., Milbrandt, J., & Mitra, R. D. (2018). Single-cell RNA-seq uncovers a robust transcriptional response to morphine by glia. *Cell reports*, *24*(13), 3619–3629.e4. https://doi.org/10.1016/j.celrep.2018.08.080

Bhattacherjee, A., Djekidel, M. N., Chen, R., Chen, W., Tuesta, L. M., & Zhang, Y. (2019). Cell type-specific transcriptional programs in mouse prefrontal cortex during adolescence and addiction. *Nature Communications*, *10*(1), 4169. https://doi.org/10.1038/s41467-019-12054-3

Davie, K., Janssens, J., Koldere, D., De Waegeneer, M., Pech, U., Kreft, Ł., Aibar, S., Makhzami, S., Christiaens, V., Bravo González-Blas, C., Poovathingal, S., Hulselmans, G., Spanier, K. I., Moerman, T., Vanspauwen, B., Geurs, S., Voet, T., Lammertyn, J., Thienpont, B., . . . Aerts, S. (2018). A single-cell transcriptome atlas of the aging drosophila brain. *Cell*, *174*(4), 982–998.e20. https://doi.org/10.1016/j.cell.2018.05.057

Grubman, A., Chew, G., Ouyang, J. F., Sun, G., Choo, X. Y., McLean, C., Simmons, R. K., Buckberry, S., Vargas-Landin, D. B., Poppe, D., Pflueger, J., Lister, R., Rackham, O. J. L., Petretto, E., & Polo, J. M. (2019). A single-cell atlas of entorhinal cortex from individuals with alzheimer's disease reveals cell-type-specific gene expression regulation. *Nature Neuroscience*, *22*(12), 2087–2097. https://doi.org/10.1038/s41593-019-0539-4

Hrvatin, S., Hochbaum, D. R., Nagy, M. A., Cicconet, M., Robertson, K., Cheadle, L., Zilionis, R., Ratner, A., Borges-Monroy, R., Klein, A. M., Sabatini, B. L., & Greenberg, M. E. (2018). Single-

cell analysis of experience-dependent transcriptomic states in the mouse visual cortex. *Nature Neuroscience*, *21*(1), 120–129. https://doi.org/10.1038/s41593-017-0029-5

Hu, P., Fabyanic, E., Kwon, D. Y., Tang, S., Zhou, Z., & Wu, H. (2017). Dissecting cell-type composition and activity-dependent transcriptional state in mammalian brains by massively parallel single-nucleus RNA-seq. *Molecular Cell*, *68*(5), 1006–1015.e7. https://doi.org/10.1016/j.molcel.2017.11.017

Kim, D.-W., Yao, Z., Graybuck, L. T., Kim, T. K., Nguyen, T. N., Smith, K. A., Fong, O., Yi, L., Koulena, N., Pierson, N., Shah, S., Lo, L., Pool, A.-H., Oka, Y., Pachter, L., Cai, L., Tasic, B., Zeng, H., & Anderson, D. J. (2019). Multimodal analysis of cell types in a hypothalamic node controlling social behavior. *Cell*, *179*(3), 713–728.e17. https://doi.org/10.1016/j.cell.2019.09.020

Mathys, H., Davila-Velderrain, J., Peng, Z., Gao, F., Mohammadi, S., Young, J. Z., Menon, M., He, L., Abdurrob, F., Jiang, X., Martorell, A. J., Ransohoff, R. M., Hafler, B. P., Bennett, D. A., Kellis, M., & Tsai, L.-H. (2019). Single-cell transcriptomic analysis of alzheimer's disease. *Nature*, *570*(7761), 332–337. https://doi.org/10.1038/s41586-019-1195-2

Ximerakis, M., Lipnick, S. L., Innes, B. T., Simmons, S. K., Adiconis, X., Dionne, D., Mayweather, B. A., Nguyen, L., Niziolek, Z., Ozek, C., Butty, V. L., Isserlin, R., Buchanan, S. M., Levine, S. S., Regev, A., Bader, G. D., Levin, J. Z., & Rubin, L. L. (2019). Single-cell transcriptomic profiling of the aging mouse brain. *Nature Neuroscience*, *22*(10), 1696–1708. https://doi.org/10.1038/s41593-019-0491-3

Kathe, C., Skinnider, M. A., Hutson, T. H., Regazzi, N., Gautier, M., Demesmaeker, R., Komi, S., Ceto, S., James, N. D., Cho, N., Baud, L., Galan, K., Matson, K. J. E., Rowald, A., Kim, K., Wang, R., Minassian, K., Prior, J. O., Asboth, L., . . . Courtine, G. (2022). The neurons that restore walking after paralysis. *Nature*, *611*(7936), 540–547. https://doi.org/10.1038/s41586-022-05385-7

Hrvatin, S., Sun, S., Wilcox, O. F., Yao, H., Lavin-Peter, A. J., Cicconet, M., Assad, E. G., Palmer, M. E., Aronson, S., Banks, A. S., Griffith, E. C., & Greenberg, M. E. (2020). Neurons that regulate mouse torpor. *Nature*, *583*(7814), 115–121. https://doi.org/10.1038/s41586-020-2387-5

Ayyaz, A., Kumar, S., Sangiorgi, B., Ghoshal, B., Gosio, J., Ouladan, S., Fink, M., Barutcu, S., Trcka, D., Shen, J., Chan, K., Wrana, J. L., & Gregorieff, A. (2019). Single-cell transcriptomes of the regenerating intestine reveal a revival stem cell. *Nature*, *569*(7754), 121–125. https://doi.org/10.1038/s41586-019-1154-y

Aztekin, C., Hiscock, T. W., Marioni, J. C., Gurdon, J. B., Simons, B. D., & Jullien, J. (2019). Identification of a regeneration-organizing cell in the xenopus tail. *Science*, *364*(6441), 653–658. https://doi.org/10.1126/science.aav9996

Fincher, C. T., Wurtzel, O., de Hoog, T., Kravarik, K. M., & Reddien, P. W. (2018). Cell type transcriptome atlas for the planarian schmidtea mediterranea. *Science*, *360*(6391). https://doi.org/10.1126/science.aaq1736

Plass, M., Solana, J., Wolf, F. A., Ayoub, S., Misios, A., Glažar, P., Obermayer, B., Theis, F. J., Kocks, C., & Rajewsky, N. (2018). Cell type atlas and lineage tree of a whole complex animal by single-cell transcriptomics. *Science*, *360*(6391). https://doi.org/10.1126/science.aaq1723

Siebert, S., Farrell, J. A., Cazet, J. F., Abeykoon, Y., Primack, A. S., Schnitzler, C. E., & Juliano, C. E. (2019). Stem cell differentiation trajectories in hydra resolved at single-cell resolution. *Science*, *365*(6451). https://doi.org/10.1126/science.aav9314

Esposito, M. S., Capelli, P., & Arber, S. (2014). Brainstem nucleus MdV mediates skilled forelimb motor tasks. *Nature*, *508*(7496), 351–356. https://doi.org/10.1038/nature13023

Ruder, L., Schina, R., Kanodia, H., Valencia-Garcia, S., Pivetta, C., & Arber, S. (2021). A functional map for diverse forelimb actions within brainstem circuitry. *Nature*, *590*(7846), 445–450. https://doi.org/10.1038/s41586-020-03080-z

Asboth, L., Friedli, L., Beauparlant, J., Martinez-Gonzalez, C., Anil, S., Rey, E., Baud, L., Pidpruzh-nykova, G., Anderson, M. A., Shkorbatova, P., Batti, L., Pagès, S., Kreider, J., Schneider, B. L., Barraud, Q., & Courtine, G. (2018). Cortico-reticulo-spinal circuit reorganization enables functional recovery after severe spinal cord contusion. *Nature Neuroscience*, *21*(4), 576–588. https://doi.org/10.1038/s41593-018-0093-5

Capelli, P., Pivetta, C., Soledad Esposito, M., & Arber, S. (2017). Locomotor speed control circuits in the caudal brainstem. *Nature*, *551*(7680), 373–377. https://doi.org/10.1038/nature24064

Choi, S., Hachisuka, J., Brett, M. A., Magee, A. R., Omori, Y., Iqbal, N.-U.-A., Zhang, D., DeLisle, M. M., Wolfson, R. L., Bai, L., Santiago, C., Gong, S., Goulding, M., Heintz, N., Koerber, H. R., Ross, S. E., & Ginty, D. D. (2020). Parallel ascending spinal pathways for affective touch and pain. *Nature*, *587*(7833), 258–263. https://doi.org/10.1038/s41586-020-2860-1

Gatto, G., Bourane, S., Ren, X., Di Costanzo, S., Fenton, P. K., Halder, P., Seal, R. P., & Goulding, M. D. (2021). A functional topographic map for spinal sensorimotor reflexes. *Neuron*, *109*(1), 91–104.e5. https://doi.org/10.1016/j.neuron.2020.10.003

Leung, L. C., Wang, G. X., Madelaine, R., Skariah, G., Kawakami, K., Deisseroth, K., Urban, A. E., & Mourrain, P. (2019). Neural signatures of sleep in zebrafish. *Nature*, *571*(7764), 198–204. https://doi.org/10.1038/s41586-019-1336-7

Betley, J. N., Xu, S., Cao, Z. F. H., Gong, R., Magnus, C. J., Yu, Y., & Sternson, S. M. (2015). Neurons for hunger and thirst transmit a negative-valence teaching signal. *Nature*, *521*(7551), 180–185. https://doi.org/10.1038/nature14416

Nagano, T., Lubling, Y., Stevens, T. J., Schoenfelder, S., Yaffe, E., Dean, W., Laue, E. D., Tanay, A., & Fraser, P. (2013). Single-cell hi-c reveals cell-to-cell variability in chromosome structure. *Nature*, *502*(7469), 59–64. https://doi.org/10.1038/nature12593

Buenrostro, J. D., Wu, B., Litzenburger, U. M., Ruff, D., Gonzales, M. L., Snyder, M. P., Chang, H. Y., & Greenleaf, W. J. (2015). Single-cell chromatin accessibility reveals principles of regulatory variation. *Nature*, *523*(7561), 486–490. https://doi.org/10.1038/nature14590

Cusanovich, D. A., Daza, R., Adey, A., Pliner, H. A., Christiansen, L., Gunderson, K. L., Steemers, F. J., Trapnell, C., & Shendure, J. (2015). Multiplex single cell profiling of chromatin accessibility by combinatorial cellular indexing. *Science*, *348*(6237), 910–914. https://doi.org/10.1126/science.aab1601

Carter, B., Ku, W. L., Kang, J. Y., Hu, G., Perrie, J., Tang, Q., & Zhao, K. (2019). Mapping histone modi-fications in low cell number and single cells using antibody-guided chromatin tagmentation

(ACT-seq). *Nature Communications*, *10*(1), 3747. https://doi.org/10.1038/s41467-019-11559-1

Harada, A., Maehara, K., Handa, T., Arimura, Y., Nogami, J., Hayashi-Takanaka, Y., Shirahige, K., Kurumizaka, H., Kimura, H., & Ohkawa, Y. (2019). A chromatin integration labelling method enables epigenomic profiling with lower input. *Nature Cell Biology*, *21*(2), 287–296. https://doi.org/10.1038/s41556-018-0248-3

Kaya-Okur, H. S., Wu, S. J., Codomo, C. A., Pledger, E. S., Bryson, T. D., Henikoff, J. G., Ahmad, K., & Henikoff, S. (2019). Cuttag for efficient epigenomic profiling of small samples and single cells. *Nature Communications*, *10*(1), 1930. https://doi.org/10.1038/s41467-019-09982-5

Hainer, S. J., Bošković, A., McCannell, K. N., Rando, O. J., & Fazzio, T. G. (2019). Profiling of pluripotency factors in single cells and early embryos. *Cell*, *177*(5), 1319–1329.e11. https://doi.org/10.1016/j.cell.2019.03.014

Rotem, A., Ram, O., Shoresh, N., Sperling, R. A., Goren, A., Weitz, D. A., & Bernstein, B. E. (2015). Single-cell ChIP-seq reveals cell subpopulations defined by chromatin state. *Nature Biotechnology*, *33*(11), 1165–1172. https://doi.org/10.1038/nbt.3383

Guo, H., Zhu, P., Wu, X., Li, X., Wen, L., & Tang, F. (2013). Single-cell methylome landscapes of mouse embryonic stem cells and early embryos analyzed using reduced representation bisulfite sequencing. *Genome Research*, *23*(12), 2126–2135. https://doi.org/10.1101/gr.161679.113

Mooijman, D., Dey, S. S., Boisset, J.-C., Crosetto, N., & van Oudenaarden, A. (2016). Single-cell 5hmC sequencing reveals chromosome-wide cell-to-cell variability and enables lineage reconstruction. *Nature Biotechnology*, *34*(8), 852–856. https://doi.org/10.1038/nbt.3598

Wu, X., Inoue, A., Suzuki, T., & Zhang, Y. (2017). Simultaneous mapping of active DNA demethylation and sister chromatid exchange in single cells. *Genes & Development*, *31*(5), 511–523. https://doi.org/10.1101/gad.294843.116

Zhu, C., Gao, Y., Guo, H., Xia, B., Song, J., Wu, X., Zeng, H., Kee, K., Tang, F., & Yi, C. (2017). Single-cell 5-formylcytosine landscapes of mammalian early embryos and ESCs at single-base resolution. *Cell Stem Cell*, *20*(5), 720–731.e5. https://doi.org/10.1016/j.stem.2017.02.013

Lareau, C. A., Ludwig, L. S., Muus, C., Gohil, S. H., Zhao, T., Chiang, Z., Pelka, K., Verboon, J. M., Luo, W., Christian, E., Rosebrock, D., Getz, G., Boland, G. M., Chen, F., Buenrostro, J. D., Hacohen, N., Wu, C. J., Aryee, M. J., Regev, A., & Sankaran, V. G. (2021). Massively parallel single-cell mitochondrial DNA genotyping and chromatin profiling. *Nature Biotechnology*, *39*(4), 451–461. https://doi.org/10.1038/s41587-020-0645-6

Cao, J., Cusanovich, D. A., Ramani, V., Aghamirzaie, D., Pliner, H. A., Hill, A. J., Daza, R. M., McFaline-Figueroa, J. L., Packer, J. S., Christiansen, L., Steemers, F. J., Adey, A. C., Trapnell, C., & Shendure, J. (2018). Joint profiling of chromatin accessibility and gene expression in thousands of single cells. *Science*, *361*(6409), 1380–1385. https://doi.org/10.1126/science.aau0730

Chen, S., Lake, B. B., & Zhang, K. (2019). High-throughput sequencing of the transcriptome and chromatin accessibility in the same cell. *Nature Biotechnology*, *37*(12), 1452–1457. https://doi.org/10.1038/s41587-019-0290-0

Fiskin, E., Lareau, C. A., Ludwig, L. S., Eraslan, G., Liu, F., Ring, A. M., Xavier, R. J., & Regev, A. (2022). Single-cell profiling of proteins and chromatin accessibility using PHAGE-ATAC. *Nature Biotechnology*, *40*(3), 374–381. https://doi.org/10.1038/s41587-021-01065-5

Luo, C., Liu, H., Xie, F., Armand, E. J., Siletti, K., Bakken, T. E., Fang, R., Doyle, W. I., Stuart, T., Hodge, R. D., Hu, L., Wang, B.-A., Zhang, Z., Preissl, S., Lee, D.-S., Zhou, J., Niu, S.-Y., Castanon, R., Bartlett, A., … Ecker, J. R. (2022). Single nucleus multi-omics identifies human cortical cell regulatory genome diversity. *Cell Genomics*, *2*(3). https://doi.org/10.1016/j.xgen.2022.100107

Ma, S., Zhang, B., LaFave, L. M., Earl, A. S., Chiang, Z., Hu, Y., Ding, J., Brack, A., Kartha, V. K., Tay, T., Law, T., Lareau, C., Hsu, Y.-C., Regev, A., & Buenrostro, J. D. (2020). Chromatin potential identified by shared single-cell profiling of RNA and chromatin. *Cell*, *183*(4), 1103–1116.e20. https://doi.org/10.1016/j.cell.2020.09.056

Mimitou, E. P., Lareau, C. A., Chen, K. Y., Zorzetto-Fernandes, A. L., Hao, Y., Takeshima, Y., Luo, W., Huang, T.-S., Yeung, B. Z., Papalexi, E., Thakore, P. I., Kibayashi, T., Wing, J. B., Hata, M., Satija, R., Nazor, K. L., Sakaguchi, S., Ludwig, L. S., Sankaran, V. G., … Smibert, P. (2021). Scalable, multimodal profiling of chromatin accessibility, gene expression and protein levels in single cells. *Nature Biotechnology*, *39*(10), 1246–1258. https://doi.org/10.1038/s41587-021-00927-2

Zhu, C., Yu, M., Huang, H., Juric, I., Abnousi, A., Hu, R., Lucero, J., Behrens, M. M., Hu, M., & Ren, B. (2019). An ultra high-throughput method for single-cell joint analysis of open chromatin and transcriptome. *Nature Structural & Molecular Biology*, *26*(11), 1063–1070. https://doi.org/10.1038/s41594-019-0323-x

Zhu, C., Preissl, S., & Ren, B. (2020). Single-cell multimodal omics: The power of many. *Nature Methods*, *17*(1), 11–14. https://doi.org/10.1038/s41592-019-0691-5

Zhu, C., Zhang, Y., Li, Y. E., Lucero, J., Behrens, M. M., & Ren, B. (2021). Joint profiling of histone modifications and transcriptome in single cells from mouse brain. *Nature Methods*, *18*(3), 283–292. https://doi.org/10.1038/s41592-021-01060-3

Maynard, K., Collado-Torres, L., Weber, L., Uytingco, C., Barry, B., Williams, S., Catallini, J., Tran, M., Besich, Z., Tippani, M., Chew, J., Yin, Y., Kleinman, J., Hyde, T., Rao, N., Hicks, S., Martinowich, K., & Jaffe, A. (2021). Transcriptome-scale spatial gene expression in the human dorsolateral prefrontal cortex. *Nature Neuroscience*, *24*(3), 425–436. https://doi.org/10.1038/s41593-020-00787-0

Rao, A., Barkley, D., França, G. S., & Yanai, I. (2021). Exploring tissue architecture using spatial transcriptomics. *Nature*, *596*(7871), 211–220. https://doi.org/10.1038/s41586-021-03634-9

Asp, M., Giacomello, S., Larsson, L., Wu, C., Fürth, D., Qian, X., Wärdell, E., Custodio, J., Reimeg, J., Salmén, F., Österholm, C., St, P. L., Sundström, E., E., Bergmann, O., Bienko, M., M-Broberg, A., Nilsson, M., Sylvén, C., & Lundeberg, J. (2019). A spatiotemporal organ-wide gene expression and cell atlas of the developing human heart. *Cell*, *179*(7), 1647–1660.e19. https://doi.org/10.1016/j.cell.2019.11.025

(BICCN), B. I. C. C. N. (2021). A multimodal cell census and atlas of the mammalian primary motor cortex. *Nature*, *598*(7879), 86–102. https://doi.org/10.1038/s41586-021-03950-0

Lake, B. B., Menon, R., Winfree, S., Hu, Q., Melo Ferreira, R., Kalhor, K., Barwinska, D., Otto, E. A., Ferkowicz, M., Diep, D., Plongthongkum, N., Knoten, A., Urata, S., Mariani, L. H., Naik, A. S., Eddy, S., Zhang, B., Wu, Y., Salamon, D., ... Jain, S. (2023). An atlas of healthy and injured cell states and niches in the human kidney. *Nature*, *619*(7970), 585–594. https://doi.org/10.1038/s41586-023-05769-3

Maniatis, S., Äijö, T., Vickovic, S., Braine, C., Kang, K., Mollbrink, A., Fagegaltier, D., Andrusivová, Ž., Saarenpää, S., Saiz-Castro, G., Cuevas, M., Watters, A., Lundeberg, J., Bonneau, R., & Phatnani, H. (2019). Spatiotemporal dynamics of molecular pathology in amyotrophic lateral sclerosis. *Science*, *364*(6435), 89–93. https://doi.org/10.1126/science.aav9776

Baccin, C., Al-Sabah, J., Velten, L., Helbling, P. M., Grünschläger, F., Hernández-Malmierca, P., Nombela-Arrieta, C., Steinmetz, L. M., Trumpp, A., & Haas, S. (2020). Combined single-cell and spatial transcriptomics reveal the molecular, cellular and spatial bone marrow niche organization. *Nature Cell Biology*, *22*(1), 38–48. https://doi.org/10.1038/s41556-019-0439-6

Chen, H., Murray, E., Sinha, A., Laumas, A., Li, J., Lesman, D., Nie, X., Hotaling, J., Guo, J., Cairns, B. R., Macosko, E. Z., Cheng, C. Y., & Chen, F. (2021). Dissecting mammalian spermatogenesis using spatial transcriptomics. *Cell reports*, *37*(5), 109915. https://doi.org/10.1016/j.celrep.2021.109915

Foster, D. S., Januszyk, M., Yost, K. E., Chinta, M. S., Gulati, G. S., Nguyen, A. T., Burcham, A. R., Salhotra, A., Ransom, R. C., Henn, D., Chen, K., Mascharak, S., Tolentino, K., Titan, A. L., Jones, R. E., da Silva, O., Leavitt, W. T., Marshall, C. D., des Jardins-Park, H. E., ... Longaker, M. T. (2021). Integrated spatial multiomics reveals fibroblast fate during tissue repair. *Proceedings of the National Academy of Sciences of the United States of America*, *118*(41). https://doi.org/10.1073/pnas.2110025118

Srivatsan, S. R., Regier, M. C., Barkan, E., Franks, J. M., Packer, J. S., Grosjean, P., Duran, M., Saxton, S., Ladd, J. J., Spielmann, M., Lois, C., Lampe, P. D., Shendure, J., Stevens, K. R., & Trapnell, C. (2021). Embryo-scale, single-cell spatial transcriptomics. *Science*, *373*(6550), 111–117. https://doi.org/10.1126/science.abb9536

Kuppe, C., Ramirez Flores, R. O., Li, Z., Hayat, S., Levinson, R. T., Liao, X., Hannani, M. T., Tanevski, J., Wünnemann, F., Nagai, J. S., Halder, M., Schumacher, D., Menzel, S., Schäfer, G., Hoeft, K., Cheng, M., Ziegler, S., Zhang, X., Peisker, F., ... Kramann, R. (2022). Spatial multi-omic map of human myocardial infarction. *Nature*, *608*(7924), 766–777. https://doi.org/10.1038/s41586-022-05060-x

Squair, J. W., Milano, M., de Coucy, A., Gautier, M., Skinnider, M. A., James, N. D., Cho, N., Lasne, A., Kathe, C., Hutson, T. H., Ceto, S., Baud, L., Galan, K., Aureli, V., Laskaratos, A., Barraud, Q., Deming, T. J., Kohman, R. E., Schneider, B. L., ... Anderson, M. A. (2023). Recovery of walking after paralysis by regenerating characterized neurons to their natural target region. *Science*, *381*(6664), 1338–1345. https://doi.org/10.1126/science.adi6412

# MATTHIEU GAUTIER, Msc

PhD candidate

## Neuroscience and Bioinformatic

EPFL | Swiss Federal Institute of Technology, Lausanne
.NeuroRestore | Defitech Center for Interventional Neurotherapies

📞 +33 6 66 91 88 16

📍 301 chemin du crêt
01170 GEX, FRANCE

✉ matthieu.bgl@gmail.com

## EDUCATION

2019 - present
**EPFL, Lausanne**
PhD candidate

2017 - 2018
**University of Bordeaux**
Msc in cognitive science

2011 - 2016
**University of Bordeaux & Nantes**
Bachelor in biology

Self education
**Coursera - University of Michigan**
Applied data science with Python

## EXPERIENCE

PhD assistant, .NeuroRestore
2019 - *present*

Designed and executed analysis pipelines investigating spinal cord injury microenvironnement at the single cell resolution

Research assistant, .NeuroRestore
2018 - 2019

Development of a neuroprosthesis to preserve autonomic functions after spinal cord injury

Intern, Laboratory of Pr. Courtine
2018

Analysis of telemetry data in freely moving animals

Intern, Laboratory of Dr. de Rugy
2017

Modeled the evolution of electromyography signals and muscle torque

## SKILLS

| | |
|---|---|
| Programming | R, Python, Java, Bash |
| Bioinformatics | Analysis of sequencing data: Single cell, Multiome, Spatial transcriptomics |

## LANGUAGE

| | |
|---|---|
| Native language | French |
| Fluent | English |

## PUBLICATIONS

*Michael A. Skinnider\*, **Matthieu Gautier\***, Alan Yue Yang Teo, Claudia Kathe, Thomas H. Hutson, Achilleas Laskaratos [...] Jocelyne Bloch, Mark A. Anderson#, Jordan W. Squair#, Grégoire Courtine#*
The Tabulae Paralytica: Multimodal single-cell and spatial atlases of spinal cord injury
**BioRxiv | Nature (accepted manuscript)**
DOI: https://doi.org/10.1101/2023.06.23.544348

# PUBLICATIONS

*Jordan W. Squair\*, Marco Milano\*, Alexandra De Coucy,* **Matthieu Gautier**, *Michael A. Skinnider, Nicholas D. James [...] Jocelyne Bloch, Michael V. Sofroniew, Gregoire Courtine# and Mark A. Anderson#*
Recovery of walking after paralysis by regenerating characterized neurons to their natural target region
**Science**
DOI: 10.1126/science.adi6412

*Mark A. Anderson\*, Jordan W. Squair\*,* **Matthieu Gautier**, *Thomas H. Hutson, Claudia Kathe, Quentin Barraud, Jocelyne Bloch and Grégoire Courtine*
Natural and targeted circuit reorganization after spinal cord injury
**Nature Neuroscience**
DOI: doi.org/10.1038/s41593-022-01196-1

*Jan Elaine Soriano#, Rémi Hudelle#, Jordan W. Squair#, Lois Mahe, Suje Amir,* **Matthieu Gautier**, *Victor Perez Puchalt, Quentin Barraud, Aaron A. Phillips\* and Gregoire Courtine\**
Longitudinal interrogation of sympathetic neural circuits and hemodynamics in preclinical models
**Nature Protocols**
DOI: 10.1038/s41596-022-00764-w

*Claudia Kathe#, Michael A. Skinnider#, Thomas H. Hutson#, Nicola Regazzi,* **Matthieu Gautier**, *Robin Demesmaeker [...] Jocelyne Bloch\*, Jordan W. Squair\* and Grégoire Courtine\**
The neurons that restore walking after paralysis
**Nature**
DOI: 10.1038/s41593-022-01196-1

*Jordan W. Squair,* **Matthieu Gautier**, *Michael V. Sofroniew, Grégoire Courtine, Mark A. Anderson*
Engineering spinal cord repair
**Current Opinion in Biotechnology**
DOI: 10.1016/j.copbio.2021.10.006

*Jordan W. Squair,* **Matthieu Gautier**, *Claudia Kathe, Mark A. Anderson, Nicholas D. James, Thomas H. Hutson, Rémi Hudelle [...] Gioele La Manno, Michael A. Skinnider\* and Grégoire Courtine\**
Confronting false discoveries in single-cell differential expression
**Nature communications**
DOI: https://doi.org/10.1038/s41467-021-25960-2

*Jordan W. Squair\*, Michael Skinnider\*,* **Matthieu Gautier,** *Leonard J. Foster, Grégoire Courtine.*
Prioritization of cell types responsive to biological perturbations in single-cell data with Augur
**Nature Protocols**
DOI: https://doi.org/10.1038/s41596-021-00561-x

*Jordan W. Squair,* **Matthieu Gautier\***, *Lois Mahe\*, Jan Elaine Soriano\*, Andreas Rowald\* [...] Grégoire Courtine# and Aaron A. Phillips#.*
Neuroprosthetics baroreflex controls hemodynamics after spinal cord injury.
**Nature**
DOI: https://doi.org/10.1038/s41586-020-03180-w

*Skinnider, M.A.\*, Squair, J.W.\*, Kathe, C.#, Anderson, M.A.#,* **Gautier, M.#**, *Matson, K.J.E, Milano, M., Hutson, T.H., Barraud, Q., Phillips, A.A., Foster, L.J, La Manno, G., Levine, A.J., and Courtine, G.*
Cell type prioritization in single cell data.
**Nature Biotechnology**
DOI: https://doi.org/10.1101/2019.12.20.884916